Bioactivity of Substituted Copper Pyrithione Complexes

ATREYEE MISHRA

MISHRA, ATREYEE (2022) Bioactivity of Substituted Copper Pyrithione Complexes. Doctoral thesis, Durham University.

Durham University

Department of Chemistry

Bioactivity of Substituted Copper Pyrithione Complexes

Atreyee Mishra

A thesis submitted for the degree of Doctor of Philosophy

August 2022

Dedicated to my Family

Abstract

Over the last century, metal complexes have been popularised in therapeutic drug design. Copper complexes have been particularly interesting due to their high stability constants and unique redox chemistry. Simple copper salts, such as $CuCl_2$ have little cytotoxicity, but ligands have been designed that lead to therapeutically activity copper complexes. The copper complex of pyrithione, a well-known ionophore, has recently been identified as a potent antibacterial and anticancer agent. Copper pyrithione has been shown to inactivate β-lactamase enzymes (such as NDM-1), a key enzyme in the mechanism of antibiotic resistance of multidrug-resistant bacteria. Antibiotic resistance being a great threat to human health around the world, copper pyrithione has potential in the development of new drug molecules. Key issues of this complex remain, including its low bacterial selectivity and poor aqueous solubility. This thesis focuses on structural modifications of the copper pyrithione complex with an aim to improve aqueous solubility, as well as optimise bioactivity as antibacterial and anticancer agents.

The synthesis and characterisation are described of series of novel copper pyrithione complexes with functional groups variation in the pyrithione ligand. Derivatives include electron donating and electron withdrawing groups, aromatic substituents, and polyethylene glycol (PEG) chains. These complexes are subjected to physiochemical property analysis. Binding constant (log K), lipophilicity (log P) and solubility of some selected complexes are determined, and structure-property correlations are established in some cases. PEG-substituted complexes are highly soluble in water and possess a good balance of solubility and lipophilicity.

All complexes are screened against various multidrug-resistant bacterial species and the majority show good activity against Gram-positive bacterial species. One complex, $[Cu(5\text{-Me-}PT)_2]$, shows good selectivity towards bacterial cells over healthy mammalian Vero cells, which augurs well for their use as novel antibiotics. Antibiotic synergy studies of copper pyrithione complexes alongside β-lactam antibiotics are performed, which shows that copper pyrithione complexes can act in combination with known antibiotics (meropenem and ertapenem) to overcome resistance in β-lactam resistant bacterial strains. Furthermore, cytotoxicity studies are performed with pancreatic carcinoma, bone osteosarcoma and healthy retinal epithelial cells, leading to structure-activity relationships to be proposed. Many novel complexes show high anticancer activity, with one complex $[Cu(3\text{-OMe-}PT)_2]$ showing particularly notable activity, with nanomolar inhibitory concentration (IC_{50} value) against pancreatic cancer.

In next part of this project, the synthesis and characterisation of a fluorescent tagged copper pyrithione derivative using an alkyne-azide ‘click’ reaction is described. Photoluminescence properties of this complex are determined utilising UV/Vis absorption and fluorescence spectroscopies. Copper conjugation quenches the fluorescence emission of the fluorescent tag to some extent. Fluorescence microscopy study reveals this complex can enter and be visible inside live cells, showing specific localisation around the endoplasmic reticulum.

Finally, some non-pyrithione copper complexes are described with an oxygen analogue of pyrithione showing particularly good bioactivity against both bacteria and cancer cells.

Declaration

The work described in this thesis was undertaken at the Department of Chemistry, Durham University between February 2019 and July 2022. All the work reported is my own, except where specifically stated otherwise. No part has previously been submitted for a degree at this or any other university.

Signed: Atreyee Mishra

Date: 23.08.2022

Statement of Copyright

Acknowledgement

It is a genuine pleasure to extend my deepest and sincere gratitude to my supervisor, Dr. James Walton, for his help and guidance over the last three and a half years. I wouldn't be here today completing my PhD thesis without his relentless support, constant encouragement, endless optimism and profound belief towards this project and my abilities. I will always be thankful to him for guiding me through this difficult journey and building up my confidence as a chemist as well as a person with his motivational words and valuable advice. I am eternally grateful that I got an opportunity to work under his mentorship and will owe my present and future successes to him.

I would like to express my sincere thanks to Dr. Karrera Djoko, for being an amazing co-supervisor to me. Her scientific advice, timely guidance and comprehensive training have played a crucial role in this thesis. I will forever be grateful to her for the opportunity to get hands-on experience in biological work in her laboratory during my PhD.

Special thanks to our collaborators, Dr. Sidharth Chopra and Dr. Rianne Lord for performing the biological assays and Prof. Robert Pal for the fluorescence microscopy findings. Without their help my PhD project wouldn't have achieve its goal and I am extremely grateful for their time and collaborative works.

I would like to extend my heartfelt gratitude to Durham University technical stuffs, who have always been extremely helpful and approachable. Special mention to Dr Aileen Congreve for helping out with crucial HPLC purification, Dr. Emily Unsworth for performing endless amounts of elemental analysis and Dr. Dmitry Yufit for providing the beautiful crystal data. I would also like to thank Dr. Juan A Aguilar Malavia from NMR spectroscopy and Mr. Peter stokes and Dr. David Parker from Mass spectrometry services for all their help.

My sincere thanks to Dr. Paul McGonigal for providing me with academic advice and being an immense help whenever needed.

I am grateful to Durham University and GCRF-CDT for providing me with funding and resources to work on my project over the past years. I want to express sincere gratitude to Prof. Douglas Halliday and Mrs. Abir Van-Huen from GCRF-CDT, who have always been there as the support system and have extended their help to enrich my experience as a postgraduate researcher, both personally and professionally.

I am also thankful to each and every one in my life who has been a part of this PhD journey.

Luke Williams, thank you for being the best lab mate I could have ever asked for. I will always be thankful for your research help, endless patience in listening to my life and PhD frustrations, late evening writing company and many more things. It has been amazing to do our PhDs together and I am grateful to have you as my friend.

Akkharadet Piyasaengthong (Rak), you have been a true inspiration to me. You have motivated me in every possible way during the most difficult times in lab and been the mentor and elder brother I needed much. Thank you for all the hour-long discussions on research and life-philosophy, helping with lab and so much more.

Walton group all past and present members; David Bradley, thank you for sharing your fume hood, helping me settling down in lab and being my first friend here. Beth Beck, thank you for always being a great help in sorting out the lab and many more other stuffs; Marcus Dennington, thank you for all the brain-storming discussions we had; Libby, Silvia, Alex, Lauren, you all have been amazing to share the lab with.

CG235 past and present members, I am grateful to you all for being amazing colleagues and giving me some lovely memories. Aisha Bismillah, thank you for being so warm to welcome and include me in everything, Abhijit Mallick and Pavan Yerramasetti, thank you for all the brotherly advice, lunch-time stories and food. Phil, Kas, Burhan and Senthil thank you for all the research help and advice. Andrew, Jack, Promeet, Ho-chi, Will, Ash, Rob, Yuzhen, Yulong, Juliet, you all have been wonderful.

Amit Sil and Ishita Dutta, I couldn’t have possibly asked for a better company to spend my most of the PhD life, especially COVID time with. Thank you for turning into my elder brother and sister and giving me the home away from home and endless memories to cherish forever.

My Friends in Durham, Divya, Vaishnavi and Hirunika, thank you girls for all your help and support and filling these three years in Durham with amazing memories. My friends from India, Shilpa, Cavya, Sajina and Sreya; my lovely housemate, Areesha; GCRF-cohort members, and Sheraton house 110 girls, thank you all for being a part of my PhD life.

My parents Debi Prasad Mishra and Seema Mishra, and my brother, Bedangshu Mishra, without whom nothing would have been possible. Thank you for being everything in my life and giving me the strength and courage to go on this journey, always being the best support system and anchors for me. No thanks will be ever enough.

List Of Abbreviations

Ala	alanine
Ar	aryl
Asp	aspartic acid
ASAP	atmospheric solids analysis probe
BDP	boron-dipyrromethene
Bu	butyl
$CHCl_3$	chloroform
d	doublet
DCM	dichloromethane
dd	doublet of doublets
ddd	doublet of doublets of doublets
ddt	doublet of doublets of triplets
DMF	*N*,*N*-dimethylformamide
DNA	deoxyribonucleic acid
dt	doublet of triplets
Cys	cysteine
ESI	electrospray ionisation
ESKAPE	*Enterococcus faecium, Staphylococcus aureus, Klebsiella pneumoniae, Acinetobacter baumannii, Pseudomonas aeruginosa, and Enterobacter spp.*
equiv	equivalent
Et	ethyl
g	gram
h	hours

His	histidine
HPLC	high performance liquid chromatography
HSAB	hard and soft acids and bases
HRMS	high resolution mass spectrometry
Hz	Hertz
hν	irradiation
ICP-OES	inductively coupled plasma optical emission spectroscopy
i	iso
L	litre
LRMS	low resolution mass spectrometry
Lys	lysine
M	molar
m	multiplet
MBL	metallo-β-lactamases
*m*CPBA	*meta*-chloro-perbenzoic acid
MeCN	methanol
MeOH	acetonitrile
Mass Spec	mass spectrometry
Me	methyl
mg	milligram
MIC	minimum inhibitory concentration
ml	millilitre
mmol	millimole
MHz	megahertz
m/z	mass to charge ratio

NBS	*N*-bromosuccinimide
NMR	nuclear magnetic resonance
OMe	methoxy
OEt	ethoxy
o	*ortho*
PEG	Polyethylene glycol
Ph	phenyl
ppm	parts per million
Pr	propyl
PT	pyrithione
q	quartet
RNA	ribonucleic acid
ROS	reactive oxygen species
rt	room temperature
s	singlet
Satd.	saturated
Ser	serine
SM	starting material
S_NAr	nucleophilic aromatic substitution
t	triplet
t	tertiary
td	triplet of doublets
TFA	trifluoroacetic acid
TFAA	trifluoroacetic anhydride
THF	tetrahydrofuran

TLC	thin layer chromatography
Spp.	species
UHP	urea hydrogen peroxide
UV	ultraviolet
Vis	visible

Table of Contents:

2. Modified Copper Pyrithione Complexes 70

3. Increasing Solubility of Copper Pyrithione with Polyethylene Glycol (PEG) Chain Substitution 111

1. Introduction to Antibiotics, Chemotherapy and the Role of Metals in Medicine

1.1 Bacteria and Antibiotics: A Perpetual Battle of Survival

The main aims of this thesis have revolved around developing copper complexes as therapeutic agents against the multi-drug resistant pathogens, bacteria that show high levels of antibiotic resistance. In the following section, an overview of bacterial infection is given, followed by discussion on the development of resistance and the various strategies that are undertaken to overcome this resistance. One key class of enzymes believed to be involved in antibiotic resistance is the metallo-β-lactamases and a specific example, the New-Dehli metallo-β-lactamase-1 (NDM-1) has recently been shown to be inhibited by copper complexes. In the latter part of this section, NDM-1 is introduced and inhibition by copper is discussed, ultimately leading to the hypothesis that copper complexes have the potential to overcome antibiotic resistance various pathogens.

1.1.1 Background to Bacterial Infection

1.1.1.1 Overview of Bacterial Cell and Classification

Bacteria have been one of the most-researched pathogens in medicinal chemistry due to their continuous threat to human health. This oldest life-form on earth is classified as a prokaryotic organism and unlike human and other types of eukaryotic organism cells, bacteria do not contain nucleus or mitochondria/chloroplasts in their cell. Bacterial cells are generally composed of a capsule, cell wall and cell membrane in their outer structure, which encloses their inner cytoplasm containing genetic material (DNA, RNA), ribosomes and other essential proteins and biomolecules (Figure 1.1). Bacterial chromosome is usually of a circular shape, which contains a single stretch of DNA and is situated inside an irregular shaped body named as nucleoid, along with associated RNA and proteins. Bacterial reproduction is very rapid and takes place asexually through binary fission.[1, 2]

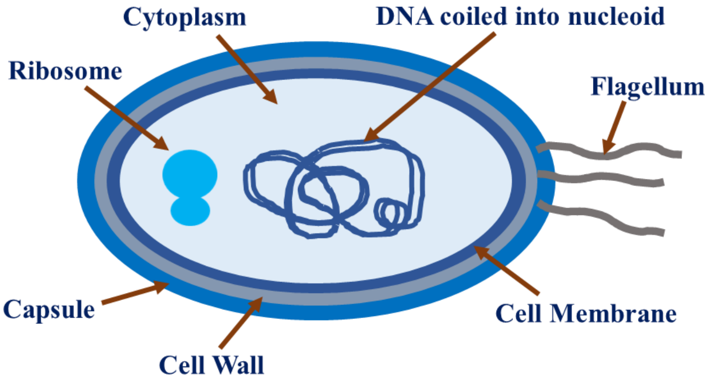

Figure 1.1: General outline of bacterial cell structure

Based on differing extracellular structures, bacterial cells can be broadly categorised into two main categories: Gram-positive and Gram-negative bacteria. The name is associated with the Gram-staining experiment, where bacterial species are stained differently based on the thickness of peptidoglycan (polysaccharide chains with peptide cross-linking) layers in their cell walls.[3] In Gram-positive bacteria (e. g., *Staphylococcus aureus*), the peptidoglycan layers form a thick cell wall and therefore retain the crystal violet stain used in the experiment and appear as purple-coloured under microscope. On the other hand, the cell envelopes of Gram-negative species (e.g., *Escherichia coli*) possess very thin layer of peptidoglycan and an additional membrane layer of lipopolysaccharides (Figure 1.2), and therefore, they do not retain Gram-staining and appear as pink-red in microscopy studies. Due to this difference in extracellular envelopes, the two classes of bacterial species exhibit different susceptibility towards antibiotics and therefore the related bacterial infections require different treatments.[4]

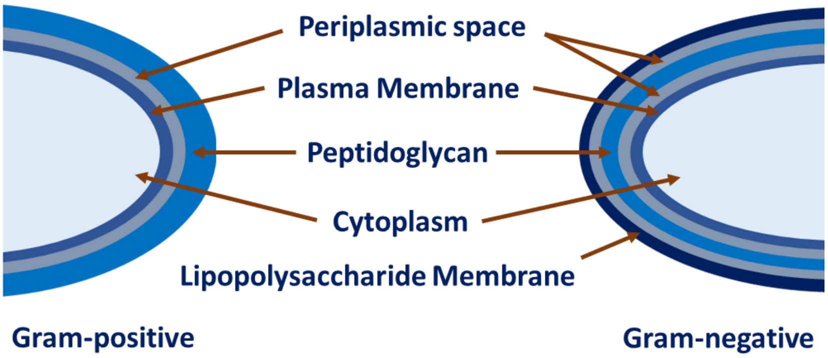

Figure 1.2: Outline of bacterial extracellular structure for Gram-positive and Gram-negative Bacteria

1.1.1.2 Statistics of Bacterial Infections

Bacteria are ubiquitous and make up the majority of Earth's biomass. Many bacterial species are beneficial to human life, but others are considered to be a threat to mankind, due to their infectious properties. Several life-threatening diseases such as pneumonia, meningitis, tuberculosis, gonorrhoea, tetanus, cholera and syphilis are caused by bacterial infections.[4] All over the world and especially in developing countries, several million people die every year due to diseases caused by bacterial infections. According to a WHO report in 2019, lower respiratory tract infections (e.g., pneumonia) stand as the fourth leading cause of death worldwide, taking around 2.6 million lives away every year.[5] Diseases like cholera and tuberculosis also contribute to around 1.6 million deaths yearly.[6,7] Bacterial infection can often lead to sepsis, which is a condition of septic shock, multiple organ failure and ultimately death.

Sepsis is often the final pathway for various infectious diseases, when the immune response of the host towards infection is dysregulated. As stated in a WHO report, sepsis causes roughly 11 million deaths globally per year.[7]

1.1.2 Antibiotics and Antimicrobial Resistance

1.1.2.1 The History of Antibiotics and their Role in Medicinal Chemistry

The surge of deaths from bacterial infections throughout the twentieth century has pushed medicinal chemistry towards developing antibacterial drugs.[8] The earliest example of a bacteriostatic agent is an organoarsenic compound, salvarsan, which was discovered in 1910 and was used for more than three decades to treat bacterial infection.[9] Sulfonamides are another class of bacteriostatic agents, which emerged around 1932 and are used to treat bacterial infection by inducing inhibition of DNA, RNA and protein synthesis in bacteria.[10] Antibacterial treatment was transformed with the discovery of the first ever bactericidal agent called penicillin by Alexander Fleming in the 1920s, which started the modern era of antibiotics.[11] This valuable drug was first isolated from a species of fungi called *Penicillium notatum*, and was observed to affect the growth of a common bacterial species, *S. aureus.* The first generation of penicillin was found to have quite a narrow spectrum of bacterial susceptibility. In the 1960s, ampicillin and amoxicillin were discovered as the second generation penicillins, which act against a broad spectrum of bacterial species such as *Haemophilus influenza, E. coli, Listeria monocytogenes, Bacillus anthracis etc.*[12] In 1943, streptomycin was discovered, which was the first treatment for tuberculosis. This drug has since been used to treat infections caused by a broad spectrum of Gram-negative bacteria (e.g. - *Klebsiella pneumoniae, E. coli, Proteus spp*.) and Gram-positive bacteria (e.g., *Streptococcus viridans* and *Enterococcus faecalis*). Since their discovery, these drugs have saved many lives and continue to do so (Figure 1.3).[13]

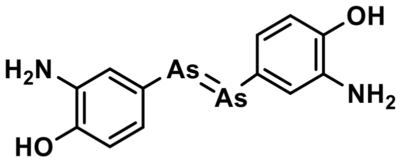

Salvarsan

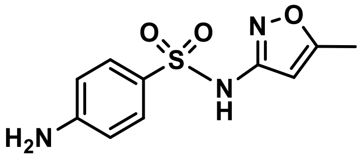

Sulfonamide

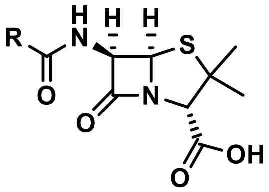

Penicillins

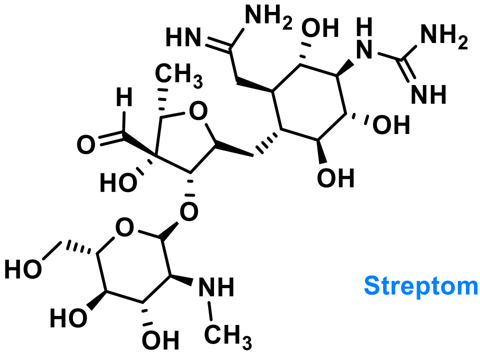

Streptomycins

Figure 1.3: Structure of some early antibiotic drugs

1.1.2.2 Mechanisms of Antibiotic Activity

Antibiotics act selectively on bacterial cells over human cells and cause bacterial cell death through several different mechanisms.[14] Below are listed the five main mechanisms by which antibacterial agents function (Figure 1.4).

1. *Inhibition of the bacterial cell metabolism*: compounds that act via this mechanism are known as antimetabolites. The best examples of this type of compounds are sulfonamides.[15]

2. *Inhibition of cell wall synthesis*: this mechanism leads to cell lysis and cell death of bacteria. β-Lactam antibiotics such as penicillins and cephalosporins come under this category of antibacterial agents. They do not affect eukaryotic cells due to absence of cell walls.[16,17]

3. *Disruption of membrane-permeability*: this mechanism occurs through interaction of drugs with plasma membrane of bacteria cell. Polymyxins and tyrothricin are this type of operators.[18,19]

4. *Inhibition of enzyme and protein synthesis:* antibiotics like rifamycins, chloramphenicols disrupt synthesis of protein and enzymes essential for survival of bacterial cells.[20]

5. *Inhibition of nucleic acid synthesis:* some antibacterial agents (e.g., proflavine) inhibit nucleic acid synthesis, resulting in prevention of bacterial cell division and cell existence.[21]

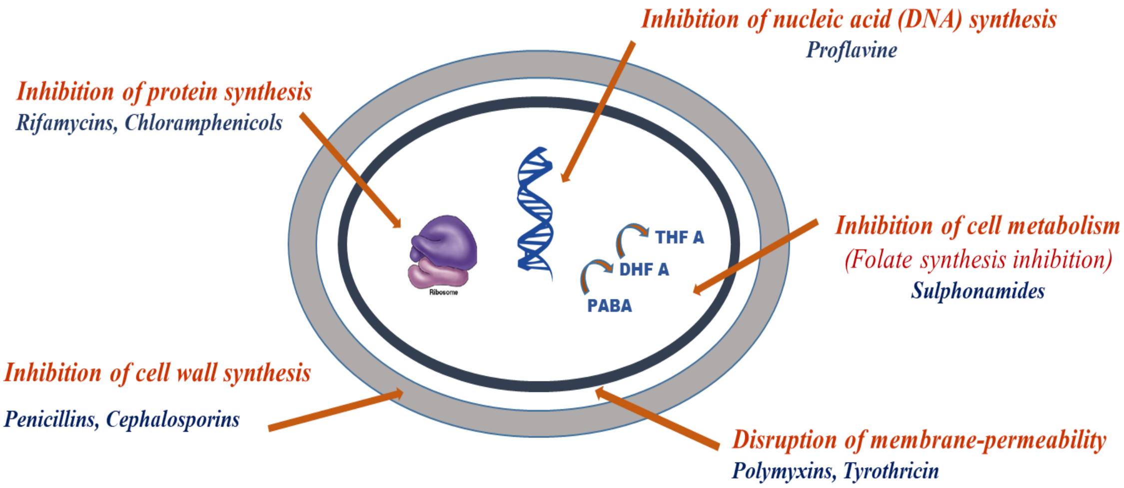

Figure 1.4: Different modes of action of various antibiotics in bacterial cell β-Lactam Antibiotics (PABA = para-aminobenzoic acid, DHF A = dihydofolic acid, THF A = tetrahydrofolic acid)

The most prevalent mechanism of antibiotic activity is via disruption of cell wall synthesis, with the majority of antibiotics of this class described as β-lactam antibiotics. Penicillin was the first β-lactam antibiotic to be discovered and to date, many new penicillin derivatives and related β-lactam classes of cephalosporins, cephamycins, monobactams, and carbapenems have been discovered (Figure 1.5). Each class has similar structural aspects and mechanism of action against bacteria. However, each class has some key structural differences that address or overcome limitations of the earlier classes, usually relating to resistance.[22]

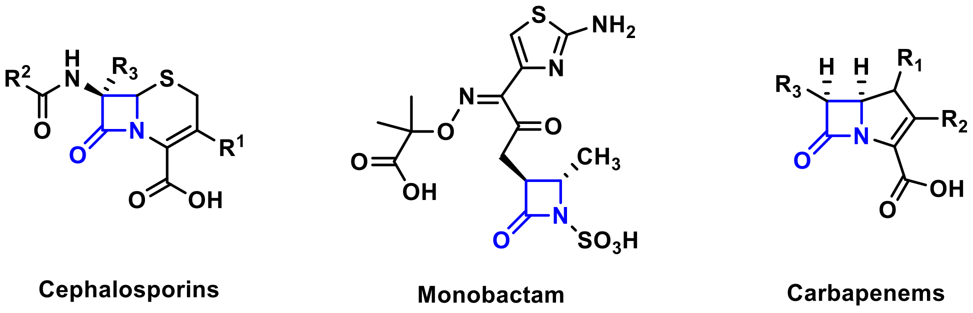

Figure 1.5: Various classes of penicillin derivative drugs

The key structural feature of all classes of β-lactam antibiotics is their strained four-membered β-lactam ring. It possesses two very unique characteristics which lead to the explanation of its structure-activity correlation.[14]

1. *Ring strain:* The four-membered ring is usually fused with another five or six-membered ring. As a result of this bicyclic system, these molecules suffer large angle and torsional strains.

Acid-catalysed ring-opening relieves these strains by breaking highly strained β-lactam ring (Figure 1.6).

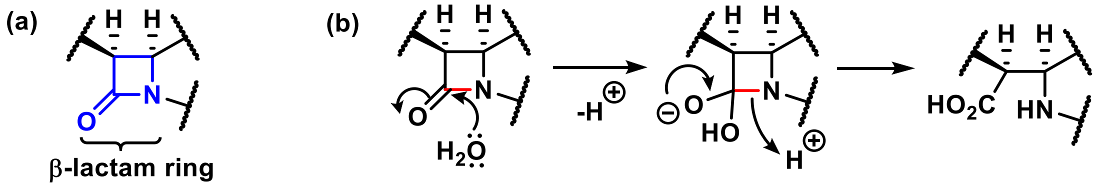

Figure 1.6: (a) β-Lactam ring and (b) Acid hydrolysis of β-lactam ring

2. *β-lactam carbonyl group:* The carbonyl group in the β-lactam ring does not behave like a normal tertiary amide group. The latter is resistant to nucleophilic attack due to stabilization of the carbonyl group by the neighbouring nitrogen atom. In a non-cyclic amide, the lone pair of electrons on nitrogen is donated to the carbonyl group to form a resonance-stabilized structure with bond angles of 120˚. This resonance-stabilization is impossible in the β-lactam ring because of the constrained bond angle (90˚) of a four-membered ring, which disfavours the formation of a double bond (preferred angle is 120˚). As a result, the lone pair is localised on nitrogen atom and the carbonyl group is more electrophilic than an acyclic tertiary amide (Figure 1.7).

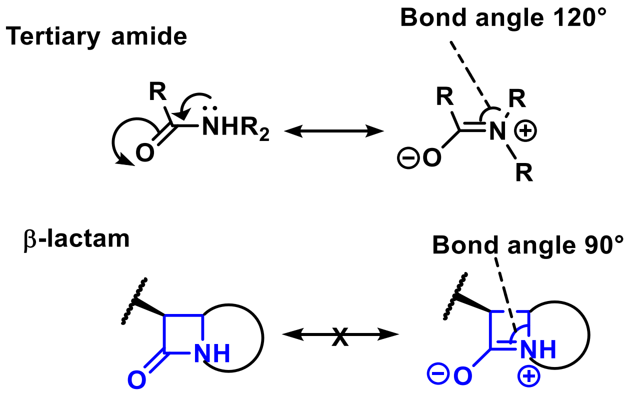

Figure 1.7: The difference between normal tertiary amide and the β-lactam ring

β-Lactam antibiotics exhibit their bactericidal effect by disrupting bacterial cell-wall synthesis.[23] Bacterial cell wall synthesis requires transpeptidase enzymes known as the penicillin binding proteins (PBPs) for cross-linking of the peptidoglycans in the terminal step.[24] There is a structural similarity between the β-lactam antibiotic molecules and the transition-state conformer of the D-Ala-D-Ala dipeptide moiety of the nascent peptidoglycan during the cross-linking reactions. Consequently, the β-lactam antibiotic binds to the enzyme active site. Once bound, the β-lactam ring is subjected to nucleophilic attack by serine from the transpeptidase enzyme. It cleaves the ring in the similar way to peptide bond cleavage to form an ester. Due to the cyclic structure, the whole β-lactam system blocks hydrolysis of the ester, resulting a rather stable non-catalytic acyl-enzyme, which is inactivated (Figure 1.8). The compromised cell wall synthesis eventually causes cell lysis. In this way, interruption of transpeptidation by β-lactam antibiotics leads to the bacterial cell death.[14]

Transpeptidase cross-linking

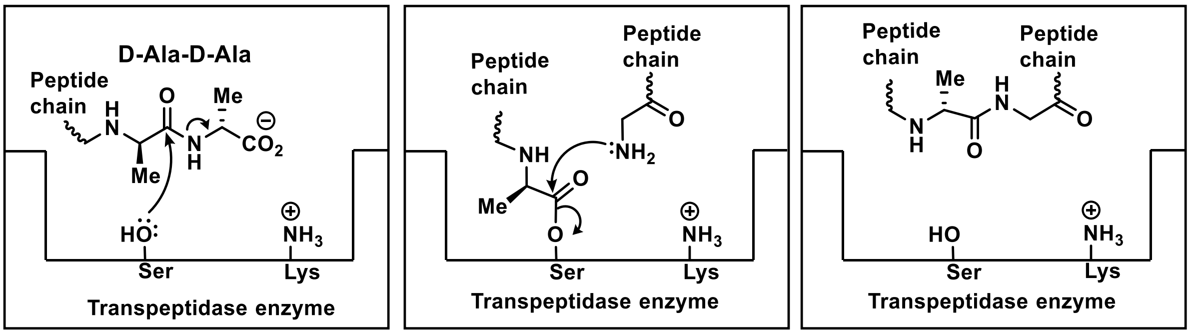

Penicillin inhibition

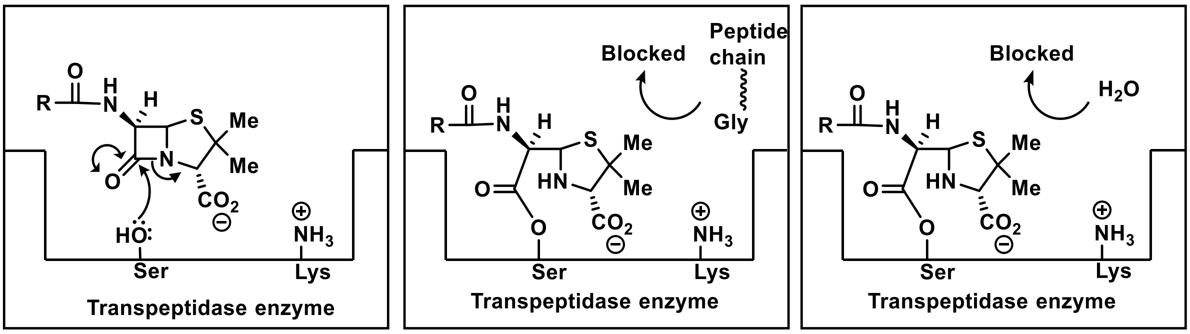

Figure 1.8: The comparative presentation of the mechanism of cross-linking by transpeptidase enzyme for the cell wall synthesis and the mechanism of inhibition of that process by penicillin

1.1.2.3 The Surge of Bacterial Resistance against Antibiotics

The widespread use of antibiotics in health and animal-farming over time has led bacteria to grow resistance against antibacterial agents. The inevitable consequence is the emergence of antibiotic-resistant pathogens around the globe. In 2019, antimicrobial resistance (AMR) directly contributed to 1.27 million deaths, more than that for HIV/AIDS or malaria.[25] Some globally common and health-threatening examples of AMR are rifampicin-resistance in *Mycobacterium tuberculosis,*[26] fluoroquinolone-resistance in *E. coli,*[27] resistance against carbapenem antibiotics against *K. pneumoniae*[28] and many more. This surge in AMR over the last twenty years has left medicinal chemistry in an alarming situation of not having new suitable antibiotics to treat even common bacterial infections. Antibacterial resistance has led to the spread of ‘superbugs’, infectious bacteria or pathogens which cannot be treated by existing antibiotics. Some common superbugs are carbapenem-resistant *Enterobacteriaceae* (CRE)[29] and methicillin-resistant *S. aureus* (MRSA)[30] and the so-called ESKAPE organisms (an acronym for *Enterococcus faecium, S. aureus, K. pneumoniae, A. baumannii, P. aeruginosa,* and *Enterobacter* species).[31] According to a WHO report, these 'superbugs' are one of the biggest threats to the human race. Death rates associated with these superbugs range from 18% to 67% per year, varying across the different countries.[32]

There are four primary mechanisms acquired by bacteria to overcome the bactericidal effect of antibiotics (Figure 1.9).[33]

1. The presence of inactivating enzymes is the most common and important mechanism of resistance to the bactericidal activity of antibiotics. These enzymes help to break down the antibiotic molecular structure, inactivating the antibiotics and thus restoring the infectious properties of the bacteria. The three main antibiotic-inhibiting enzymes are β-lactamases (produced by Gram-negative bacteria which inhibit β-lactam antibiotics such as penicillins, cephalosporins),[34] aminoglycoside-modifying enzymes (identified in *S. aureus, S. pneumoniae* etc. which inhibit aminoglycoside antibiotics such as neomycin, streptomycin)[35] and chloramphenicol acetyltransferases (produced by *H. influenzae* and inhibits chloramphenicol antibiotic).[36]

2. Modification of the molecular target of the antibiotics leads to the antibiotics not binding to or inhibiting their targets successfully. For example, **penicillin binding proteins (PBPs)** can carry a variety of random mutations at the active site residues. Some of these modifications will affect the affinity of β-lactam antibiotics towards the active sites and subsequently increase resistance in bacteria (e.g., *Neisseria* spp. and *Streptococcus* spp.).[37] Furthermore, modifications in **ribosome subunits** 30S and 50S affect the binding of antibacterial drugs to the ribosome. Macrolides, tetracycline, chloramphenicol and aminoglycoside antibiotics usually bind to ribosomes, which suppresses protein synthesis and thus alteration in ribosomes leads to antibiotic inactivation.[38]

3. β-lactam can access PBPs in the inner plasma membrane either through diffusion or by traversing through **porin channels** in the outer membrane of Gram-negative bacterial cell walls. Some bacteria (e.g. - *Enterobacter* spp., *K. pneumoniae* and *E. coli*) exhibit resistance against β-lactam antibiotics based on the **decreased expression of these outer membrane proteins (OMPs).**[39,40]

4. Efflux systems are capable of pumping out unwanted substances from the periplasmic space of bacterial cells. Cytoplasmic membrane proteins can export antimicrobial agents outside the cell, which reduces the intracellular concentrations and therefore antibiotics are unable to reach their targets. These efflux pumps are responsible for multidrug resistance in many Gram-negative bacteria, such as *P. aeruginosa* and *Acinetobacter* spp.[40,41]

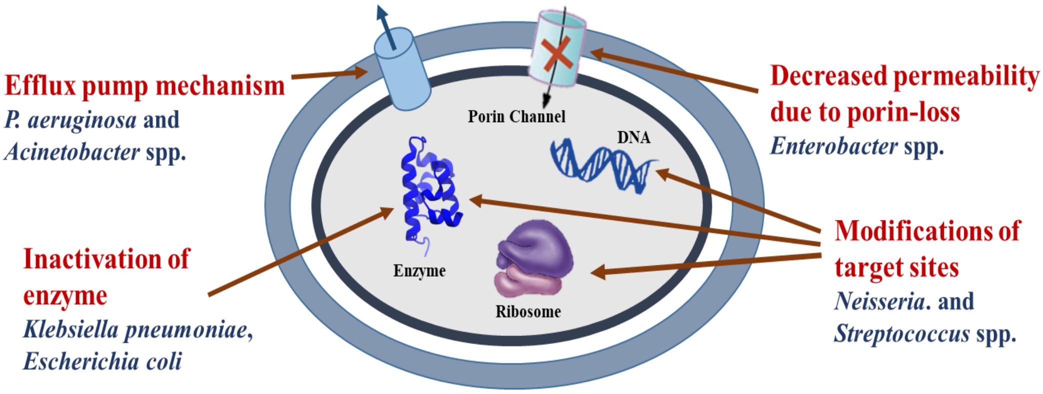

Figure 1.9: Primary mechanisms of antibiotic resistance in various bacterial species

1.1.3 The Role of Bacterial Enzymes in Antibiotic Resistance

1.1.3.1 β-Lactamase Enzymes and their Classification

As explained above, the emergence of inactivating enzymes is a key mechanism for bacteria to grow resistance against antibiotics. As a prime example, the β-lactamase enzymes lead to widespread resistance against various β-lactam antibiotics. These enzymes are evolved from transpeptidase enzymes and thus they possess similar activity. The Ser residue present in the active site of this enzyme can open up the β-lactam ring in a similar manner to form an ester. But, unlike transpeptidase enzymes, β-lactamases can also hydrolyse the ester link. This results in ring-opened β-lactam antibiotics, which are incapable of antimicrobial effects (Figure 1.10). As β-lactam is then released from the β-lactamase active site, the enzyme can act catalytically to deactivate more drug compounds.[14]

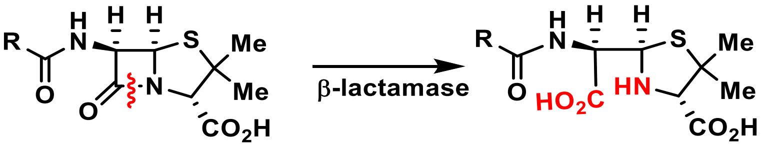

Figure 1.10: Inhibition of penicillins by β-lactamase enzymes

As proposed by Ambler in 1980, β-lactamase enzymes can be classified into four major categories, based on their structural properties and amino acid sequences (Figure 1.11). They are designated as Classes A to D. Classes A, C and D are known as serine β-lactamases and Class B is metallo-β-lactamases containing Zn^{2+} ions.[42]

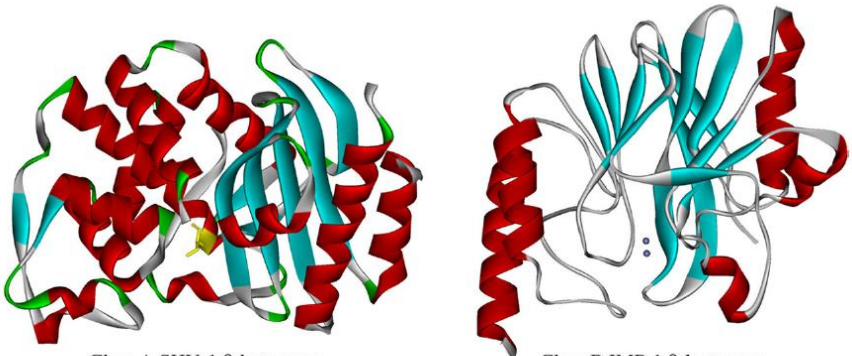

Class A SHV-1 β-lactamase

Class B IMP-1 β-lactamase

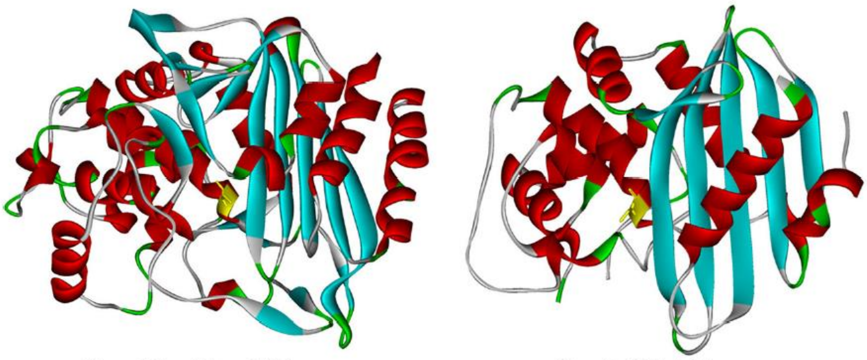

Class C *E.coli* AmpC β-lactamase

Class D OXA-1 β-lactamase

Figure 1.11: Representative structural features of Class A, B, C and D β-lactamases[23]

Serine β-lactamases:

Serine-β-lactamases resemble PBPs and acylate β-lactam antibiotics. The acylated β-lactam is then hydrolysed by water to regenerate the β-lactamase enzyme, which goes on to react with another β-lactam molecule. This catalytic mechanism can be described as followed.[23]

$$E + S \rightleftharpoons E{:}S \longrightarrow E{-}S \longrightarrow E + P$$

Where E is a β-lactamase, S is a β-lactam substrate, E:S is the Michaelis complex, E - S is the acyl-enzyme, and P is the product with no antibacterial property. The substrate-specific catalytic profiles of the serine β-lactamases also contribute to the recognition of class A enzymes as ‘penicillinases’, class C enzymes as ‘cephalosporinases’ and class D enzymes as ‘oxaciltinases’.[43] However, this classification is based on very much generalised data and found to be misleading sometimes.

Metallo-β-lactamases:

Class B, metallo-β-lactamases (MBLs) are active against a broad spectrum of antibiotics. They display a very large range of substrate scope, being capable of inactivating almost every kind of β-lactam antibiotic. In contrast to serine β-lactamases, class B is comprised of Zn^{2+} containing enzymes and utilises Zn^{2+} as a Lewis acid to activate water in order to hydrolyse the amide bond in β-lactams (Figure 1.12).

MBLs have been divided into three subclasses according to their structural variation, breadth of substrate spectrum and dependency on Zn^{2+} ions for activation. They are known as subclasses B1 (e.g., IMP-1, VIM-2, BcII and CcrA), B2 (e.g., CphA) and B3 (e.g., L1).[44] B1 actively binds to one or two Zn^{2+} ions whereas B2 and B3 exclusively binds with one and two Zn^{2+} ions respectively.

Subclass B2 MBLs are known to be active against carbapenemases, a specific β-lactamase class of enzymes which target the carbapenem antibiotics. Carbapenems have a very broad spectrum of antibacterial activity and are active against hundreds of β-lactam-resistant strains of bacteria. This class of antibiotics are also known as 'drugs of last resort'. Therefore, growing resistance against carbapenems is of major concern. CphA is one example of a subclass B2 enzyme, known strictly for its carbapenemase activity.[45] In this mechanism (Figure 1.12), His118 and Asp120 binds to a water molecule which eventually serves as the nucleophile to cleave the β-lactam ring of carbapenem. Also, Asp120, Cys221, and His263 along with a water molecule coordinate with Zn^{2+} ion in this stage. This second water molecule makes a hydrogen bond with the carboxylate group from carbapenem moiety and serves as a hydrogen donor to the β-lactam nitrogen in order to complete the hydrolysis process. Here the role of Zn^{2+} ion is to anchor the second water molecule for the deacylation step.[44] Furthermore, a recent study on carbapenem resistant MBLs has revealed the emergence of a newly developed enzyme, NDM-1.[46]

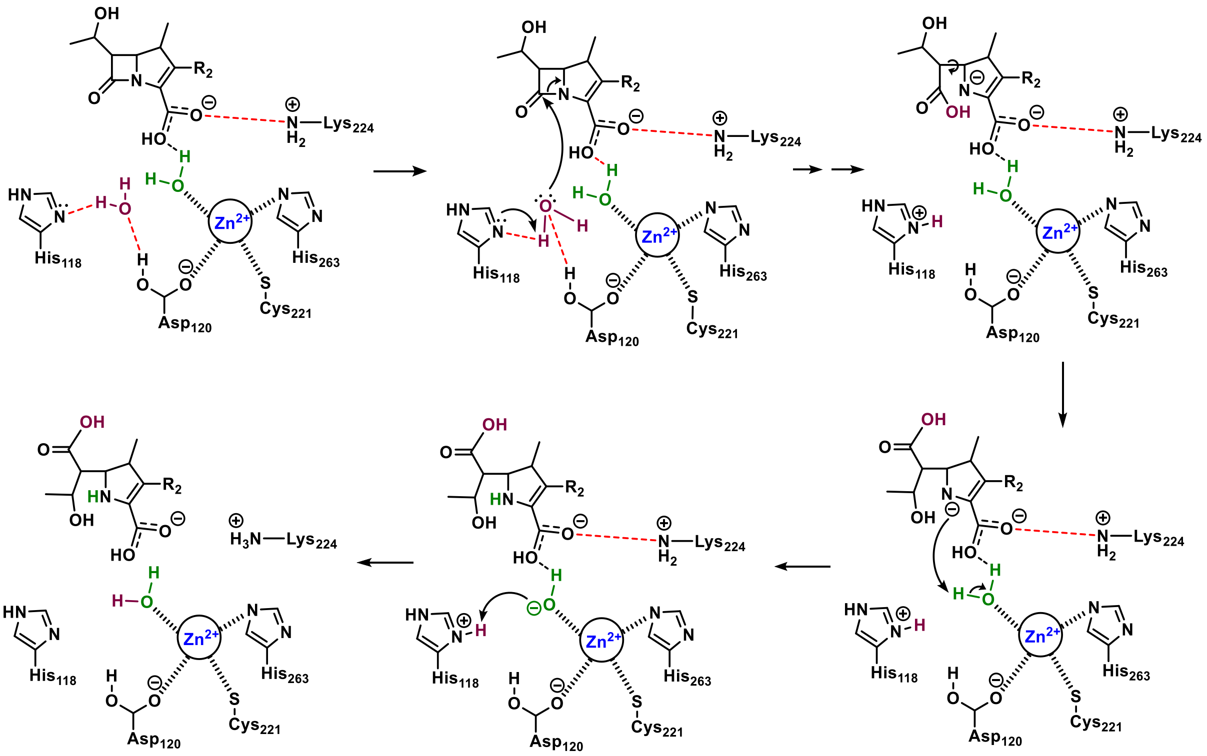

Figure 1.12: The mechanism of carbapenem inactivation by CphA (Subclass B2)

1.1.3.2 New Delhi Metallo-β-lactamase-1 (NDM-1)

New Delhi metallo-β-lactamase-1 (NDM-1) is one of the newly reported MBLs (subclass B1) which has prompted widespread concern in clinical field because of its broad range of antibiotic resistance. This is one of the most threatening enzymes produced by carbapenem-resistant *Enterobacteriaceae* (CRE), a class of pathogen which are often designated as 'superbugs' because of their un-commonly wide spectrum of resistance against all available antibiotics. NDM-1 was first discovered in a strain of *K. pneumoniae* and isolated from a Swedish man, who travelled to New Delhi, India in 2008. By 2009, a study in Mumbai suggested an outbreak of 24 carbapenem resistance *Enterobacteriaceae*, 22 of which were NDM-1 producers.[46,47,48] The spread of these bacteria strains all over the world creates an alarming situation for human health. Since 2010, NDM-1 producers have been identified on all continents except in Central and South America with, in most of the cases, a direct link with the Indian subcontinent. Few cases have been reported from the United States and Canada. Recent findings suggest that the Balkan states and the Middle East may act as secondary reservoirs of NDM-1 producers (Figure 1.13).[49]

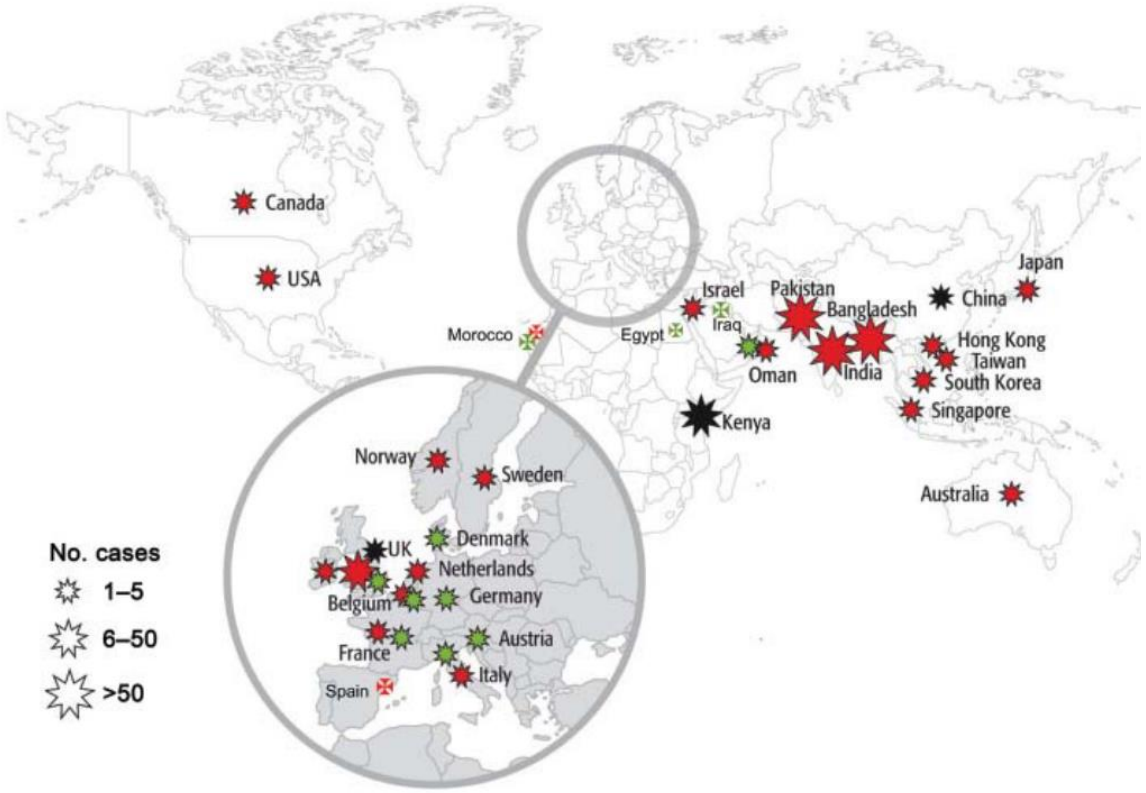

Figure 1.13: Geographic distribution of NDM-1 producers, July 15, 2011[50]

1.1.3.3 β-Lactamase Inhibitors

The quest to combat resistance of bacteria against β-lactam antibiotics started in 1970 with the introduction of clavulanic acid (Figure 1.14); the first β-lactamase inhibitor isolated from *Streptomyces clavuligerus.* Since then, attempts to identify β-lactamase inhibitors have been an area of great interest in field of drug design. There are two strategies to deal with the destructive actions of β-lactamases. The first approach involves modifying the structure of β-lactams, making them insensitive towards hydrolysis by β-lactamases while still retaining their antibacterial activity. The second strategy involves using agents that disable the β-lactamase activity, allowing the β-lactam antibiotic to carry out its function.

Within the first strategy, a key advancement was the production of a deacylated penem, 6-aminopenicillanic acid and a related cephem, 7-aminocephalosporanic acid (Figure 1.14), which contain the β-lactam motif, modified to avoid attack by β-lactamases. This strategy, however, is limited by the fact that with increasing modification, these drugs lose their efficiency as antibiotics.[51] Inefficiency of this method led to the second strategy of neutralizing β-lactamase enzymes against their hydrolytic actions. This strategy is described as “suicidal” or “mechanism-based” approach. Using this method, inhibitors of β-lactamases act as substrate mimics that react with the enzymes, forming strong covalent bonds that block the active site of the lactamases, thus lead to the inactivation of enzymes.[52] Some examples of β-lactamase inhibitors following this pathway are asparenomycin A and 6-(acetylmethylene)penicillanic acid (Figure 1.14).

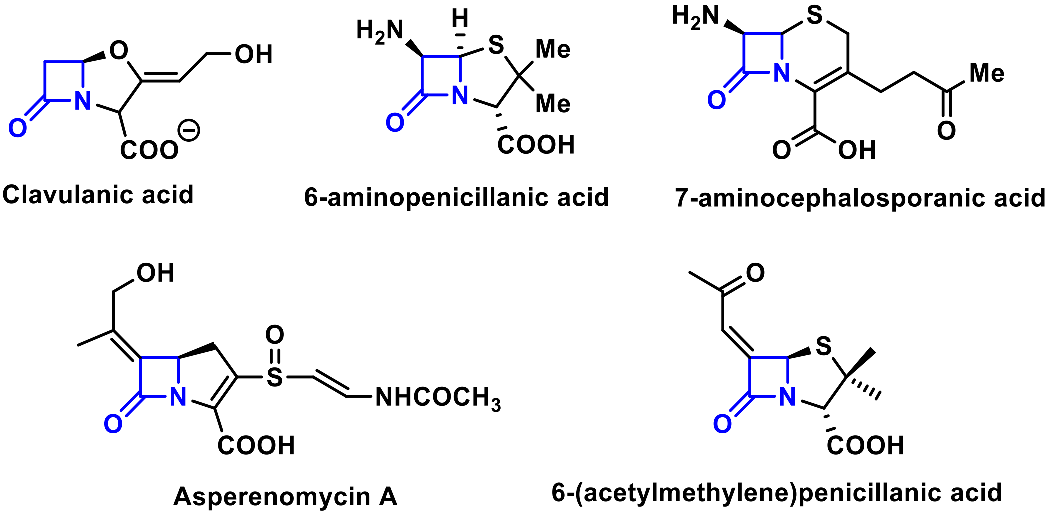

Clavulanic acid

6-aminopenicillanic acid

7-aminocephalosporanic acid

Asperenomycin A

6-(acetylmethylene)penicillanic acid

Figure 1.14: Structure of few early β-lactamase (SBL) inhibitors

Strategies to address metallo-β-lactamase (MBL1)-induced resistance include ligands that bind selectively to Zn in the active site.[53] For example, thiols, thiones, sulfonic acids, triazoles, tetrazoles, hydroxamates, and carboxylic acid functional groups in various pre-existing drug molecules have all been shown to have activity (Figure 1.15).[54] In addition L- and D-captopril (1-(D-3-mercapto-2-methylpropionyl)-proline), thiorphan,[55] dimercaprol, 2-(4-fluorobenzoyl)benzoic acid[56], cyclic boronate vaborbactam[57] have all been found to inhibit MBLs.

An alternative mechanism of MBL inhibition is displacement of one or more Zn^{2+} ions from active site of the enzyme. For example, a Zn-specific spiro-indoline-thiadiazole (SIT-Z5) has been identified to rescue meropenem activity in NDM-1 producing *E. coli* by removing Zn from the MBL active site.[58] Another compound, aspergillomarasmine A (AMA) has also been found to inactivate VIM-2 and NDM-1 enzymes.[59] However, these compounds are not yet used clinically. Therefore, efforts to combat continuously evolving antibiotic resistance from various MBL-producing bacterial species are still ongoing.

A final proposed method to inhibit the MBL enzymes is to transmetallate the Zn ion with an alternative metal ion, which ultimately inactivates the enzymes. Very recent studies suggest that copper complexes have the potential to induce this process. More details on copper pyrithione as an inhibitor of the MBL enzymes are given in Section 1.4.

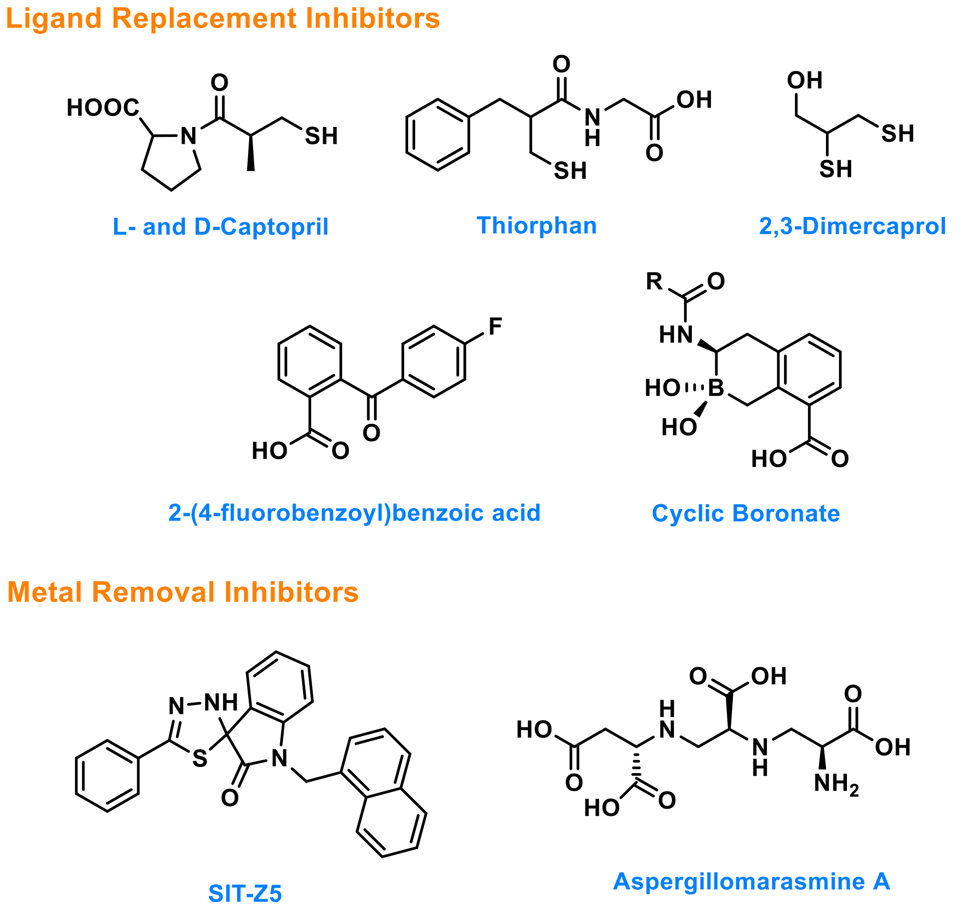

Figure 1.15: Structure of metallo- β-lactamase (MBL) inhibitors following two different mechanism of inhibition

1.2 Cancer and Chemotherapy

Initial aims of this thesis were to address bacterial infections, however, as the project developed the compounds showed activity against cancer cells. In the following section, a brief overview of the factors affecting cancer progression is given, including some discussion on the development of chemotherapeutics.

1.2.1 Background to Cancer

Cancer is one of the most life-threatening diseases for humans. In 2020 it was reported that around 19 million people globally fell victim to cancer every year, among whom almost 10 million died.[60] Therefore, understanding how cancer develops and designing new therapeutics to prevent and treat it are vital targets for medicinal chemistry.

Cancer is a condition in which unregulated and rapid cell-proliferation leads to illness and often death. Generally, the first stage of cancer development starts with growth of a tumour from a single origin cell, which has an altered genetic code. In later stages, malignant carcinomas arise and continue to spread and proliferate in the connecting tissues. Cancer cells also invade blood cells and metastasis develops around the whole body.[61]

Understanding the basic mechanism behind the development and spread of different types of cancer helps to develop treatments. With development of newer genomics and computational technologies, now it is possible to analyse the microenvironment surrounding the tumour growth, the roles of DNA, RNA and various proteins/enzymes behind its malignancy and different chemical reactions leading to metastasis.

1.2.2 Development of Chemotherapeutics

Developing new cancer therapeutics has been at the forefront of medical research for many years.[62] The history of chemotherapy started with the discovery of nitrogen mustards to treat cancer proliferation in 1942 by Louis Goodman and Alfred Gilman (Figure 1.16).[63] In the late 1940s, Sydney Farber discovered the role of folic acid in cancer development and discovered antifolate compounds - aminopterin[64] and amethopterin (methotrexate)[65] - which block the function of folate-requiring enzymes and thus cause remission of various types of carcinoma including blood, breast, ovarian, bladder, head and neck cancers (Figure 1.16). In the early 1950s, George Hitchings and Gertrude Elion investigated purine analogues, such as 6-mercaptopurine (6-MP), as potential antitumour agents (Figure 1.16).[66] However, a significant problem with chemotherapy faced by researchers is the acute toxicity to healthy cells. With improvement in the understanding of molecular biology and genetics during late 1980s, treatment started focusing on the repair of cellular level defects in cancer cells. That led to the beginning of the era of ‘targeted therapy’ which exclusively studied various targets of chemotherapeutic drugs and inhibition of their functions in order to stop proliferation of cancer cells.[67] These targets includes DNA, various proteins, essential enzymatic pathways, and the production of reactive oxygen species (ROS).

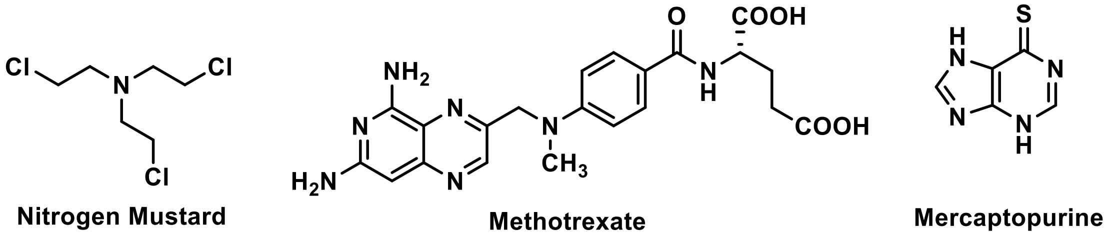

Nitrogen Mustard

Methotrexate

Mercaptopurine

Figure 1.16: Some early chemotherapeutic agents for cancer treatment

1.2.2.1 Chemotherapeutic Agents that Target DNA

DNA was first observed to be a potential cellular target for anticancer drugs.[68] As an example, nitrogen mustard compounds alkylate the DNA bases through formation of aziridinium ions and show interstrand cross-linking with DNA.[69] Metal complexes, such as cisplatin, tend to bind to the exposed nitrogen atoms of the heterocyclic bases, especially of adenine and guanine or to the oxygen atoms of the phosphodiester backbone, forming intrastrand and interstrand crosslinks.[70] Cisplatin is a platinum-based drug that was first observed by Rosenberg in 1971 and works against a broad spectrum of cancerous growth, including ovarian, testicular, bladder, lung, head and neck cancers (Figure 1.17).[71,72] Another way in which drugs can target DNA is through intercalation, where molecule inserts non-covalently in the gaps between base pairs. Compounds are typically flat and aromatic to maximise pi-stacking with the DNA bases. This ultimately leads to apoptotic cell death. Examples of anticancer compounds that operate *via* intercalation include doxorubicin, acridine orange and metal complexes containing aromatic ligands, such as [Pt(terpyridine)(HET)]$^+$, HET = 2-hydroxyethanethiolato-2,2′,2″-terpyridine (Figure 1.17).[73,74]

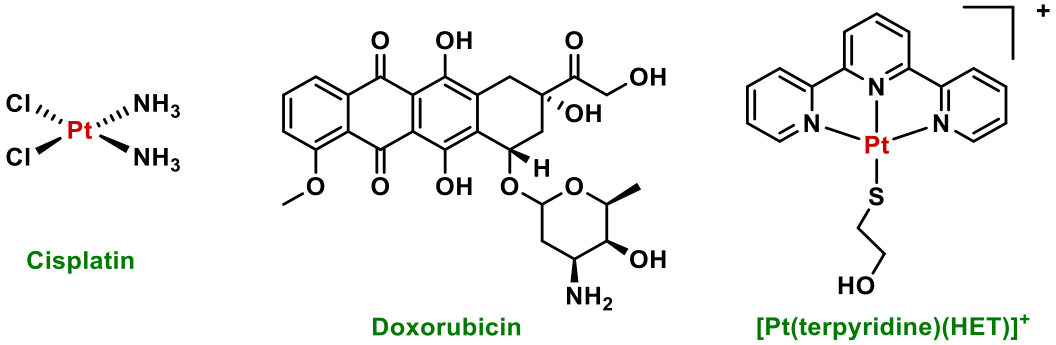

Cisplatin

Doxorubicin

[Pt(terpyridine)(HET)]$^+$

Figure 1.17: Structure of two popular DNA binding agents as chemotherapeutic agents

1.2.2.2 Chemotherapeutic Drugs for Enzyme Inhibition

In recent years, various enzymatic pathways have been found to play pivotal roles in cancer development. Therefore, targeting these pathways and inhibiting the respective enzymatic functions have great potential towards causing apoptosis and preventing cancer metastasis.[75] Some of such major enzyme classes are histone-deacetylases (HDAC), tyrosine kinases, DNA topoisomerases and deubiquitinases (DUB).

Histone deacetylase (HDAC) enzymes catalyse the removal of acetyl groups from Lys residues of histones.[76] Inhibitors of HDAC enzyme have been observed to alter the catalytic process of acetylation and deacetylation of chromatin and other non-histone proteins, which leads to modification in gene expression and induce cell cycle arrest and apoptosis, inhibiting cancer metastasis and angiogenesis.[77,78] An example of such HDAC inhibitor is suberoylanilide hydroxamic acid (SAHA, vorinostat), which has reached pre-clinical trial due to its potential in anticancer activity (Figure 1.18).[79]

DNA topoisomerase enzymes are responsible for unlinking of non-necessary winding of DNA strands during DNA replication and transcription. The small molecule inhibitors (e.g., Doxorubicin) of these enzymes manage to manipulate their enzymatic activity for the therapeutics purpose (Figure 1.18).[80,81]

Deubiquitinases (DUBs) are enzymes that cleave the carboxyl terminus of ubiquitin proteins and contribute to the ubiquitin–proteasomal pathways, which regulates the content, signalling and function of most proteins related to cellular activities. Therefore, inhibitor of these pathways can act as anticancer agents (e.g., ALM4) and induce apoptosis (Figure 1.18).[82,83]

Tyrosine kinase enzymes are involved in the phosphorylation of tyrosine residues in various substrates. This class of protein kinases have recently come to light as possible anticancer targets, due to their roles in oncogene formation.[84] Small molecule inhibitors, such as Gleevec (Imatinib), have been shown to compromise phosphorylation reactions by these enzymes (Figure 1.18).[85]

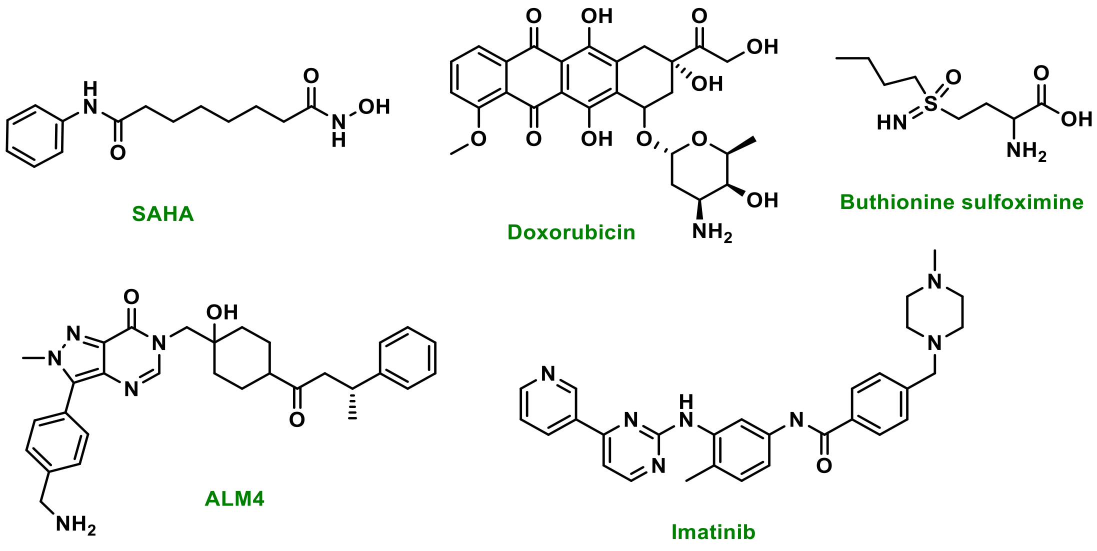

Figure 1.18: Structure of various class of enzyme inhibitors as anticancer agents

1.2.2.3 Chemotherapy and Generation of Reactive Oxygen Species (ROS)

In number of studies, free radicals, especially reactive oxygen species (ROS) have been observed to play fundamental roles in mediating apoptosis of cancer cells.[86] Reactive oxygen species are free radicals or non-radical molecules derived from diatomic oxygen and can readily oxidise biological molecules such as proteins, lipids, nucleic acids and amino acids. The most common ROS present in biological systems is superoxide (O^{2-}), hydrogen peroxide (H_2O_2), singlet oxygen ($^1O_2$) and hydroxyl radicals ($^{\bullet}OH$) (Figure 1.19). In living system, ROS are usually generated by single- or multi-electron reductions from ground state triplet oxygen as by-products of several biological metabolism processes, enzymatic pathways and chemical reactions.[87]

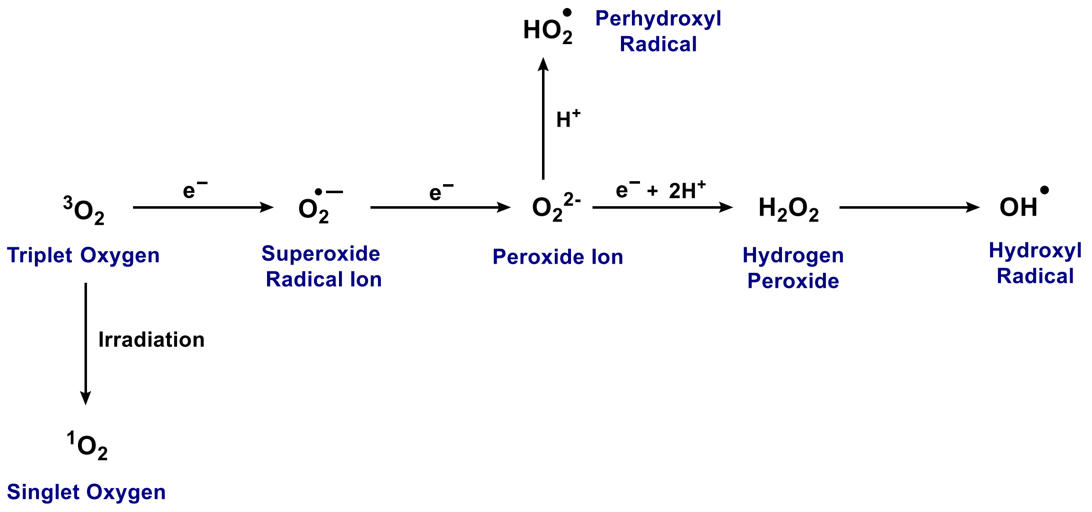

Figure 1.19: ROS generation pathways

Enhanced oxidative stress, due to ROS generation, contributes significantly towards both beneficial and harmful effects in the human body. Therefore regulation of ROS level is crucial for survival of human cells.[88] However, numerous studies have suggested strong links between production of ROS and anticancer activity. Various cellular processes in the cancer cell are affected by ROS levels (e.g., DNA transcription, protein translation, tumour development etc.) and, therefore, enhanced ROS level can be utilised to induce or increase apoptosis in cancer cells.[89] Induction of exogenous ROS by anticancer agents leads to redox buffering and upregulation of antioxidant enzymes inside cancer cells, ultimately leading to apoptosis.[90] ROS also oxidise proteins which are essential for roles of various metalloenzymes such as cytochrome c oxidase, glutathione peroxidase and catalases.[91] Another mechanism of attack by ROS leads to peroxidation of lipid membranes, which enhances their permeability, stimulating further apoptosis.[92] Elevated level of ROS even causes malfunction and degradation of various cellular organelles such as mitochondria, DNA and RNA, which eventually causes cell-death.[93,94] Various examples of anticancer agents which have been observed to induce apoptosis by generation of ROS are listed below (Table 1.1).

Table 1.1: Various anticancer agents utilising ROS to induce apoptosis

Entry	Anticancer Agent	Type of Cancer	Structure
1	**Decitabine**	**Skin Cancer**[95]	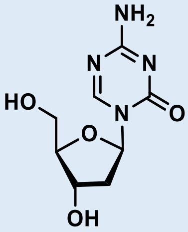
2	**Vinblastine**	**Lung Cancer** **Breast Cancer**[96]	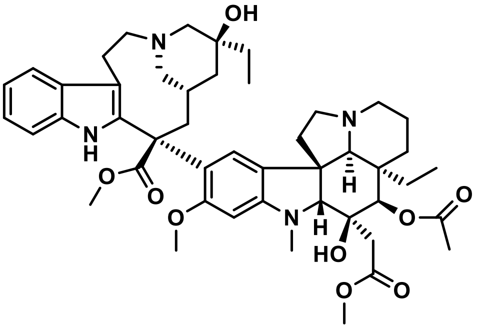
3	**Taxol**	**Blood Cancer**[97]	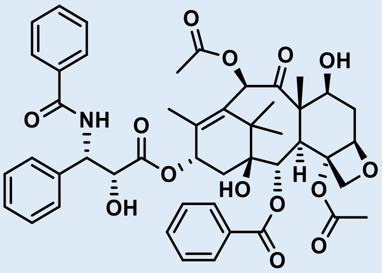
4	**Resveratrol**	**Colon Cancer**[98]	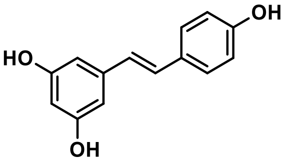
5	**Colchicine**	**Colon Cancer**[99]	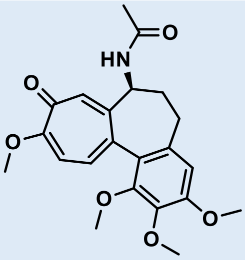

Beyond organic compounds, many examples of metal complexes have been tested to treat cancer, as well as bacterial infections. In the following sections, the use of metal complexes in medicine is summarised, before a section focussing on copper complexes with therapeutic activity is given.

1.3 Metals in Medicine

Metals are essential nutrients in the human body and play major roles in various cellular metabolic pathways and as components of enzymes and proteins. Deficiency in certain metals can lead to disease, whilst increased levels of metals can also lead to cytotoxicity. Therefore, regulation of metal levels in the human body is essential for many biological processes and overall survival. For several centuries, the various beneficial and toxic effects of metal complexes have been used for therapeutic purposes and have been in forefront of medicinal chemistry research.[68]

One factor affecting the stability of metal complexes is the chelate effect, which describes how multidentate ligands are energetically more stable than monodentate ligands. The chelation effect also favours 5 and 6-membered rings, due to minimal angle and ring strain.[100]

Two other key properties of metallodrug design are lipophilicity and water-solubility. These two properties greatly affect metallo-drug delivery and bioavailability. More lipophilic complexes will allow permeation through lipid membrane. However, higher lipophilicity leads to a lower solubility in water, which discourages drugs to be dissolved in intracellular environment. A balance between aqueous solubility and lipophilicity is always an important consideration while designing and assessing metallodrugs.

1.3.1 Unique Properties of Metal-Ligand Complexes, leading to Therapeutic Applications

One of the key properties of metals that contributes towards their activity is their variable oxidation states. Under aqueous conditions, most metals possess positive charges, but oxidation states can be tuned depending on their coordination environments. Variation in oxidation states indicates the stability of the metal complex and can regulate the rate of ligand exchange with targeted biomolecules. Furthermore, variable oxidation states allow metals to take part in redox reactions with biomolecules, leading to ROS generation during biological processes.[101]

A second important property of metal complexes is their ability to undergo ligand exchange at a rate determined by the metal, its oxidation state and the ligands around the metal centre. The ability to undergo ligand exchange allows metal complexes to bind to biomolecules, such as proteins and DNA. Taking advantage of the metal's coordinating activity, seven amino acids from the active sites of proteins can bind with metal leading to changes in the protein activity (Figure 1.20).[102] As an alternative approach, transmetallation of the native metals of a metalloenzyme by an alternative metal can greatly disrupt the structure and functional activity of the protein. For example, the structure of zinc-fingers proteins is maintained by Zn(II) and the tertiary structure and, therefore, function of the protein will change if bound to an alternative metal, for example a metallo-drug.[103] Metal-based drug complexes also undergo ligand exchange and coordination to DNA. The target ligands in DNA are the nucleobases, typically the nucleophilic N7 of adenine (A) and guanine (G) bases, exposed through the major groove of DNA double helix, ultimately leading to cell death.[104]

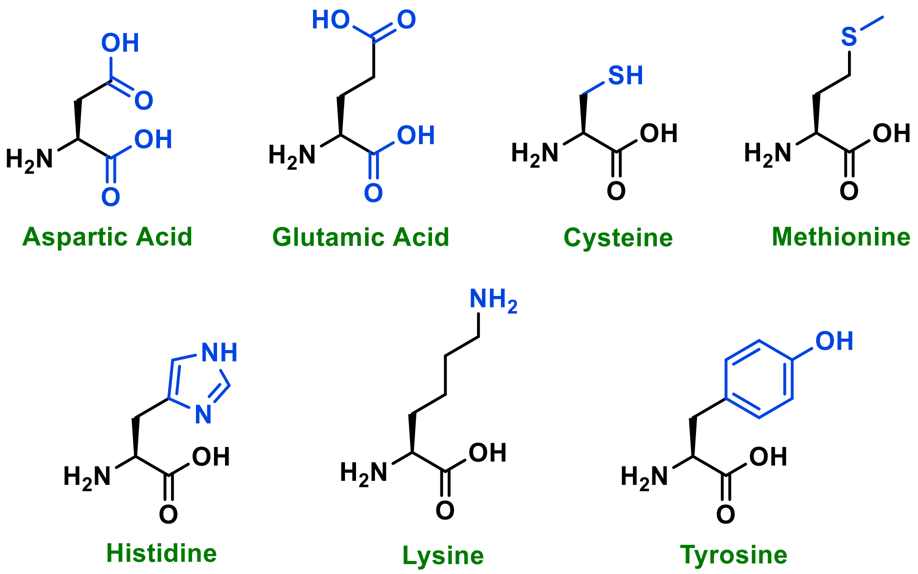

Figure 1.20: Seven amino acids (L form) of protein active sites and their donor functional groups as ligands towards metal centres

Another advantage of metal complexes in drug design is their variable geometry, which can vary depending on oxidation states. Geometry can be explained using ligand field stabilisation energy (LFSE).[68]

In summary, metals have been found to possess many therapeutic applications based on their unique properties, such as their ability to undergo ligand exchange, their unique and intricate 3D geometries and their ability to undergo redox changes. Specific examples of metal complexes in disease therapy are presented in the following sections.

1.3.2 Metal Complexes as Antibacterial Agents

Arsenic and Bismuth

The first example of metallo-drugs for antimicrobial treatment was an arsenic compound, salvarsan (Figure 1.21), which was discovered in the early 20th century to treat syphillis.[9]

Although arsenic has been determined to be a highly cytotoxic metal, it has been widely used in therapeutic field for a long time.[105] Bismuth has also been used in this context. Bismuth is less toxic than arsenic and exhibits moderate antimicrobial properties in its subcitrate, subnitrate or subsalicylate forms (Figure 1.21), especially against the bacterium *Helicobacter pylori*, which is responsible for gastric ulcers and can lead to gastric cancer.[106] Another example of a bismuth compound used against bacteria is tribromophenolatebismuth(III), known as xeroform (Figure 1.21), which is used to treat infections caused by *K. pneumonia* or *E. coli* species.[107] An arseno–bismuth compound, bimarsen, has also been used to treat neurosyphillis due to lower toxicity compared to salvarsan (Figure 1.21).[108]

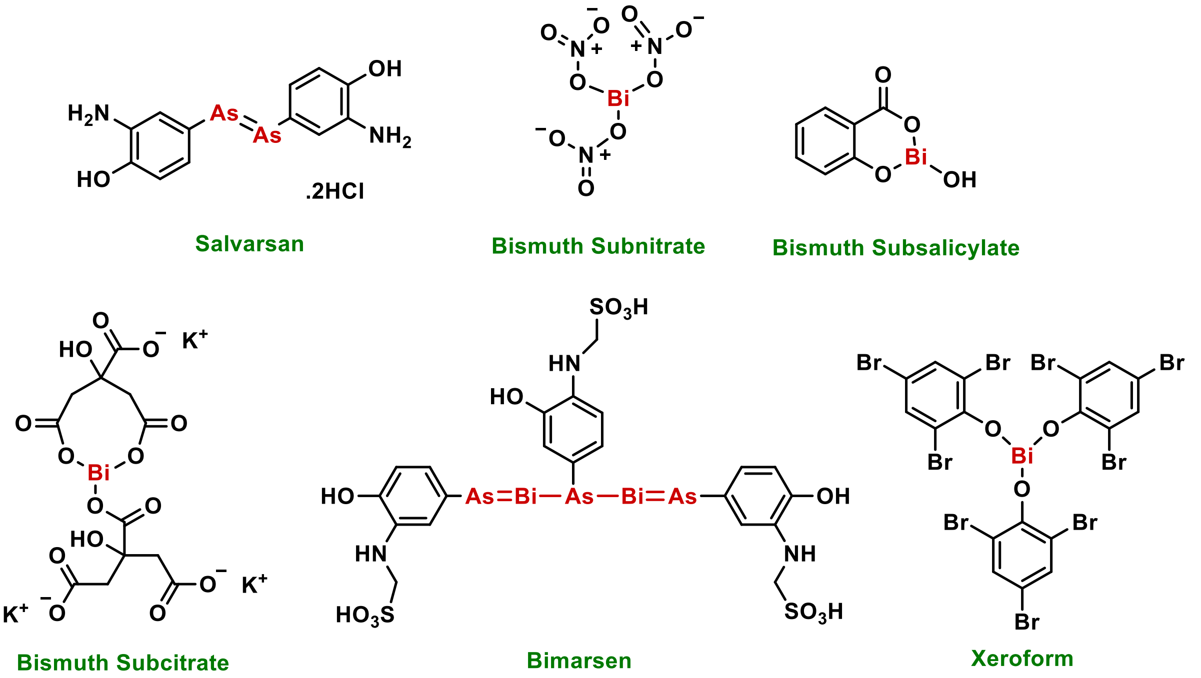

Salvarsan

Bismuth Subnitrate

Bismuth Subsalicylate

Bismuth Subcitrate

Bimarsen

Xeroform

Figure 1.21: Arsenic and Bismuth complexes as antibacterial agents

Due to high cytotoxicity of these early antibacterial metallo-drugs, various other metals such as copper, cobalt, ruthenium, palladium and zinc were used in designing new therapeutic metal complexes.[109]

Cobalt

Both divalent and trivalent cobalt ions have been observed to employ higher antimicrobial activity upon complexation with bioactive N, and O donor ligands. A well-known example of such cobalt complexes are 5-methoxy-2-[(2-morpholin-4-ylethylimino)methyl]phenol cobalt(III) (Figure 1.22 A), which shows activity in the micromolar range against *B. subtilis, E. coli* and *S. aureus.*[110] Divalent cobalt also binds with terephthalaldehyde and *ortho-*

substituted aniline derivatives (Figure 1.22 B), which increase their bioactivity against both Gram-positive and Gram-negative bacteria.[111] The antimicrobial activity against *E. coli* of sparfloxacin, a known drug of the floroquinolone class, significantly increases when coordinated to a cobalt(II) phenanthroline complex (Figure 1.22 C).[112] Ethylene diamine complexes with a Co(II) 1,10-phenanthrloline complex have also been observed to possess high potency against *E. coli* (Figure 1.22 D). [113]

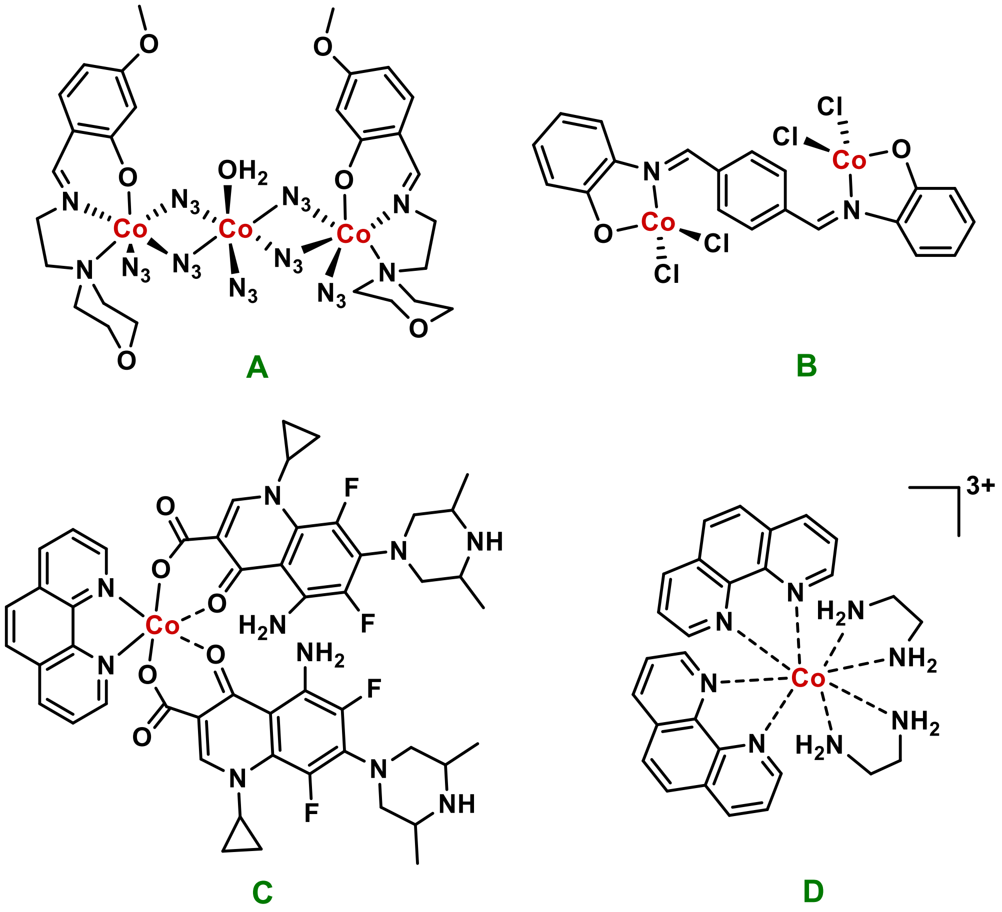

Figure 1.22: Divalent and Trivalent cobalt complexes as antibacterial agents

Palladium and Platinum

Chelation of existing bioactive ligands with palladium and platinum metals has been observed to increase their antimicrobial activity, especially against resistant bacterial species.[114] For example, Pd(II) complexes of two well-known antibiotics, tetracycline (Figure 1.23A) and doxycycline have been found to be sixteen times more potent against *E.coli* strains than the corresponding compounds without Pd(II).[115] Pd(II) and Pt(II) also bind with thiosemicarbazone and dithiocarbamate based ligands via N and S-donor atoms, leading to improved antibacterial activities against *M. tuberculosis*, *E. coli* and other Gram-negative species (Figure 1.23 B and

C).[116,117] Polynuclear palladium and platinum complexes have been recently shown to possess potent antimicrobial activity. Lunagariya *et al*. suggested formation of binuclear platinum complexes of pyrazolo[1,5-a]pyrimidine scaffold (Figure 1.23 D) which have activity against both Gram-positive (*B. subtilis* and *S. aureus*) and Gram negative (*E. coli* and *P. aeruginosa*) species and show antituberculosis activity *in vitro*.[118] Binuclear complexes of Pd(II) with phenylthiourea derivatives (Figure 1.23 E) have been reported by Terbouche *et al*. that show potential against methicillin-resistant and methicillin-sensitive *S. aureus* (MRSA and MSSA).[119]

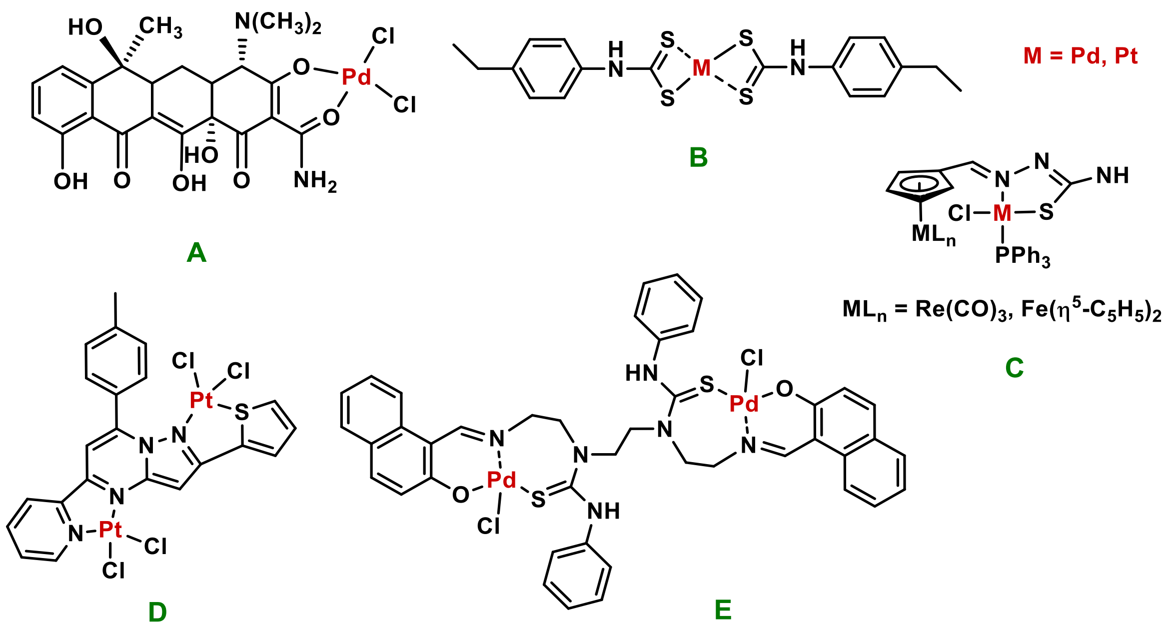

Figure 1.23: Palladium and Platinum based antibacterial agents

Ruthenium

An early example of a bacteriostatic ruthenium phenanthroline complex (Figure 1.24A) was reported in late 1960s to inhibit bacterial growth of *C. diphtheriae*, *M. tuberculosis* and *S. aureus* by interfering in biological redox mechanisms.[120] More recently, the complex $[Ru(2,9\text{-}Me_2phen)_2(dppz)]^{2+}$ (Figure 1.24 B), was found to inhibit bacterial growth of Gram-positive species such as MRSA, MSSA and *B. subtilis in vitro* and *in vivo*.[121] Ruthenium complexes of cyclopentadienyl and thiosemicarbazone ligands (Figure 1.24 C) have also been shown to be active against *S. aureus via* a DNA intercalating mechanism.[122] A recent approach for targeting bacteria is known as antibacterial photodynamic therapy (aPDT), where sensitiser molecules (e.g., Ru complexes) damage enzymes, proteins and DNA/RNA through photo-activated ROS generation.[123] In a recent study, polypyridyl based ruthenium complexes (e.g., Figure 1.24 D) have been observed to possess significant activity against MRSA.[124] Overall the positive charge of these complexes facilitates their interaction with negatively charged bacterial membrane. A ruthenocene complex conjugated with β-lactam 6-aminopenicillinic antibiotic (Figure 1.24 E) has also been found to increase the potency of the antibiotic against MSSA species such as *S. epidermidis* and *E. faecalis*.[125] In a different approach, a binuclear ruthenium complex including terpyridine based ligands (Figure 1.24 F) was shown to have significant activity against MSSA, MRSA and *E. coli*.[126] An example of a heterometallic complex of ruthenium and ferrocene (Figure 1.24 G) has been observed to have antibacterial potency against *S. epidermidis*.[127]

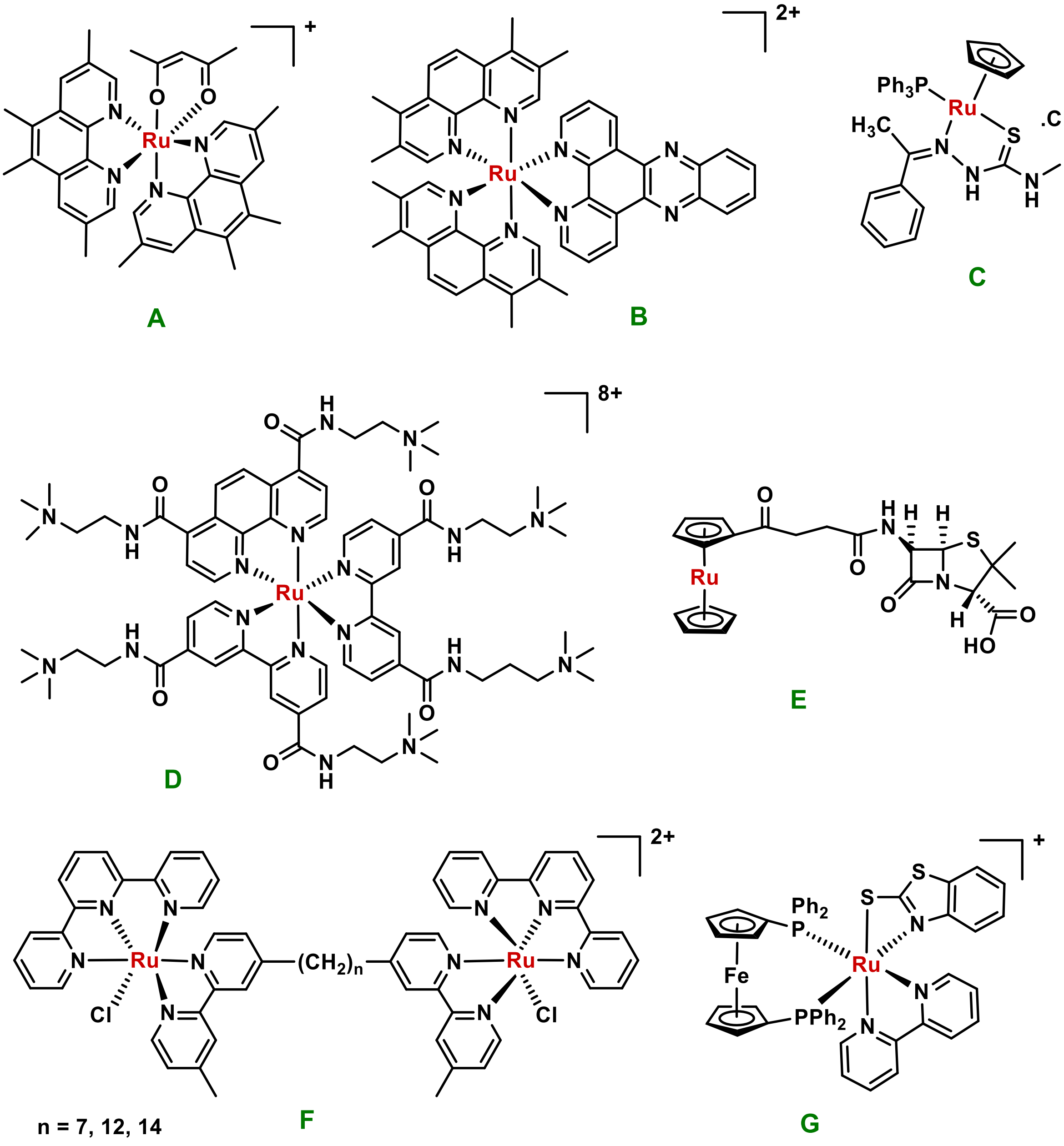

Figure 1.24: Ruthenium based complexes with potential antibacterial activity

Iridium

Trivalent iridium complexes have been studied for their potential antimicrobial properties. One of the first cyclometallated, substitutionally inert, selective inhibitors of *S. aureus* was reported to be an iridium complex with polypyridyl based ligands (Figure 1.25 A).[128] Another cyclometallated iridium(III) dipyridylamine complex conjugated with biotin (Figure 1.25 B) shows bactericidal effects against Gram-negative *P. aeruginosa* upon irradiation of visible blue light.[129] Later, another remarkable example was presented by Fiorini *et al.*, where a simple methylation of tetrazolato ligand in pyridine based Ir(III) complex (Figure 1.25 C) induces significant bioactivity against Gram-positive and Gram-negative bacterial strains (MIC = 1µg/mL against *D. radiodurans* species).[130] Another unique example by Chen *et al.* comprises of an organoiridium complex of biguanide derivatives (Figure 1.25 D) possessing MIC activity in the ng/mL range against both Gram-positive and Gram-negative strains including MRSA.[131] A piano-stool Ir(III) complex with a 1,2-diaminoethane ligand (Figure 1.25 E) has also been found to be highly potent against MRSA.[132]

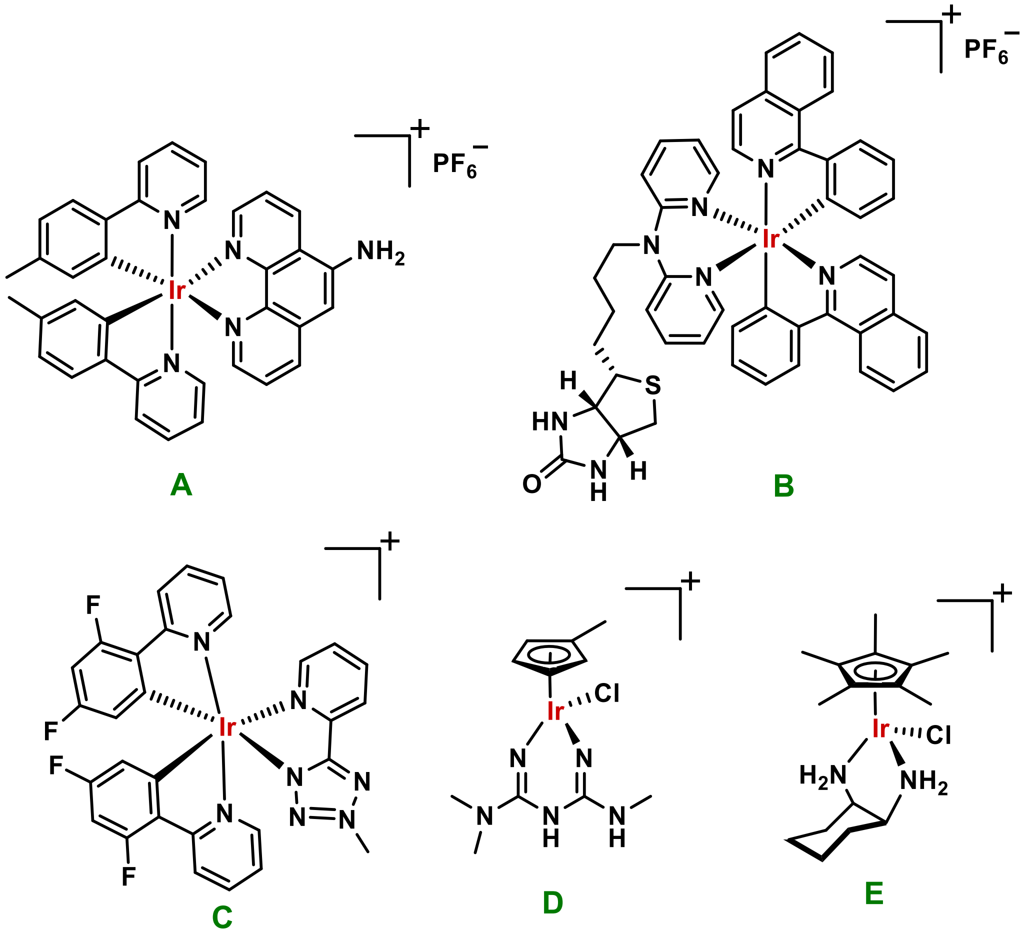

Figure 1.25: Iridium complexes with potent antibacterial activity

Zinc

Several zinc containing antibacterial agents have been reported.[109] Complexation of zinc with nicotine (Figure 1.26 A) has been observed to give complexes with significant potency against various Gram-positive and Gram-negative bacterial strains.[133] Another example of an antibacterial zinc metal complex is based on Schiff base ligands derived from trimethylsilyl-propyl-p-aminobenzoate, which upon coordination with zinc (Figure 1.26 B) gives remarkable activity against *Bacillus sp.* and *Pseudomonas sp.*[134] Furthermore, a very recent publication by Boughougal *et al.* suggests an interesting combination of two popular classes of antibiotics, sulfadiazine and enrofloxacin, combined with divalent zinc ion (Figure 1.26 C), giving a complex that possesses a nano-gram range MIC value against *E. Coli*, *S. Aureus* and *E. Faecalis* species, higher than either of the individual ligands.[135]

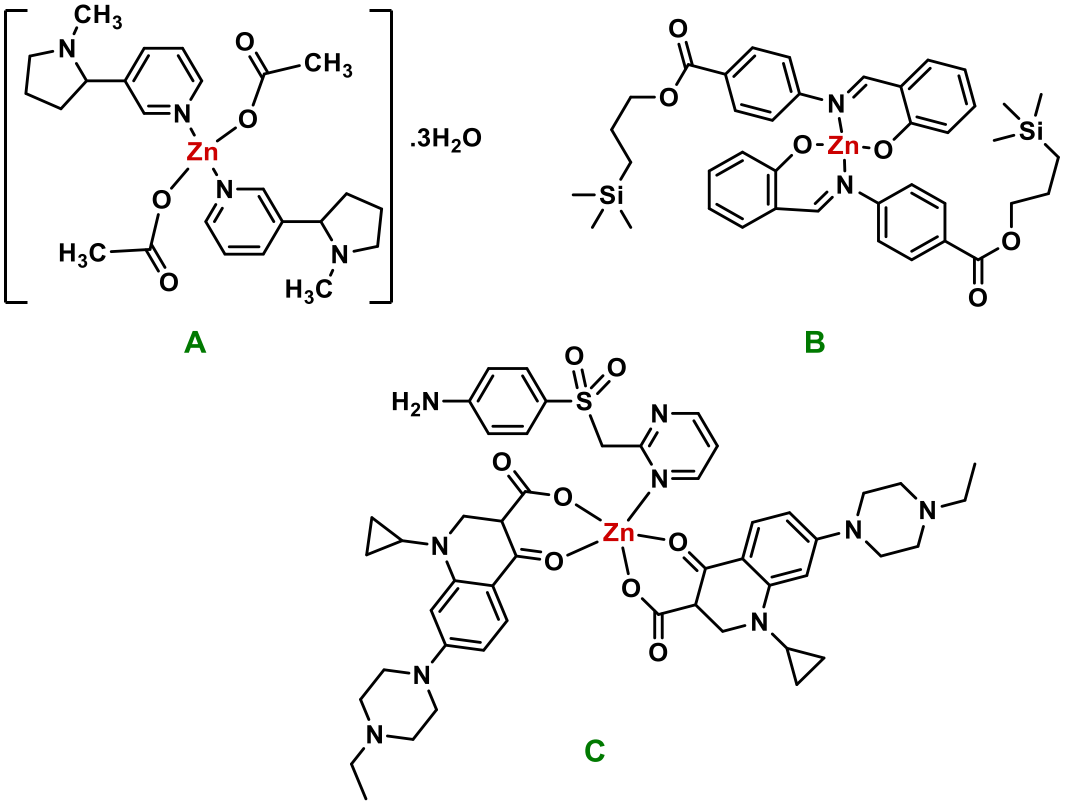

Figure 1.26: Zinc complexes as antibacterial agents

Gold

The earliest example of a gold complex to show antibacterial activity was in 1890, when potassium dicyanidoaurate(I) ($K[Au(CN)_2]$) was reported to be active against *M. tuberculosis*.[136] In more recent times, NHC complexes of gold as potent antibacterial agents have garnered attention of researchers.[123] However, among them only auranofin (Figure 1.27

A), an antirheumatic drug, and its analogues have been observed to show potential as non-cytotoxic antibiotics. These gold based complexes are very selectively active against only Gram-positive strains such as *S. aureus*, *M. tuberculosis*, *E. faecium* and *E. faecalis*, staying inactive against Gram negative species.[137] Furthermore, gold(I) alkynyl chromone complexes (Figure 1.27 B) have been studied by Hikisz *et al*. as potential inhibitor of *S. aureus* selectively over *E. coli*.[138] Trivalent gold binuclear complexes with bridging aromatic nitrogen-containing heterocyclic ligands have been found to be active against a broad spectrum of bacterial species (Figure 1.27 **C** is particularly active against *M. luteus*).[139]

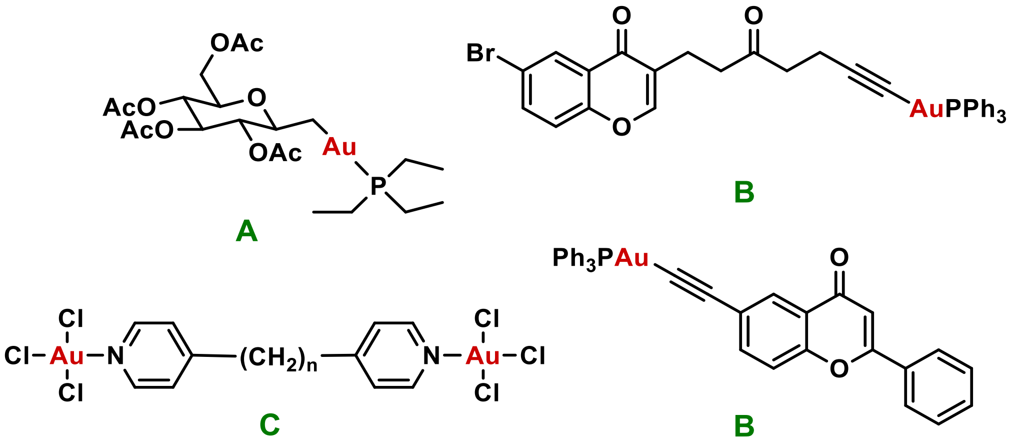

Figure 1.27: Gold complexes with potential antibacterial activity

Silver

Silver complexes are perhaps the most studied metal complexes with antibacterial activity. Silver cations (from salts, such as $AgNO_3$) have long been known to be more toxic towards bacterial cells than human cells.[140] In 1960, the era of silver-based antibiotics started with discovery of silver sulfadiazine (SSD), which has been widely used in subsequent decades as an antibiotic for burns to prevent infections (Figure 1.28).[141] Silver has also been used in eye drops, wound dressings and catheters because of its antibacterial properties.[142] Ag(I) complexes with oxygen donor ligands such as 4-isopropyltopolone (hino)[143] and 2-pyrollidone-2-carboxylic acid[144] have been observed to possess bactericidal activity against a broad spectrum of bacterial species. Silver(I) also forms complexes with saccharine and its derivatives as ligands, which possess antibacterial activity in the micro molar range against both Gram-negative and Gram-positive bacteria (Figure 1.28).[145] In these complexes, the weakness of the Ag-O and Ag-N bonds contributes to the ease of interaction between the silver ion and the biological ligand target (e.g., protein, membrane, enzymes etc.).[146] By comparison, silver complexes with sulfur donor ligands show a narrower spectrum of antibacterial activity. Examples such as $[Ag(Hmna)]_6 \cdot 4H_2O$ (Hmna = 2-mercaptonicotinic acid)[147] and [Ag(Hmba)]n (Hmba = 2-mercaptobenzoic acid)[148] are mainly active against some specific species of Gram-negative bacteria.

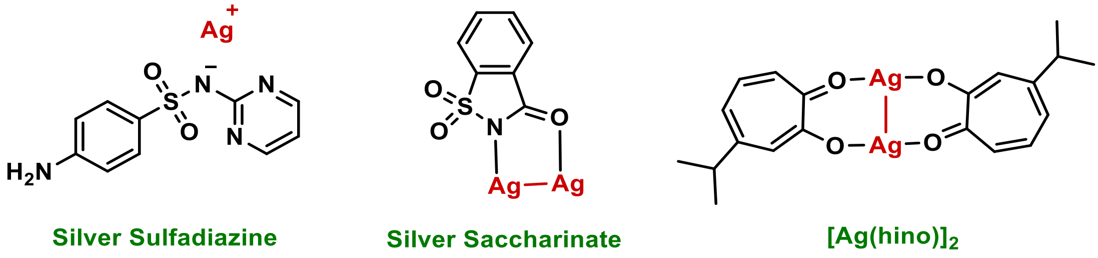

Figure 1.28: Structures of some silver complexes with antibacterial activity

Recent progress has focussed on silver nanoparticles (AgNPs). It has been determined that smaller particles possess greater antibacterial effects, due to greater surface area per unit mass.[149] The modes of actions of these nanoparticles are multifaceted and not fully understood yet.[150] Some probable mechanistic pathways for these silver compounds in bacterial cells can be classified by their interactions with: (i) cell wall; (ii) DNA, (iii) enzymes and membrane proteins. Formation of reactive oxygen species (ROS) has also been associated with antibacterial activity of Ag (Figure 1.29).[151] The advantageous position of silver is its multidimensional mechanism for the bactericidal activity, which prevents the bacteria from developing resistance against the silver compounds.[150] However, the resistance against silver-based antibiotics has been found in some species of *Salmonella*.[152]

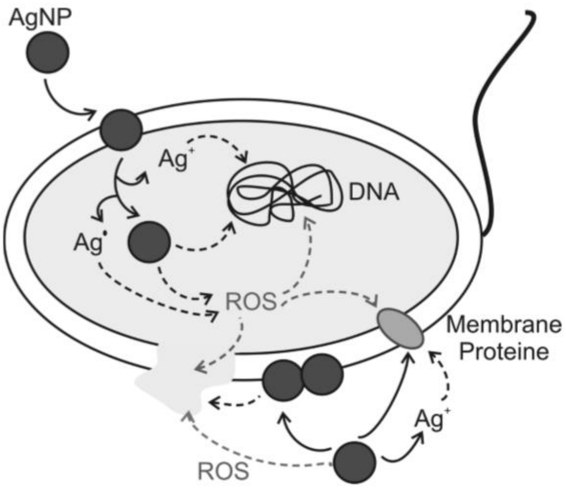

Figure 1.29: Possible interaction pathways of silver nano-compounds in bacterial cells[150]

There are other transition metals such as iron (Fe), nickel (Ni), chromium (Cr), mercury (Hg), rhodium (Rh) etc. which have been observed to form metal-ligand complexes with potential antimicrobial activity, but these will not be covered in depth here. Copper-based antimicrobial agents are discussed in depth in Section 1.4.

1.3.3 Metal Complexes as Anticancer Agents

Platinum

As stated earlier, cisplatin and analogous platinum based drugs started the era of metal-based anticancer chemotherapy.[153] Despite being a highly successful drug over the decades, cisplatin has issues of significant dose-limiting cytotoxicity, leading to severe side effects, such as nephrotoxicity, ototoxicity, nausea and vomiting.[154] Moreover, sensitive neoplasms eventually grow resistance against this platinum complex, resulting in increased dosages. Therefore, the next generation of platinum-based drugs, carboplatin and oxaliplatin, were designed, which showed better selectivity for cancer cells over normal cells (Figure 1.30). Carboplatin offers less reactivity and neurotoxicity, but causes thrombocytopenia and has limited efficacy towards some malignancies.[155] Oxaliplatin has even lower toxicity than carboplatin and a better ability to tackle resistance related issues.[156] Several other cisplatin-analogues with various carrier ligands have been designed over the years and reached different phases of clinical trials. Some examples of such complexes are lobaplatin, heptaplatin, aroplatin, nedaplatin etc. In recent studies, various other non-classical ligands have been utilised in conjugation with platinum to improve the overall pharmacokinetic parameters, spectrum of activity and toxicity profile.[157] For example, the use of carbohydrate moieties as ligands to bind with platinum ([Pt(II)Cl_2(AcGlc-pyta)]) has been observed to contribute to reducing cytotoxicity towards HeLa cells (Figure 1.30).[158] Phenanthriplatin (Figure 1.30) is another type of divalent platinum complex which also addresses this problem through formation of a mono-functional adduct with DNA through chloride ligand exchange and shows a better overall cytotoxic effect.[159] Octahedral platinum(IV) complexes have also been recognised to possess potential anticancer activity, through an activation by reduction mechanism. [$PtCl_4$(bipy)] and [$PtCl_4$(dach)] are examples two such Pt(IV) based anticancer agents which have been explored for treatment of colon cancer (Figure 1.30).[160] Multinuclear platinum complexes has also been studied against tumour cell activities. Generally in these complexes two or more divalent platinum centres are bridged through flexible aliphatic chain or rigid azole molecule and therefore DNA adduct formations with these complexes are very different to cisplatin adducts.[161] [{*trans*-

$Pt(NH_3)_2Cl\}_2(\mu$-1,2-bis(4-pyridyl)ethane)]$(ClO_4)_2$ was represented by Arsenijević *et al.* as an example of a multi-platinum complex that shows significant activity against ovarian cancer cells (Figure 1.30).[160]

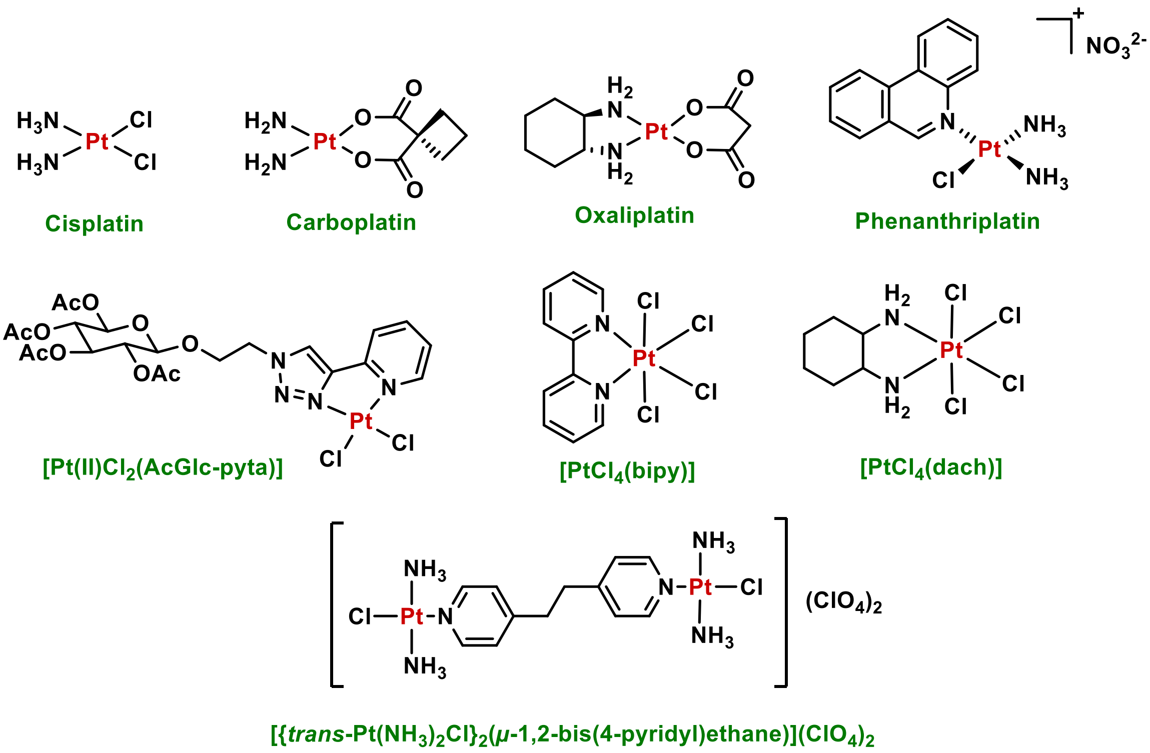

Figure 1.30: Platinum complexes as potential anticancer agents

Ruthenium

Despite their success as anticancer agents, platinum drugs have significant issues regarding cytotoxicity and resistance. Therefore, ruthenium complexes have been developed as alternative therapeutics with much milder toxicity. Ruthenium ions typically form octahedral complexes.[157,162] NAMI-A (Na[trans-$RuCl_4$(DMSO)Im]) is one of the first known examples of ruthenium-based complexes to possess potential as an antimetastatic drug (Figure 1.31).[163] NAMI-A has a different mode of interaction with DNA compared to cisplatin and shows far lower toxicity to normal cells.[164] Relatively stable Ru(III) complexes are designed as prodrugs, which after selective cellular uptake by tumour cells are reduced in the hypoxic regions of tumours to the more efficient Ru(II) form. As a result of this activation by reduction, the complexes are found to be less toxic towards normal healthy cells.[165] Some examples of these redox-active, antineoplastic prodrugs have a general formula of $[Ru(III)Cl_{(6-n)}(ind)_n](3-n)^-$ (n = 0-4; ind = indazole; counter ions = $Hind^+$ or Cl^-) (Figure 1.31).[166]

Another class of active Ru complexes are the Ru(II) piano stool complexes.[167] An example of such complexes is RAPTA-C (PTA = 1,3,5-triaza-7-phosphaadamantane) (Figure 1.31), which targets the histone core of chromatin instead of DNA and show high antiangiogenic effect and significant antitumor effects without toxic side effects.[168] In recent times, another 'piano-stool' ruthenium complex based on the SAHA ligand (Figure 1.31) was reported by Walton *et al.* and has been observed to be potent against lung carcinoma following a mechanism of inhibiting the class of histone deacetylase enzymes.[167,169] Cyclometallated complexes of ruthenium ions with polypyridyl based ligands (e.g. - $[Ru(phpy)(bpy)\text{-}(dppn)]^+$) were studied for their potential antiproliferative activity (Figure 1.31).[170] In another study, half-sandwiched complexes of ruthenium with 5-fuloroaracil derivative ligands (e.g. - $[(\eta^6\text{-}p\text{-cymene})Ru(5\text{-}FU)Cl_2]$) have been observed to exert potential anticancer activity through DNA intercalation (Figure 1.31).[171] Furthermore, Thomas *et. al.* reported a unique dinuclear ruthenium(II) polypyridyl system which targets human breast cancer cells with a comparable potency to that of cisplatin and shows high affinity towards DNA binding.[172] Two main examples of this system are $[(Ru(phen)_2)_2(tpphz)]^{4+}$ and $[(Ru(bpy)_2)_2(tpphz)]^{4+}$, which function as structure-specific DNA imaging agents by switching on the quenched luminescence in aqueous media upon non-covalent reversible binding with DNA groove (Figure 1.31).[173] Besides being well known as the 'light switch' DNA probes, these complexes have also shown potential to target endoplasmic reticulum as an imaging agent.[174]

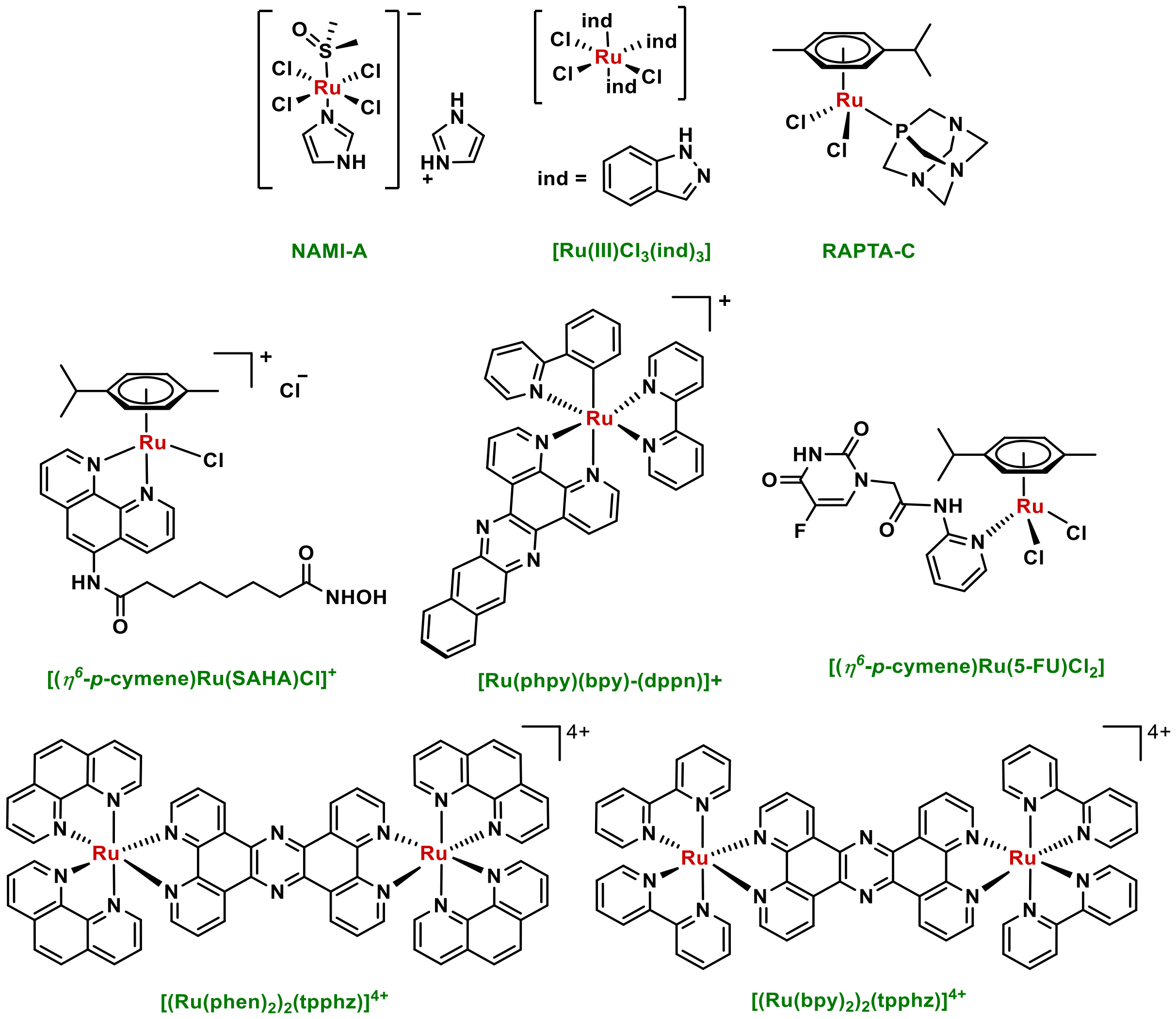

Figure 1.31: Ruthenium based potential anticancer agents

In addition, some radioactive metals are used to inhibit or kill cancerous tumour cell. Yttrium-90, samarium-153 and rhenium-188 are some common radioactive metal nuclei which pursue localised emission of α or β^- particles.[175] For example, two very common β^- emitters, ^{90}Y-based Zevalin and ^{153}Sm-based Quadramet are clinically useful to treat non-Hodgkin's lymphoma and bone metastases respectively.[176] Further, commonly investigated α-emitting radiopharmaceutical are based on bismuth-213, actinium-225 and radium-223 metal isotopes.

Various other metals such as copper (see Section 1.4 for a detailed discussion), titanium, gallium, cobalt, iron, zinc, gold, etc. have been observed to form metal-ligand complexes with potential anticancer activity, each taking advantages of the beneficial properties of metal complexes to affect cancer cell progression.

1.4 Copper – an Element of High Therapeutic Potential

1.4.1 Introduction to Copper Chemistry and its Relevance in Biological Activity

Many copper complexes have found potential use as therapeutic agents. The redox chemistry of copper is an important reason behind its biological relevance. Copper has two main oxidation states: the reduced cuprous form, Cu(I) and the oxidised cupric form, Cu(II). In the oxidising conditions of the extracellular environments, Cu(II) is more thermodynamically stable. However, in the intracellular more reducing environment, it readily converts to Cu(I). The coordination geometry of Cu is based on the principles of ligand field theory (LFT). Cu(II) has a $3d^9$ electronic configuration whereas Cu(I) possesses a closed shell $3d^{10}$ electron system.[177] As a result, in the oxidised d^9 state, there is a geometric preference for 4, 5 or 6 ligands in a square planar, square pyramidal, or axially distorted octahedral geometry respectively. On the other hand, the d^{10} reduced Cu(I) show no ligand field stabilisation energy and adopt linear, trigonal planar, or tetrahedral geometries, with an observed preference for tetrahedral geometry in copper containing proteins. (Figure 1.32).[178]

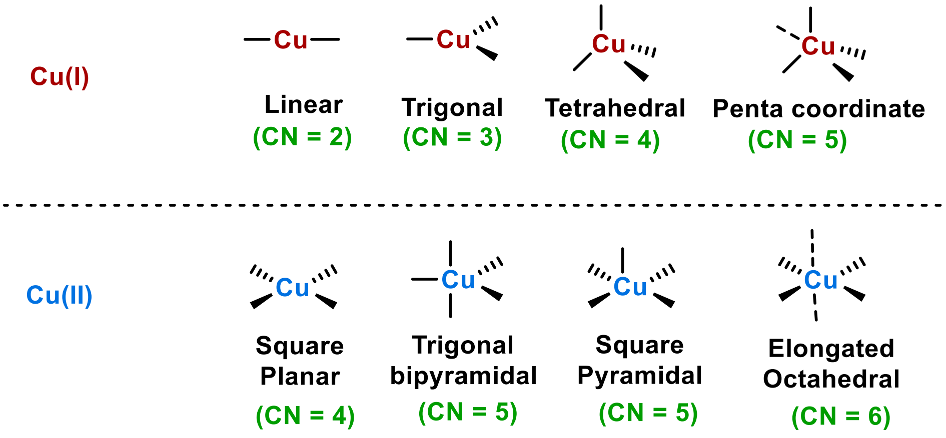

Figure 1.32: Various coordination geometry of copper metal

Moreover, according to the HSAB principle, Cu(I) is considered as a soft acid and Cu(II) lies in the category of borderline acids and therefore amino acids comprising of side chains with soft or borderline basic functional groups are more prone towards acting as copper binding ligands. Cu(II) prefers to bind with the harder Lewis bases like oxygen or amide nitrogen groups and borderline bases like imidazole nitrogen of amino acids (e.g. – histidine), whereas, Cu(I) tends to bind soft Lewis bases such as thiolate and thioether sulfurs of methionine and cysteine amino acids.[179] Such different characteristics due to the changing redox states of Cu contributes to the formation and activity of various organometallic copper complexes inside the cellular environment.[180]

Due to high redox potential of the Cu(I)/Cu(II) couple and their coordination preferences, copper is found to be a cofactor for some essential proteins, including cytochrome *c* oxidase (involved in energy metabolism), superoxide dismutase (involved in repairing oxidative damage) and tyrosinase (necessary for melanin synthesis).[181] Depending on the ligands, copper exhibits a range redox potential from +200 mV to +800 mV. This redox activity of Cu metal also contributes towards the generation of reactive oxygen species (ROS), such as hydroxyl radicals through Fenton like chemistry, which causes oxidative damage of cells, especially oxidising large biomolecules like DNA, proteins and lipids.[182] Also, Cu(II) reacts with sulfhydryls such as cysteine (RSH) or glutathione (GSH) and is reduced to Cu(I), which further catalyses the formation of toxic hydroxyl radicals (ROS) from hydrogen peroxide (Figure 1.33). In excess amounts, copper contributes towards toxicity and oxidative stress related health disorders *via* ROS generation.[183]

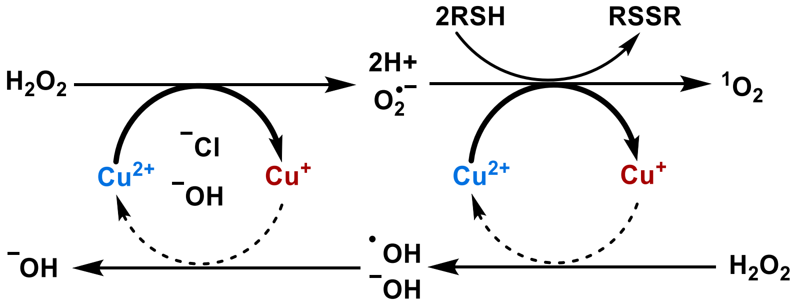

Figure 1.33: Key steps in copper-based Fenton chemistry, leading to generation of hydroxyl radicals as ROS

Copper serves as a major component of several proteins in living organisms. Some examples of copper-containing proteins are lysyl oxidase, dopamine β-hydroxylase, plastocyanins and azurins. These proteins play essential roles in different biological reaction pathways and work as electron carriers.[184]

Another way in which copper exhibits toxicity is by displacing iron from iron-sulfur clusters coordinating with the sulfur-donor ligand, thereby disabling enzyme activity.[185] Copper can also replace the native metal ions (e.g., Zn) in the binding sites of macromolecules (such as proteins) in living systems and thus rendering toxicity through alteration of their structures and functions. This biotoxicity of copper has been used to fight against the microbial infections, although the toxicity towards humans has limited the use of Cu in this area. However, with increasing resistance of bacteria against antimicrobial drugs, attention of antibacterial research has again been drawn towards this unique transition metal.[181]

Ionic copper salts (e.g., copper sulfate) have been used previously for the treatment of various infections. These ionic salts have a very poor ability to cross cell membranes. This restricted penetration of Cu ions leads to exceptionally high doses of Cu needed for any clinical treatment, thus causing increased level of Cu poisoning in the human body. This is the main reason behind the failure of Cu in medicinal drugs.[186]

Delivery of Cu can be assisted by the choice of ligand carriers. Ligands that assist in carrying Cu into the bacteria cell are known as ionophores and they selectively bind to copper ions and form lipophilic Cu complexes that enable access to the intracellular environment. The chemical properties that affect the metal-coordination ability of these ionophores include: (i) metal affinity (preferable choice of copper over other metal), (ii) redox potential (contributes to the stability and reactivity of the complex) and (iii) lipophilicity (controls the ease of metal ion permeation across the lipid layer of cell membrane).

1.4.2 Copper Complexes as Antibacterial Agents

Although the trace element Cu acts as an essential micronutrient in bacterial cells, it has been proven to be highly bacteriotoxic if employed in excess. The oldest medical record of using copper as an antiseptic and sterilizer can be found in the Smith Papyrus, which dates back to around 4500 years ago.[181] The recent emergence of widespread bacterial resistance against antibiotics has led researchers to consider whether copper complexes can also help in designing new therapeutic drugs against antimicrobial resistance.[187]

Copper can act as an antibacterial agents in two ways: (i) permeation through bacterial cell membrane with help of Cu-carriers and (ii) contact killing of bacteria upon exposure to dry metallic copper surfaces.[181,188]

1.4.2.1 Permeation of Copper Coordination Complexes through the Bacterial Cell Membrane

The challenges associated with the antimicrobial activity of copper lie in the fact that almost all the bacterial species have evolved a range of homeostatic systems to protect themselves from the toxic effects of excess copper ions. These systems are mainly based on the active regulation of copper ion levels in cellular environment through the efflux pumps, controlled by some Cu-specific regulatory proteins. These defence mechanisms also include copperscavenging by copper storage proteins and the impermeability of copper ions through the inner and outer membrane of bacterial cells.[189] The challenge for researchers is to produce copper complexes that can overcome the bacterial cell regulation.

In spite of all these challenges, several copper complexes have been reported to exhibit antibacterial activities. Cu(II) complexes of quinolone derivative sparfloxacin or oxolinic acid and pyridine based *N*-donor ligands (1,10-phenanthroline, 2,2'-bipyridine or 2,2'-dipyridylamine) (Figure 1.34 A) have been observed to be highly active against *E. coli*, *P. aeruginosa* and *S. aureus* species.[190,191] The antimicrobial activity of the copper complexes of Schiff bases derived from salicylidene-4-aminoantipyrine and substituted anilines (Figure 1.34 B) are also reported as active against the bacterial species *S. aureus, K. pneumoniae, S. typhi, P. aerugenosa and B. subtilis*.[192] 8-Hydroxyquinoline (8HQ) and its derivatives clioquinol (CQ) and PBT2 are planar, bidentate ionophoric ligands (Figure 1.34) that bind to Cu through the oxygen and nitrogen atoms. These donor atoms provide a preference for Cu(II) over Cu(I) with moderate binding affinity (Cu(II), $\log\beta_2 = 26.2$).[193] 8HQ has been long known to exhibit antimicrobial activity in the presence of divalent metal ions such as Cu.[194]

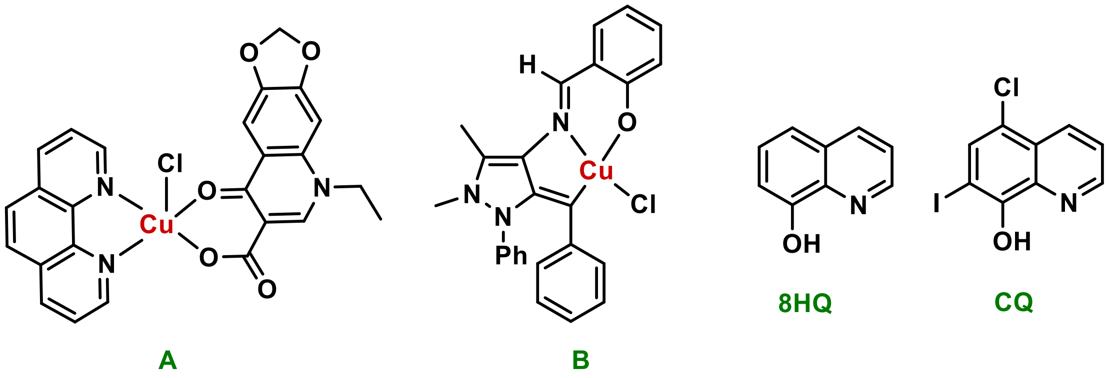

Figure 1.34: Various N- and O-donor ligands and their copper complexes as potential antibacterial agents

Two thiosemicarbazone derivatives, glyoxal-bis(4-methylthiosemicarbazonato)copper(II) (Cu^{II}(GTSM)) and its dimethyl containing analogue (Cu^{II}(ATSM)) (Figure 1.35 A), have been tested for antibacterial activity against *N. gonorrhoeae*, where these complexes exhibit at least 100 times better bactericidal activity than $Cu(NO_3)_2$ (therapeutic index ~1000). The antimicrobial activity of these Cu(II) bis-thiosemicarbazones arises due to inhibition of NADH dehydrogenases in the bacterial respiratory chain.[195] Cu^{II}(GTSM) also works against *M. tuberculosis* and *S. aureus*. Furthermore, other thiosemicarbazone derived ligands (e.g.- 5-methyl-3-formylpyrazole-*N*(4)-benzyl-*N(*4)-methylthiosemicarbazone) (Figure 1.35 B) have been observed to display antimicrobial properties against various Gram-positive and Gram-negative bacteria.[196]

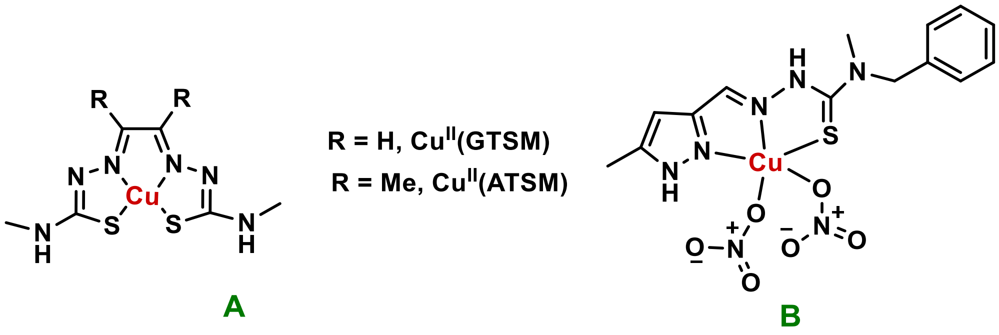

Figure 1.35: Sulfur donor-based copper complexes as potential antibacterial agents

Phenanthroline-derived ligands have also been exploited for their copper-dependent activity against bacterial species. Specifically, the Cu(I) complex of neocuproine (Figure 1.36 A) works as a novel inhibitor of transcription processes catalysed by RNA polymerase in *E. coli* and thus kills the bacteria.[197] This complex has also been studied for its effect on the growth of *M. gallisepticum* and *P. denitrificans* species, through inhibition of their energy-yielding metabolism. Moreover, it was suggested that this complex interferes with the actions of several bacterial enzymes, such as NADH oxidase and lactate dehydrogenase, through the interaction of copper with the enzyme sulfhydryl groups.[198] Another type of potential antibacterial agents are copper complexes of 1, 1′-symmetric ferrocene-derived Schiff-base ligands (Figure 1.36 B), which have been evaluated for activity against *E. coli, S. aureus, P. aeruginosa and K. pneumonae* species.[199]

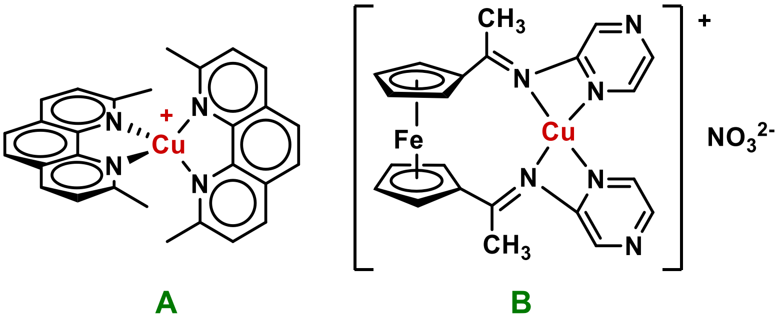

Figure 1.36: Some copper based antibacterial agents

In a different approach, already existing bioactive organic molecules are conjugated with copper, leading to modulation of their bioactivity. An example is the fluoroquinolone ligand, which upon binding with copper (Figure 1.37), shows a ~10 fold increase in lethal activity against Gram-negative *E. coli*, whereas activity against Gram-positive *S. aureus* was not enhanced.[200] Another example is ATP-6i, which shows A significant increase (~40 fold) in activity against *S. aureus* upon complexation with copper (MIC = 0.3 μM) (Figure 1.37).[201] This class of bioactive ligands form a unique complex with an unusual binding to Cu through the carbon atom of a pyrazole ring.[202]

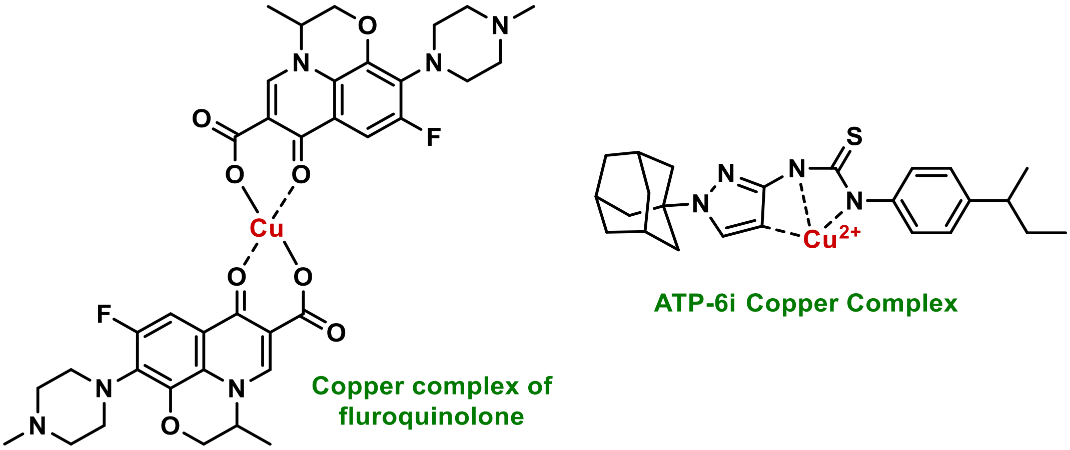

Figure 1.37: Copper complexes of existing bioactive molecules as antibacterial agents

1.4.2.2 Contact Killing

In recent times, antimicrobial properties of metallic copper or copper-alloy (>70% Cu) surfaces are being discussed and explored with great attention. Numerous bacterial species have been observed to be killed when they come in contact with a copper surface.[203] The release of free copper ions from the surface is understood to lead to a destructive interaction with the bacterial cell wall and cell membrane. As a result, a high influx of copper ions in the cytoplasm of the bacterial cell leads to inhibition of bacterial enzyme activity and damage to other cellular components. Various studies have also observed the generation of various ROS species, whose production is likely catalysed by the release of Cu ions from the surface. Overall, this new phenomenon has been quite significant in antibacterial study, especially against resistant strains. In the cases of heat- or radiation-resistant bacteria, such as *Bacilli* and *Clostridia*, the copper surface approach has been found to destroy most of their endospores in hours.[204]

1.4.3 Copper Complexes as Anticancer Agents

In principle, copper complexes have very different mechanism of action and toxicity effect than conventional platinum based anticancer drugs.[177]

Thiosemicarbazone (TSC) based ligands were the earliest choices for conjugation with copper and their complexes were observed to possess inhibitory action against cancer due to their activity against ribonucleotide diphosphate reductase enzymes. However, poor water-solubility and high toxicity limited the potential of this class of complex. To address this issue, 1,2-diazine was introduced in place of classical 2-pyridine and further addition of the N4-azabicyclo[3.2.2]-nonane group, led to a 100 fold increase in solubility of the respective copper complex, while retaining potency against lymphoblastic leukaemia, colon carcinoma and lung cancer, which was in the nanomolar range (Figure 1.38 A).[205] Furthermore, a copper complex of 3-formylchromone has been reported to be stable in both Cu(II) and Cu(I) redox states (Figure 1.38 B). This complex was found to bind to the active site of a kinase enzyme better than the non-complexed ligand, leading to a >100 fold increase in inhibition than it parent ligand. This complex is significantly active against human pancreatic cancer cells.[206] In another study, a 1:1 complex of a quinolone derivatised ligand (Figure 1.38 C) with copper has been tested against human prostate cancer cell lines and noted to induce significant apoptosis through inhibition of proteasome activity, without increasing oxidative stress.[207]

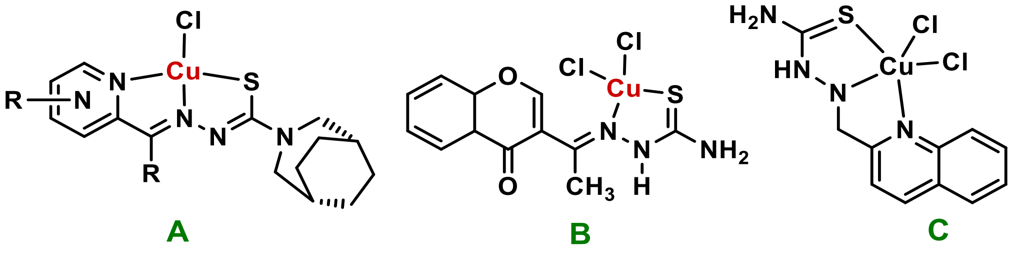

Figure 1.38: Thiosemicarbazone based copper complexes as potential anticancer agents

Copper complexes of benzimidazole derivatives such as 1-[3-(2-pyridyl)pyrazol-1-ylmethyl]naphthalene[208] (Figure 1.39 A) and bis(3,6-pyrazol-1-yl)pyridazine[209] (Figure 1.39 B) have been explored for their significant activity in the nanomolar range against various human cancer cell lines through DNA intercalation. In addition, Dallavalle *et al.* reported that employing copper with disulfiram-based ligands gives complexes that exhibit programmed cell death of human fibrosarcoma cells and non-sensitivity towards normal cell lines (Figure 1.39 C).[210]

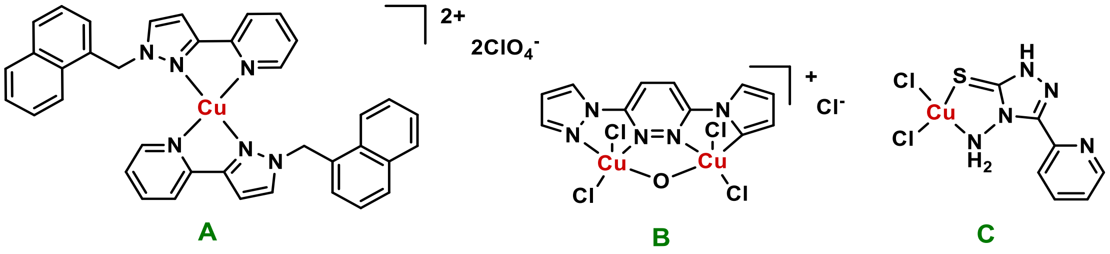

Figure 1.39: Benzimidazole based copper complexes as potential apoptotic agents

Another popular chelator, 1,10-phenanthroline has been found to have anticancer activity upon coordination with copper through DNA/RNA degradation, but the non-specific targeting of biomolecules and poor stability of the ligand-metal bonding limits its applicability. To solve this problem, researchers have conjugated additional ligands with copper phenanthroline system. For example, $[Cu(phen)_2(mal)].2H_2O$ (mal = malonate) exerts better activity than cisplatin against kidney carcinoma, through inhibition of DNA synthesis (Figure 1.40 A).[211] Escriba` *et al*. further reported a ternary complex based on two phenanthroline ligands and an iodohippuric acid conjugation, which leads to selective apoptosis of lung carcinoma cells through generation of free $[Cu(Phen)_2]^+$ that cleaves DNA (Figure 1.40 B).[212] Furthermore, octahedral complexes formed by copper coordination with some N and O based tetradentate ligand and phenanthroline (Figure 1.40 C) have been studied owing to their antiproliferative activity against cervical carcinoma through cell cycle arrest, with a potency 100 fold greater than cisplatin.[213] Recently, Kogularamanan *et al.* have also reported some variation of ligands to conjugate with copper along with phenanthroline derivatives. Among them, a metallopeptide containing Cu(II) complex (Figure 1.40 D) has been observed to disrupt mitochondrial function and generate ROS in breast cancer stem cells and thus induce apoptosis.[214] Another example of a similar phenanthroline derivative showed conjugation of copper with a non-steroidal anti-inflammatory drug, indomethacin, and the copper complex kills breast cancer cells through DNA damage *via* ROS formation and inhibition of cyclooxegenase-2 activity (Figure 1.40 E).[215] In another study, Casiopeinas®, a novel class of copper based drugs has been found to have quite high antineoplastic activity. Casiopeina IIgly, Casiopeina IIIia, show antiproliferation activity through induction of cell apoptosis even at lower doses than that by cisplatin (Figure 1.40 F).[216] These complexes are also effective in disruption of membrane potential of mitochondria, which play a crucial role in apoptosis of cancer cells.[217]

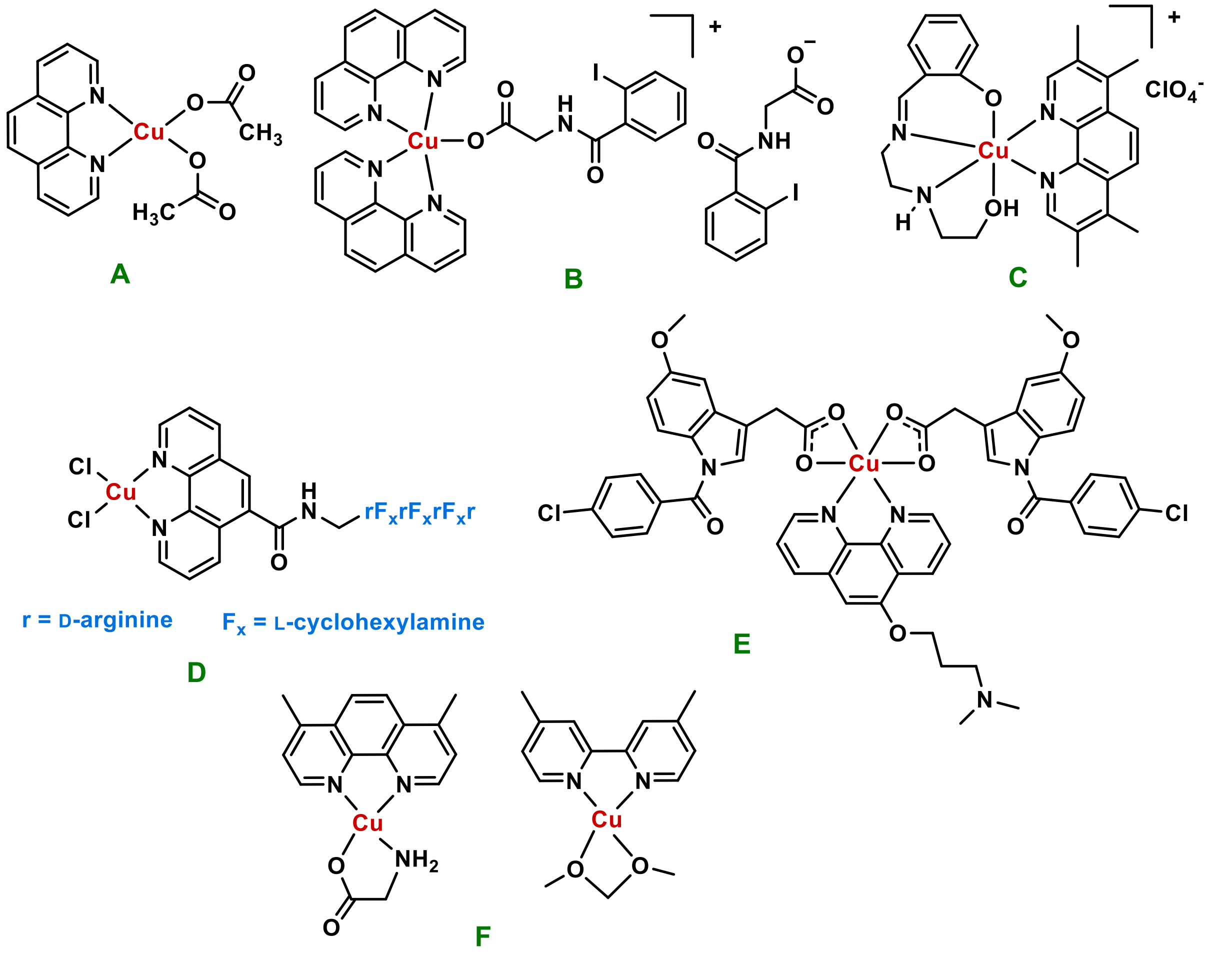

Figure 1.40: Phenanthroline and its derivative based copper complexes as anticancer agents

Phosphine derived ligands have been extensively studied for their potential in therapeutic purposes. With constant efforts to increase their bioavailability, various phosphine derivative ligands have been synthesised and conjugated with copper ion in a ‘‘CuP$_3$’’ type of coordination sphere in order to contribute towards anticancer activity. Among them, $[Cu_2(dppe)_3(CH_3CN)_2][ClO_4]_2$ has found to be significantly cytotoxic against human lung carcinoma through DNA cleavage and p53 pathway activation (Figure 1.41 A).[218] A similar mixed ligand approach has been applied to design water soluble $[HC(CO_2)(pzMe_2)_2]Cu(thp)_2$, which provides antiproliferative activity against various tumour cell lines, including cisplatin resistant ones (Figure 1.41 B).[219]

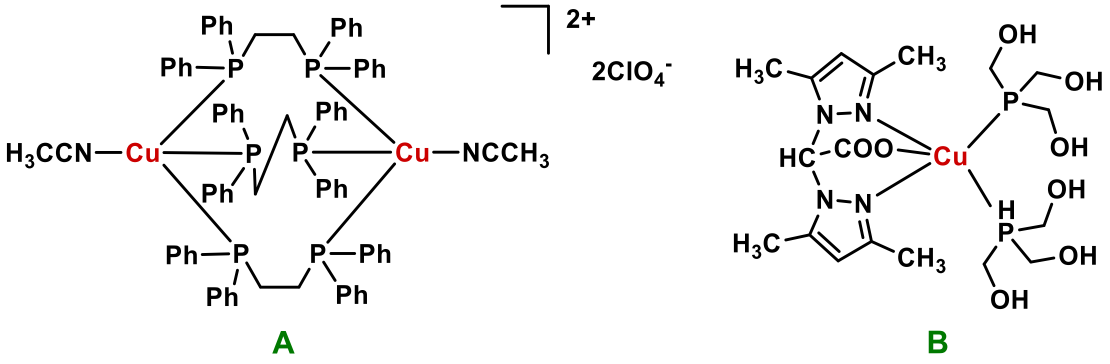

Figure 1.41: Phosphine based copper complexes as antiproliferative agents

In more recent times, bi-or tri nuclear copper complexes of polypyridyl based ligands have been studied as potent DNA intercalators.[220] For example, a binuclear Cu(II) complex of bis-tridentate tetrakis (2-pyridyl-methyl)benzene-1,4-diamine (1,4-tpbd) and 2,2'-bipyridine ligands (Figure 1.42 A) exhibits a very high efficiency of DNA cleavage through intercalation (DNA binding strength (K_a) = 7.5 × 10^6 M^{-1}) and thus potency as anticancer agent.[221] Furthermore, a trinuclear copper complex of disubstituted terpyridine based ligands (Figure 1.42 B) has been reported to render cytotoxicity against a wide range of cancer cell lines and have a higher activity of DNA cleaving compared to its mono- and di-nuclear analogues.

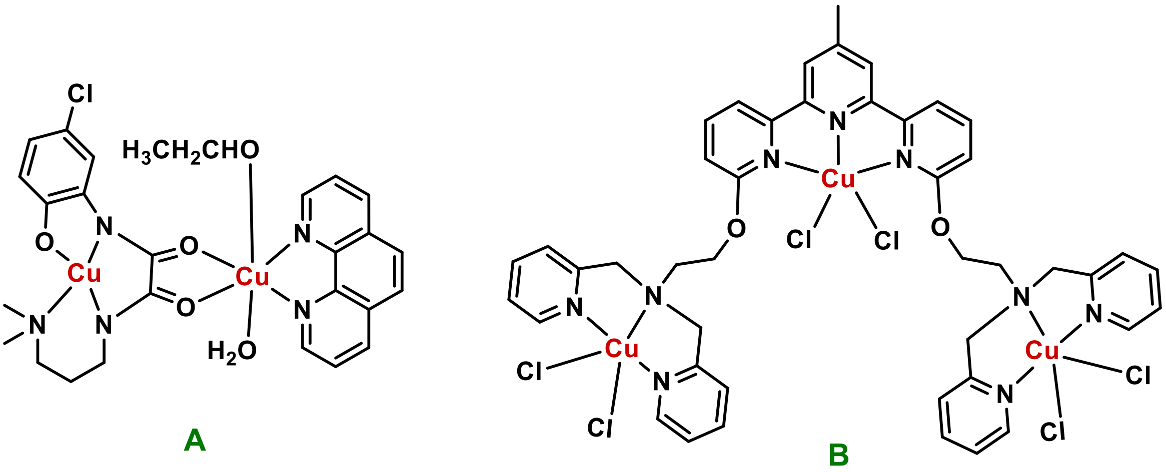

Figure 1.42: Multinuclear copper complexes with considerable potency for apoptosis

There are several other O, N and S-based donor ligands that have been used in new copper complex formations for potential anticancer activity. However, issues with solubility and bioavailability have significantly limited copper-based complexes in reaching clinical trials.

1.4.4 Copper Pyrithione

1.4.4.1 Pyrithione Ligand as Lipophilic Ionophore

Pyrithione (PT) or 2-mercapto-pyridine-*N*-oxide is a pyridine based bidentate ligand which is well known for its ability to coordinate with divalent transition metal ions. In solution, this ligand undergoes a thiol-thione tautomerization *via* an associative or dissociative mechanism (Figure 1.43). This tautomeric equilibrium is solvent dependent and the thione isomer is preferred in polar environments whereas the thiol form predominates in non-polar and aprotic medium. In aprotic non-polar solvents, the thiol-form is better stabilised through an intramolecular hydrogen bond. In aqueous medium, the thione form is preferred and a molar ratio of 54 has been observed for thione:thiol forms. Pyrithione ligand also exhibits an acid-base equilibrium with a pK_a of 4.67. Various photochemical studies of pyrithione have reported formation of a 2-pyridylthiyl radical (PyS•) along with a hydroxyl radical (OH•) upon photo-triggered homolysis. This generation of hydroxyl radicals has been considered for its potential use in photodynamic therapy (Figure 1.43).[222]

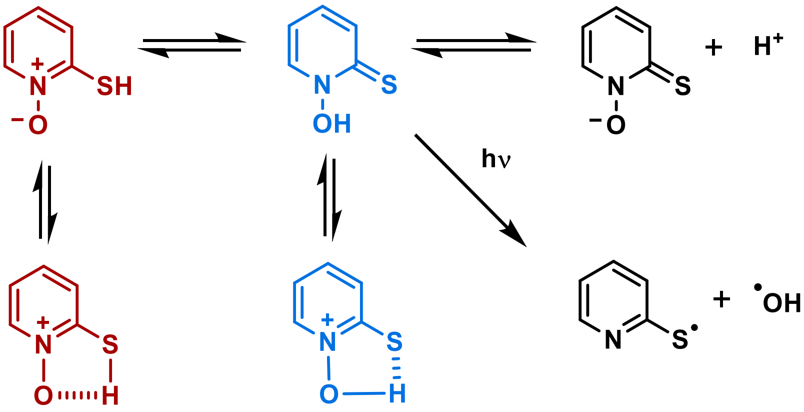

Figure 1.43: Tautomerisation, acid base equilibrium and photolysis of pyrithione ligand

In its deprotonated form, PT conjugates to metals through S and O donor atoms and usually forms 2:1 complex with metals such as zinc, copper, nickel etc (Figure 1.44). A crystal structure of Zn(pyrithionate)$_2$ ([Zn(PT)$_2$]) reveals formation of dimers, where Zn(II) from one unit coordinates with the oxygen donor from other unit, leading to a trigonal bipyramidal geometry around Zn.[223] However, according to crystal data, [Cu(PT)$_2$] and [Ni(PT)$_2$] adopt square planar geometry where the pyrithione ligands are *trans* and *cis* configurations, respectively.[224,225]

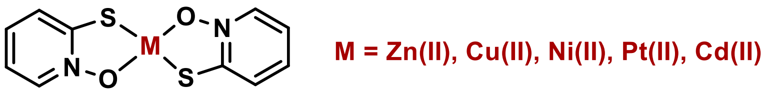

Figure 1.44: General structure of metal-pyrithione complex

PT and its derivatives have shown potential to act as small molecule lipophilic ionophores and inhibitors of biomolecules. In the cellular system, $[Cu(PT)_2]$ can readily release copper in enzyme active sites and form stable bispyrithiones, containing a disulphide bond. The free PT ligand can also chelate with metal co-factors of metalloenzymes, leading to enzyme disruption. An amino acid derivative of PT has been reported to exert significant and selective inhibition of HDAC 8 enzyme, leading to potency against cancer cells (Figure 1.45 A).[226] Substitutions at the sulphur atom of PT have also been shown to produce potential antibacterial agents against *M. tuberculosis* (Figure 1.45 B).[227] PT has also been suggested to indirectly inhibit membrane transport systems.

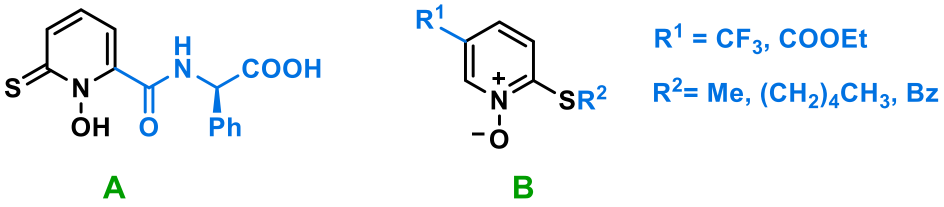

Figure 1.45: Pyrithione derivatives as potential bioactive agents

$[Zn(PT)_2]$ has been commercially used for decades as an active ingredient of antidandruff shampoos and marine antifouling paint.[180] As an anti-dandruff agent, $[Zn(PT)_2]$ affects the growth of *Malassezia restricta*, the main microbe responsible for dandruff in human skin, by increasing cellular Zn level, which leads to inhibition of Fe-S cluster protein synthesis and reducing lipase expression.[228] $[Zn(PT)_2]$ also hinders membrane transport and inhibits ATP synthesis in prokaryotic cells and thus possesses potency against a wide range of microbial organisms such as fungi and bacteria. In combination with $[Zn(PT)_2]$, the activity of silver sulfadiazine against *S. aureus*, *P. aeruginosa* and *A. baumannii* bacterial species has been observed to enhance significantly.[229] Combining $[Zn(PT)_2]$ with phosphorylated fabric cellulose (Figure 1.46) has been found to produce an antibacterial effect against *E. coli*, *S. aureus* and *C. albicans species*.[230] According to another study, $[Zn(PT)_2]$ is active against oral squamous cell carcinoma by altering various biochemical signalling pathways and reducing enzyme expression.[231] This complex has also been shown to target proteasome associated deubiquitinases (DUBs) and inhibit them as a mechanism of anticancer activity against lung carcinoma and leukemia.[232] [Zn(PT)$_2$] also induces apoptosis in human ovarian cancer cells by targeting the lysosome and inhibiting mitochondrial function.[233]

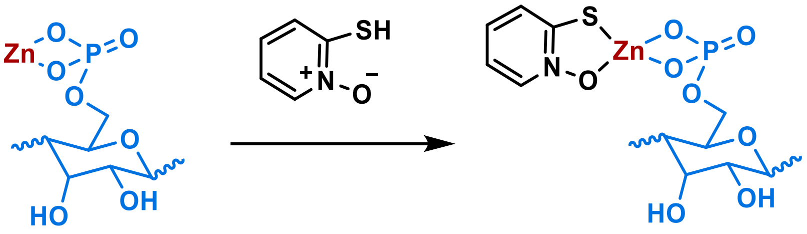

Figure 1.46: Coordination of ZnPT with phosphorylated fabric cellulose

Complexation of ruthenium with one pyrithione ligand (RuPT) along with an arene ligand gives rise to a number of complexes that have been studied extensively for their potential as anticancer agents. Turel *et al.* reported *p*-cymene conjugation with RuPT, which gives selective potency against hormone dependent breast cancer cells and inhibits related aldo-keto reductase enzymes (Figure 1.47 A).[234] Similar *p*-cymene based organoruthenium chloride complexes of PT possess significant inhibitory properties against cholinesterase enzymes, an important drug target for Alzheimer diseases.[235] Next, the same research group studied the anticancer activity of these complexes of with a trithiacyclononane ligand to give complexes that were active against lung, colon and ovarian cancer cell lines (Figure 1.47 B).[236] Further study was conducted for a similar class of complexes with benzo-fused pyrithione ligands against ovarian cancer cells and results showed their potential to overcome multidrug (e.g.- cisplatin and adriamycin) resistance and induce apoptosis through cell cycle arrest and inhibition of thioredoxin reductase enzyme (Figure 1.47 C).[237]

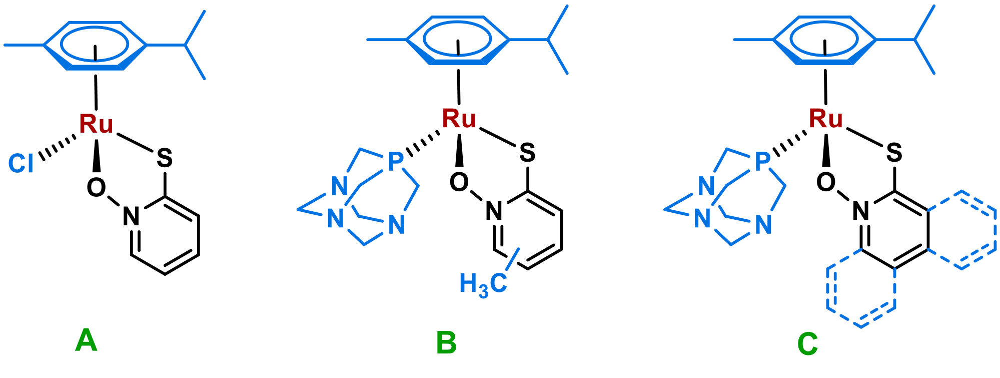

Figure 1.47: Ruthenium pyrithione based complexes as potential anticancer agents

[Ni(PT)$_2$] and [Pt(PT)$_2$] complexes have been shown to have an apoptotic effect against imatinib-resistant chronic myeloid leukaemia cells by downregulation of the Bcr-Abl gene and selective inhibition of 19S and 26S-proteasome-associated DUBs respectively.[238] This approach does not involve DNA damage and therefore lowers the cytotoxicity to normal cells, for example, compared to cisplatin. [Pt(PT)$_2$] also follows a similar pathway to treat ovarian cancer cells.[239] Furthermore, cadmium pyrithione complex also exerts potency against carcinoma *via* a similar mechanism.[240]

In addition, complexes of three pyrithione ligands with trivalent iron (Fe), gallium (Ga) and bismuth (Bi) metal ions have been found to possess significant activity against rifampicin-resistant *M. tuberculosis*.[241]

1.4.4.2 Copper Pyrithione and its Biological Activity

Copper pyrithione ([Cu(PT)$_2$]) has been used as an antifouling agent. However, its potential for therapeutic purposes has not yet been well-studied. There are, however, a few studies of copper [Cu(PT)$_2$] as a potential antibacterial and anticancer agent.

In a study by Liu *et al.*, copper complex of PT has been studied for its potential as an anticancer agent. [Cu(PT)$_2$] has been found to possess very good cytotoxicity (IC_{50} <0.5 µM) against various cancer cell lines and shows a significant (~100 fold) improvement in activity than that by a well-known anticancer agent [Cu(DDTC)$_2$] (DDTC = diethyldithiocarbamate) (IC_{50} = 50 µM). In this study, the main mechanism for the anticancer activity of [Cu(PT)$_2$] is suggested to be inhibition of ubiquitin proteasome pathway. The ubiquitin proteasome pathway is highly important in various cellular functions such as protein degradation, immune response, DNA repair and cell cycle regulation. This pathway mainly consists of three different events (Figure 1.48). The first step is ubiquitination, a post-translational modification which involves attaching ubiquitin with intracellular protein substrates to regulate their degradation, catalysed by ubiquitin-activating enzyme (E1), ubiquitin-conjugating enzymes (E2), and ubiquitin ligases (E3). This process is reversible and therefore deubiquitination happens simultaneously, catalysed by deubiquitinases (DUBs), facilitating further use of free ubiquitin. Lastly, the ubiquitinated substrates are degraded at the 20S proteasome site with help from 19S proteasomal-DUBs.[242] The proteasomal-DUBs are highly expressed and play fundamental roles in the regulation of various signalling pathways in tumour cells. Therefore, they have emerged as novel targets for anticancer agents. [Cu(PT)$_2$] has been observed to inhibit proteasomal-DUBs, leading to accumulation of ubiquitinated proteins and therefore inducing apoptosis in cancer cells.[243] Another study also supports the potency of [Cu(PT)$_2$] against various cancer cell lines with IC_{50} value of 0.1-7.4 µM.[244]

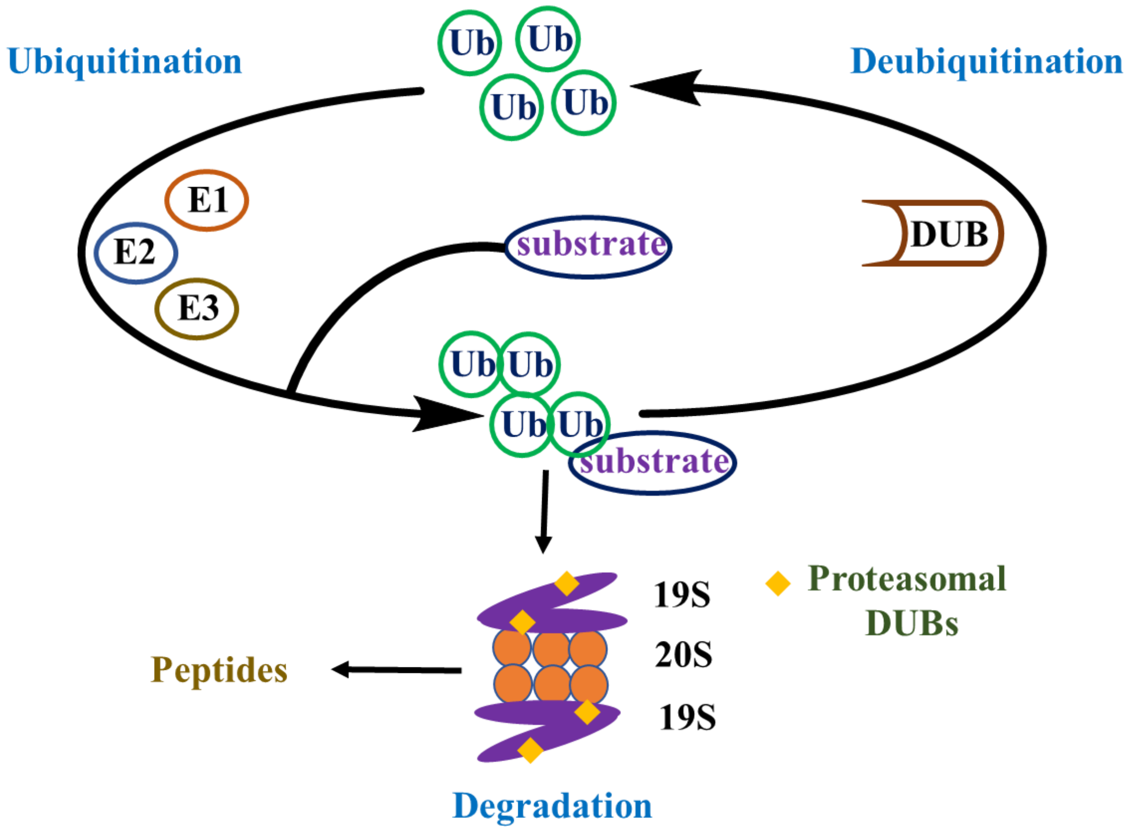

Figure 1.48: Ubiquitin proteasome pathway

Beyond anticancer activity, [Cu(PT)$_2$] has been employed in antibacterial studies against various bacterial species. Growth of amikacin-resistant *K. pneumoniae* bacterial strains have been observed to be altered in the presence of [Cu(PT)$_2$] along with amikacin, an aminoglycoside-based antibiotic. The mechanism of resistance by this bacteria is primarily acetylation of the antibiotic by plasmid mediated catalytic activity of aminoglycoside 6'-*N*-acetyltransferase type Ib [AAC(6=)-Ib] enzyme, which is inhibited by [Cu(PT)$_2$] and [Zn(PT)$_2$], thereby allowing the amikacin to operate.[245] In addition, [Cu(PT)$_2$] inhibits the growth of the drug resistant bacteria species *M. tuberculosis*[246] and fungal species *Cryptococcus neoformans.*[247] Another approach by Franz *et al.* suggested in situ formation of [Cu(PT)$_2$] from a pyrithione based prochelator molecule, which utilises β-lactamase enzyme produced by drug-resistant bacteria for this conversion, leading towards inhibition of β-lactam resistant *E. coli* strain (Figure 1.49).[248] They also suggested the mechanism of inhibition to be hyper-accumulation of copper in bacterial cell due to [Cu(PT)$_2$] insertion.

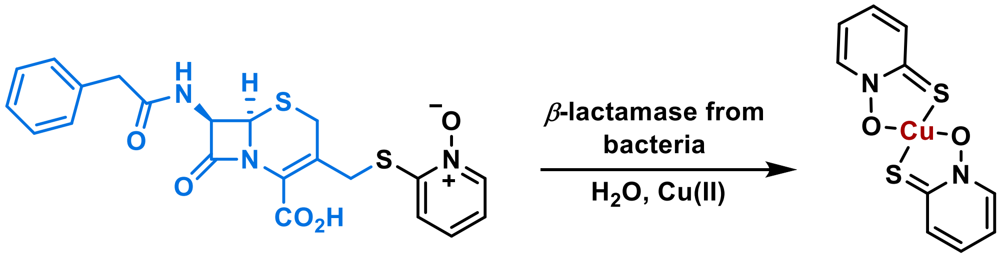

Figure 1.49: Generation of [Cu(PT)$_2$] utilising bacterial β-lactamase from a pyrithione derivative prochelator

In 2018, another extensive study suggested that Cu(II) can inhibit the growth of carbapenem-resistant *E. coli, in vitro* by inactivating the targeted enzyme, NDM-1. NDM-1 was highlighted in Section **1.1.3.2** as a key enzyme in the development of multidrug resistant 'superbugs'. It was also shown that using pyrithione as a carrier helps Cu to permeate through the bacterial cell membrane more efficiently and thus needing ~100 times lower concentration than that of ionic Cu salts. Nonetheless, this concentration of [Cu(PT)$_2$] is still higher (~10 µM) than is tolerated physiologically.[249] This study also proposed that the copper ion works through the mechanism of interference in Zn-binding in the NDM-1 active site (Figure 1.50). In this mechanism, Cu(II) binds to either the Zn-containing pocket or an outside allosteric pocket of NDM-1. In addition, copper can also disrupt the synthesis, folding, metal site assembly and stability of NDM-1 enzymes, leading to their degradation. Precisely which mechanism is involved remains under investigation.

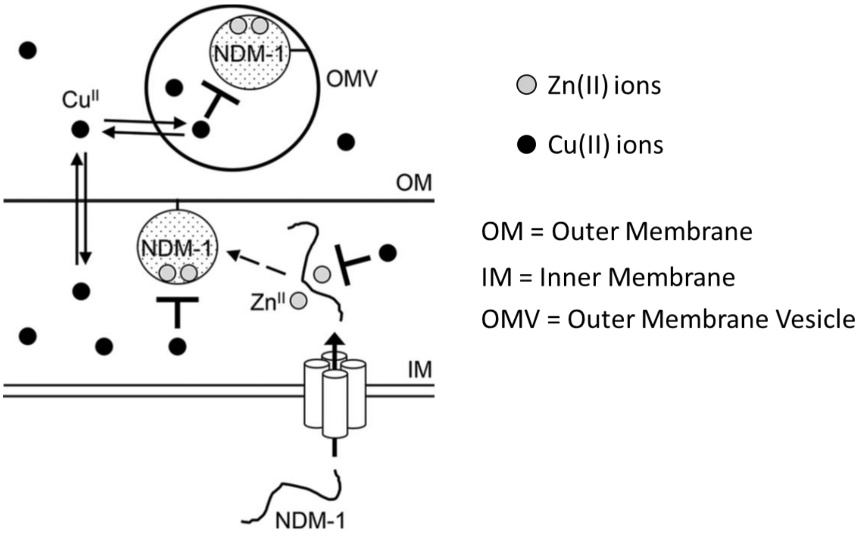

Figure 1.50: General schematic of the effects of copper on NDM-1; adapted from reference 249

Due to its lipophilic characteristic and unique mechanism of anticancer activity, the copper pyrithione complex carries remarkable potential for therapeutical purposes. However, high insolubility in aqueous medium decreases its bioavailability significantly. Therefore, implementation of its potential in clinical purposes has not been successful yet and draws attention of further research to develop pyrithione derivatives with higher solubility.

This Chapter has summarised some key factors in bacterial infection and cancer progression. A focus was given to the NDM-1 enzyme, which is believed to have a role in antibiotic resistance in the so-called ‘superbugs’. Many metal complexes are known for their excellent therapeutic activity and recent studies have identified copper pyrithione as a potential inhibitor of the NDM-1 enzyme, with potential to combat the antibiotic resistance. Copper pyrithione has also shown some potential anticancer activity. Despite these preliminary studies, there is much more still to explore with the copper pyrithione complex.

1.5 Aims and Objectives

The overall aim of this project is to develop and design derivatives of copper pyrithione with an objective of improving its bioactivity, along with its physiochemical properties. The parent complex, copper pyrithione possesses fairly good antibacterial activity and some anticancer activity. However, one key issue this project will focus on is the poor water-solubility of this complex, which hampers its bioactivity. Another focus is to understand how structural modifications of the pyrithione ligand can help to enhance the bioactivity against bacterial species and cancerous cells. Specific aims are as follows:

1. ***Introduction of small functional group substituents on copper pyrithione:***

   This part of the project broadly aims to design and synthesise derivatives of copper pyrithione, with various electron donating, electron withdrawing and amphiphilic substituents, in a variety of positions around the pyrithione ring. Characterisation of all ligands and complexes will be carried out using NMR spectroscopy, mass spectrometry, elemental analysis and X-ray crystallography.

2. ***Measurement of physiochemical properties:***

   Next, we will focus on measuring various physiochemical properties, such as metal:ligand binding constants, lipophilicity and solubility of these copper complexes, using UV/vis spectroscopy and ICP-OES as the quantification techniques. The main objective of these studies is to develop complexes with maximised water solubility, reasonably high lipophilicity for membrane permeability and optimised complex stability to retain the metal until it is released at the site of action.

3. Determining antibacterial and anticancer activities:

The newly developed copper pyrithione complexes will be subjected to antibacterial susceptibility screening against multidrug-resistant bacteria, *in vitro* cytotoxicity assays against healthy and cancerous cells and antibiotic synergy studies. The main objective is to develop complexes with good activity and selectivity and also to determine any trends in the structure-activity correlation in these complexes.

4. Development a fluorescent copper pyrithione derivative for microscopy:

Designing a fluorescent pyrithione derivative will allow us to determine the localisation of these complexes inside the cellular environment and potentially give information on a mechanism of action. The azide-alkyne ‘click’ chemistry will be used to attach a fluorophore tag onto the copper pyrithione complex. Measurement of the photophysical properties for this complex will be determined using UV/Vis and fluorescence spectroscopies and live-cell fluorescence microscopy.

5. Synthesis and bioactivity of pyridine based ionophores:

Alternative copper complexes, based on pyridine ligands, will also be synthesised and analysed with a view to finding novel copper complexes with good bioactivity and selectivity.

2. Modified Copper Pyrithione Complexes

2.1 Introduction

2.1.1 Relationship between Crystal Structure and Solubility of Copper Pyrithione

The X-ray crystal structure of non-substituted copper pyrithione was first determined in 1997.[250] The complex adopts a *trans*-square-planar geometry with the copper atom at the centre of inversion (Figure 2.1 A). This structure reveals that oxygen-copper bonds (bond length = 1.9 Å) are slightly shorter than sulfur-copper bonds (bond length = 2.2 Å). This crystallography provides insight into the stability and solubility of [Cu(PT)$_2$]. In the crystal packing, it can be observed that molecules in same plane interact with each other through hydrogen-like bonding between donor oxygen atom and aromatic hydrogens (Figure 2.1 B). The aromatic carbon is not strictly an example of H-bond donor, but the overall electron density of the aromatic ring allows for the H bonding observed, which is measured at a distance of 2.41 Å. By contrast, zinc pyrithione shows a *cis* arrangement of the coordinating atoms and, this H-bonding interaction only occurs between two molecules rather than across an extended plane. In copper pyrithione, a further intermolecular interaction is observed. Molecules from adjacent planes interact through intermolecular copper-sulfur linkages (Figure 2.1 C, Cu…S distance is 3.25 Å), leading to an overall stacking in the crystal structures. This interaction leads to tetragonally distorted octahedral structure around copper, which shows the classical Jahn-Teller distortion of Cu(II) (d^9 system). Moreover, π-π interactions between two pyridine rings of complexes from two adjacent planes can also be observed.

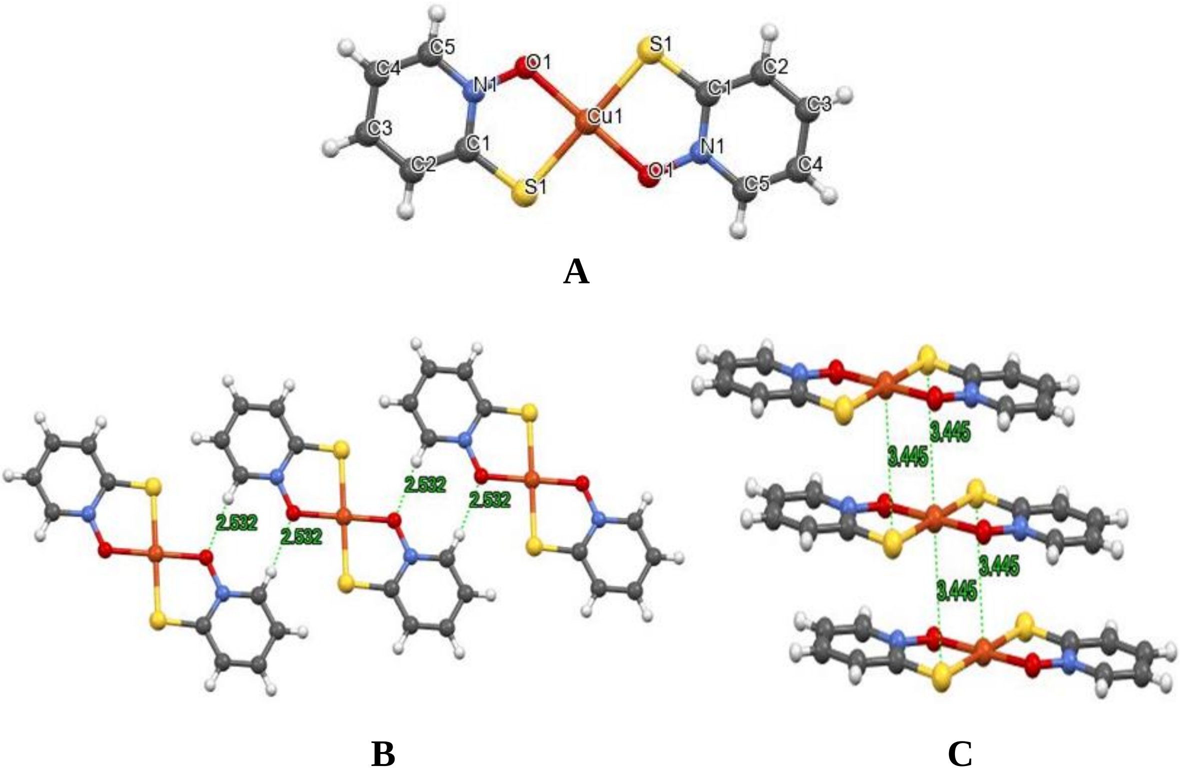

*Figure 2.1: (**A**) Crystal structure of copper pyrithione crystal, (**B**) adjacent molecules forming chain through hydrogen bonding and (**C**) copper-sulfur interaction within molecules in adjacent planes*

The combination of these intermolecular interactions between complexes both within a plane and between planes leads to very poor solubility of the copper complex in almost every solvent, polar and non-polar. Such low solubility represents a challenge to test its potential as a bioactive molecule *via in vitro* or *in vivo* biological assays

2.1.3 Enhancing Bioactivity through Additional Functional Groups

To exploit the potential of copper pyrithione complexes as bioactive reagents, the aqueous solubility and uptake into biological systems must be optimised. There are two main factors, solubility and lipophilicity, which play key roles in the uptake of bioactive compounds into the cytosol and movement between intracellular systems.

Copper pyrithione is highly insoluble in water (1-2 ppm or 0.001 g/L). Even adding 1-2% DMSO (as is common in biological assays) is not enough to keep this complex dissolved in water. Consequently, aqueous biological assays are challenging and require high levels of solubilising DMSO. As discussed previously, intermolecular interactions are considered to be the primary reasons behind water-insolubility of copper pyrithione. As such, destabilising the stacked structure formation of copper pyrithione is a potential route to increasing solubility.

Introduction of substituents on the pyrithione ligand may disrupt the stacking formation either through steric hindrance between two adjacent planes or by facilitating interactions with water molecule through formation of stronger hydrogen bonds.

Along with solubility, another key physical property of any potential drug molecule is lipophilicity, which impacts a drug's ability to permeate through lipopolysaccharide membrane, a main component of outer cellular structure. Bioavailability and cell uptake of drug molecules highly depend on the regulation of lipophilicity. Introduction of small, branched hydrocarbon moieties could increase the lipophilicity of the pyrithione complexes and thereby improve their uptake through the lipid bilayer of the cell membrane.

A further key criterion to consider while designing modified copper pyrithione complexes is their stability. The potency of bioactive metal complexes often relates to their ability to release their metal from the ligand – for example, to allow transmetallation with metalloenzymes or allow metal binding to other biomolecules. In this context, the metal-ligand bonds need to be labile enough to release the metal inside cellular system, but stable enough to stay intact during transport around the body and cell uptake. Achieving this balance is the key to developing new metal-based drugs. The stability of the copper pyrithione complexes will be affected by the electronics on the pyrithione ring, which can be modulated through substitutions.

In this chapter, we introduce small functional groups on the pyrithione ring in an attempt to achieve higher water-solubility, while balancing the lipophilicity and stability of the complexes. By varying these properties, the aim is to enhance the bioactivity and related physiochemical properties of the complexes. Employing electron donating or electron withdrawing substituents can help to vary the electronics of the pyrithione and therefore the copper-ligand bond strength. Furthermore, introduction of branched hydrocarbon chains can contribute to increasing lipophilicity, as well as potentially disrupting the copper pyrithione crystal structure and increasing solubility.

2.2 Results and Discussions

2.2.1 Synthesis and Characterisations of substituted Copper Pyrithione Complexes

In accordance with above hypothesis, the pyrithione ligands were substituted with various small functional groups (Figure 2.2). The substitutions can be largely categorised into three groups, which are – electron donating groups (alkyl, alkoxy, hydroxyl groups), electron withdrawing groups (trifluoromethyl group) and aromatic groups with (phenyl group, benzene ring extension). All the substituted along with non-substituted pyrithione ligands and their respective copper complexes have been synthesised and characterised using various analytic techniques, as described below.

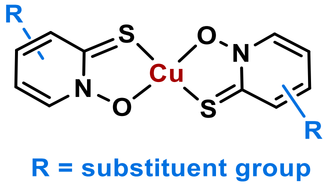

Figure 2.2: Substituted copper pyrithione complex

Non-substituted Pyrithione

[Cu(PT)$_2$] containing non-substituted pyrithionate ligand was synthesised in good yield (>70%), via a known procedure (Figure 2.3).[251] The commercially available sodium salt of pyrithione was dissolved in water and addition of an aqueous solution of $CuCl_2.2H_2O$ led to immediate precipitation of [Cu(PT)$_2$] as a green solid.

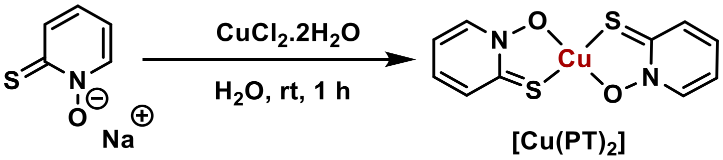

Figure 2.3: Synthesis of [Cu(PT)$_2$] from sodium salt of 2-mercaptopyridine-N-oxide

Characterisation of [Cu(PT)$_2$] using NMR spectroscopy is challenging due to the paramagnetic character of Cu(II) (d^9 system). The complex was characterized using atmospheric solids analysis probe (ASAP) mass spectrometry and elemental analysis data. In the ASAP mass spectrum, a *m/z* peak of 315.943 confirms formation of copper pyrithione ([$CuL_2 + H^+$]) (Figure 2.4). The isotope pattern is also consistent with that expected. In addition, the mass spectrum also shows formation of other metal-ligand species, such as [Cu_2L_3]$^+$ (m/z = 505.862). Elemental analysis of the product obtained supports formation of the desired complex with empirical formula CuL_2. Therefore, the additional mass peaks (e.g., Cu_2L_3) are likely formed in the mass spectrometer where various fragmentations and adducts can form.

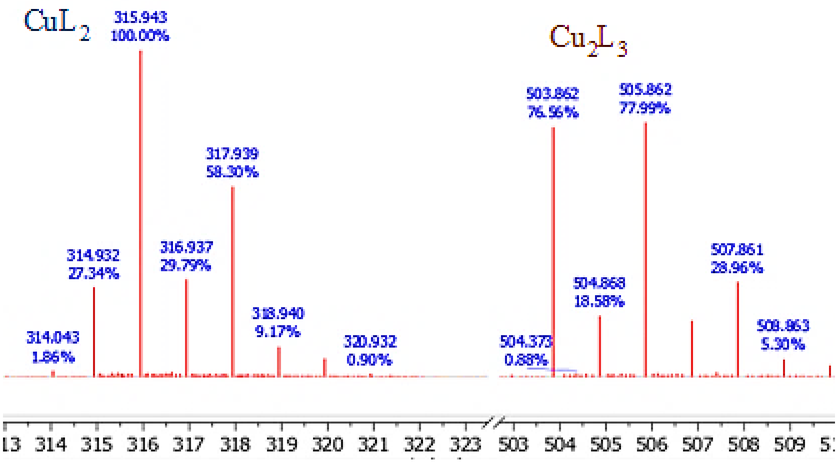

Figure 2.4: ASAP mass spectrum for complex [Cu(PT)₂]

Next, we focused on synthesising substituted pyrithione ligands and their respective copper complexes. A common synthetic pathway was developed to synthesise the ligands, which involves an oxidation of a substituted halo-pyridine, followed by a nucleophilic aromatic substitution of the halogen with a metal sulfide. Next, addition of a divalent copper salt to a basic aqueous solution of the ligand gave the copper complex (Figure 2.5). All ligands were characterised using NMR spectroscopy and electrospray ionisation (ESI) mass spectrometry. All copper complexes were characterised using ASAP mass spectrometry data and elemental analysis.

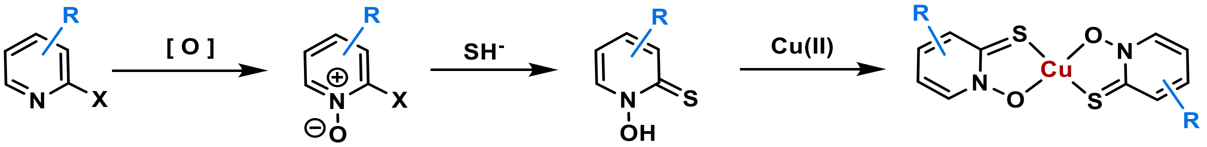

Figure 2.5: General synthetic route for formation of substituted copper pyrithione complexes (R = substituent)

Alkyl substituents

To introduce steric bulk and lipophilicity through small hydrocarbon groups, methyl, isopropyl and tertiary-butyl substitutions on various positions of pyrithione ring have been explored. Initially, the synthesis of 6-methyl substituted pyrithione (6-Me-PT) was attempted to determine the optimum reaction conditions.

Several reaction conditions were attempted for each step of the reaction pathway. In the first step, oxidation of 2-bromo-6-methylpyridine was attempted, using hydrogen peroxide as the oxidising agent in acetic acid solvent (Figure 2.6 pathway a). These conditions resulted in a very low yield of the *N*-oxide. As an alternative, excess *meta*-chloroperbenzoic acid (*m*CPBA) in dichloromethane solvent was used (Figure 2.6 pathway b), which gave formation of *N*-oxide compound in a satisfactory yield of 55%. The water-soluble *N*-oxide compound **2.1a** was purified through extraction and washing, without the need for chromatography.

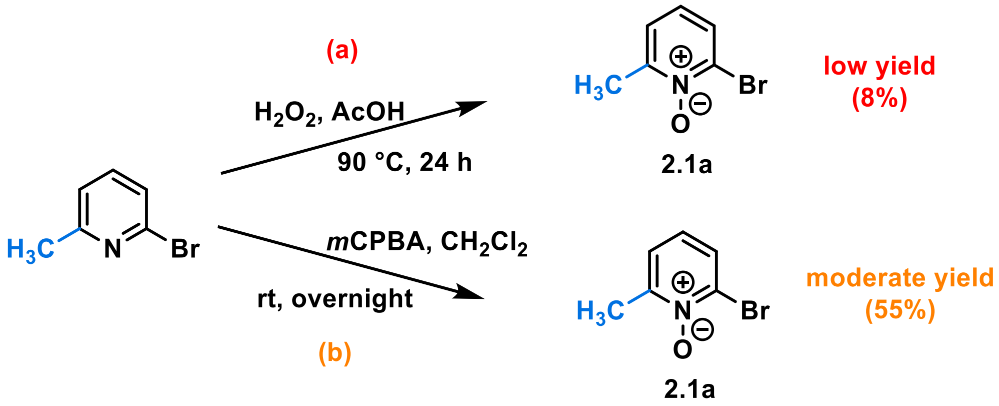

Figure 2.6: Formation of respective N-oxide from 2-bromo-6-methylpyridine

In the next step, nucleophilic aromatic substitution (S_NAr) of the aryl bromine was attempted by reaction with an aqueous solution of Na_2S (4-6 equiv.). This reaction predominantly formed a new product (*m/z* = 249), along with a very small amount of the desired ligand (m/z = 142) (Figure 2.7). The NMR spectrum suggested a species with three aromatic proton environments and six carbon environments, as expected for the desired product, however the identity remained inconclusive as the next step of copper complexation was unsuccessful. The side product of the oxidation step with *m/z* = 249 is potentially methyl substituted 2,2'-dipyridyldisulfide (**2.3**), a common by-product of pyrithione. To determine whether this proposal was correct, the newly observed product was reacted with DTT (dithiothreitol), which is known to disrupt disulfide bond formation however, no change was observed in the subsequent ^{1}H-NMR spectrum. An alternative proposed by-product, **2.4**, is shown in Figure 2.7, which also has *m/z* = 249, although the identity of this product remains unconfirmed. The use of Na_2S in the S_NAr step proved unsuccessful, which led to the strategy of using a saturated solution of $NaSH \cdot H_2O$ as the sulfhydryl source in reaction.[252] These new conditions gave the desired product 6-Me-PT (*m/z* = 142) upon quenching of the reaction mixture with aqueous HCl solution (4 M) (Figure 2.7).

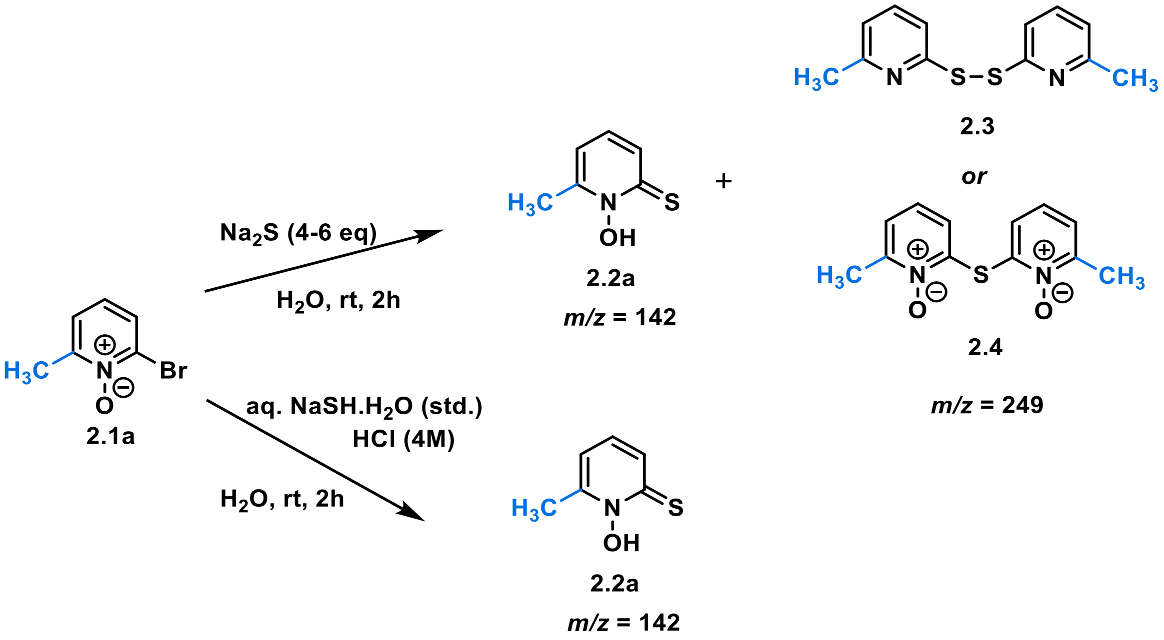

Figure 2.7: Nucleophilic aromatic substitution of bromine by sulfhydryl group

^{1}H NMR spectroscopy data suggests that 6-Me-PT gradually degrades in organic solvents, such as ethyl acetate or acetone, within a few hours and forms **2.3** or **2.4** (Figure 2.8). To avoid degradation of the ligand before Cu complexation, the following purification and stabilisation process was undertaken: (i) the desired compound (**2.2a**) was extracted in EtOAc from the acidic water layer of the reaction work up and the solvent was evaporated under reduced pressure, (ii) solid sulfur impurities were removed by precipitation from acetone solution, (iii) after removing the acetone solvent, the solid ligand residue was dissolved in basic aqueous solution. Under these basic conditions, the ligand remains stable. The purified ligand was characterised using NMR spectroscopy and mass spectrometry.

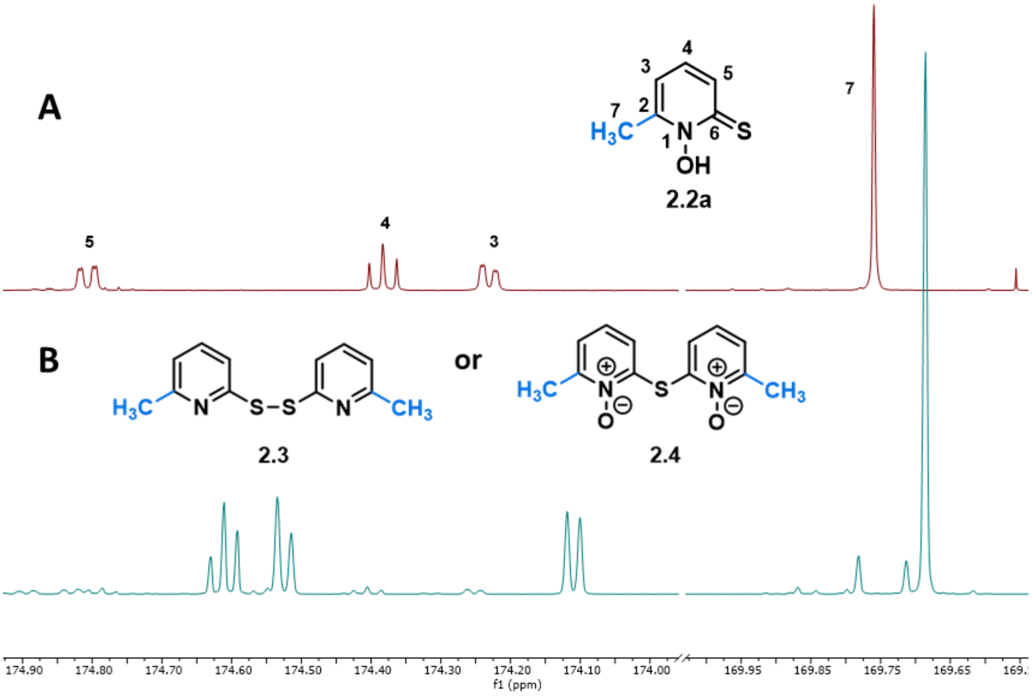

*Figure 2.8: (**A**) ^{1}H-NMR spectrum of desired compound 2.2a (400 MHz, Chloroform-d, 25 °C) and (**B**) the same sample after 6 hours in solution*

In the final synthetic step, an aqueous solution of $CuCl_2.2H_2O$ was added to 6-Me-PT, stabilised in aqueous basic medium. The desired product, [Cu(6-Me-PT)$_2$], precipitated from solution as a grey solid (Figure 2.9). This crude solid was found to be impure, due to presence of copper hydroxide and remaining elemental sulfur from the previous ligand formation step. Evidence of these impurities came from elemental analysis data and a crystal structure of hexagonal S_8, which formed during crystallisation trials. The copper hydroxide impurity might be generated due to the presence of excess sodium hydroxide, used to stabilise the ligand in aqueous system. Copper hydroxide is insoluble in CH_2Cl_2, therefore, purification was carried out via trituration in CH_2Cl_2 solvent. Next silica gel column chromatography using CH_2Cl_2 as the eluting solvent was performed for further purification, as sulfur and the desired complex have very different polarity and solubility in CH_2Cl_2. The outcome was pure desired copper complex [Cu(6-Me-PT)$_2$] as a brown solid. The purified complex was analysed and characterised using mass spectrometry and elemental analysis data. Similar to the non-substituted complex [Cu(PT)$_2$], mass spectrometry data for [Cu(6-Me-PT)$_2$] showed peaks for Cu_2L_3 (m/z = 545), along with desired complex peak $[CuL_2 + H]^+$ (m/z = 342).

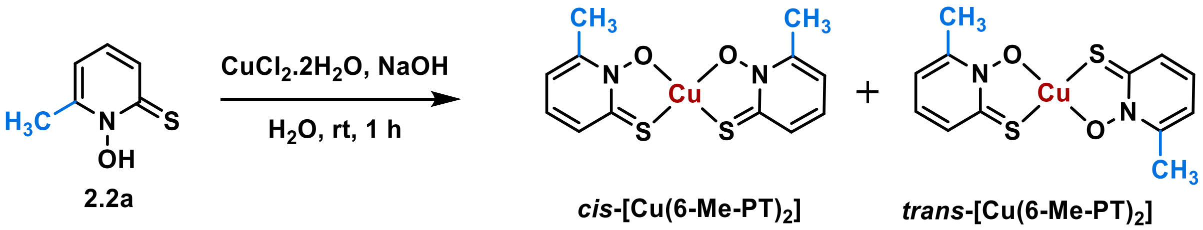

Figure 2.9: Synthesis of cis- and trans-[Cu(6-Me-PT)$_2$]

Crystallisation attempts were made for [Cu(6-Me-PT)$_2$], through various methods in different solvents. The main challenge here was the poor solubility of this complex in almost all the solvents used. However, after several attempts, crystals of this complex were grown from slow evaporation of CH_2Cl_2 and were analysed by X-ray diffraction. The crystallography data provided evidence for formation of both *cis*- and *trans*- isomers, as separate crystals (Figure 2.10 A and B). The *cis* isomer is previously published, but the *trans* isomer is unique.[253] The *cis* isomer appears as brown plate shaped crystals and make up the majority of crystals that form. Under the same crystallisation conditions, a second crystal structure forms, appearing as small iridescent plates, which are the *trans*-isomers as a minor species. The crystals of the *trans*-form were very poor in terms of crystal quality. From the evidence of the extended crystal structure packing data, it was proposed that the preference for the *cis* isomer could arise due to intermolecular steric hindrance. In the monoclinic *trans*-isomer crystals, the two methyl groups hinder space on either side of the complex, blocking the space for another molecule to interact. By contrast in the orthorhombic *cis* form, the two methyl groups are located on one side of the complex, leaving the other side free to accommodate another molecule. This intermolecular stabilisation in the *cis* form must compensate for the effect of additional intramolecular steric hindrance between the two methyl groups.

Both *cis* and *trans* isomers possess the same metal ligand bond lengths as that of [Cu(PT)$_2$], but the complexes differ in the geometry around copper. The *trans* isomer was observed to have a square planar geometry (bond angle = 180° from S–Cu–S), whereas the S-Cu-O angle in the *cis* isomer is distorted (bond angle = 170°). The distortion is probably due to steric bulk caused by having two larger sulfur atoms on the same side of the copper. In terms of the extended crystal structure, the crystal packing shows that the *cis* isomer is arranged in a herringbone pattern (Figure 2.10 C), whereas the *trans* isomer is stacked in parallel sheets (Figure 2.10 E). In the case of the *cis* isomer, formation of intermolecular hydrogen like bonding (CH……O, bond length = 2.7 Å) between two molecules in different planes can be observed, (Figure 2.10 D). The *trans* isomer shows π-π stacking interactions between molecules in two adjacent planes (Figure 2.10 F). From the crystallography data, it can be concluded that the packing behaviour of [Cu(PT)$_2$] changes significantly, due to 6-methyl substitution.

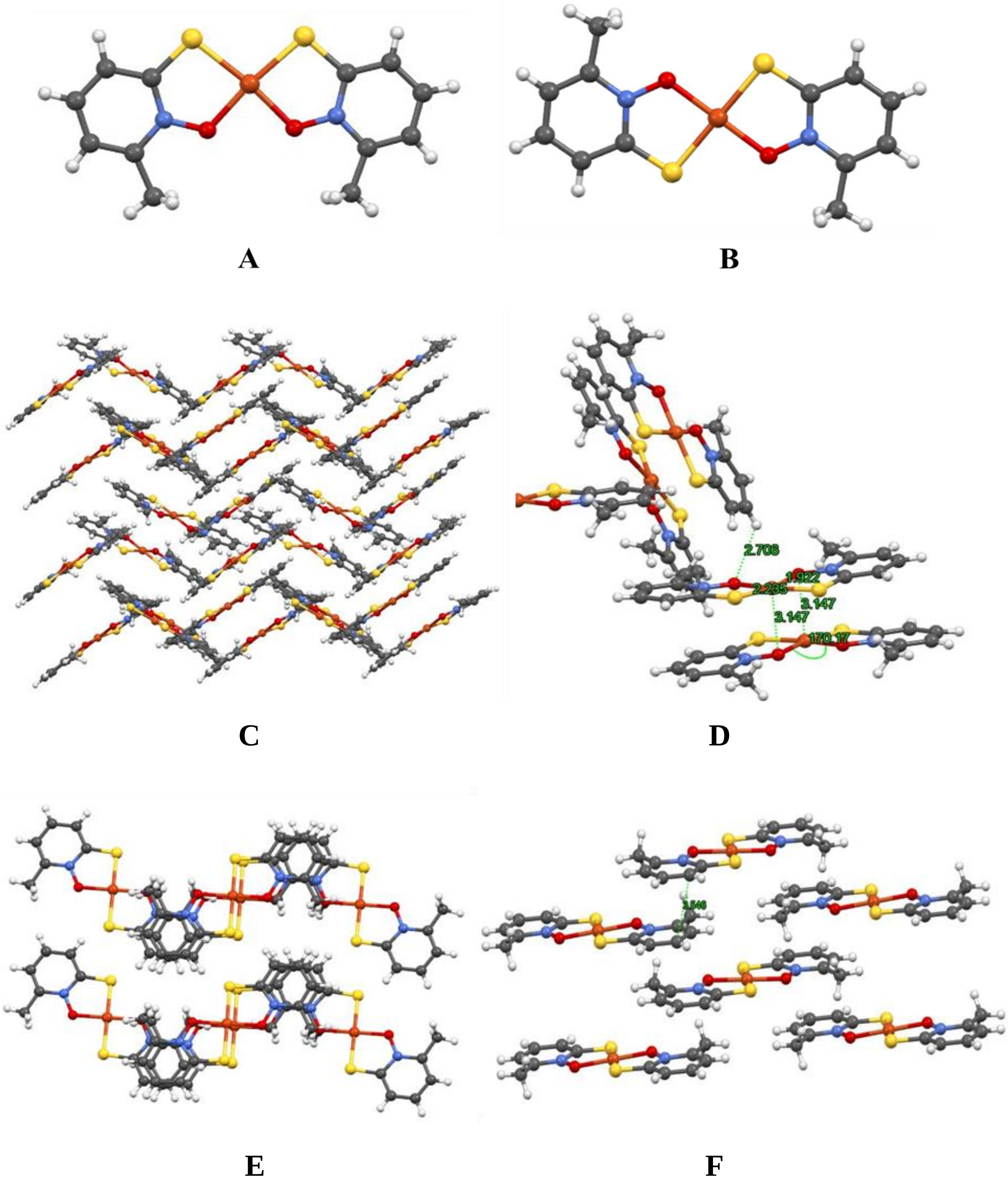

Figure 2.10: Crystal structures for ***(A)*** *cis- and* ***(B)*** *trans isomers of complex [Cu(6-Me-PT)$_2$], along with (**C**) and (**D**) extended crystal packing of cis isomer; (**E**) and (**F**)) extended crystal packing of trans isomer*

Next, the position of the methyl substituent on the pyrithione ring was varied. The full set of 3-, 4-, and 5-Me substituted PT (**2.2b**, **2.2c** and **2.2d** respectively) and their respective copper complexes were synthesised and characterised following the procedure described above (Figure 2.11). One exception in the case of the synthesis of the 4-Me substituent was that a 2-chloro precursor was used instead of the 2-bromo precursor, due to the cost-effective commercial availability. All complexes were synthesised successfully in good yields and high purity. Crystallography data were collected for [Cu(3-Me-PT)$_2$] and [Cu(4-Me-PT)$_2$] complexes. Both crystal structures suggest exclusive formation of the *trans* isomers. Furthermore, each extended crystal structure shows Cu-S interactions between two adjacent parallel molecules (distance = 3.5 Å) (Figure 2.12 A and C). The [Cu(4-Me-PT)$_2$] complex also shows the formation of intermolecular hydrogen bonds, similar to that for [Cu(PT)$_2$] (bond length = 2.6 Å) (Figure 2.12 B). Both crystal structures show the same metal-ligand bond lengths and geometries as that for [Cu(PT)$_2$].

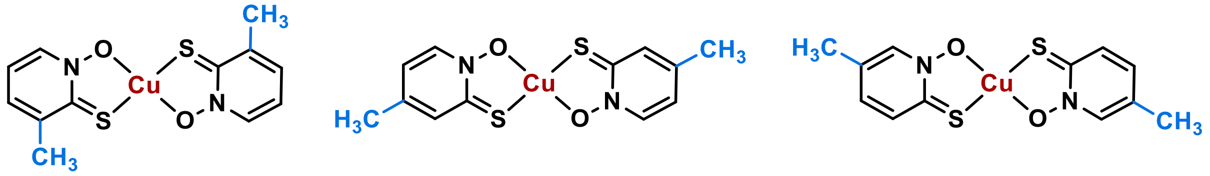

[Cu(3-Me-PT)$_2$] **[Cu(4-Me-PT)$_2$]** **[Cu(5-Me-PT)$_2$]**

Figure 2.11: Structures for methyl-substituted copper pyrithione in the various positions of the ring

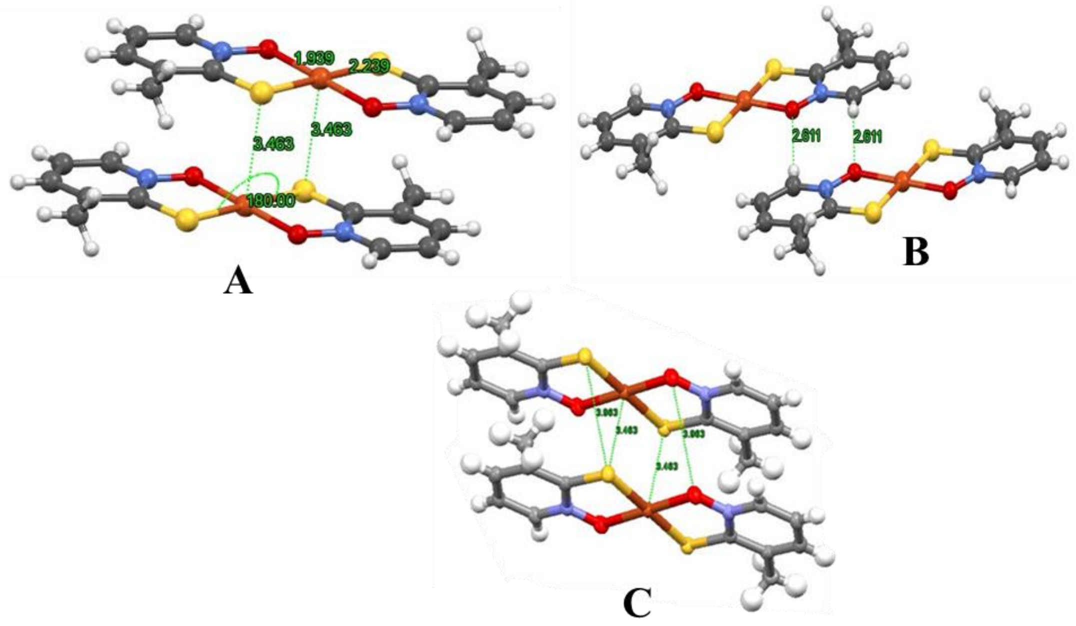

*Figure 2.12: **(A)** and (**B**) Crystal packing structure of [Cu(4-Me-PT)$_2$]; **(C)** crystal packing structure of [Cu(3-Me-PT)$_2$]*

Next, attempts were made to introduce further branching of the alkyl substituent in the pyrithione ligand. Synthetic trials for *i*-propyl and *t*-butyl substituents in the 6 position of pyrithione were partially successful.

Grignard reactions were employed to produce *i*-propyl and *t*-butyl substituted halopyridines as starting materials. Grignard reagent *i*-PrMgCl was obtained commercially, while *t*-BuMgCl was synthesised from *t*-BuCl and Mg turnings (Figure 2.13).

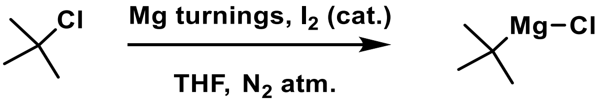

2.5

Figure 2.13: Preparation of Grignard reagent t-BuMgCl

Two potential routes to the *t*-butyl-*N*-oxide intermediate **2.8** were proposed, starting from 2,6-dibromopyridine (Figure 2.14). Pathway A involved an *N*-oxidation followed by Grignard reaction. This route was found to be inefficient, due to low yields in both steps. An alternative approach of a Grignard reaction followed by the *N*-oxidation step (Pathway **B**) was found to be a better strategy, giving compound **2.8** with moderate yield. Reaction conditions for the *N*-oxidation step used urea hydrogen peroxide (UHP) and trifluoroacetic anhydride (TFAA), which represent stronger oxidising conditions compared to the *m*CPBA oxidation of the methyl derivatives above.

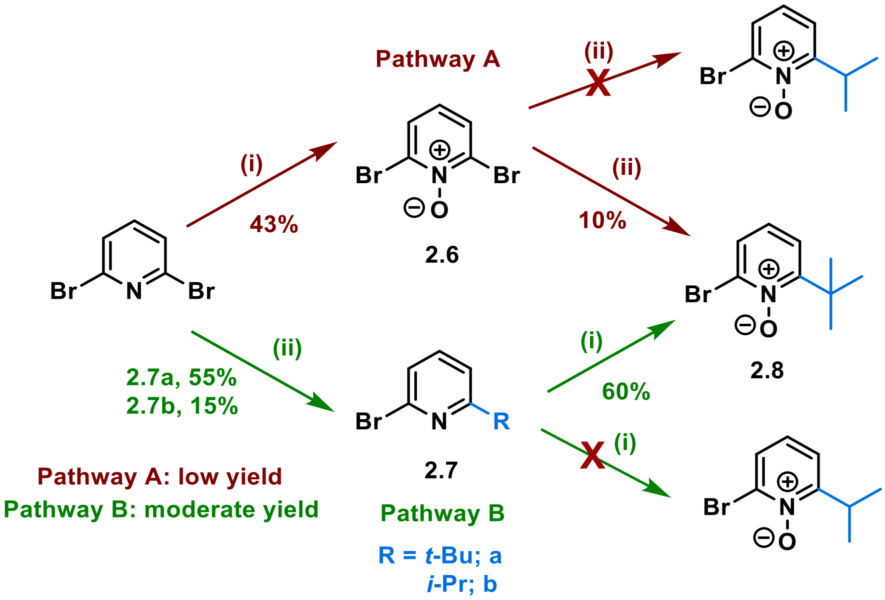

Figure 2.14: Competitive synthetic routes for formation of ligand precursor of alkyl substituted pyrithione[254]; (i) UHP, TFAA, CH_2Cl_2, 0 °C - rt, 20 h, (ii) RMgCl, CuI, THF, N_2 atm., 0 °C - rt, 3 h.

The subsequent S$_N$Ar reaction to introduce the sulfur substituent was challenging and the alkyl precursors needed harsh conditions to react. A high temperature of 80 °C along with >15 hours of vigorous stirring helped to achieve the crude pyrithione ligand with *t*-butyl substitution (**2.9**) (Figure 2.15). Formation of crude product was confirmed using NMR spectroscopy and mass spectrometry. Subsequent reaction-quenching and purification steps followed a similar pathway to that for 6-Me-PT. However, stabilised ligand in aqueous basic medium couldn't be obtained due to its poor solubility and very low stability. As a result, copper complex formation of the 6-*t*-Bu-PT ligand was not possible. The attempted synthesis of 6-*i*-Pr-PT followed the same reaction conditions but was only successful up to formation of 2-bromo-6-*i*-propylpyridine (**2.7b**) with very low yield following pathway B (Figure 2.14). It can be concluded that steric hindrance from bulkier alkyl chains is probably playing some negative role towards the sulfur substitution reaction. The additional inductive electron donating effect of the larger alkyl groups may also disfavour the nucleophilic addition of the sulfur nucleophile.

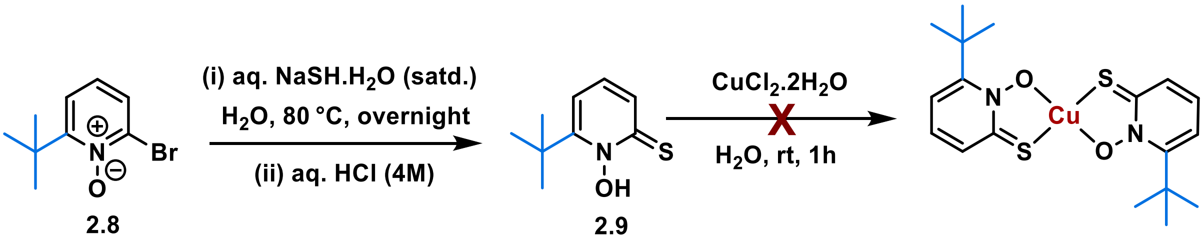

Figure 2.15: Ligand and copper complex formation trials for i-pr and t-butyl substitutions

Alkoxy substituents

After alkyl substituents, we shifted our focus towards alkoxy functional groups as these substituents are electron donating through resonance and electron withdrawing through induction. Hence, they are likely to affect the stability and properties of the copper pyrithione complexes. Herein, we attempted methoxy, ethoxy and *t*-butoxy groups as potential substituents at various positions around the pyrithione ring.

For methoxy (OMe) substitutions, commercially available methoxy-substituted 2-halopyridines were used as the starting materials. Generally, an oxidation of these starting materials using trifluoroacetic anhydride and UHP resulted in the corresponding *N*-oxides (**2.10**) in moderate yield. These *N*-oxides were reacted with $NaSH\cdot H_2O$ at 80 °C to achieve the desired methoxy-substituted pyrithione ligand (**2.11**) (Figure 2.16). NMR spectroscopy and ESI mass-spectrometric data (*m*/*z* $[M+H]^+ = 158$) of the crude reaction mixtures confirmed product formation.

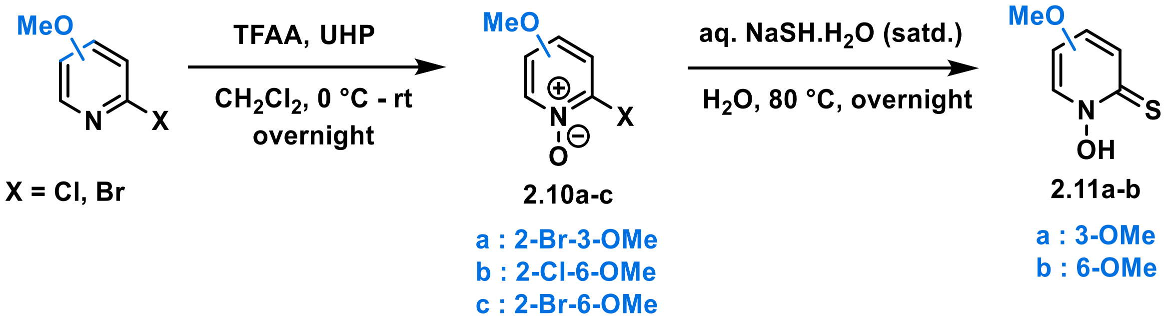

*Figure 2.16: Synthesis of methoxy-substituted pyrithione ligand (**2.11**)*

Following the described pathway, 3-methoxy (**2.11a**) and 6-methoxy (**2.11b**) substituted pyrithione ligands were synthesised starting from the 2-bromo and 2-chloro precursors respectively (Figure 2.16). Copper complex formation from 6-OMe-PT (**2.11b**) was not successful, as the ligand was not stable after quenching of the previous $\mathrm{S_NAr}$ reaction. Preparation of **2.11b** was further attempted using the bromo precursor but remained unsuccessful after the respective *N*-oxide (**2.10c**) formation step. The 3-methoxy compound led to a more stable pyrithione ligand (**2.11a**), which reacted with copper chloride to form the desired complex as a green solid (Figure 2.17). This complex was characterised using mass spectrometry (*m/z* $[M+H]^+$ = 375.962) after purification through trituration in dichloromethane and then through silica gel column chromatography using 5% methanol-dichloromethane as eluting solvent.

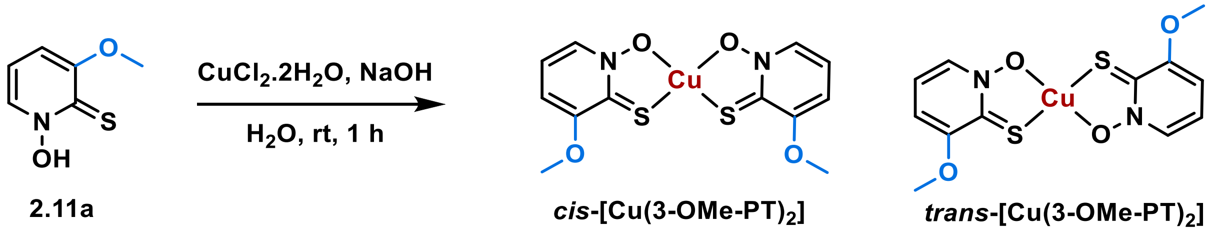

Figure 2.17: Synthesis of complex [Cu(3-OMe-PT)$_2$]

Single crystals of [Cu(3-OMe-PT)$_2$] were grown using slow evaporation of a methanol-dichloromethane solvent system. Two types of single crystalline solids were obtained by this method, brown plate shaped solids and needle-shaped structures. Characterisation using X-ray crystallography suggested the brown plates to be an unusual formation of both *cis* and *trans* isomers as a co-crystal, while the needle shaped crystals contained only the *cis* isomer (Figure 2.18). The crystal data for the *cis* isomer shows a parallel sheet type packing structure with non-parallel π-π interactions between two planes (Figure 2.18 A and B). The crystal data of the co-crystal structure depicted arrangement of *cis* and *trans* isomers as alternatives, where one *trans*-complex is sitting in the centre of symmetry between two *cis* isomers. The overall packing gives rise to herringbone like structure where intermolecular Cu-O and Cu-S interactions (distances = 3.3 Å) can be observed between one *cis* and one *trans* isomer, parallel to each other (Figure 2.18 C and D). In the same way as the *cis* isomer of the 6-Me substituted complex, the *cis* isomer shows a distorted square planar structure with bond angle (O–Cu–S) of 166°.

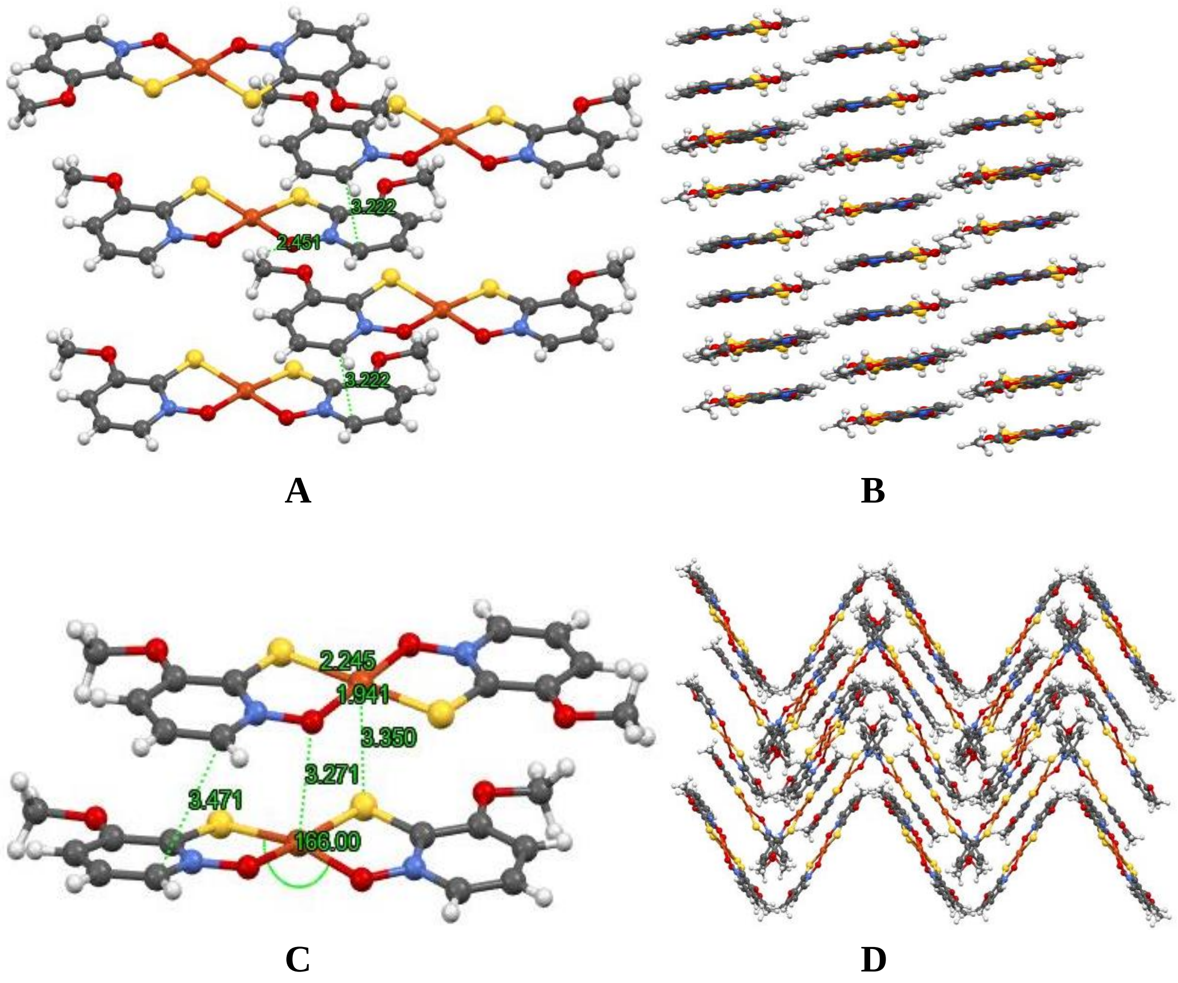

*Figure 2.18: (**A**) and (**B**) Crystal structure of cis [Cu(3-OMe-PT)$_2$], (**C**) and (**D**) co-crystal of trans and cis isomers of [Cu(3-OMe-PT)$_2$]*

Introduction of an ethoxy group (OEt) at the 3-position was carried out *via* an etherification reaction of commercially available 2-bromo-3-hydroxypyridine using ethyl iodide and potassium carbonate (Figure 2.19).[255] Next, similar conditions to the previous syntheses were used for *N*-oxidation and sulfur substitution (Figure 2.19). Formation of each product was confirmed using NMR spectroscopy and mass spectrometry. Copper complex formation with

3-OEt-PT also followed the same pathway as that for previous examples to achieve a brown solid as the final product [Cu(3-OEt-PT)$_2$].

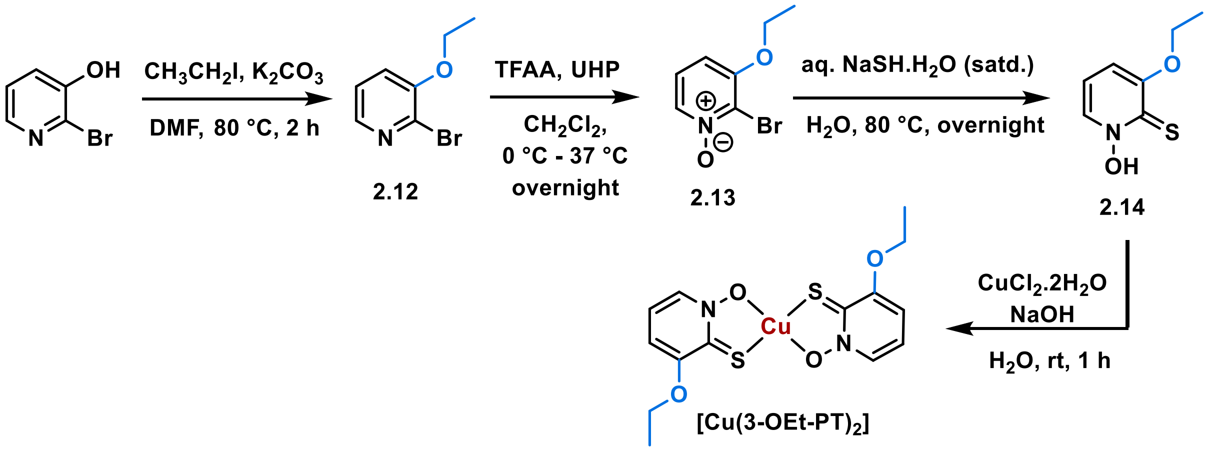

Figure 2.19: Synthetic pathway for formation of [Cu(3-OEt-PT)$_2$]

Hydroxyl substituent

Addition of a hydroxyl group (OH) to the pyrithione core has the potential to influence the electronics of the ring, affecting the stability of the resultant copper complexes. Hydroxy groups are also potential hydrogen bond donors, which could modulate both lipophilicity and aqueous solubility of complexes in the cytosol.

Oxidation of commercially available 2-bromo-3-hydroxypyridine resulted in the respective *N*-oxide product (**2.15,** Figure 2.20). Instead of using UHP at room temperature, aqueous hydrogen peroxide solution and trifluoroacetic anhydride as the oxidising agents in trifluoroacetic acid solvent at 80 °C were used. The crude product was purified though trituration in dichloromethane and methanol to obtain the pure *N*-oxide. Next, aromatic sulfur substitution and copper complex formation followed the same pathway as that of the alkoxy substituents (Figure 2.20). The ligand was characterised using multinuclear NMR spectroscopy and the final complex [Cu(3-OH-PT)$_2$] was characterised using ESI-HRMS data.

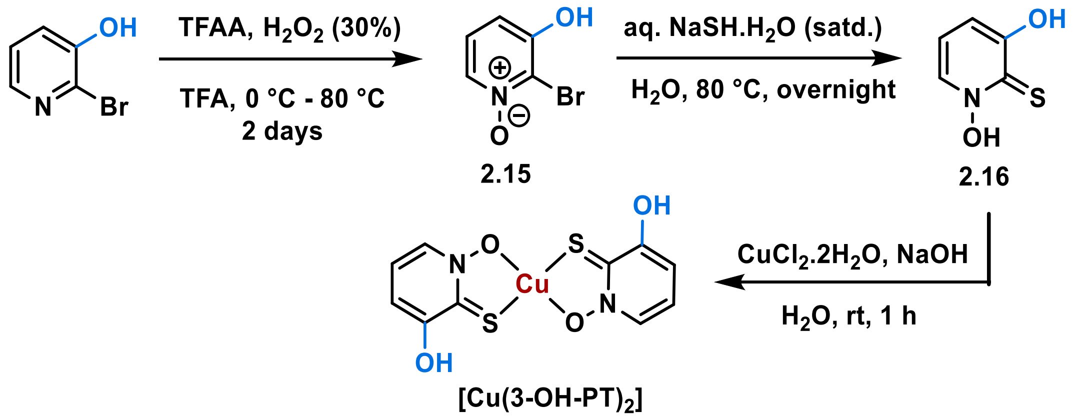

Figure 2.20: Synthetic pathway for [Cu(3-OH-PT)$_2$] formation

Trifluoromethyl substituent

The trifluoromethyl (CF_3) group is an electron withdrawing substituent due to the high electronegativity of the fluorine atoms. Incorporation of a CF_3 substitution on 4- and 6- position of the pyrithione ligand (Figure 2.21) was carried out *via* similar pathways to those described above for the hydroxyl substitution. First, *N*-oxidation of commercially available CF_3-substituted 2-chloropyridines was performed using strong oxidising agents, trifluoroacetic anhydride (TFAA) and hydrogen peroxide (H_2O_2). Attempts to carry out this oxidation with *m*CPBA were unsuccessful, likely due to the electron-withdrawing nature of CF_3 group decreasing the availability of the pyridyl nitrogen lone pair. Second, S_NAr reactions to introduce sulfur were carried out in the same manner as in the previous synthesis of OMe-PT. Newly formed ligands, 4-CF_3-PT (**2.18a**) and 6-CF_3-PT (**2.18b**) were reacted with copper chloride, resulting in precipitation of green compounds as the respective copper complexes, which were further purified *via* similar procedures described for the previous complexes.

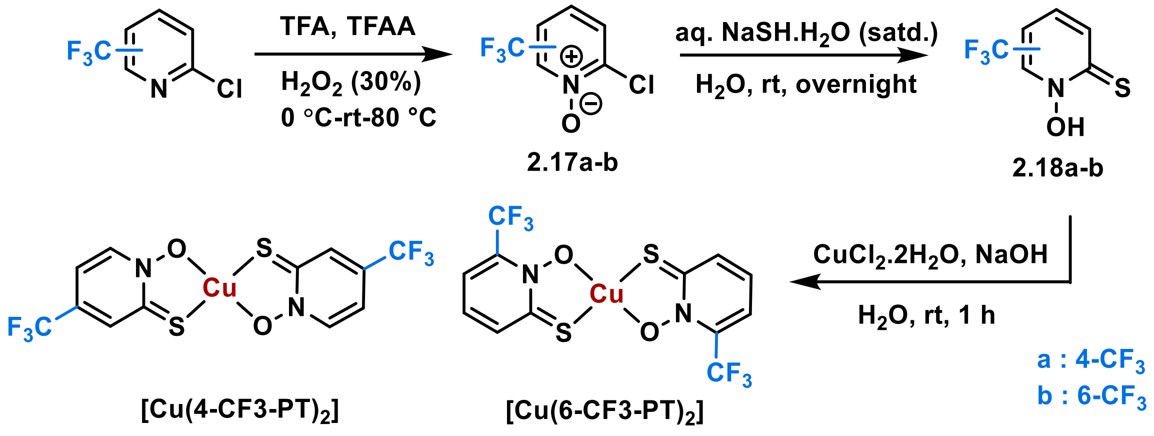

Figure 2.21: Synthesis of [Cu(4-CF_3-PT)$_2$] and [Cu(6-CF_3-PT)$_2$] complexes

Single crystals of both the 6-CF_3 pyrithione ligand and its copper complex were grown. The crystals of the ligand formed in the round bottomed flask in which the pure ligand was being stored after solvent evaporation. The crystals for the copper complex were grown from vapour diffusion of hexane in dichloromethane. The crystal structure of the ligand suggests the ligand to be in the thione form instead of the thiol form, evidenced by a hydrogen bond (bond length = 2.2 Å) between the sulfur and hydroxyl group (Figure 2.22 A). The overall packing reveals a herringbone type structure (Figure 2.22 B). In the case of the copper complex, the crystal data again shows a herringbone structure, where the observed *trans* isomers of the complex shows Cu-S interactions between two adjacent parallel molecules with a Cu-S distance of 3.7Å (Figure 2.22 C and E). Furthermore, intermolecular hydrogen-like bonds can be observed between two non-parallelly arranged molecules of the copper complex, where fluorine operates as the H-bond acceptor atom to the aromatic hydrogen (Figure 2.22 D).

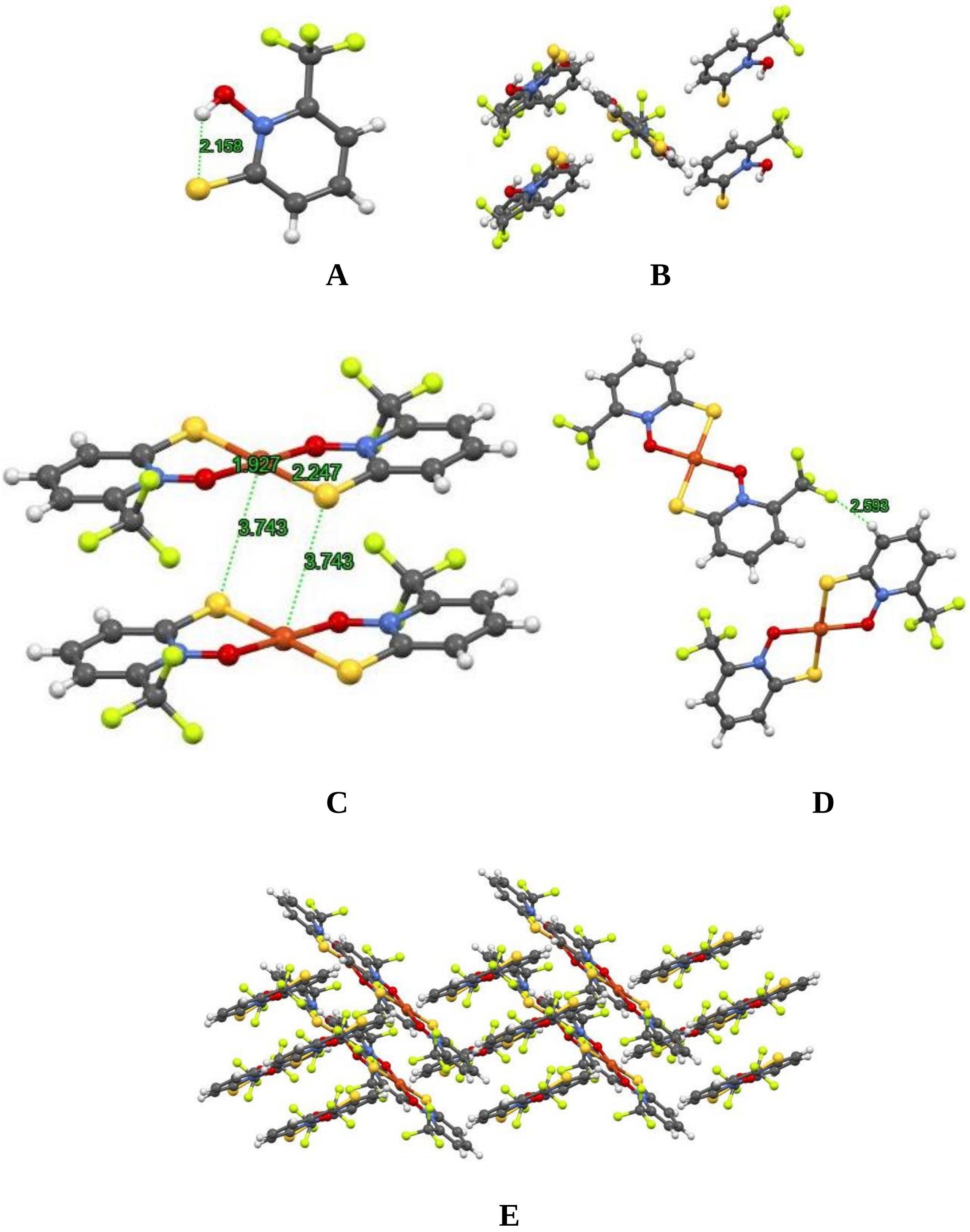

*Figure 2.22: Crystal packing structures of (**A**)and (**B**) 6-CF_3-PT (**2.18 b**) and (**C**) and (**D**) [Cu(6-CF_3-PT)$_2$]*

Phenyl substituent

Incorporation of phenyl groups generally helps to improve lipophilicity and may allow π-stacking with a biological target moiety (e.g., enzyme or DNA). A phenyl group was introduced to the 5-position of the pyrithione ligand via the same pathways of oxidation and sulfur substitution, followed by copper complexation as described for hydroxyl substituent (Figure 2.23). The oxidation product (**2.19**) formed in 92% conversion in 16 hours and purification was achieved by a trituration with chloroform. The final copper complex was characterised using high resolution ASAP mass spectrometry and elemental analysis data.

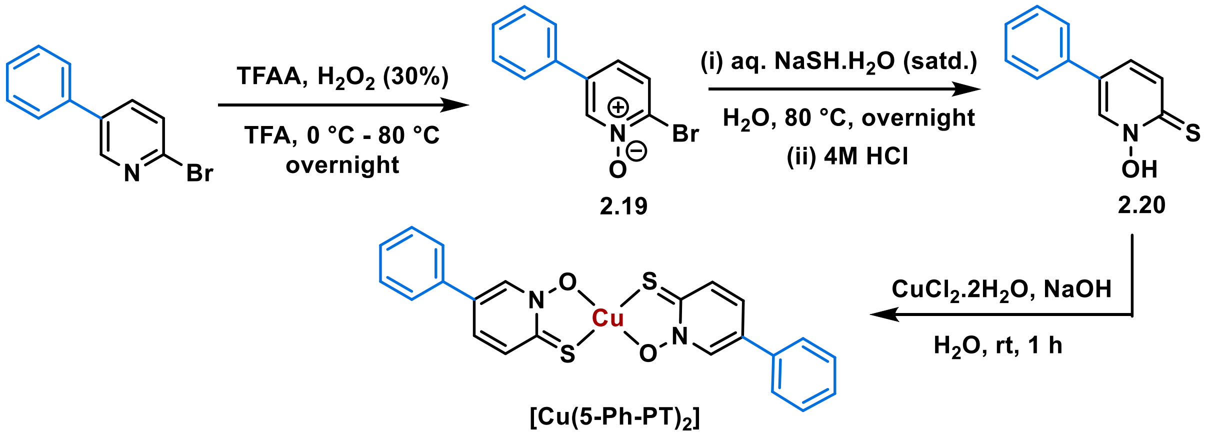

Figure 2.23: Synthesis of complex [Cu(5-Ph-PT)$_2$]

Benzene ring extension

Extending the ring structure of the pyrithione ligand was attempted with a view to increasing the aromaticity and lipophilicity of the subsequent complex. Synthesis of a thiol substituted quinoline-*N*-oxide ligand was carried out via a two steps procedure (Figure 2.24). First, oxidation of commercially available 2-chloroquinoline was conducted using a combination of TFAA and UHP as the oxidising agents. This was followed by a sulfur substitution step utilising the same conditions as that for the phenyl substitution above, giving the desired quinoline-derived PT ligand (Q-PT) (**2.22**). Characterisation through NMR spectroscopy and ESI mass spectrometry data confirmed ligand formation. Next, addition of NaOH and copper chloride in an aqueous solution of the ligand rendered the expected copper complex [Cu(Q-PT)$_2$], which was characterised using mass spectrometry and elemental analysis data.

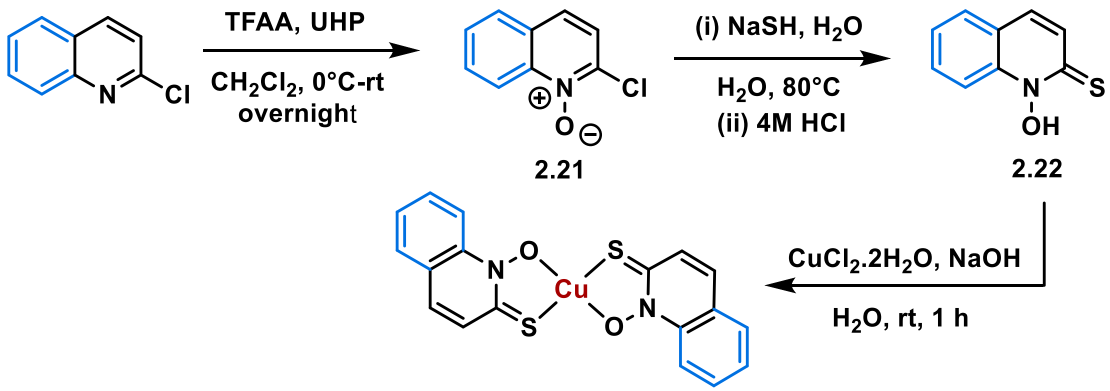

[Cu(Q-PT)$_2$]

Figure 2.24: Synthetic pathway for copper complex of [Cu(Q-PT)$_2$]

Further attempts to introduce other electron withdrawing groups, such as carboxylic acid and esters at the 4-position of PT, were unsuccessful.

Other than the above library of copper complexes, Alexander Lee, a MChem student in James W. Walton research group has synthesised 5-methoxy ([Cu(5-OMe-PT)$_2$]) and 3-fluoro ([Cu(3-F-PT)$_2$]) substituted copper pyrithione complexes. These complexes have also been included in some biological screening that follows. In Figure 2.25 all newly synthesised copper pyrithione complexes are shown.

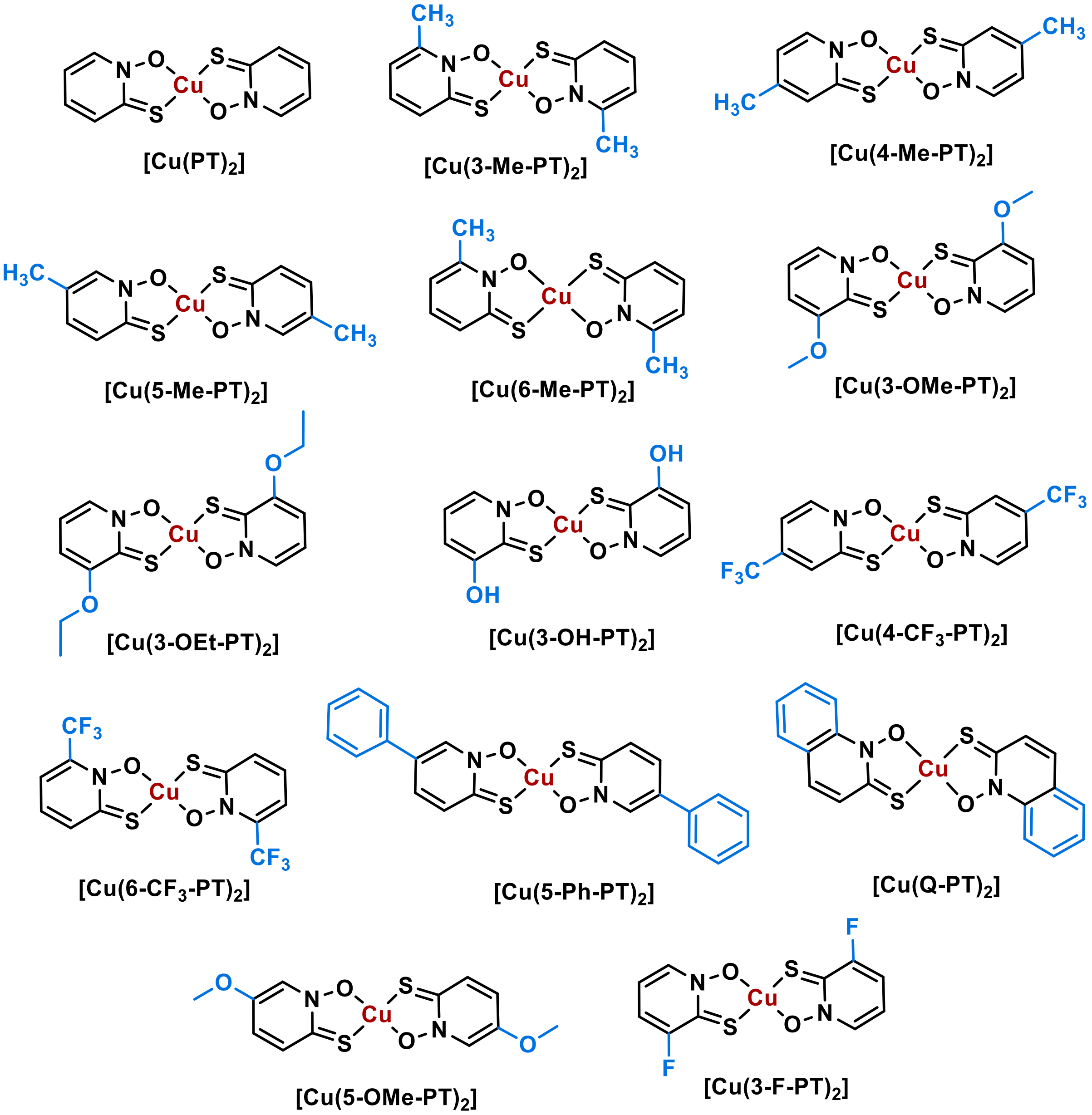

$[Cu(PT)_2]$ $[Cu(3\text{-}Me\text{-}PT)_2]$ $[Cu(4\text{-}Me\text{-}PT)_2]$

$[Cu(5\text{-}Me\text{-}PT)_2]$ $[Cu(6\text{-}Me\text{-}PT)_2]$ $[Cu(3\text{-}OMe\text{-}PT)_2]$

$[Cu(3\text{-}OEt\text{-}PT)_2]$ $[Cu(3\text{-}OH\text{-}PT)_2]$ $[Cu(4\text{-}CF_3\text{-}PT)_2]$

$[Cu(6\text{-}CF_3\text{-}PT)_2]$ $[Cu(5\text{-}Ph\text{-}PT)_2]$ $[Cu(Q\text{-}PT)_2]$

$[Cu(5\text{-}OMe\text{-}PT)_2]$ $[Cu(3\text{-}F\text{-}PT)_2]$

Figure 2.25: The full library of non-substituted and substituted copper pyrithione complexes

2.2.2 Chemical Property Analysis

All complexes were analysed further to determine their various physiochemical properties and understand any trends that emerge from the substitution patterns. These studies include measuring lipophilicity and binding constants of these complexes.

2.2.2.1 Lipophilicity studies

Lipophilicity, which can affect the permeability of compounds through lipid membranes, is usually described as a compound's affinity towards water-immiscible organic solvent over water. This term is generally represented as a partition coefficient *P*, where *P* describes the equilibrium concentrations of the compound dissolved in a two-phase system of *n*-octanol and water (Equation 1).

$$\log P = \log\left(\frac{[Cu(octanol)]}{[Cu(water)]}\right) \qquad (1)$$

Conventionally, lipophilicity is measured using a shake-flask method, where UV/Vis spectroscopy is used to quantify the amount of a compound in the organic and aqueous layers. To quantify the amount of compound in each layer, extinction coefficients are measured first. In our investigations, we tried using this method to measure a log *P* value for the unsubstituted copper pyrithione complex. However, due to the low solubility of this complex in water, we were unable to measure the extinction coefficient (ε) in water. To aid solubility, we next attempted 1-2% DMSO in water as the aqueous solvent. However, the poor solubility issue remained. Instead, we resorted to inductively coupled plasma optical emission spectroscopy (ICP-OES) as a technique to quantify the Cu levels present in both the octanol and aqueous layers. A similar procedure to the shake-flask method was used, before quantification of complex in each layer was carried out using ICP-OES. The complex was first dissolved in DMSO and then the stock solution was added to the separating flask containing water and octanol layers pre-saturated with the other solvent. The amount of DMSO was kept constant in both solvent layers to be 1%. Next, the water layer was diluted 10 fold using 5% HNO_3/H_2O in order to digest the copper complex in solution. From the octanol layer, the solvent was evaporated and 100 fold 5% HNO_3/H_2O solution was added. Finally, Cu levels were measured in ppm using ICP-OES. Similar samples for both layers without copper complexes were prepared as references and analysed using ICP-OES to calibrate the measurement. Finally, log *P* values were calculated after conversion of ppm values to concentrations in the two solvent layers.

The ICP-OES method was conducted to measure log *P* on a selection of complexes to determine any trends in the series. Along with non-substituted $[Cu(PT)_2]$, log *P* values were determined for 3-Me, 6-Me, 6-CF_3, 3-OMe and 5-Ph substituted copper pyrithione complexes (Figure 2.26). The log *P* values showed a decrease in lipophilicity upon introduction of substituents, with the unsubstituted complex giving the highest value of 2.33. Both methyl and methoxy groups in the 3-position of PT led to similar values of log *P*, 1.73 and 1.75, respectively. However, changing the position of the methyl group to the 6- position led to a higher log *P* value of 2.11. Introduction of the electron withdrawing CF_3 group resulted in the lowest measured log P of 1.45 for the 6-CF_3 complex. Moreover, the phenyl substitution shows a similar log *P* value (log *P* = 1.50) to that of the CF_3 substitution.

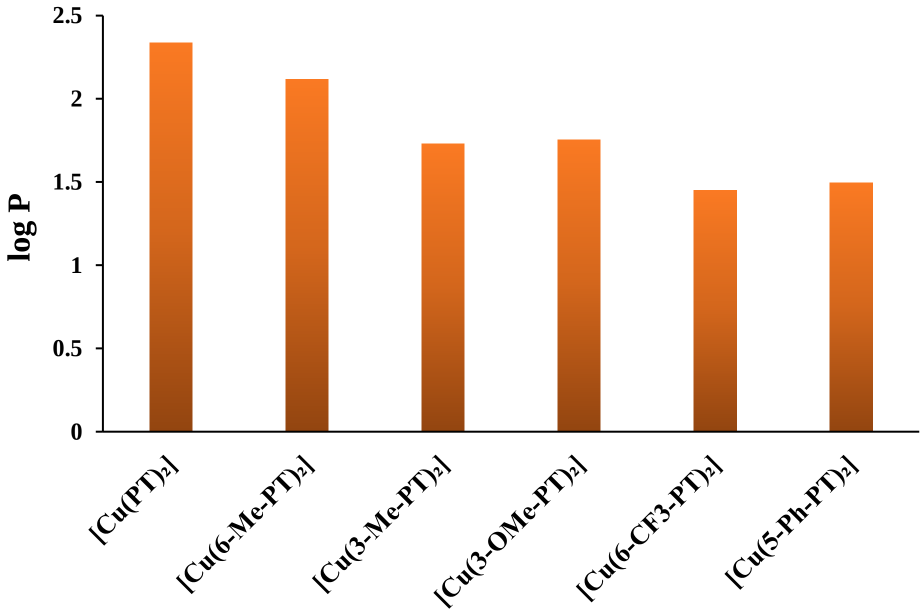

Figure 2.26: Log P values for substituted copper pyrithione complexes

2.2.2.2 Binding constant study

The binding constant, also known as the stability constant or the formation constant, is the equilibrium constant for a ligand-metal complexation reaction in solution. This concept is important for understanding the thermodynamic stability and binding strength of a metal-ligand bond and therefore their tendency to stay in the complexed form or dissociate in a particular solution.

Here, binding constant studies were conducted following the Benessi-Hildebrand Method.[256] Following this method, an equation for the binding constant, *K*, was derived from the following equilibrium:

$$\mathrm{M} + 2\mathrm{L} \rightleftharpoons \mathrm{ML_2}$$

With a binding constant for the above equilibrium:

$$K = \frac{[\mathrm{ML_2}]}{([\mathrm{M}]_0 - [\mathrm{ML}] - [\mathrm{ML_2}])[\mathrm{L}]^2} \qquad (2)$$

Where [ML] is molar concentration of the mono-ligated complex, $[M]_0$ is initial molar concentration of the free metal ion, $[ML_2]$ is the concentration of the bis-ligated metal-ligand complex and [L] is molar concentration of the ligand. The concentration of free metal ions changes with complex formation, as the metal is consumed by the complex. However, formation of ML_2 is much faster than that of ML and hence [ML] is considered as negligible. Therefore, $[M]_0 – [ML_2]$ is utilised as the working concentration of free metal at any point of the experiment.

Metal complexation reactions are assumed to be very fast. UV/Vis spectroscopy was used to quantify the species in solution. Copper ions do not contribute towards any UV absorption in 250-360 wavelength region, therefore, the spectra produced can solely be attributed to the metal-ligand complex.

According to the Beer-Lambert law, the molar extinction coefficient, ε, of the complex at the wavelength of maximum absorption is given by the following equation.

$$\varepsilon = \frac{A}{cl} = \frac{A}{[ML_2]b}$$

$$\therefore\ [ML_2] = \frac{A}{\varepsilon b} \qquad (3)$$

Where c is concentration of the solution, b is pathlength of light and A is absorbance.

Equations (2) and (3) can be combined to give:

$$K = \frac{A/\varepsilon b}{([M]_0 - A/\varepsilon b)([L])^2}$$

$$K = \frac{A}{\varepsilon b[M]_0[L]^2 - A[L]^2}$$

$$A = K\varepsilon b[M]_0[L]^2 - KA[L]^2$$

$$K\varepsilon b[M]_0[L]^2 = A + KA[L]^2$$

$$K\varepsilon b[M]_0[L]^2 = A\ (1+ K[L]^2)$$

$$\frac{[M]_0 b}{A} = \frac{1}{K\varepsilon[L]^2} + \frac{1}{\varepsilon} \qquad (4)$$

Equation 4 is the ‘Benessi-Hildebrand equation’ in y = mx + c form, which can be used to calculate the binding constant (K) of copper pyrithione complexes by measuring A as a function of [L].[257]

To carry out the experiment, an initial solution (0.1 mM) of copper chloride was added to a cuvette and the ligand was gradually added in aliquots up to an excess (more than 2 equivalence of copper concentration). All ligands were used as their sodium salts and both ligand and copper chloride salt solutions were prepared in a 1:1 solvent system of acetonitrile:water. With each addition of ligand solution, UV/Vis absorbance of the solution was recorded, and gradual formation of copper complex was observed by stepwise increase of absorbance at around 320 nm wavelength (Figure 2.27). The relationship of $[M]_0/A$ versus $1/[L]^2$ was plotted, and the intercept and slope of the graph were utilised to calculate the binding constant (K) value for respective copper complex formation. Absorbance 'A' has been considered after subtracting the maximum absorbance value of free copper (A_0) from the absorbance maxima after addition of ligands (A_{max}) at the same wavelength. Absorbance spectra titration for $[Cu(PT)_2]$ (Figure 2.27) and the respective Benessi-Hildebrand plot (Figure 2.28 A) are presented here. Later data points (lower $1/[L]^2$ values) are used to calculate K, as the data deviates from linearity at lower ligand concentration. This deviation can probably be explained by the fact that at lower concentration of ligands, formation rate of ML_2 is not much higher than that of ML and hence neglecting ML in the calculation develops errors. In this plot, data points related to ligand concentrations from 1 equivalent to 2 equivalent with respect to copper concentration have been considered for the graph (Figure 2.28 B).

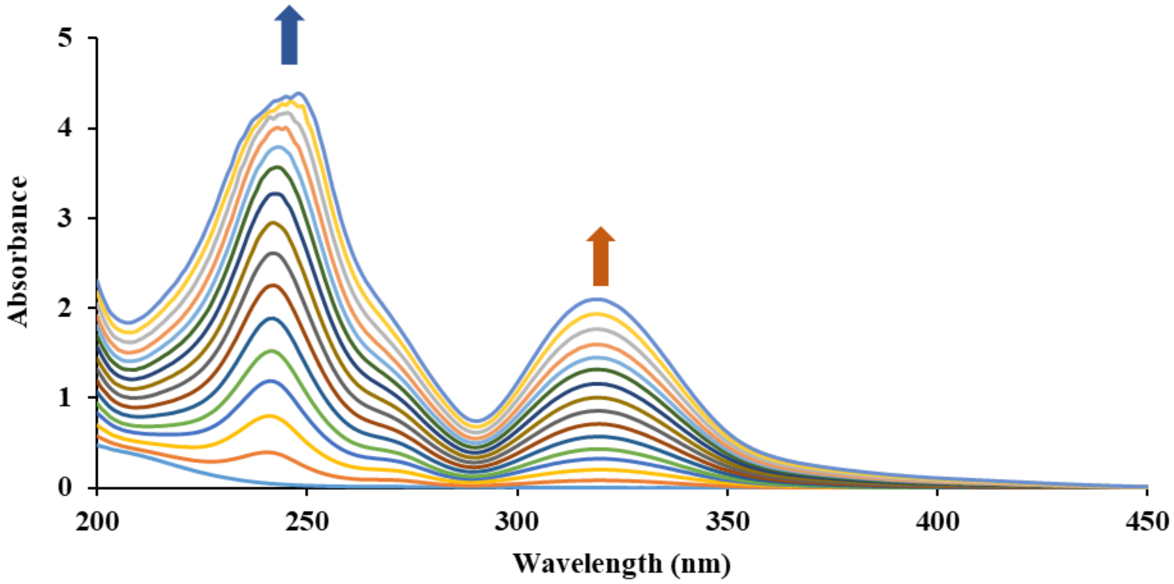

Figure 2.27: Absorbance spectra for binding constant study of $[Cu(PT)_2]$

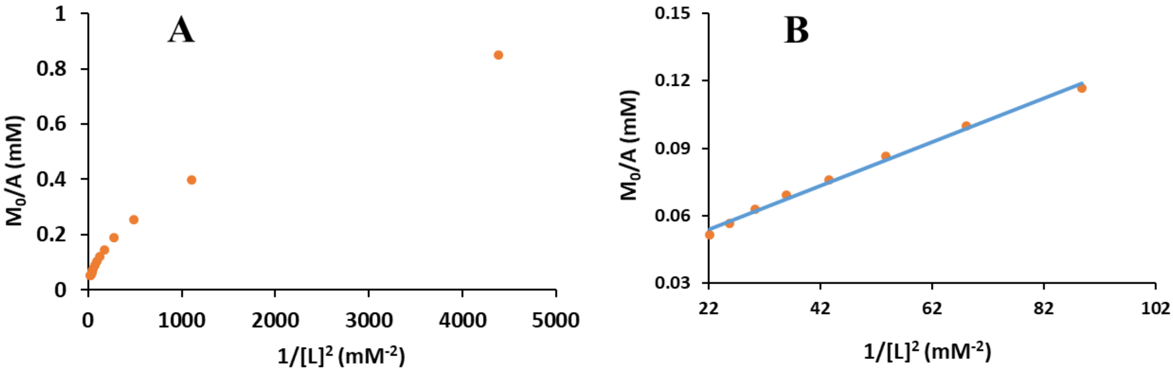

*Figure 2.28: Benessi-Hildebrand plot (absorbance maxima at 320 nm wavelength) for binding constant study of [Cu(PT)$_2$]; (**A**) the whole plot and (**B**) the data points considered for log K calculation between 1-2 equivalents of L*

The UV/Vis spectrum of the free ligand PT and the spectrum of [Cu(PT)$_2$] are shown in Figure 2.29. This data confirms that the gradual increase of absorbance in Figure 2.27 was not simply due to increasing ligand concentration but due to the formation of the metal complex. The free ligand possessed three absorption maxima whilst [Cu(PT)$_2$] has only two, with a unique absorption at 320 nm. The ligand absorption maxima around 290 nm and 340 nm, respectively, correspond to the n-π* and π-π* transitions related to the N→O bond.[258]

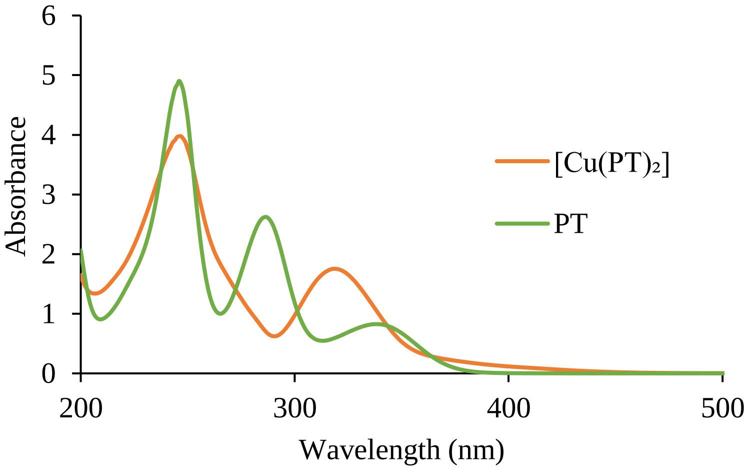

Figure 2.29: Absorption spectra for non-substituted pyrithione ligand and respective copper complex

The same method was used to calculate binding constants for other complexes, including the 6-Me, 6-CF$_3$ and 3-OMe substituted copper pyrithione complexes. The log *K* values for these substituted copper pyrithione complexes fall in the range 7.498-7.619, as does the value for the unsubstituted [Cu(PT)$_2$] (Table 2.1). Therefore, it can be concluded that the introduction of small electron donating (Me, OMe) or electron withdrawing (CF$_3$) functional groups does not greatly affect the binding ability or thermodynamic stability of pyrithione ligand to copper. Absorption spectra and Benessi-Hildebrand plots for all other complexes are included in the experimental section. One limitation of using the Benessi-Hildebrand method for 2:1 ligand-metal systems is that it is not well-studied and validated for many other systems, with the majority of examples using 1:1 complexes.[259] The assumptions, such as formation of no [ML] species and the fast reaction rate of ML_2 complexation, could lead to some inaccuracy in the data.

Table 2.1: Binding constant (Log K) values of copper pyrithione complexes

Complex	**Log *K* (± SD)**
$[Cu(PT)_2]$	7.528 ± 0.004
$[Cu(6\text{-}Me\text{-}PT)_2]$	7.498 ± 0.005
$[Cu(6\text{-}CF_3\text{-}PT)_2]$	7.619 ± 0.008
$[Cu(3\text{-}OMe\text{-}PT)_2]$	7.560 ± 0.002

To investigate whether the binding constants would change under conditions that more closely matching the biological cytosol, similar studies were carried out in HEPES buffer (pH: 7.3) solution as the solvent system, instead of acetonitrile:H_2O. Although both ligand and copper salt individually dissolved very well in HEPES buffer solution, after formation of the copper complex, the solution became turbid, due to precipitation of the copper complex. This led to saturation of the absorption spectra and therefore data couldn’t be evaluated. Addition of 1% DMSO to the solvent system was hoped to increase solubility and the concentrations of both metal and ligand solution was reduced 10-20 fold from that for the acetonitrile:H_2O system, however, the issue of low complex solubility remained and the data generated did not provide conclusive binding constant values.

2.2.3 Bioactivity of Substituted Copper pyrithione Complexes

To establish potential structure-activity relationship, all copper complexes with substituted and non-substituted pyrithione ligands were subjected to various tests for their anticancer and antibacterial properties, with most complexes from the library observed to possess significant bioactivity.

2.2.3.1 Antibacterial Activity

To find out the potential of substituted copper pyrithione complexes to act against bacteria, first they were tested against a range of Gram-positive and Gram-negative bacterial species.

Furthermore, these complexes were subjected to antibiotic synergy testing against β-lactam-resistant *E. coli*.

In vitro activity against ESKAPE panel organism and cytotoxicity data

The following study was conducted by our collaborator Dr. Sidharth Chopra, principal scientist, Central Drug Research Institute, Lucknow, India.

The 'ESKAPE' panel of pathogens, which consists of *E. coli, S. aureus, K. pneumoniae, A. baumanii, P. aeruginosa*. and *Enterobacter* species, is one of the leading causes for hospital acquired multidrug-resistant infections. Multidrug resistance is considered to be one of the three top threats to global human health. According to a survey in 2011 in United States, 75000 deaths have been reported to be associated with nosocomial infections caused by ESKAPE pathogens.[260] The library of copper pyrithione complexes, along with reference compounds $CuCl_2$ and levofloxacin, were screened against the ESKAPE panel of pathogens. Screening was conducted to determine the minimum inhibitory concentration (MIC) values against wild type strains of these bacterial species (Table 2.2). The reference compound, levofloxacin is a broad-spectrum antibiotic of fluoroquinolone class of drugs which is known for its rapid bactericidal activity against both Gram-positive and Gram-negative bacteria.

Table 2.2:MIC value data for substituted copper pyrithione complexes against ESKAPE panel pathogen

		MIC (µM)				
S. No	**Complex**	***E.coli* ATCC 25922**	***S.aureus* ATCC 29213**	***K.pneumoniae* BAA 1705**	***A.baumannii* BAA 1605**	***P.aerugi nosa* ATCC 27853**
1	**[Cu(PT)$_2$]**	6.3	1.6	12.7	25.3	>100
2	**[Cu(3-Me-PT)$_2$]**	>100	1.5	>100	>100	>100
3	**[Cu(4-Me-PT)$_2$]**	11.6	1.5	>100	>100	>100
4	**[Cu(5-Me-PT)$_2$]**	5.8	1.5	>100	>100	>100
5	**[Cu(6-Me-PT)$_2$]**	11.6	2.9	>100	>100	>100
6	**[Cu(4-CF3-PT)$_2$]**	>100	4.4	>100	>100	>100
7	**[Cu(6-CF3-PT)$_2$]**	17.7	4.4	>100	>100	>100
8	**[Cu(3-OMe-PT)$_2$]**	10.6	1.3	>100	>100	>100
9	**[Cu(5-OMe-PT)$_2$]**	5.3	1.3	>100	>100	>100
10	**[Cu(3-OEt-PT)$_2$]**	>100	1.2	>100	>100	>100
11	**[Cu(3-F-PT)$_2$]**	5.7	2.8	11.4	>100	>100
12	**[Cu(3-OH-PT)$_2$]**	11.5	2.9	>100	>100	>100
13	**[Cu(5-Ph-PT)$_2$]**	>100	>100	>100	>100	>100
14	**[Cu(Q-PT)$_2$]**	>100	9.6	>100	>100	>100
15	**$CuCl_2$**	>100	>100	>100	>100	>100
16	**Levofloxacin**	0.04	0.69	>100	22	2.8

Among the *ESKAPE* pathogens, *E. coli* and *S. aureus* are the most susceptible to inhibition by the set of copper complexes. Of these two strains, the Gram-positive bacteria *S. aureus* was more susceptible to inhibition than the Gram-negative *E. coli* strain. The presence of an extra layer of lipid membrane in Gram negative bacteria affects the permeability of potential antibacterial agents into the cellular system of bacteria, thus decreasing their inhibitory effect.

In the case of *S. aureus*, several complexes retained the activity observed from [Cu(PT)$_2$]. These include the 3-Me 4-Me, 5-Me, 3-OMe, 5-OMe and 3-OEt substituted pyrithione complexes. These substitution patterns would broadly fall into the class of electron donating groups. The more electron withdrawing substituents led to a reduction in activity. For example, 4- and 6- CF_3 substituted complexes show increased MIC values of 4.4 µM. Substitutions of 3-F and 3-OH groups also lead to a slight increase in MIC value to 2.9 and 2.8 µM, respectively. Interestingly, the addition of aromatic groups in [Cu(5-Ph-PT)$_2$] and [Cu(Q-PT)$_2$] complexes led to lower activity, with the latter showing MIC values greater than 100 µM. Figure 2.30 illustrates these trends in graphical form (Figure 2.30).

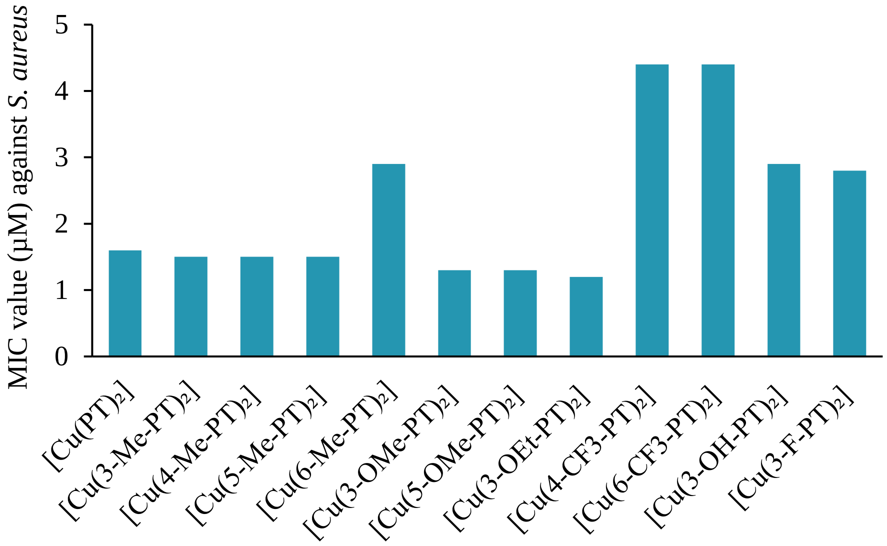

Figure 2.30: Antibiotic susceptibility data against S. aureus

In the case of *E. coli*, the effect of substituents leads to more variation in the data and the trends do not follow the data for *S. Aureus*. For *E. coli*, the introduction of methyl and methoxy groups in the 5-position and the fluoro group in the 3- position of PT made little difference to the MIC value compared to the non-substituted complex. However, introduction of ethoxy and methyl group in the 3 position and extension of the aromaticity show large increases in the MIC values (Figure 2.31). The two CF_3 substituted complexes showed lower activity than the parent [Cu(PT)$_2$] with evidence for the importance of regiochemistry, as the [Cu(6-CF_3-PT)$_2$] complex was the only regio-isomer to return a MIC value under 100 µM.

Other Gram-negative bacteria in this panel were mostly unaffected by the library of copper complexes. The exceptions are non-substituted [Cu(PT)$_2$] and the 3-fluoro substituted complex. [Cu(PT)$_2$] shows activity against *K. pneumoniae* and *A. baumannii* while [Cu(3-F-PT)$_2$] is the only substituted complex to be active against *K. pneumoniae*. Notably, the reference antibacterial drug levofloxacin is not active against *K. pneumoniae* and the MIC value of [Cu(PT)$_2$] against *A. baumannii* is very close to that of levofloxacin.

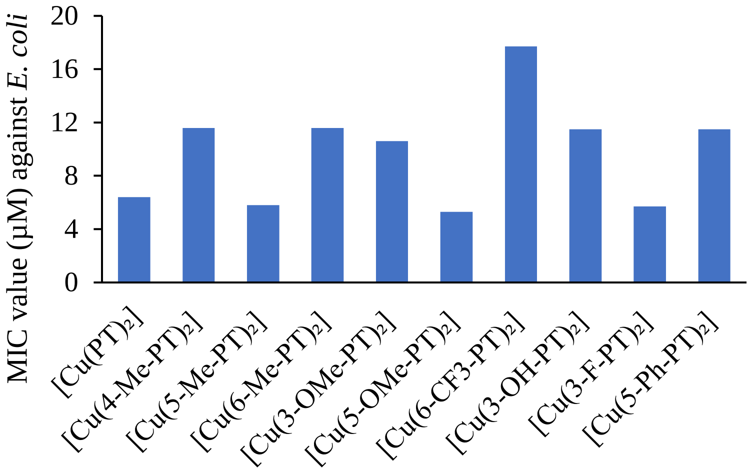

Figure 2.31: Antibiotic susceptibility data against E. coli

The library of complexes was tested against mammalian Vero cells, using the MTT assay method to establish their cytotoxicity towards normal healthy cells and determine any selectivity. In general, most of the substituted and non-substituted complexes from this library were observed to exhibit >80% inhibition of Vero cells even in very low concentrations (5 µg/ml) with selectivity indices (SI) of <10. The selectivity index is defined as the ratio of cytotoxic activity (CC_{50}) to MIC values and typically a minimum selectivity of 10 is required for further study of a potential antibacterial candidate. The only exception found in this study was the [Cu(5-Me-PT)$_2$] complex, which possess a SI = 10 and exhibits only 38% inhibition of cellular growth when applied in 5 µg/ml concentration (Table 2.3). It can be noted that this inhibition rate of Vero cells is lower than that by doxorubicin, a well-known drug molecule. Surprisingly, none of the other methyl substitutions in the 3, 4 and 6 positions of PT showed such selectivity. Although this apparent regioselectivity is not well-understood, perhaps the size and position of this particular functional group results in the lower inhibition rate against Vero cells. In general, the overall high cytotoxicity of this library of complexes presents a challenge for their use as antibacterial agents, however, the results do imply potential for these complexes as anticancer agents.

Table 2.3: Percentage inhibition data against mammalian Vero cells

Concentration (µg/ml)	**Average % Inhibition**		
	[Cu(PT)$_2$]	**[Cu(5-Me-PT)$_2$]**	**Doxorubicin**
100	91.8 ± 0.3	93.2 ± 0.6	-
80	91.8 ± 0.1	92.4 ± 1.4	-
40	91.7 ± 0.1	91.6 ± 1.8	-
20	91.5 ± 0.1	89.4 ± 1.4	-
10	91.2 ± 0.0	69.1 ± 5.5	55.5 ± 1.6
5	91.0 ± 0.1	38.3 ± 4.1	54.6 ± 2.2

Furthermore, the promising results for [Cu(5-Me-PT)$_2$] have opened the scope for more studies on this complex. For example, a preliminary biofilm assay for this compound, along with levofloxacin, vanomycin and disulfiram as reference compounds, has been carried out by our collaborator, Dr Sidharth Chopra. The data for percentage inhibition of *S. aureus* biofilm mass by this compound suggests its potential to be comparable with that of disulfiram and better than that of levofloxacin and vanomycin, two well-known antibiotics (Figure 2.32). Although these results are preliminary and need further repeats, there is clearly a lot of promise for this complex.

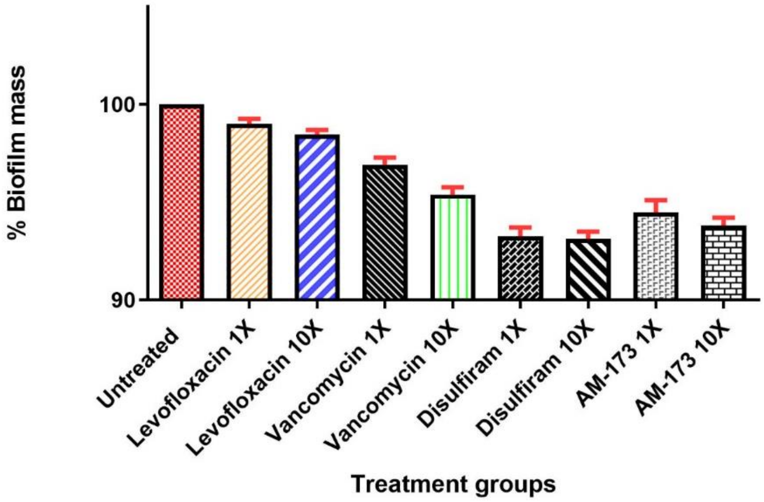

*Figure 2.32: Biofilm data for complex [Cu(5-Me-PT)$_2$] (**AM 173**)*

Antibiotic synergy study against β-lactam resistant E. coli

The above library of substituted copper pyrithione complexes, along with [Cu(PT)$_2$] and CuCl$_2$ as references, were tested against a β-lactam resistant strain of *E. coli* that produces the New Delhi metallo-β-lactamase 1 (NDM-1). When dosed on their own, all complexes showed low activity against the *E. coli* strain, with MIC values mostly >100 µM. The only exceptions were [Cu(PT)$_2$] (MIC = 50 µM), the 3-hydroxyl complex (MIC = 50 µM), and the 3-fluoro complex, which showed the best activity with a MIC value of 6.25 µM.

Next, the study with a β-lactam resistant strain of *E. coli* was further extended to determine any synergistic effects of the copper complexes with two well-known β-lactam antibiotics, meropenem and ertapenem. The hypothesis here relates to the mechanism of antibiotic resistance. As explained in Chapter 1, resistant *E. coli* strains are able to break down β-lactam antibiotics, through activity of the NDM-1 enzyme. NDM-1 is a zinc-containing metalloenzyme, which has been shown to be susceptible to transmetallation with copper, leading to inactivation of the enzyme activity. Our hypothesis is that Cu will inactivate the NDM-1 enzyme, thus reinstating the activity of the β-lactam antibiotic against the resistant strain. In the absence of copper complexes, meropenem and ertapenem display MIC values of 1 µM and 6 µM, respectively. These values are unaffected by the addition of CuCl$_2$ (up to 100 µM) (Figure 2.33). By contrast, addition of [Cu(PT)$_2$] leads to a significant reduction of both MIC values (Figure 2.33). In a similar way, the 3-hydroxy, 3-fluoro and 3-methoxy substituted complexes, also led to a lowering of the antibiotic MIC values (Figure 2.33). However, other substituted complexes, such as methyl, trifluoromethyl, ethoxy etc. failed to show any such effect.

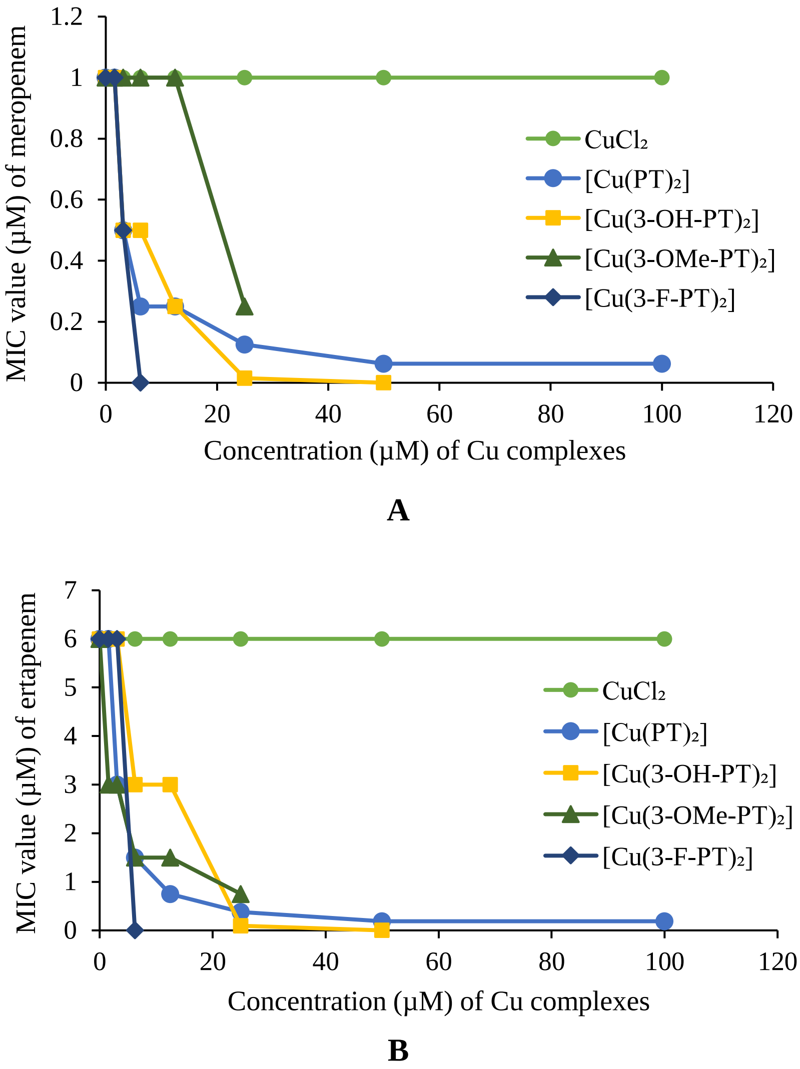

*Figure 2.33: Synergy study data for effective copper complexes with (**A**) meropenem and (**B**) ertapenem antibiotics*

To determine whether the lowering of the MIC values is due to a synergistic effect or an additive effect, the fractional inhibitory concentrations (FIC) index can be calculated. The FIC value for each compound is determined by dividing each of their MIC when used in combination by each compound's MIC when used alone. The sum of FIC values for the tested compounds is known as the FIC index. A range of FIC index from 0.5 to 4 is defined as a result of an additive effect and the index below 0.5 defined as synergistic. Among the four PT based complexes, only [Cu(PT)$_2$] displays a synergistic effect with both meropenem and ertapenem antibiotics, exhibiting the fractional inhibitory concentration (FIC) index value of 0.375. Among the other complexes, the 3-F species exhibits an additive effect (FIC = 1) in combination with meropenem, but not with ertapenem. For the 3-OH substituted complex, the MIC values of both meropenem and ertapenem are reduced due to an additive effect (FIC =

0.52-0.63). Introduction of the 3-OMe group on PT also affects the MIC values of both antibiotics, but the FIC values couldn't be determined due to the MIC value of [Cu(3-OMe-PT)$_2$] being >100 µM and the complex precipitating at higher concentrations.

Overall, this study helped to show that copper pyrithione complexes do lead to improvement in the antibacterial activity of common β-lactam antibiotics against β-lactam resistant bacterial species, which is promising for future work in this area.

2.2.3.2 Anticancer Activity

All anticancer activity tests were performed by our collaborator Dr. Rianne M. Lord at the University of East Angila, Norwich, UK.

Data from the antimicrobial testing had indicated that the copper pyrithione complexes had high antiproliferative activity against human cells. These results inspired us to explore whether the complexes could have potential as anticancer agents. Each complex was submitted to *in vitro* antiproliferation studies, against MIA PaCa-2 pancreatic carcinoma cells, 143B bone osteosarcoma cells and normal healthy ARPE-19 retinal epithelial cells, using the MTT assay, over the course of 24 h. Reference compounds $CuCl_2$, cisplatin and carboplatin were also included for comparison. The results, shown in Table 2.4, revealed that the majority of the copper complexes showed good activity against MIA PaCa-2 and 143B cell lines with IC_{50} values (concentration of the complex to inhibit the cell-growth by 50%) typically lower than 1 µM. This antiproliferation activity was far greater than $CuCl_2$ (Entry 9), which illustrates the importance of the pyrithione ligand in the activity. Furthermore, the platinum reference compounds cisplatin and carboplatin each showed significantly lower activity than the majority of the copper pyrithione complexes. For example, [Cu(PT)$_2$] was found to possess significant anticancer activity ~50 times better than cisplatin with IC_{50} values in the sub-micromolar range against both MIA PaCa-2 and 143B cell lines. Methyl substitutions in various positions of PT led to small increases in the IC_{50} values against both cell lines (Entries 2–4), while trifluoromethylated complexes showed lower activity (Entry 6–7), with IC_{50} values similar to that of cisplatin. Notably, the 3-methoxy substituted complex (Entry 5) exhibits a very low IC_{50} value of 018 ± 0.004 µM against MIA PaCa-2. This nanomolar activity suggests a highly potent complex against the pancreatic cancer cell line – 8 fold more active than [Cu(PT)$_2$] and >300 fold more active than cisplatin. Against the 143B cell line, the same complex showed activity more similar to that of [Cu(PT)$_2$]. These results demonstrate the excellent potential of substituted copper pyrithione complexes as anticancer agent.

Table 2.4: MTT assay data of substituted copper pyrithione complexes against MIA PaCa-2 pancreatic carcinoma cells, 143B bone osteosarcoma cells and normal ARPE-19 retinal epithelial cells

S. No.	**Compound**	**IC_{50} values (µM ± SD) after 24 h incubation**		
		MIA PaCa-2	**143B**	**ARPE-19**
1	**[Cu(PT)$_2$]**	0.15 ± 0.04	0.20 ± 0.02	0.22 ± 0.02
2	**[Cu(6-Me-PT)$_2$]**	0.33 ± 0.03	0.53 ± 0.05	1.10 ± 0.05
3	**[Cu(3-Me-PT)$_2$]**	0.47 ± 0.08	0.57 ± 0.07	2.39 ± 0.08
4	**[Cu(4-Me-PT)$_2$]**	0.55 ± 0.03	0.91 ± 0.05	2.33 ± 0.05
5	**[Cu(3-OMe-PT)$_2$]**	0.018 ± 0.004	0.220 ± 0.009	0.17 ± 0.01
6	**[Cu(6-CF$_3$-PT)$_2$]**	9.1 ± 0.7	7.4± 0.2	17.1 ± 0.7
7	**[Cu(4-CF$_3$-PT)$_2$]**	8.5 ± 0.6	15 ± 1	23.2 ± 0.6
8	**[Cu(Q-PT)$_2$]**	9 ± 1	12.9 ± 0.6	7.88 ± 0.06
9	**$CuCl_2$**	>100	75 ± 3	83 ± 2
10	**Cisplatin**	5.7 ± 0.1	14 ± 2	13.01 ± 0.1
11	**Carboplatin**	>100	70.8 ± 0.9	>100

The complexes were also screened against healthy ARPE-19 cells to determine their selectivity towards carcinoma cell lines over normal healthy cells (Table 2.5). The data suggests that in general the complexes are quite toxic towards healthy cells, showing similar selectivity to cisplatin. Among the copper complexes, the 3-OMe substituted species shows the highest selectivity. Against MIA PaCa-2, the selectivity index (SI) = 9.1, where selectivity index is defined as the ratio of IC_{50} values between the healthy and cancerous cell lines. Against the bone cancer cell line 143B this selectivity decreases, due to the lower activity against the cancer cell line. According to this screening, the 3-OMe substituted copper pyrithione complex exhibits a 4-fold improvement in selectivity, compared to cisplatin against MIA PaCa-2 cells. The origin of this improved selectivity is unclear, but we can tentatively propose that this particular substitution pattern is linked in some way to the mechanistic pathway of inhibition of cell-growth. It has been proposed that antiproliferative copper complexes typically show their activity via a ROS pathway for anticancer activity. However, this can only be confirmed through further mechanistic studies, which are ongoing.

Table 2.5: Selectivity data for substituted copper complexes

S. No.	**Compound**	**Selectivity Index**	
		MIA PaCa-2	**143B**
1	**[Cu(PT)$_2$]**	1.5	1.1
2	**[Cu(6-Me-PT)$_2$]**	3.3	2.1
3	**[Cu(3-Me-PT)$_2$]**	5.1	4.2
4	**[Cu(4-Me-PT)$_2$]**	4.2	2.6
5	**[Cu(3-OMe-PT)$_2$]**	9.1	0.8
6	**[Cu(6-CF$_3$-PT)$_2$]**	1.9	2.3
7	**[Cu(4-CF$_3$-PT)$_2$]**	2.7	1.6
8	**[Cu(Q-PT)$_2$]**	0.9	0.6
9	**CuCl$_2$**	<0.8*	1.1
10	**CDDP**	2.3	1.0
11	**CARB**	n.d.	>1.4

* Cannot be correctly calculated as IC$_{50}$ value >100

2.3 Conclusion and Future Work

To summarise, a library of substituted copper pyrithione complexes have been synthesised and their chemical properties and biological activities have been assessed to gain an insight into their structure-activity correlation. A range of functional groups, including alkyl, alkoxy, hydroxy, trifluoromethyl and aromatics, and regiochemistry were introduced in order to determine trends within the series. All complexes were synthesised following a common pathway involving pyridyl oxidation, sulfur S$_N$Ar and copper complexation. Yields were generally moderate to high, although several attempted syntheses were not possible. Unsuccessful synthetic targets included 6-substituted *i*-propyl and *t*-butyl substituents, likely due to the steric hinderance they induce around the pyridyl nitrogen.

Lipophilicity and thermodynamic stability of a selection of complexes were measured. Addition of substituents to the pyrithione core of [Cu(PT)$_2$] led to a reduction in lipophilicity, with CF$_3$ substituents being the lowest lipophilic. Lipophilicity is known to be an important consideration in cellular studies. Stability constants were measured for four complexes, containing electron withdrawing and donating substituents. In general, the substituent had almost no effect upon the binding constant, which remained similar to the unsubstituted complex. This result indicates that binding strength is primarily due to the chelation and ligand–metal bond strength of pyrithione, although it is somewhat surprising that changes in the electron density around the pyrithione ring don't have a more significant effect upon the binding constant.

The novel copper complexes were tested for biological activity in both antibacterial and anticancer assays. In general, the newly developed complexes show far greater bioactivity than the ionic copper(II) chloride salt, confirming the importance of the pyrithione ligand. In the antibacterial studies, it was observed that, broadly, the electron donating substituents exerts a positive effect on the bioactivity of the copper pyrithione complexes, whereas electron withdrawing substituents lead to lower activity. This result implies that electronics play a consequential role in the bioactivity of these complexes. One possibility would be some favourable interaction of electron rich substituted PT carriers with membrane proteins during the permeation through cellular membrane, although more mechanistic data would be needed to support this theory. In anticancer assays, all complexes showed some activity, but it was, again, the electron donating substituents that showed the most activity. Distinct variation between the pyrithione complexes demonstrates the impact that this modification can have on activity. To date, the most impressive compound is [Cu(3-OMe-PT)$_2$], which has high potential as an anticancer agent, particularly towards the pancreatic cancer cell line. In the antibacterial screening, [Cu(5-Me-PT)$_2$] has emerged as the most selective complex (SI = 10) towards bacteria over human cells. Furthermore, in a quest to enhance the bioavailability and solubility of copper based pyrithione complexes, we have developed 3-OH substituted copper pyrithione complex. Its enhanced ability to form hydrogen bonds with water through stronger hydroxyl acceptors increase its aqueous solubility. However, the antibacterial activity was compromised in this case and therefore more attention is required towards designing new complexes of increased solubility without trading off the other physical and chemical aspects important for bioactivity.

In terms of future work, study with this library of copper complexes can be carried forward towards intracellular studies to identify the mechanistic pathway behind their bioactivity. In the case of the antibacterial studies, the complexes should be analysed to determine the cellular uptake of copper and the amount of copper released inside the cellular environment. Further synergy tests with the antibiotic resistant strain should be done to confirm whether they possess a bactericidal (kills the bacteria and inhibits the resistant enzyme) or bacteriostatic (doesn't kill the bacteria but inhibits the resistant enzyme) activity. For the anticancer activity, performing ROS assays, cellular uptake of the metal and cell apoptosis studies on the most effective complexes will allow further insight into the intracellular mechanism of cellular growth inhibition. In addition, alternative experimental procedures to determine the lipophilicity of poorly water-soluble compounds might enhance the accuracy of existing data and therefore can be utilised better to explain any correlation between lipophilicity and bioactivity. Furthermore, development of new pyrithione based copper complexes with a variety of electron donating substitutions has the potential to enrich this library of complexes, with a view to producing better antibacterial and anticancer activities.

3. Increasing Solubility of Copper Pyrithione with Polyethylene Glycol (PEG) Chain Substitution

3.1 Introduction

3.1.1 Balancing Lipophilicity and Solubility in Drug Development

Designing any potential drug molecule needs consideration of the essential prerequisites of its key physiochemical properties. Among them, optimisation of ADMET (absorption, distribution, metabolism, excretion, and toxicity) properties can be challenging. Solubility and lipophilicity contribute to the ADMET properties of bioactive compounds. Permeability through cell membranes and bioavailability of any compound are highly dependent on the balance between these two parameters.[261]

Lipophilicity can be described as a molecule's affinity towards a lipophilic environment and is usually measured by the molecule's distribution in a biphasic organic:aqueous solvent system. Lipophilicity affects the permeating ability of a compound through the lipopolysaccharide membrane of cells. However, it also has effects on ligand-target interactions and highly lipophilic compounds ($\log P > 5$) are generally disfavoured for biological applications, as they will likely bind to hydrophobic molecules such as cellular membranes, instead of the targeted active site. Furthermore, increased lipophilicity can reduce the water-solubility, hence affecting the delivery, absorption and bioavailability of the related drug molecule. In this context, it has been suggested by Lipinski's 'Rule of 5' that an optimal range of lipophilicity ($\log P = 1 - 5$) is required in the development of bioactive compounds.[262]

Solubility is another property that plays a vital role in determining bioavailability and permeability of a drug molecule.[263] $[Cu(PT)_2]$ has very low water-solubility, which makes the bioactivity assays challenging and renders difficulties in its further development as a potential drug molecule with a balanced pharmacokinetics. As a result, improving the aqueous solubility of pyrithione-based copper complexes, through pyrithione substitution, would be an important breakthrough. Caution must be taken however, as this type of substitution can sometime impose negative effects on the other properties, such as lipophilicity and bioactivity. In this chapter the main aim was to improve the solubility of $[Cu(PT)_2]$ without detrimentally affecting its bioactivity.

3.1.2 Polyethylene Glycol in Bioactive Molecules

Polyethylene Glycol (PEG) is a hydrophilic polyether with wide use in the medicinal chemistry research field. In its polymeric form, ethylene oxide has average molecular weight less than 20,000 g/mol and can be solubilised in various polar solvents such as water, ethanol, acetonitrile and dichloromethane. Along with being hydrophilic, PEG chains also possess an array of bio-applicable properties such as non-immunogenicity, biocompatibility, non-biodegradability, flexibility, reduced toxicity and ease of excretion from living organisms. These characteristics have led to many examples of drug modification with PEG chains, leading to bioactive lead compounds conjugates with enhanced activities.[264] In this chapter, we focus on improving the water-solubility of [Cu(PT)$_2$] through introduction of PEG chain. The ultimate goal is to develop water-soluble copper pyrithione complexes with non-compromised or enhanced bioactivity.

3.2 Results and Discussion

3.2.1 Synthesis and Characterisations of PEG-substituted Copper Pyrithione Complexes

Three water-soluble pyrithione ligands with different lengths of short PEG chains were synthesised (Figure 3.1). The general procedure started with bromination of commercially available 2-bromo-5-bromomethylpyridine using *N*-bromosuccinimide (NBS) as the bromine source and dibenzoyl peroxide as radical initiator. This reaction also produced some di-brominated compound as a by-product and column chromatography was used to separate the desired compound from the by-product. The two brominated products are not very different in polarity, which led to a low yield of purified compound, particularly when the reaction was performed on a large scale (>2 g). The mono-brominated product (**3.1**) was reacted with the respective alcohol-terminated PEG chains (n = 1, 2 and 3) using sodium hydride as the base and anhydrous THF as solvent under inert N_2 atmosphere. The three different PEG chain lengths were included to understand the effect of chain length on the properties of the pyrithione complexes.

Next, oxidation of the PEGylated products (**3.2a-c**) using *m*CPBA yielded the *N*-oxide products (**3.3a-c**) in moderate yields. Attempts to push these reactions to completion with using 3 or 4 equivalents of *m*CPBA did not achieve full conversion. The *N*-oxide products were purified by silica gel column chromatography using 5% MeOH/CH_2Cl_2 as the eluting system. In the next step, nucleophilic aromatic sulfur substitution reactions were performed on the *N*-oxides using sodium hydroxide and sodium sulfide to produce substituted pyrithione ligands (**3.4a-c**). The formation of intermediates and final ligands were confirmed and analysed using high field multinuclear NMR spectroscopy and ESI mass spectrometry. In Figure 3.2, the changes in ^{1}H NMR spectra from **3.1** to **3.4b** (n = 2 PEG chain), via the respective intermediates, are shown. In these spectra, it can be observed that substitution of bromine in **3.1** by more electronegative

PEG chain shifts the methylene resonance peak (H^7) to higher frequency in **3.2b**, however the signals for the aromatic hydrogens (3, 4 and 6) are relatively unaffected. The *N*-oxidation and sulfur substitution steps lead to notable changes in the chemical shifts of the pyridine ring protons. The signals for the PEG chain aliphatic hydrogens are not affected by these two steps but the H7 methylene peak moves to lower frequency due to their proximity to the pyridine ring (Figure 3.2).

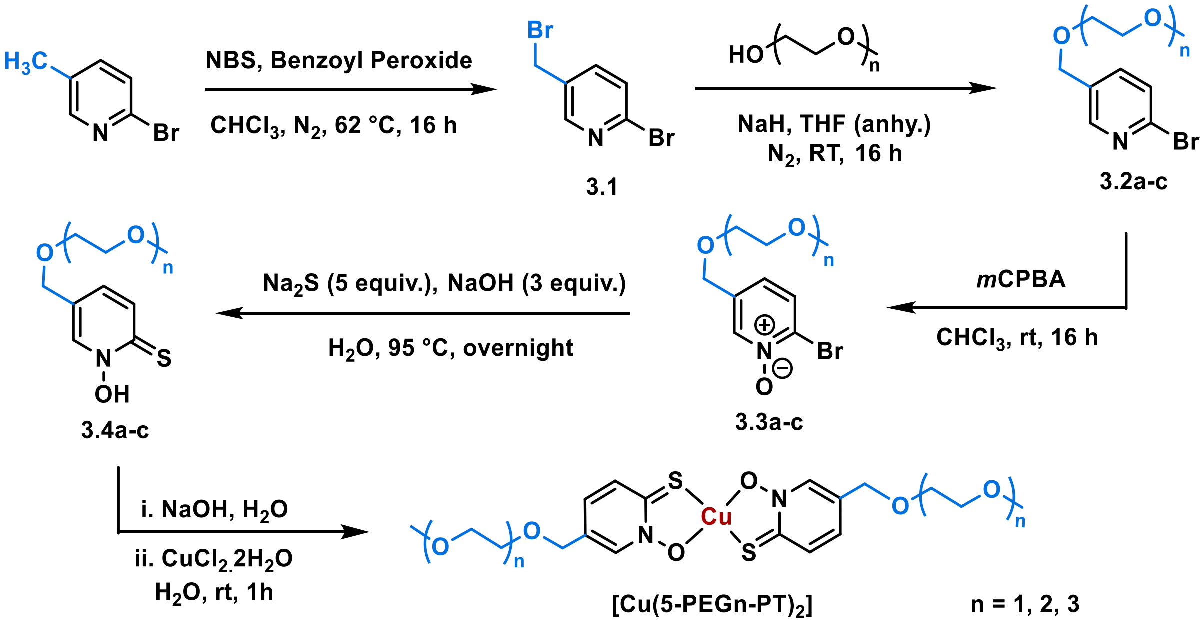

Figure 3.1: General synthetic route for copper complexes of PEG-chain substituted pyrithione ligands

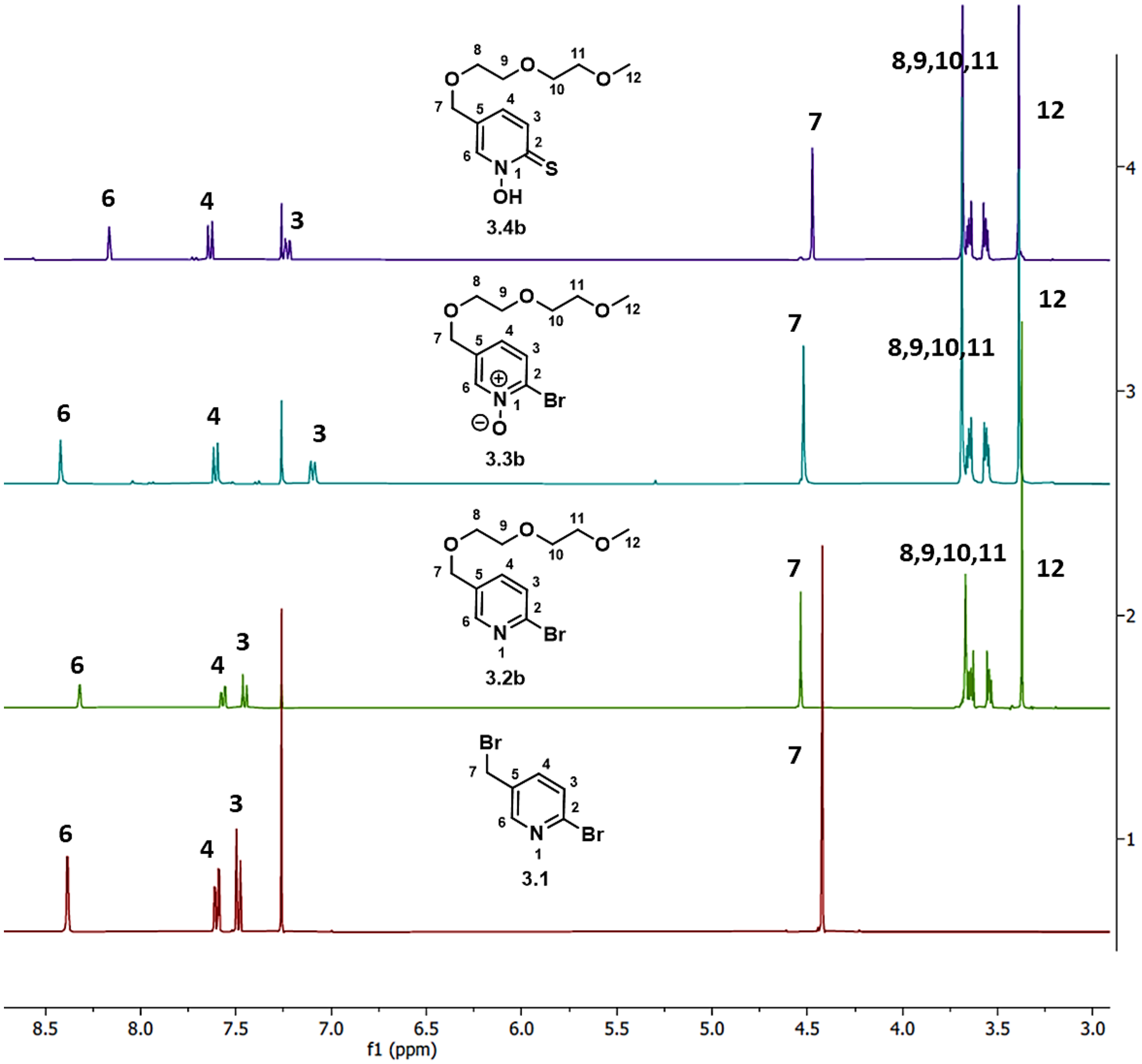

*Figure 3.2: ^{1}H NMR spectra in chloroform-d solvent (600 MHz) for formation of ligand **3.4b** from **3.1***

Complexation of these PEGylated ligands **3.4a-c** with copper was carried out by reacting the respective ligand with copper(II) chloride in a 2:1 ratio using water as solvent and sodium hydroxide as the base (Figure 3.1). The shortest PEG chain containing complex ([Cu(5-PEG1-PT)$_2$]) was isolated as a dark green solid, which precipitated from the reaction mixture. However, due to their increased aqueous solubility, the other two complexes ([Cu(5-PEG2-PT)$_2$] and [Cu(5-PEG3-PT)$_2$]) were collected as crude dark green oils, after evaporation of the reaction-solvent. ESI and ASAP mass spectrometry confirmed formation of the metal-ligand complexes (Figure 3.3). In the mass spectrometry data, *m*/*z* peaks for both $[M+H]^+$ and $[M+Na]^+$ were observed for all three complexes, with characteristic isotope patterns for Cu complexes. The complexes were purified via trituration into dichloromethane solvent. HPLC chromatography and elemental analysis data (% C, H and N) assured high purity of the final products (Figure 3.4).

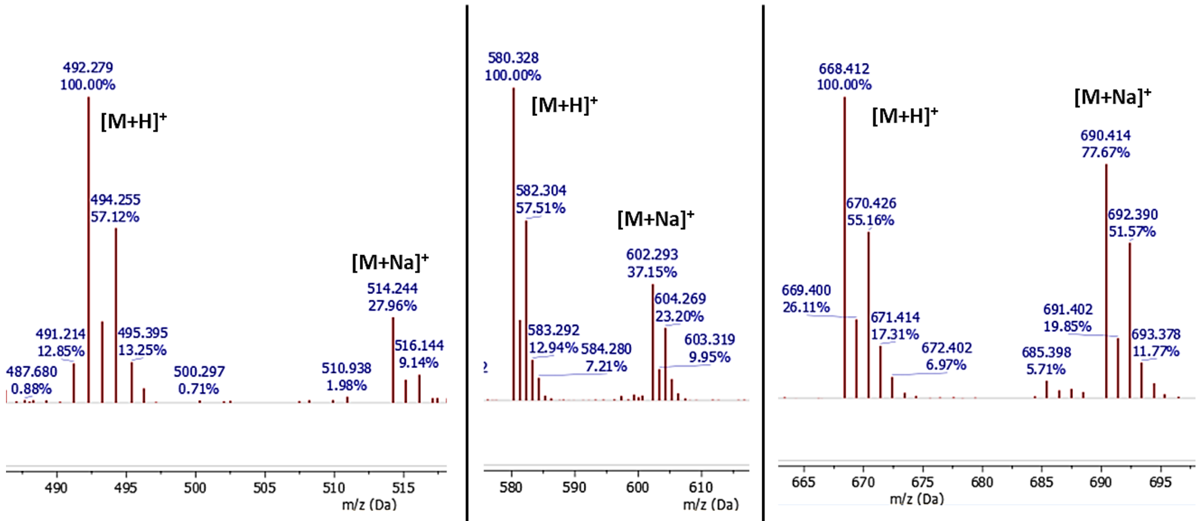

[Cu(5-PEG1-PT)$_2$] [Cu(5-PEG2-PT)$_2$] [Cu(5-PEG3-PT)$_2$]

Figure 3.3: Mass spectrometry data for three PEG chain containing complexes where 'M' represents the respective copper complexes

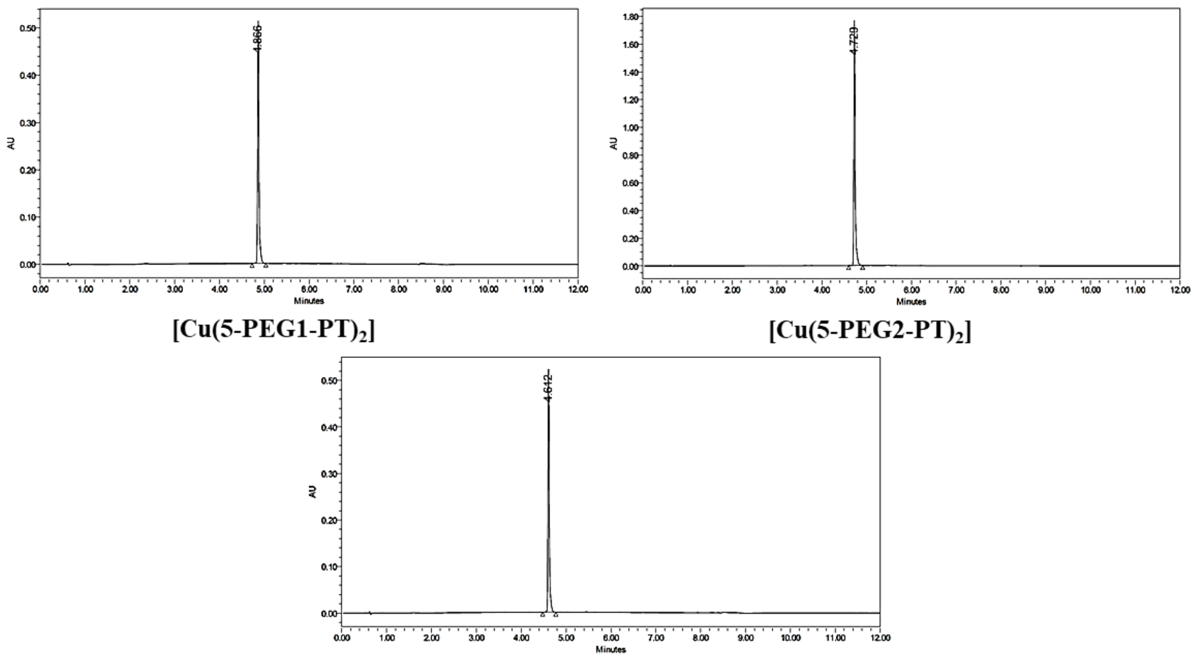

[Cu(5-PEG1-PT)$_2$] [Cu(5-PEG2-PT)$_2$]

[Cu(5-PEG3-PT)$_2$]

Figure 3.4: HPLC traces for PEGylated copper pyrithione complexes

Single crystals for the copper complex with the shortest PEG-chain [Cu(5-PEG1-PT)$_2$] were grown from slow-evaporation of a CH_2Cl_2-methanol solvent system. The X-ray crystallography data reveals formation of the square planar complex in both *cis* and *trans* isomeric forms, in the unit cell (Figure 3.5 A). The extended X-ray crystal structure shows parallel stacking interactions between isomers with the same *cis*/*trans* geometry. As shown in Figure 3.5 A, two *cis* isomers in adjacent planes stack and show intermolecular Cu–O and Cu–

S interactions (bond distances = 3.5 Å and 3.6 Å, respectively). Similarly, the *trans* isomers have two Cu–S interactions between two stacked molecules in adjacent planes (Figure 3.5 A). As seen in Figure 3.5 B, the extended structure contains alternating *cis*-*cis* and *trans*-*trans* stacked isomer pairs. Overall, the crystal structure has low overall symmetry with space group P-1.

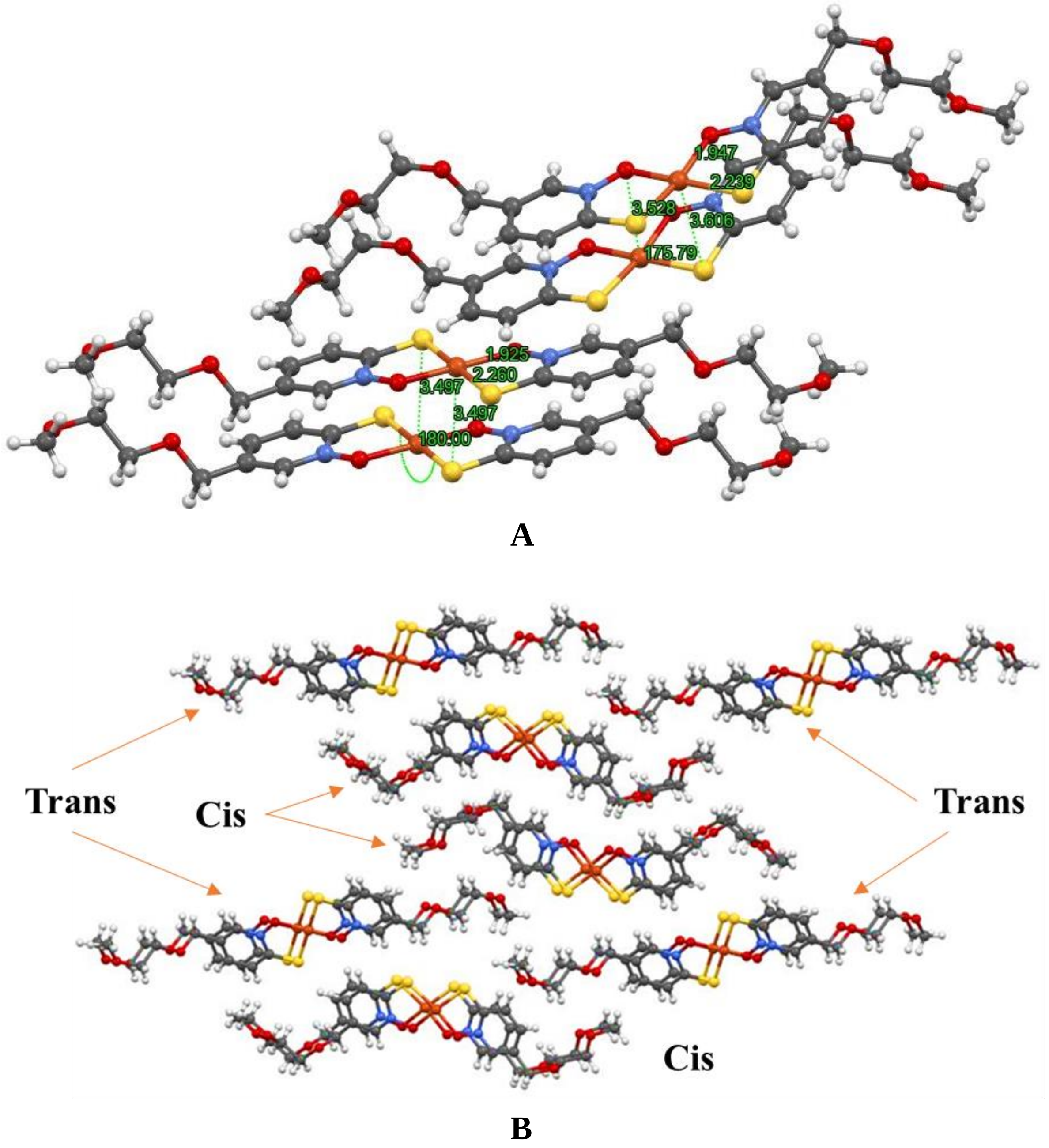

Figure 3.5: Crystal structure for cis-trans co-crystal of [Cu(5-PEG1-PT)$_2$]

Also synthesised was a reference complex with no PEG chain but containing a pre-PEG substitution (n = 0) in the 5-position of pyridine in order to compare its bioactivity with the

PEG substituted complexes. The procedure followed exactly the same pathway as that of the PEG substituted complexes (Figure 3.6). In this case, methanol was used as the alcohol source, which reacted with 5-bromomethylated intermediate **3.1** to give 2-bromo-5-methoxymethylpyridine (**3.6**). *N*-oxidation, sulfur substitution and metal complex formation proceeded smoothly to give the 5-methoxymethyl substituted copper pyrithione complex **3.9**. This complex was characterised using ASAP mass spectrometry and the purity was confirmed through elemental analysis.

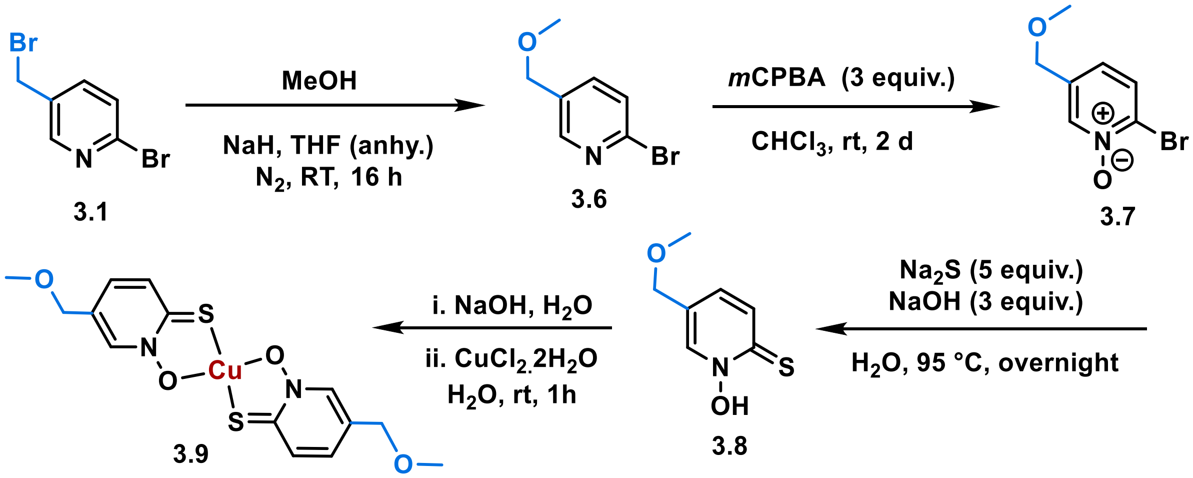

*Figure 3.6: Synthetic pathway for formation of the reference complex **3.9***

3.2.2 Analysis of Chemical Properties

Solubility and Lipophilicity Study

Water-solubility of the PEG-substituted complexes was calculated by measuring absorbance of saturated solutions in 1% DMSO/water using UV/Vis spectroscopy. As expected, solubility increases with increasing PEG chain length. [Cu(5-PEG1-PT)$_2$] was found to be the least soluble of the new complexes, with maximum solubility of 0.2 g/L. This complex was more than 200 times more soluble than the parent complex [Cu(PT)$_2$], which has solubility of around 0.001 g/L. As the PEG chain length increased, solubility increased with [Cu(5-PEG2-PT)$_2$] giving a solubility of 0.7 g/L and the longest PEG chain complex [Cu(5-PEG3-PT)$_2$], giving a solubility of >25 g/L (Table 3.2).

As discussed in the previous chapter, when measuring the lipophilicity of copper complexes, due to the low solubility of the parent complex [Cu(PT)$_2$] in water, the conventional shake flask method using UV/Vis spectroscopy was not very useful. Instead, we resorted to a modified shake-flask method, where ICP-OES was used to quantify the Cu levels present in both the octanol and aqueous layers. Thanks to the improved solubility, for the PEG complexes under discussion here, both the ICP-OES and UV/Vis methods were utilised to quantify Cu in each layer, allowing the calculation of log P values. Although aqueous solubility was high for the PEG complexes the system was kept as 1% DMSO/solvent to avoid disparity in data collection and allow direct comparison with [Cu(PT)$_2$] and the previously synthesised copper pyrithione complexes.

Initially, extinction coefficients (*ε*) in both water and octanol (containing 1% DMSO) for the three PEG complexes were calculated through measurement of UV/Vis absorbance of solutions with increasing complex concentrations (Figure 3.7) (Table 3.1). The *ε* values are quite high and therefore suggest spin and Laporte allowed transitions. The extinction coefficients and absorption maxima do not vary greatly between the two solvents. With extinction coefficients in hand, concentrations of copper complex were calculated in both solvent layers following the shake-flask process to determine the lipophilicity partition coefficient (*P*).

Table 3.1: Molar extinction coefficients for PEG-substituted complexes in water and octanol

Complex	**ε_{water} at 322 nm (M^{-1} cm^{-1})**	**$\varepsilon_{octanol}$ at 322 nm (M^{-1} cm^{-1})**
[Cu(5-PEG1-PT)$_2$]	18100 ± 300	19900 ± 200
[Cu(5-PEG2-PT)$_2$]	17900 ± 200	18700 ± 200
[Cu(5-PEG3-PT)$_2$]	17300 ± 300	18400 ± 200

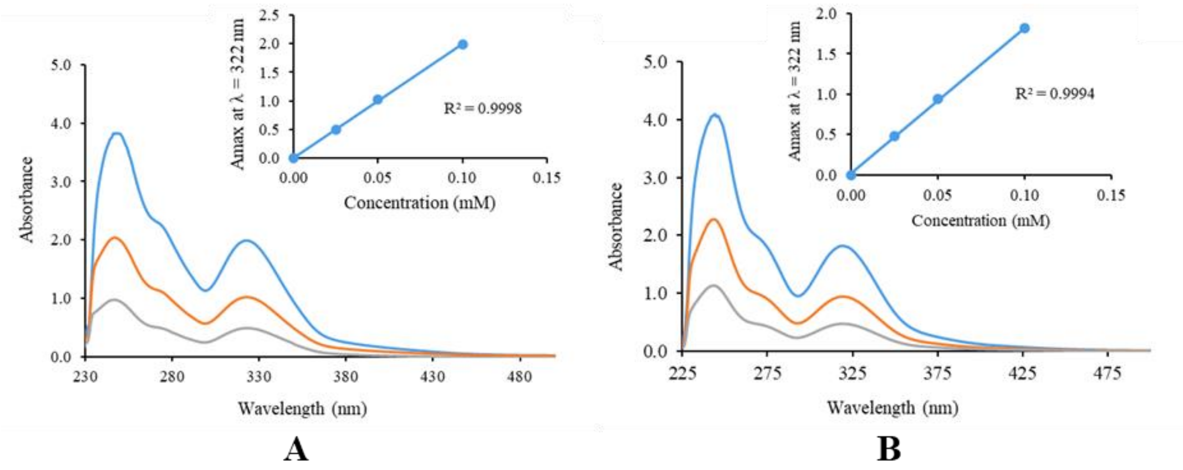

Figure 3.7: UV absorbance spectra and corresponding concentration graph for calculating extinction coefficient of the complex *[Cu(5-PEG1-PT)$_2$] in* (**A**) octanol and (**B**) *water solvents*

To allow lipophilicity comparison with [Cu(PT)$_2$], ICP-OES analysis of the shake-flask method was also carried out. The results in Table 3.2 reveal the order of lipophilicity from highest to lowest is [Cu(PT)$_2$] > [Cu(5-PEG1-PT)$_2$] > [Cu(5-PEG2-PT)$_2$] > [Cu(5-PEG3-PT)$_2$]. This trend is echoed in the analysis by UV/Vis and reveals that adding PEG-chains to the copper(II) pyrithione complex leads to a reduction in lipophilicity. The lipophilicity trend is inversely proportional to the solubility trend of the three PEG complexes, showing lipophilicity decreases with increasing aqueous solubility. However, the rate of decrease in lipophilicity is much lower than the rate of increase in solubility. Reassuringly, both methods of measuring log *P* (UV/Vis and ICP-OES) give the same trend in lipophilicity, however, the disparity in the absolute values of log *P* using the two different methods implies a lack of accuracy in one or both methods – inaccuracies in ICP-OES analysis are most likely due to the lack of prior knowledge about its utilisation in log *P* calculation, while the UV/Vis method may suffer from issues due to the DMSO present in the solution.

Table 3.2: Solubility and lipophilicity data for PEG-chain substituted copper pyrithione complexes

Complex	**Solubility (g/L)**	**log *P* (UV/Vis method)**	**log *P* (ICP-OES method)**
[Cu(PT)$_2$]	0.001	-	2.337
[Cu(5-PEG1-PT)$_2$]	0.2	1.484	1.812
[Cu(5-PEG2-PT)$_2$]	0.7	1.423	1.744
[Cu(5-PEG3-PT)$_2$]	>25	1.217	1.391

3.2.3 Biological Activity

3.2.3.1 In vitro Activity against ESKAPE Panel Organism and Cytotoxicity Data

The three novel PEG complexes, along with parent [Cu(PT)$_2$], CuCl$_2$, complex **3.9** and levofloxacin were screened against the ESKAPE panel organisms by our collaborator Dr. Sidharth Chopra, principal scientist, Central Drug Research Institute, Lucknow, India, following the same method mentioned in previous chapter.

Table 3.3: Antibacterial data for PEG chain substituted copper pyrithione complexes against ESKAPE class of pathogen

Complex	**MIC(μM)** ***E.coli*** **ATCC 25922**	***S.aureus*** **ATCC 29213**	***K.pneumoniae*** **BAA 1705**	***A.baumannii*** **BAA 1605**	***P.aeruginosa*** **ATCC 27853**
[Cu(PT)$_2$]	6.4	1.6	12.8	12.8	>100
[Cu(5-PEG1-PT)$_2$]	32.5	2	>100	>100	>100
[Cu(5-PEG2-PT)$_2$]	>100	3.4	>100	>100	>100
[Cu(5-PEG3-PT)$_2$]	>100	6	>100	>100	>100
3.9	>100	79.2	>100	>100	>100
CuCl$_2$	>100	>100	>100	>100	>100
Levofloxacin	0.022	0.35	>100	22	2.8

The lowest MIC values were found against the Gram-positive bacterium, *S. aureus* (Table 3.3), with all copper(II) pyrithione complexes showing efficacy at low micromolar (μM) concentration (high activity). By comparison, CuCl$_2$ shows no activity up to 100 μM, highlighting importance of the ligand for activity. Comparing the copper(II) pyrithione complexes, the MIC values follow a trend that the longer the PEG chain length, the lower the activity of the complex, although the activity decrease is fairly small between the three PEG complexes. Interestingly, complex **3.9** with the non-PEGylated 5-substituted pyrithione showed very low activity, which is surprising considering the high activity of the unsubstituted [Cu(PT)$_2$]. Among the panel of Gram-negative bacteria, only *E. coli* is affected by the PEG substituents. Unsubstituted [Cu(PT)$_2$] shows some activity with MIC value of 6.4 μM and the shortest PEG-chain complex, [Cu(5-PEG1-PT)$_2$], shows a lower activity of 32.5 μM, while the longer chain complexes show no activity up to 100 μM. The universal lower activity of the copper(II) complexes against Gram-negative bacteria likely relates to their poorer ability to permeate through the cell membranes, as Gram-negative species have an extra layer of lipopolysaccharide membrane which is absent in Gram-positive species. The data established here show the importance of the copper carrier molecule and the notable structure-activity correlation observed between the various lengths of PEG chain substituents.

The susceptibility of mammalian cells towards cell death by these three PEG complexes along with [Cu(PT)$_2$] and doxorubicin as references were tested. All pyrithione based complexes were found to have an average inhibition rate of ~90% against Vero cells (Table 3.4), which is higher than that of the doxorubicin reference. This data indicates low selectivity (selectivity index <10) of the complexes towards bacterial inhibition over normal cells (where selectivity is defined as the ratio of cytotoxicity to MIC values). The low selectivity means these complexes will not be appropriate for further study against bacteria. However, the high inhibition rate against mammalian cell-growth indicates the potential of these copper complexes to be active against human carcinoma cells.

Table 3.4: Cytotoxicity data of PEG chain complexes

Concentration (μg/ml)	**Average % Inhibition**				
	[Cu(PT)$_2$]	**[Cu(5-PEG1-PT)$_2$]**	**[Cu(5-PEG2-PT)$_2$]**	**[Cu(5-PEG3-PT)$_2$]**	**Doxo-rubicin**
100	-	94.2 ± 0.3	94.6 ± 0.1	94.7 ± 0.2	-
80	-	93.5 ± 0.2	94.6 ± 0.1	94.5 ± 0.3	-
40	-	92.7 ± 0.3	94.4 ± 0.3	94.1 ± 0.3	-
20	-	90.8 ± 0.3	94.0 ± 0.3	-	-
10	94.8 ± 0.4	89.3 ± 0.5	-	-	63.2 ± 1.2
5	94.5 ± 0.2	-	-	-	-
2.5	93.9 ± 0.3	-	-	-	-
1.25	93.5 ± 0.5	-	-	-	47.5± 2.3

3.2.3.2 Antibiotic Synergy Study against resistant strain of Gram-negative Bacteria

Synergy studies were carried out in a similar way to those described in Chapter 2. Namely, the novel copper complexes were tested against β-lactam resistant strain of *E. coli* that produces the New Delhi metallo-β-lactamase 1 (NDM-1). Assays were conducted with the Cu complexes alone and in combination with known β-lactam antibiotics, meropenem and ertapenem to determine any synergistic effects. As previously mentioned, the hypothesis is that Cu can inhibit the NDM-1 enzyme, restoring activity of the known antibiotics. In the absence of β-lactam antibiotic, each copper complex displayed low activity against the *E. coli* strain. The minimum inhibitory concentration (MIC) values of the copper complexes alone are 100 μM for [Cu(5-PEG1-PT)$_2$] and >100 μM for [Cu(5-PEG2-PT)$_2$] and [Cu(5-PEG3-PT)$_2$]. To determine if the copper complexes can act in synergy with known β-lactam antibiotics, the complexes were added to inhibition experiments with known antibiotics meropenem and ertapenem (Figure 3.8).

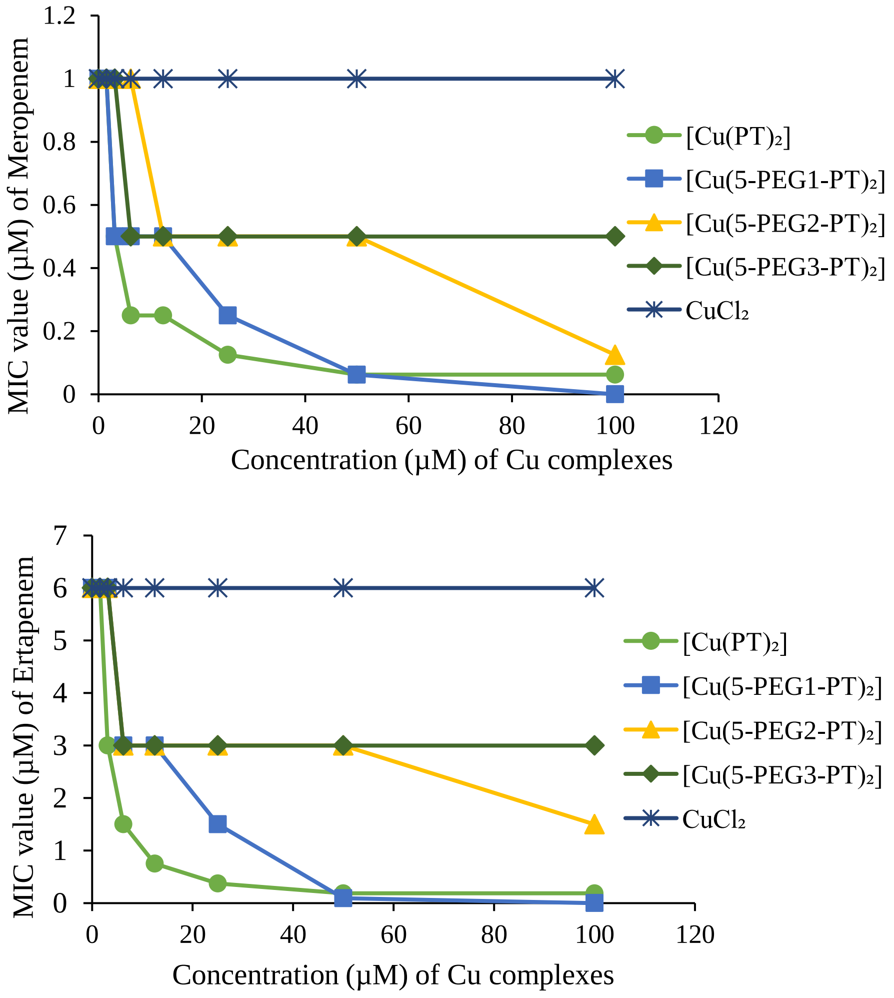

Figure 3.8: Data of antibiotic synergy study with $CuCl_2$, [$Cu(PT)_2$] and three PEG chain complexes

In the absence of copper complexes, meropenem and ertapenem display MIC values of 1 µM and 6 µM, respectively against the β-lactam resistant strain of *E. coli* (Figure 3.8). These values are unaffected by the addition of $CuCl_2$ (up to 100 µM). By contrast, addition of the novel copper pyrithione complexes leads to strong reduction in both MIC values. Addition of the longer chain PEG complexes [$Cu(5\text{-}PEG3\text{-}PT)_2$] and [$Cu(5\text{-}PEG2\text{-}PT)_2$] reduced the meropenem and ertapenem MIC values to around half of their original value at 50 µM copper complex. The shorter chain complex [$Cu(5\text{-}PEG1\text{-}PT)_2$] leads to the same halving of antibiotic MIC at only 6 µM copper concentration and, at 50 µM copper concentration, further reduced the antibiotic's MIC values by 10-fold compared to the value without copper. [$Cu(PT)_2$] slightly outperforms [$Cu(5\text{-}PEG1\text{-}PT)_2$], with a 10-fold reduction in antibiotic MIC at around 25 µM copper concentration. Overall, it is clear that the copper complexes have a positive effect in increasing the bacterial cell death. To help understand whether this is a synergistic effect or an additive effect, fractional inhibitory concentration (FIC) index values for [Cu(5-PEG1-PT)$_2$] were calculated to be in the range of 0.5-1.0. For the other two complexes, FIC value couldn't be determined accurately, as the complexes alone have MIC values >100 µM. Overall, the data clearly indicates the additive effect of these copper complexes acting alongside the meropenem and ertapenem antibiotics to increase the overall activity against the resistant bacteria.

Finally, a study was conducted to confirm whether these copper-based complexes possess bactericidal or bacteriostatic activity, adding insight into the mechanism of activity, potentially via inhibition of the NDM-1 resistance mechanism. In this study, bacterial cultures from the no-growth wells of the antibiotic synergy studies were plated in Agar plates. If complexes are bacteriostatic, further growth would be expected, while bactericidal activity would be evidenced by no further growth. In the experiments conducted, no further bacterial growth was observed after a 24 h incubation period. This data suggests that when employed in combination with β-lactam antibiotics, the activity of these copper complexes to be bactericidal along with their enzyme inhibition properties. However, lack of repeat experiments left this data inconclusive yet. Further repeat of this study is ongoing.

3.2.3.3 Anticancer Activity

All anticancer tests have been performed by Dr. Rianne M. Lord at the University of East Angila, Norwich, UK.

Antiproliferation studies were carried out against MIA PaCa-2 pancreatic carcinoma cells, 143B bone osteosarcoma cells and normal healthy ARPE-19 retinal epithelial cells, using the MTT assay over the course of 24 h. [Cu(PT)$_2$] and the three novel copper(II) complexes were screened alongside the known anticancer drugs cisplatin and carboplatin, as well as $CuCl_2$ as references. The proliferation data against pancreatic (MIA PaCa-2) and bone (143B) cancer cell show that the inhibitory activities of the novel copper(II) complexes are significantly higher than that of cisplatin and carboplatin (Table 3.5 and shown graphically in Figure 3.9). The inhibitory concentrations (IC_{50} values) of these three complexes are in the sub-micromolar range and are comparable with that of the parent [Cu(PT)$_2$] complex (Figure 3.9). This result indicates that modulation of the pyrithione ligand in order to improve solubility does not have a detrimental effect upon the activity of the complex. In fact, the shortest PEG-chain complex [Cu(PT)$_2$] displayed slightly higher activity than the parent complex against the pancreatic cell line. As the PEG-chain length increases, activity decreases slightly against both pancreatic and bone cancer cell lines, indicating a trend that lowering lipophilicity can decrease activity. By comparing activity against the healthy cell line, it can be seen that copper complexes show little selectivity, where the selectivity index (SI) is defined as the ratio of IC_{50} values for healthy cells over cancerous cells. The most selective complex $[Cu(5\text{-}PEG1\text{-}PT)_2]$ shows a slight selectivity, with a selectivity index (SI) of 1.6 between pancreatic and healthy cells (Table 3.5). Though this selectivity is comparable with that of the parent complex, cisplatin shows a slightly higher selectivity index of 2.3 for MIA PaCa-2.

Table 3.5: IC_{50} data for non-substituted and PEG-chain substituted copper pyrithione complexes along with $CuCl_2$, cisplatin and carboplatin as references against human cell lines and the selectivity indices (SI) (normal vs cancer) in parenthesis

S. No.	**Complex**	**IC_{50} values (µM ± SD)**		
		MIA PaCa-2	**143 B**	**ARPE-19**
1	**$[Cu(PT)_2]$**	0.15 ± 0.04 (1.5)	0.20 ± 0.02 (1.1)	0.22 ± 0.02
2	**$[Cu(5\text{-}PEG1\text{-}PT)_2]$**	0.125 ± 0.008 (1.6)	0.42 ± 0.04 (0.5)	0.20 ± 0.01
3	**$[Cu(5\text{-}PEG2\text{-}PT)_2]$**	0.217 ± 0.005 (0.7)	0.5 ± 0.3 (0.3)	0.162 ± 0.005
4	**$[Cu(5\text{-}PEG3\text{-}PT)_2]$**	0.255 ± 0.004 (1.1)	0.86 ± 0.07 (0.3)	0.27 ± 0.05
5	**$CuCl_2$**	>100 (<0.8)	75 ± 3 (1.1)	83 ± 2
6	**Cisplatin**	5.7 ± 0.1 (2.3)	14 ± 2 (1.0)	13.01 ± 0.1
7	**Carboplatin**	>100 (n.d.)	70.8 ± 0.9 (>1.4)	>100

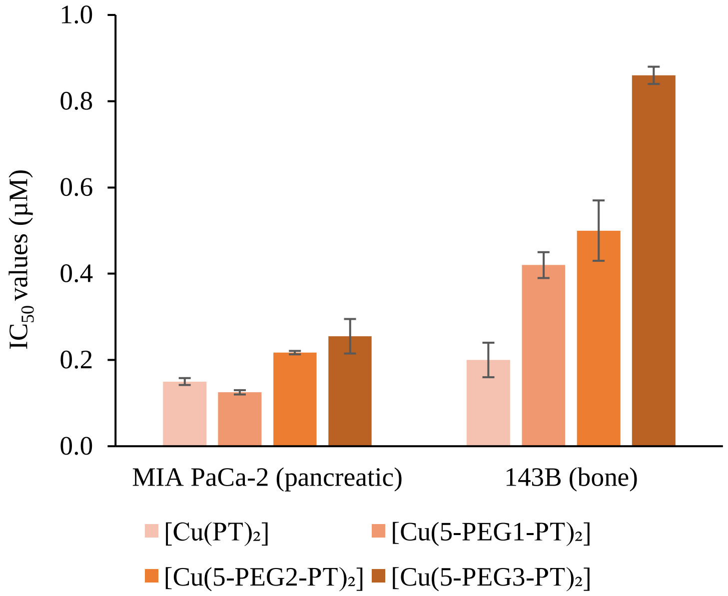

Figure 3.9: IC_{50} data for non-substituted and PEG-chain substituted copper pyrithione complexes against MIA PaCa-2 and 143B cell lines

3.3 Conclusion and Future Work

In summary, herein is presented the synthesis and characterisation of three novel water soluble pyrithione-based ionophores bearing PEG chain substitutions of varying chain length and their copper(II) complexes. Addition of the PEG chains vastly increase the aqueous solubility, compared to the parent $[Cu(PT)_2]$ complex. The longest PEG-chain complex showed >25000 fold increase in solubility, while even the shortest PEG chain length shows 200 fold improvement over the parent complex $[Cu(PT)_2]$. According to both UV/Vis and ICP-OES methods, lipophilicity decreased with increasing PEG-chain length, consistent with the introduction of polar substituents, although the change in the measured log *P* values was far less dramatic than the change in solubility. As would be predicted, aqueous solubility and lipophilicity were inversely proportional. The antimicrobial activity of the new complexes against a panel of bacteria was assessed. The new complexes showed high activity against *S. aureus*, in line with $[Cu(PT)_2]$, while the activity against Gram negative bacteria was far lower. In addition, the complexes were found to have an additive effect with carbapenem antibiotics against an NDM-resistant strain of *E. coli*. This finding supports the hypothesis that the activity of these copper complexes is, at least in part, due to inhibition of the NDM enzyme, potentially through Zn transmetallation, as shown in previous studies.

The novel copper complexes exhibited sub-micromolar potency towards pancreatic (MIA PaCa-2) and bone (143B) cancer cell lines, with $[Cu(5\text{-PEG-1-PT})_2]$ showing improved activity against MIA PaCa-2 compared to that by the parent complex. All copper(II) pyrithione complexes showed far greater anticancer activity than either cisplatin or the inactive $CuCl_2$. In both anticancer and antimicrobial assays, a trend is observed of lower activity with increasing length of PEG chain. As longer PEG-chain lead to a decrease in lipophilicity, we conclude that activity is correlated with cell uptake, which is directly associated with lipophilicity of the complexes. The most lipophilic complex is the parent $[Cu(PT)_2]$, however, this species has exceptionally low aqueous solubility making it challenging to process in biological assays. The shortest PEG chain complex $[Cu(5\text{-}PEG\text{-}1\text{-}PT)_2]$ retains activity, but with vastly increased aqueous solubility. In short, the novel complex, $[Cu(5\text{-}PEG\text{-}1\text{-}PT)_2]$, balances the increase in solubility with only a small decrease in lipophilicity, ultimately leading to an easily manipulated complex with exceptional activity in biological assays.

Considering future work, there are a few experiments that should be carried out to allow greater understanding of the complexes in hand. For instance, copper release studies in bacterial cells and ROS assays with carcinoma cells would be the next steps towards understanding the intracellular mechanisms of inhibition. We hypothesise that the variation in activity between the PEG complexes is linked to lipophilicity and cell uptake. This should be tested using cell uptake studies, for example, ICP-OES on cellular material after dosing with complex. The lipophilicity data collected here showed inconsistencies between the two methods used to calculate log P. These values could be verified by repetition and by improving the standardisation of the ICP-OES experiments.

The PEG chain complexes were found to inhibit the cell growth of normal healthy cells and therefore are non-selective as antibacterial or anticancer agents. In the longer term, improving this selectivity would be a key target for future study. For example, modification of the ligand with extra functional groups or a change in the PEG moiety could possibly lead to an increase in selectivity. Further insight into the mechanistic pathways of biological activities of these complexes would also aid in designing the modifications needed to improve their potential as drug molecules.

4. Fluorescent Copper Pyrithione Complex for Microscopy

4.1 Introduction

Fluorescence is a type of photoluminescence which can be described by the Jablonski diagram below (Figure 4.1).[265] Through absorption of light (photon) energy, a molecule is excited from its ground singlet state (S_0) to the higher energy singlet states (e.g., S_1, S_2). Next, a fast relaxation to the lowest lying excited state, S_1 occurs through non-radiative decays known as internal conversion. This process is then followed by radiative emission, namely fluorescence, through which the photon travels back to the ground state. Another type of non-radiative decay is known as the intersystem crossing, which takes place from S_1 to the first excited triplet state (T_1). This phenomenon is further followed by another luminescence process called phosphorescence.

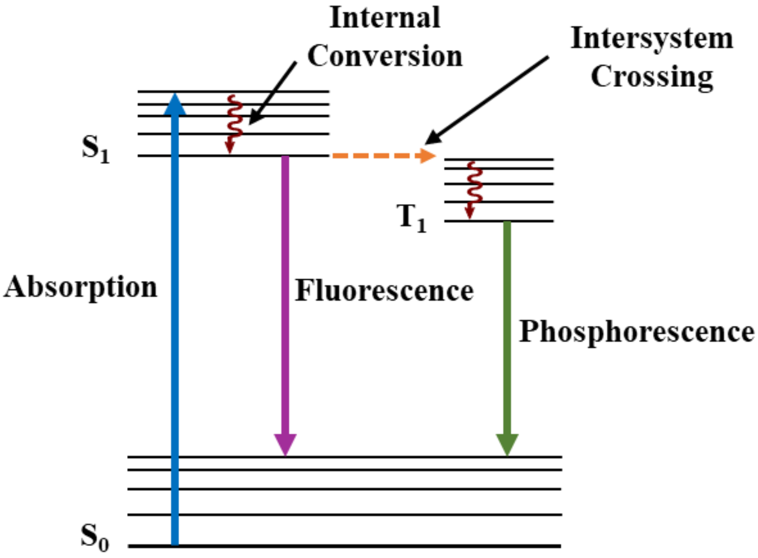

Figure 4.1: Jablonski diagram for absorption and fluorescence emission

The fluorescence quantum yield (ϕ) is defined as the ratio of the photons emitted as fluorescence to the photons absorbed. Fluorescence quantum yield describes the efficiency of a fluorophore molecule to convert absorbed light into fluorescence. The value of fluorescence quantum yield (ϕ) is usually less than 1.0 (≤100%), due to other non-radiative decay pathways, such as energy or electron transfer processes. These processes that reduce the quantum yield are termed fluorescence quenching. This quenching phenomenon is very important in designing emissive molecules. Other key properties of fluorescent molecules are the absorption wavelength, the emission wavelength and the lifetime of the emission.

4.1.1 Importance of Fluorescence in Studying Bioactivity

Fluorescence imaging using microscopy is a valuable research tool to detect the intracellular behaviour of a drug molecule. Fluorescent probes permit visualisation of the molecule of interest in specific locations with the cell, such as the nucleus, mitochondria, endoplasmic reticulum etc. Probing a molecule's localisation via fluorescence can help to understand the molecular mechanisms and mode of action of the drug molecules. For example, compounds that localise in the nucleus may be interacting with DNA, whereas those that localise in the cytoplasm are unlikely to be directly interacting with DNA. Designing fluorescent drug molecules or attaching fluorescent dyes to drug molecules is, therefore, an important area of biochemical research.

The copper pyrithione complexes, such as those described in this thesis, have not been studied for their cellular localisation and little is known about their mode of action. In this chapter, our focus was to design a fluorescent derivative of $[Cu(PT)_2]$ and carry out fluorescence microscopy studies to understand its localisation inside the cell.

4.1.2 'Click' Reaction as a Useful Tool in Biochemistry

K. B. Sharpless first introduced the term 'Click reaction' to indicate chemical reactions with high yield, wide scopes, regioselectivity and easy purifications. Since then, the pharmaceutical industry has utilised these types of reactions extensively in the design of new pharmaceuticals. One of the most utilised 'click' reactions is the azide-alkyne 1,3-dipolar cycloaddition reaction, in which a stable triazole moiety is formed. The conventional Huisgen 1,3-dipolar cycloaddition often fails to give high regioselectivity and has been replaced by a newer catalytic variation. The copper-catalysed cycloaddition shown in Figure 4.2 is the most commonly used 'click' reaction. Copper-catalyzed azide-alkyne cycloaddition (CuAAC) proceeds through coordination of Cu(I) to both alkyne and azide leading to the formation of an unusual six-membered metallocyclic intermediate, as shown in Figure 4.2. This intermediate further contracts to the five-membered triazole ring through demetallation followed by a protonolysis reaction. In this chapter, we use 'click' chemistry to introduce a fluorescent moiety onto the copper pyrithione complex.

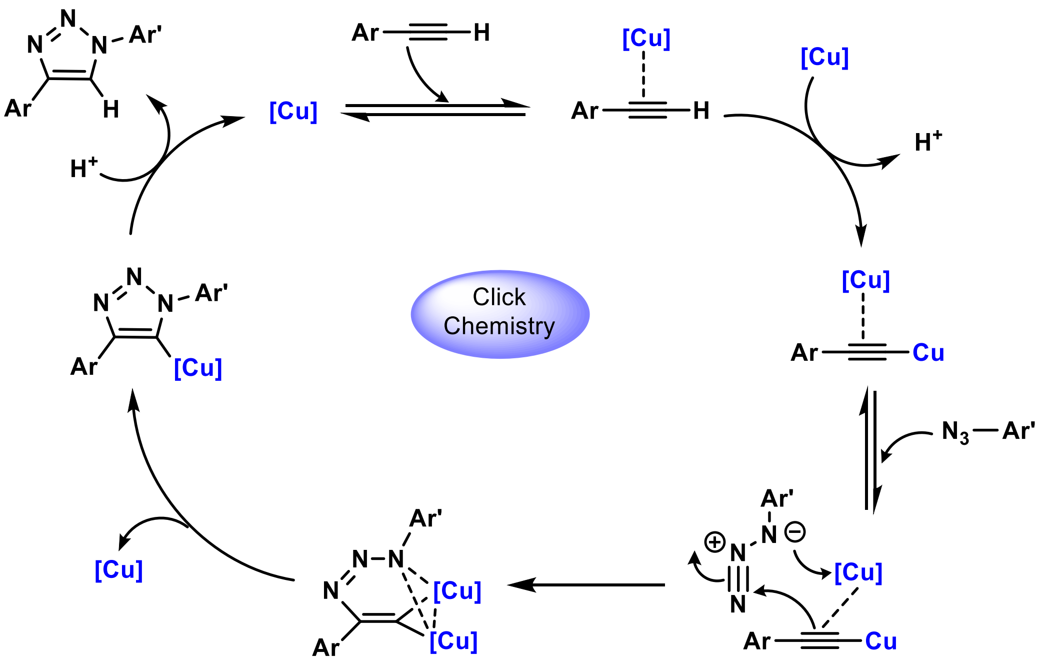

Figure 4.2: General mechanistic pathway of copper assisted 'click' reaction for aromatic systems

4.2 Results and Discussions

4.2.1 Synthesis and Characterisation of Fluorescent Moiety tagged Copper Pyrithione Complex

To utilise the CuAAC 'click' reaction, it was required first to develop a pyrithione derivative with either an alkyne or azide group to work as one of the 'click' reaction precursors.

4.2.1.1 Synthesis and Characterisation of Copper Pyrithione Derivative as 'Click' Reaction Precursors

Introduction of an alkyne functional group at the 5-position of PT followed the synthetic pathway shown in Figure 4.3. First, compound **3.1** was synthesised following the same procedure as described in Chapter 3 involving radical bromination with NBS. Next, propargyl alcohol was reacted with **3.1** using sodium hydride as a base resulting in the propargyl derivative of 2-bromopyridine (**4.1**), which was oxidised using *m*CPBA to give the *N*-oxide product **4.2**. Next, **4.2** went through our standard nucleophilic aromatic substitution (S_NAr) of bromine by sulfur to produce the propargyl derived PT ligand **4.3**. Each intermediate was characterised using NMR spectroscopy and ESI mass spectrometry data. Next, copper complexation gave the desired product **4.4** as a green solid. The copper complex was characterised using ASAP mass spectrometry and elemental analysis data.

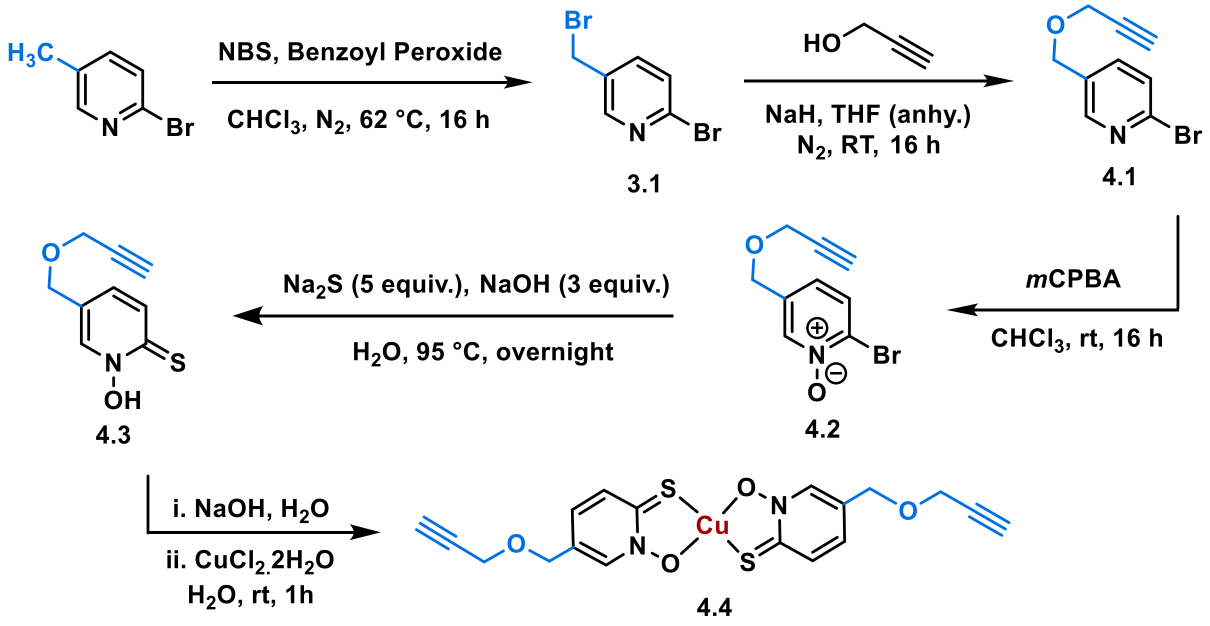

Figure 4.3: Synthetic pathway for O-alkyne derived PT and respective copper complex

Attempts were also made to synthesise the azide derived pyrithione precursor for the 'click' reaction, as shown in Figure 4.4. The previously synthesised compound **3.1** was subjected to a nucleophilic substitution reaction with sodium azide. This reaction resulted in 5-azidomethyl-2-bromopyridine (**4.5**), which underwent *N*-oxidation using *m*CPBA to form the *N*-oxide product **4.6**, whose formation was confirmed using ESI mass spectrometry on the crude compound. However, the ^{1}H NMR data of the crude compound **4.6** suggested formation of several impurities, along with excess *m*CPBA (and its corresponding carboxylic acid) and unreacted starting compound **4.5**. Several attempts were made to purify **4.6** using silica gel chromatography with various eluent systems, but the compound seemed to be unstable on the silica gel. Moreover, the by-product *m*-chloro-benzoic acid has a very similar polarity to that of **4.6**, making chromatographic purification challenging. Longer reaction times and use of fewer equivalents of *m*CPBA didn't improve the reaction outcome, therefore, the impure product **4.6** was taken forward to the sulfur substitution step. However, the substitution reaction didn't show formation of the desired product.

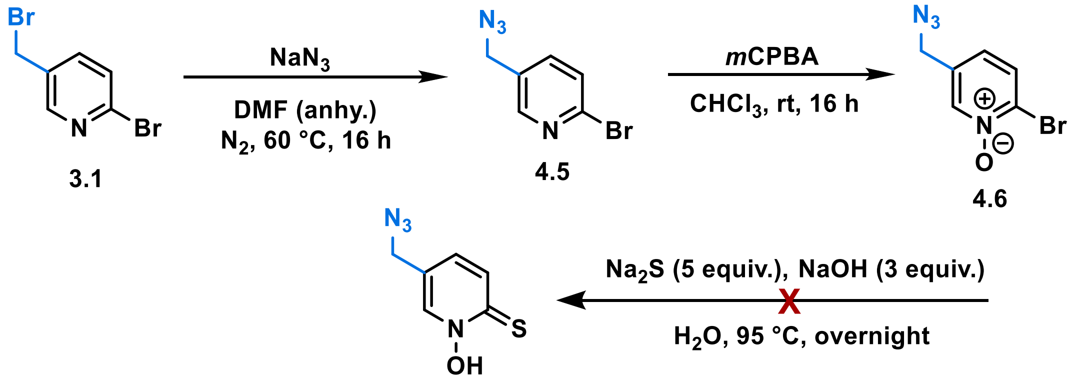

Figure 4.4: Synthetic pathway for azide derived PT ligand

Although the azide pyrithione was not synthesised, the successfully formed alkyne-derived copper pyrithione complex was taken forward as the precursor for a ‘click’ reaction with an azide-functionalised fluorescent tag.

4.2.1.2 Introduction of Fluorescent Bodipy-Azide Derivative through ‘Click’ reaction

First, a mimic ‘click’ reaction was performed using a non-fluorescent aryl azide to check the reactivity of the alkyne source (complex **4.4**). A 0.5 M solution of benzyl azide in CH_2Cl_2 was reacted with **4.4** (0.5 equivalence of the azide) in the presence of catalytic copper sulfate and (+)-sodium-L-ascorbate as the activator in THF:H_2O (1:1) as the solvent system at 55 °C (Figure 4.5). The reaction was monitored using ESI mass spectrometry. At several time points, a small aliquot of reaction mixture was quenched with a saturated aqueous solution of ammonium chloride, extracted in EtOAc and analysed by mass spectrometry. The mass data after three hours of reaction suggested formation of the desired product peak (*m/z* $[M+H]^+$ = 718) and consumption of the starting material **4.4**.

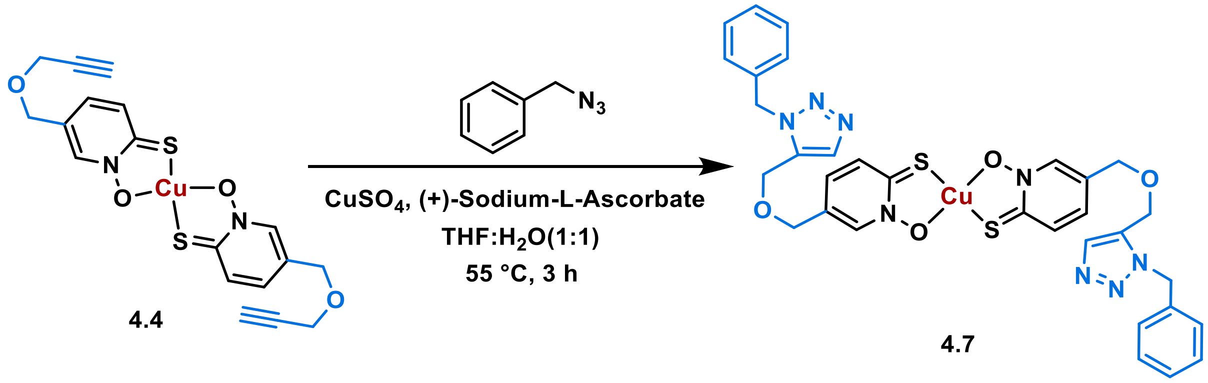

*Figure 4.5: ‘Click’ reaction of alkyl derivative of [Cu(PT)$_2$] (**4.4**) and benzyl azide*

With the successful test reaction in hand, we moved onto our main goal of attaching a fluorescent tag onto PT. The commercially available fluorescent molecule BDP-TR azide was used for the click reaction (Figure 4.6). This compound is an azide derivative of well-known fluorescent active borondipyrromethene (BDP, BODIPY) scaffold and emits red fluorescence with emission maxima at around 620 nm. This particular BDP-derivative has very high photostability and emissive brightness, which is helpful when considering biological microscopy applications.

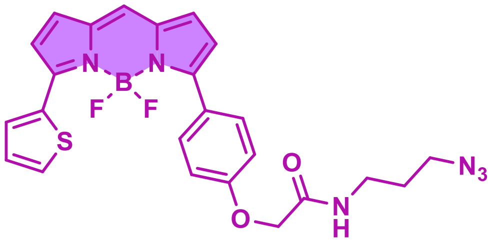

Figure 4.6: Structure of BDP-TR azide

The reaction procedure followed a similar pathway for that of the previous 'mimic' reaction with benzyl azide. In the very first attempt, BDP-TR azide and complex **4.4** (2 mg scale) were reacted in 2:1 ratio, in presence of catalytic copper sulfate and (+)-sodium-L-ascorbate as the activator in THF:H_2O (1:1). However, in this attempt, the reaction mixture was first stirred at room temperature for an hour followed by two hours at 40 °C and then at 55 °C for overnight. The reaction was monitored in a similar manner as previously, using ESI mass spectrometry. All mass spectra suggested no product formation, but both starting materials remaining unreacted. It was noticed that BDP-TR azide was not very soluble in THF, which could explain the low reactivity. In the case of the former 'mimic' reaction, the benzyl azide was purchased as a solution in CH_2Cl_2. BDP-TR azide has very good solubility in CH_2Cl_2 and it was therefore hypothesised that first dissolving the azide in CH_2Cl_2 may help the reaction. Hence, in a second attempt, the overall solvent system used was THF:H_2O:CH_2Cl_2 = 5:2.5:1 and the reaction mixture was stirred at 55 °C from the start, keeping all conditions identical to the 'mimic' reaction (Figure 4.7). Under these conditions, the mass spectra suggested formation of the desired product (**4.8**) (m/z $[M+H]^+$ = 1464.28 and m/z $[M+Na]^+$ = 1486.26) (Figure 4.8).

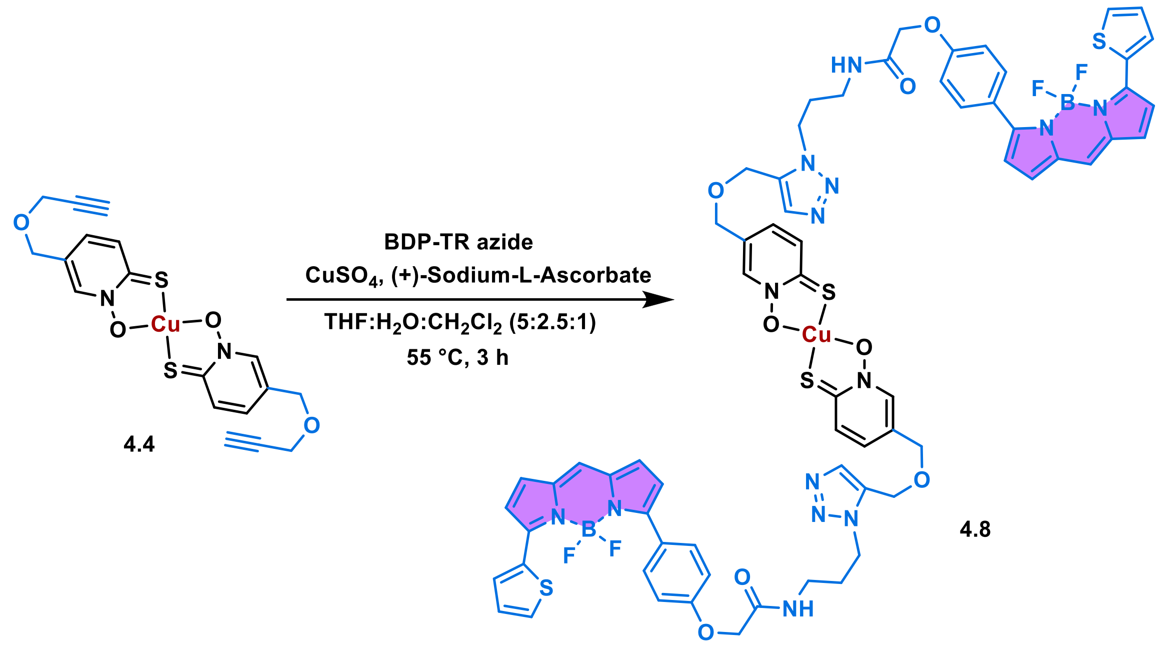

4.4

4.8

Figure 4.7: Synthetic procedure for introduction of fluorophore onto copper pyrithione scaffold

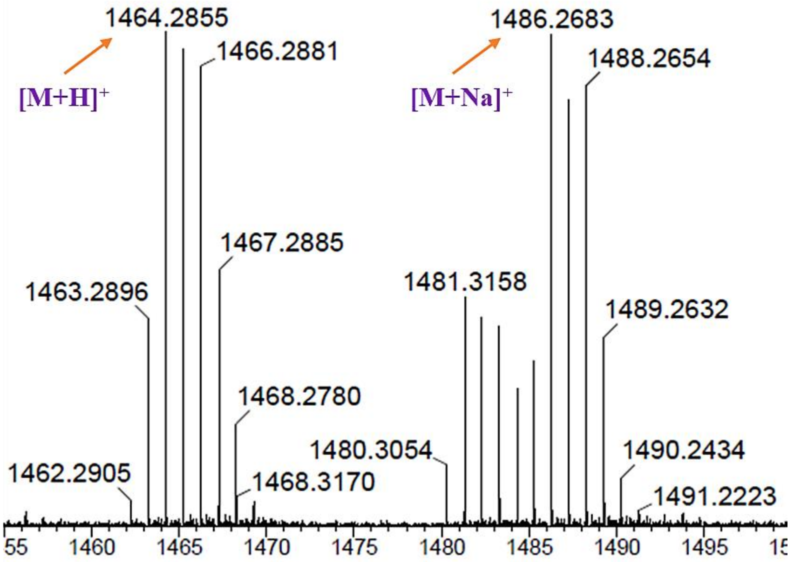

Figure 4.8: Mass spectrometry data for formation of complex ***4.8***

During reaction monitoring using liquid chromatography - mass spectrometry (LC-MS), a continuous change in the peak areas was observed for the starting materials, azide and alkyne, and the newly target molecule **4.8** (Figure 4.9). By calculating the ratio of product:starting material peak areas, it was determined that within three hours, formation of the product reached 80% (compared to azide) and 95% (compared to the alkyne). After 19 hours, no further changes in % product formation was observed (Figure 4.9 B). Hence, it was concluded that optimum time for this reaction should be 3-4 hours.

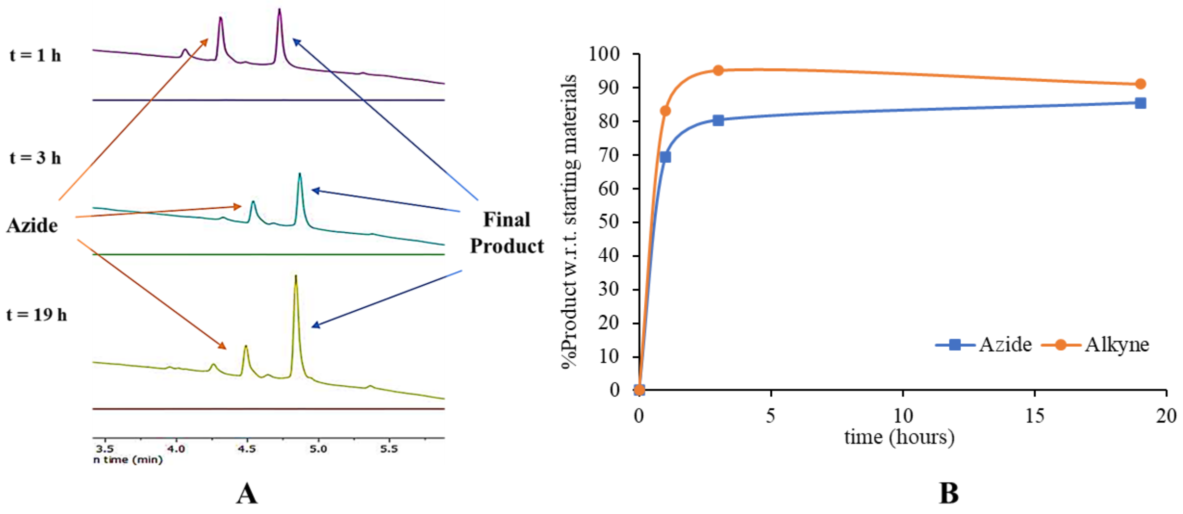

*Figure 4.9: (**A**) Change in LC-MS for formation of complex **4.8** with respect to BDP-TR azide and (**B**) plot of %product formation with respect to starting materials versus time*

The next hurdle was to achieve complex **4.8** in a purified form, as the reaction mixture contained unreacted starting materials. As the reaction scale was very small, this purification step was conducted through preparative HPLC, using acetonitrile:H_2O as the eluting solvent system. The purity of the complex was confirmed using high resolution LC-MS and analytical HPLC data (Figure 4.10).

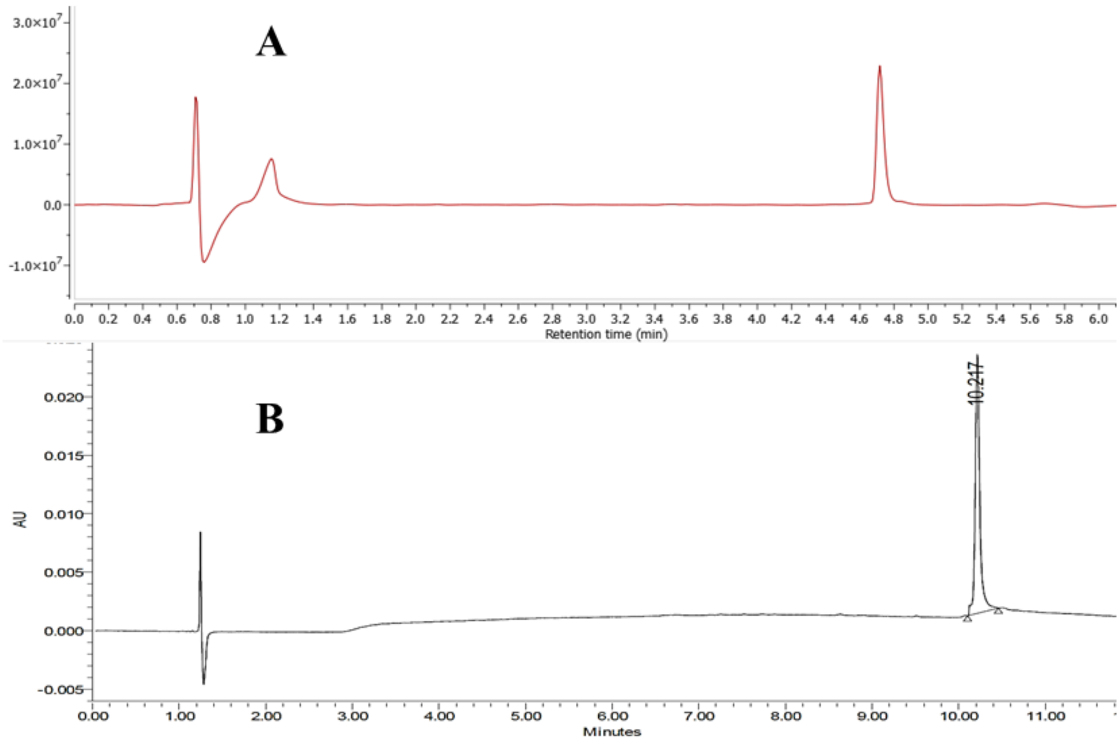

*Figure 4.10: (**A**) Total absorption peak in ESI-LCMS and (**B**) HPLC trace peak for pure complex **4.8** after prep-HPLC*

4.2.2 Photophysical Properties

During the synthesis of complex **4.8** it was noticed that there is a significant change in the colour of the fluorophore after the ‘click’ reaction. Unreacted BDP-TR azide in sunlight has a purple-pink colour, which changed after the reaction to a deep blue colour for complex **4.8**, as displayed in Figure 4.11.

*Figure 4.11: Visible colour change from BDP-TR azide to complex **4.8** in CH_2Cl_2 solvent*

To further characterise the photoluminescence properties, complex **4.8** was characterised by UV/Vis absorption and fluorescence spectroscopy. In this study, UV/Vis and fluorescence spectra for both BDP-TR azide and the newly synthesised copper pyrithione analogue (**4.8**) have been recorded to compare their luminescence properties.

BDP-TR azide and complex **4.8** shows absorption maxima at the same wavelength (MeCN solvent, λ_{max} = 587 nm) (Figure 4.12). However, their absorption spectra vary in the lower wavelength region. Figure 4.12 also depicts the difference in the molar absorptivity spectra of two starting materials, the azide (BDP-TR), alkyne (**4.4**) with the final product (**4.8**). Next, variation in the solvent was explored to understand any likely changes. Acetonitrile (polarity index = 5.8), dichloromethane (polarity index = 3.1) and toluene (polarity index = 2.4) were used for the luminescence studies. BODIPY derivatives are known to be generally unaffected by changes in solvent. Solvatochromism is defined as the effect of different solvents on ground and excited energy states and therefore change in the energy gap between them, which affects their absorption and emission properties. In case of compound **4.8**, a very small shift of absorption maxima towards lower wavelength was observed with increasing polarity of the solvents (Figure 4.13). This phenomenon is known as the negative solvatochromism where increasing polarity shows a hypsochromic (blue) shift of absorption spectra. A similarly small shift in the absorption maximum was observed for BDP-TR azide.

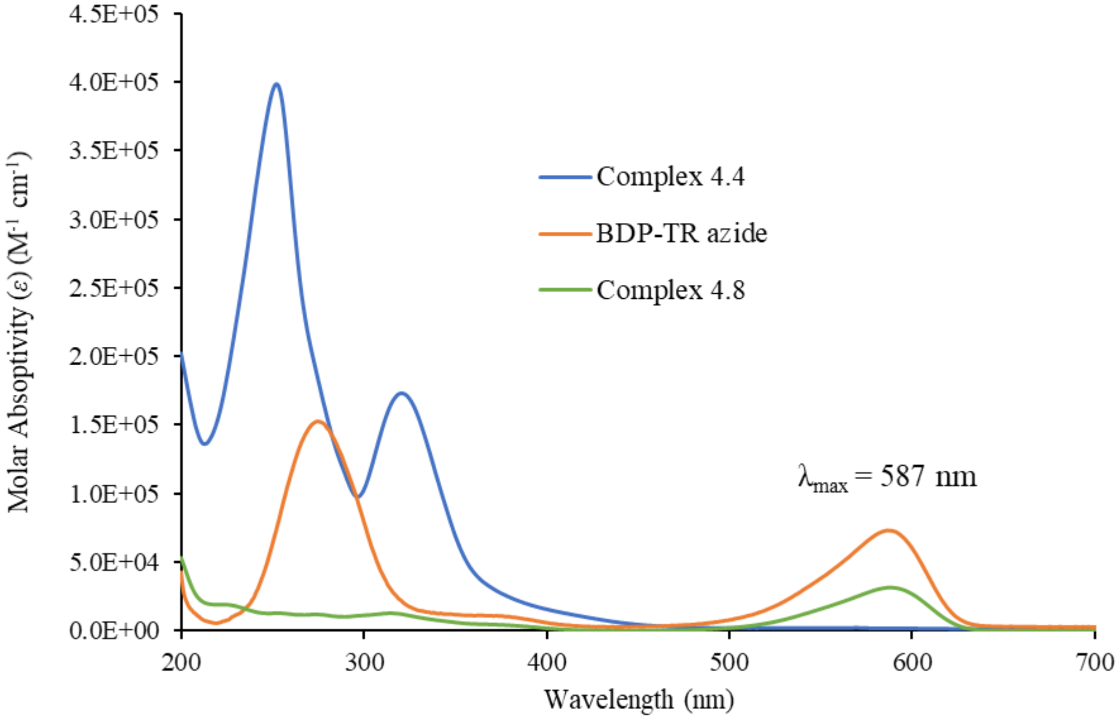

*Figure 4.12: The comparative plot of molar absorptivity (ε) vs wavelength spectra for complex **4.4**, BDP-TR azide and complex **4.8***

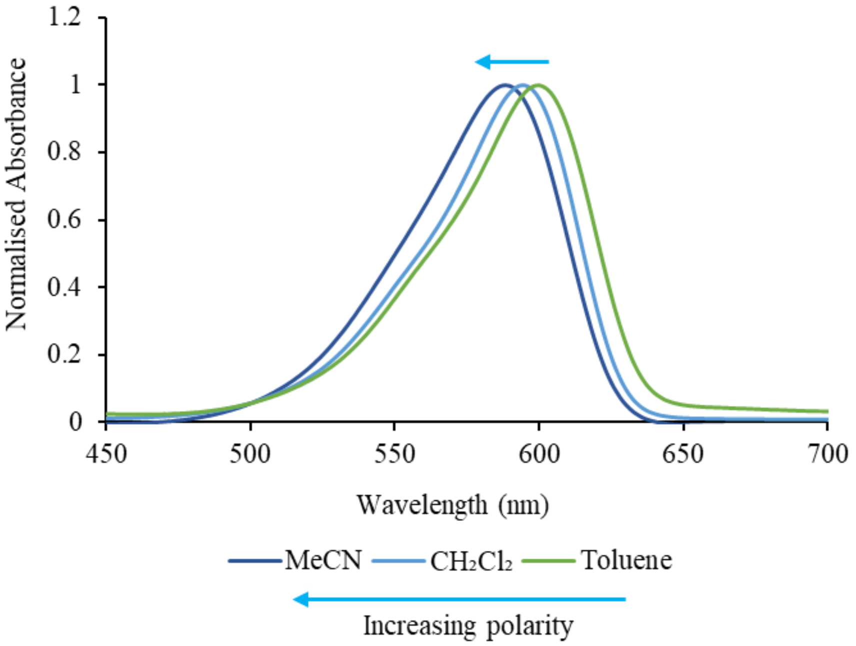

*Figure 4.13: Normalised absorption spectra of complex **4.8** at different solvents in ambient temperature*

Next, extinction coefficients (ε) for **4.8** and BDP-TR in the same three solvents were calculated through measurement of UV/Vis absorbance of solutions with increasing compound concentrations and plotting the absorbance maxima values at 587 nm against concentration (Figure 4.14). The calculated *ε* values (Table 4.1) are high and therefore suggest spin and Laporte allowed transitions. The extinction coefficients do not vary greatly between the three solvents (Table 4.1). However, *ε* values of complex **4.8** are somewhat lower (~2 fold) than that of BDP-TR azide. There is No clear rationale for this low number, however, remaining solvent from the HPLC purification may lead to inaccuracies in the mass measurement. In future, a scale up synthesis could be followed by elemental analysis to ensure no additional solvent is present.

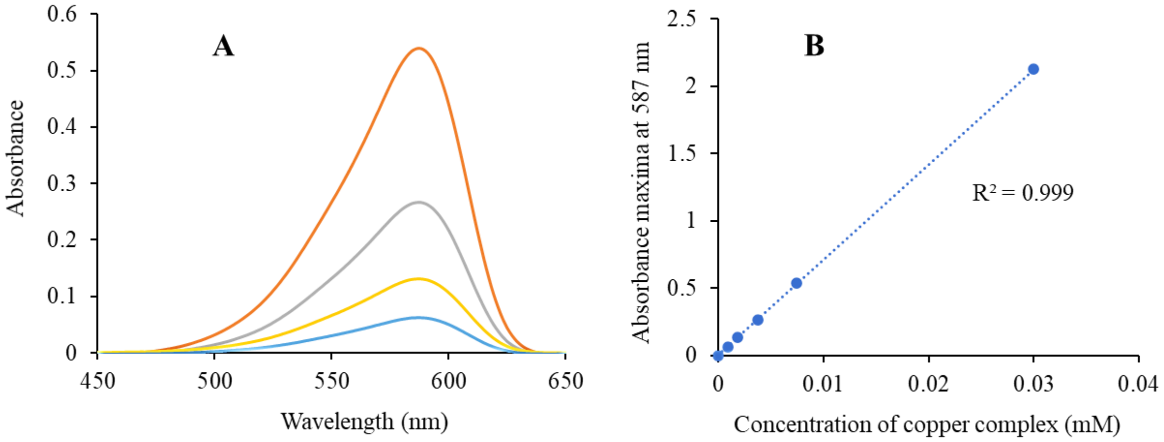

*Figure 4.14: (**A**) UV absorbance spectra and (**B**) corresponding concentration graph for calculating extinction coefficient of* the complex ***4.8** in MeCN solvent*

*Table 4.1: Extinction coefficient (ε) values of BDP-TR azide and complex **4.8** in different solvents*

Solvents	**ε ($M^{-1}cm^{-1}$)**	
	BDP-TR azide	**Complex 4.8**
MeCN	70900	38400
CH_2Cl_2	65900	35400
Toluene	78900	45000

Next, fluorescence intensity spectra of both compounds were recorded in these solvents. For all the solvents, absorption and emission spectra partially overlap and the Stokes' shift (the difference between absorption and emission maxima) is quite small. For complex **4.8**, in MeCN the Stokes' shift is calculated to be 32 nm and is similar to that of BDP-TR azide (Figure 4.15).

In CH_2Cl_2 and toluene solvents, the Stokes' shift is 26 nm, The absorption and emission maxima in these three solvents for **4.8** are listed in Table 4.2.

*Table 4.2: Absorption and emission maxima of complex **4.8** in different solvents*

Solvents	**λ_{max}(absorption) (nm)**	**λ_{max}(emission) (nm)**
MeCN	587	619
CH_2Cl_2	595	621
Toluene	599	625

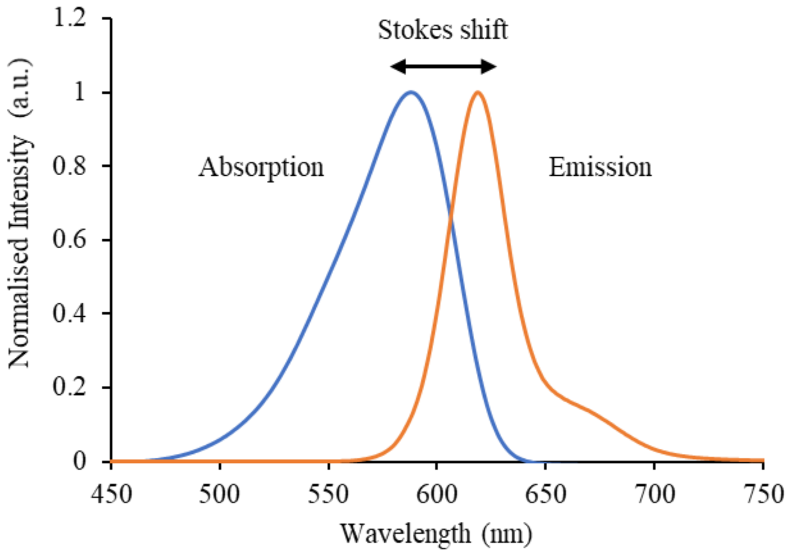

*Figure 4.15: Normalised absorption and emission spectra for complex **4.8** in MeCN solvent at ambient temperature*

The fluorescence spectra of **4.8** and BDP-TR were recorded in MeCN each at 3.7 x 10^{-6} M concentration (Figure 4.16). It can be observed that the fluorescent intensity has decreased significantly (~10 fold) for complex **4.8** with respect to that of BDP-TR azide. This decrease in emission must be attributed to some fluorescence quenching process(es), caused by the copper complex. Quenching is potentially due to an electron transfer process between the excited state fluorophore and the redox active Cu(II)/Cu(I). Alternatively, the quenching could be due to changes in the energy levels of the fluorophore due to the nearby copper coordination complex. A similar fluorescence emission quenching was observed in the other two solvents, adding further support to the quenching originating from the presence of the copper complex.

Measurement of the relative fluorescence quantum yield was carried out in MeCN and toluene solvents at ambient temperature using Rhodamine 101 as the quantum yield standard ($\phi_s = 1.0$ in MeOH solvent). The average relative quantum yield (ϕ_x) for complex **4.8** was determined to be in the range of 0.30 – 0.43. This quantum yield value is notably lower than that of BDP-TR azide ($\phi_x = 0.9$)[266], the molecule used as the main fluorescence source. Hence the quantum yield result also supports the emergence of fluorescence quenching process(es) due to presence of copper in this complex.

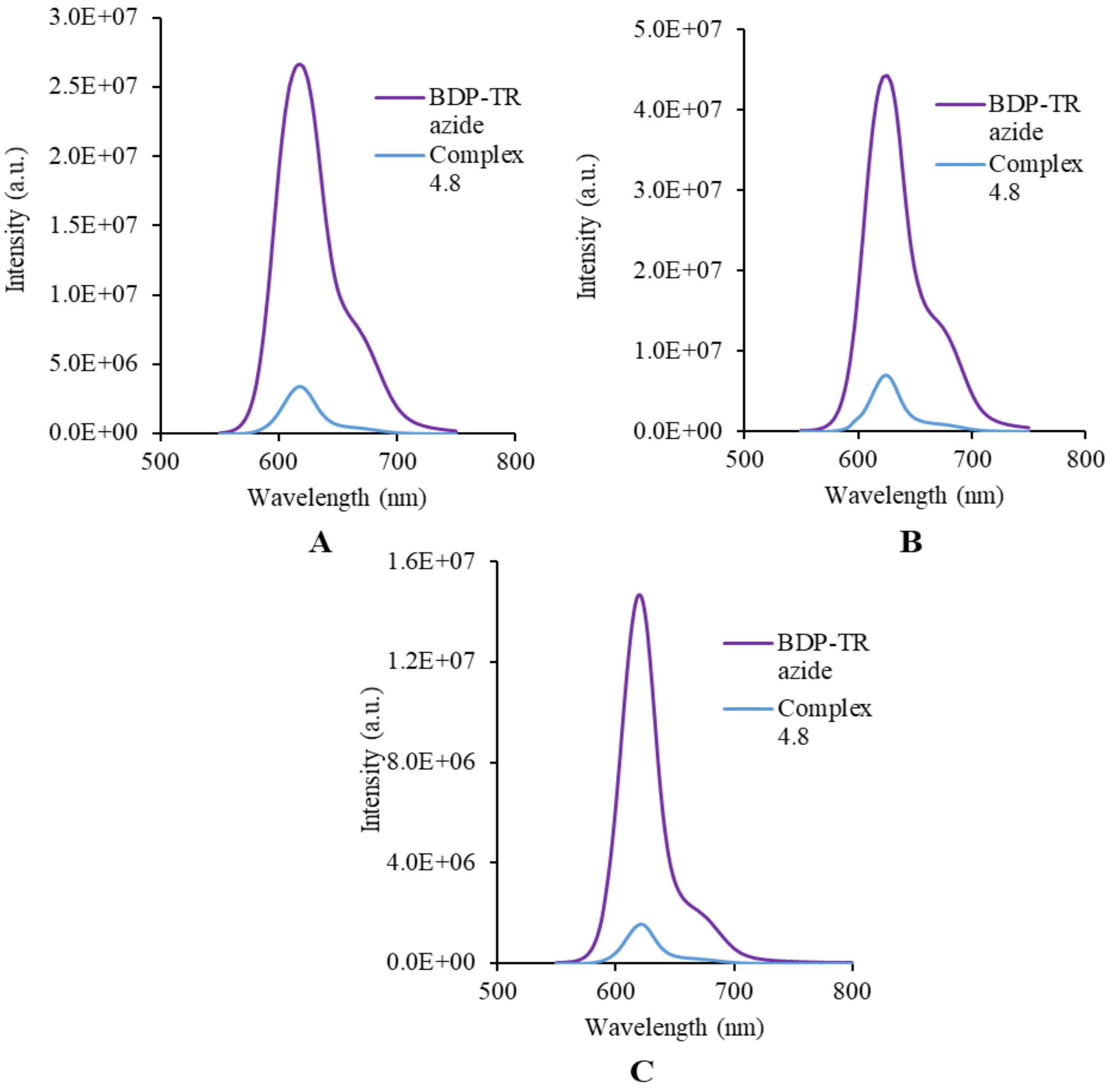

Figure 4.16: Fluorescence intensity spectra of BDP-TR azide and complex ***4.8*** *in (A) MeCN solvent (concentration = 3.7 x 10^{-6} M), (B) toluene solvent (concentration = 9.9 x 10^{-6} M), (A) CH_2Cl_2 solvent (concentration = 9.4 x 10^{-7} M) at ambient temperature*

Following the same trend as that of the absorption spectra, the fluorescence emission spectra of complex **4.8** also show a negative solvatochromism with a hypsochromic shift with increases in solvent polarity (Figure 4.17). This indicates that the excited states are more stable in less polar solvents.

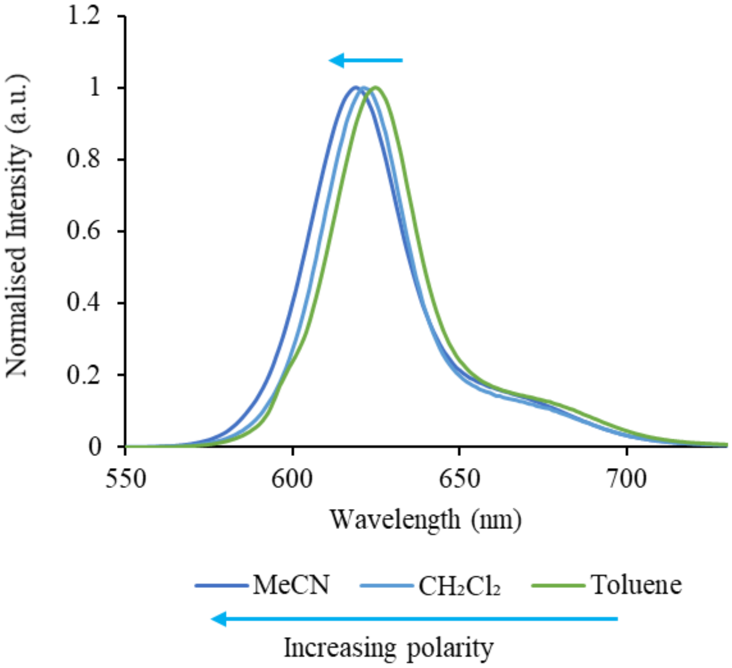

*Figure 4.17: Normalised fluorescence emission spectra of complex **4.8** at different solvents in ambient temperature*

4.2.3 Biological Activity

4.2.3.1 In vitro Antibacterial and Cytotoxicity Data

The alkyne derived copper pyrithione complex (**4.4**), along with parent [Cu(PT)$_2$], CuCl$_2$, and levofloxacin were screened against the ESKAPE panel of bacteria in collaboration with Dr. Sidharth Chopra, principal scientist, Central Drug Research Institute, Lucknow, India, following the same methods described in the previous chapters.

The antibacterial activity screening data show that the alkyne derived complex retains some of the bioactivity, similar to that of the parent complex [Cu(PT)$_2$]. Complex **4.4** has good antibacterial activity (MIC = 4.4 µM) against Gram-positive bacteria *S. aureus* and moderate activity (MIC = 35 µM) against Gram-negative *E. coli* species (Table 4.3).

Table 4.3: Antibacterial data for alkyne-derived copper pyrithione complexes against ESKAPE class of pathogen

Complex	MIC(μM)				
	E.coli ATCC 25922	*S.aureus* ATCC 29213	*K.pneumoniae* BAA 1705	*A.baumannii* BAA 1605	*P.aeruginosa* ATCC 27853
[Cu(PT)$_2$]	6.4	0.4	12.8	12.8	>100
4.4	35.4	4.4	>100	>100	>100
CuCl$_2$	>100	>100	>100	>100	>100
Levofloxacin	0.022	0.4	>100	22	2.8

The susceptibility of mammalians cells towards cell death by complex **4.4** was tested. This complex was found to have an inhibition rate of 94% against Vero cells at 10 μg/ml concentration, which is similar to that of the parent complex [Cu(PT)$_2$], but much higher than that of the doxorubicin reference (Table 4.4). Therefore, the selectivity index of this complex for bacterial cells over Vero cells was determined to be <10, indicating its high cytotoxicity.

Table 4.4: Cytotoxicity data for complex ***4.4*** *along with [Cu(PT)2] and doxorubicin as references*

Concentration (μg/ml)	Average % Inhibition		
	[Cu(PT)$_2$]	4.4	Doxorubicin
10	94.8 ± 0.4	94.4 ± 0.2	63.2 ± 1.2
5	94.5 ± 0.2	-	-
2.5	93.9 ± 0.3	-	-
1.25	93.5 ± 0.5	-	47.5 ± 2.3

4.2.3.2 Fluorescence Microscopy Study

With the fluorescent copper pyrithione compound **4.8** in hand, microscopy studies were carried out in an attempt to understand the localisation of this complex, which could add some insight into the mechanism of action. Live-cell fluorescence microscopy of copper pyrithione complex **4.8** using mouse skin fibroblast cells was performed by Tom Bradford, PhD student in the Dr. Robert Pal research group, Durham University.

Complex **4.8** was studied at 5 μM, 2.5 μM and 1 μM concentrations at 30 minutes and 2 hours incubation time using λ_{ex} = 543 nm and λ_{em} = 600-650 nm for the fluorescence microscopy.

Transmission images overlaid with the red fluorescence are shown in Figure 4.18, allowing visualisation of the cell compartments (nucleus, membrane etc.) and the localisation of the fluorescent compound. At 30 min incubation time and 5 µM complex concentration, it can be clearly seen that the complex enters the cells and retains its photoluminescence properties, showing red fluorescence (Figure 4.18 A). After 2 hours' incubation with 5 µM complex concentration, the toxicity of the complex leads to the cells undergoing complete apoptotic cell death, which can be observed as shrinking of the cell surface (Figure 4.18 B). Next, the concentration was lowered to 2.5 µM and, once again, overlay of the transmission and fluorescence images show the complex inside the living cells (Figure 4.18 C). After longer time of incubation (2 hours) at 2.5 µM, once again, apoptosis takes place, and the cells appear spherical with membrane shrinkage (Figure 4.18 D). Finally, 1 µM concentration of **4.8** was used to for the microscopy study. At this lower concentration, the cells remain alive, and fluorescence is visible at both 30 minutes (Figure 4.18 E) and 2 hours incubation time (Figure 4.18 F). Henceforth, 1 µM concentration and 2 hours incubation time were used as the standard conditions for all future studies with this complex.

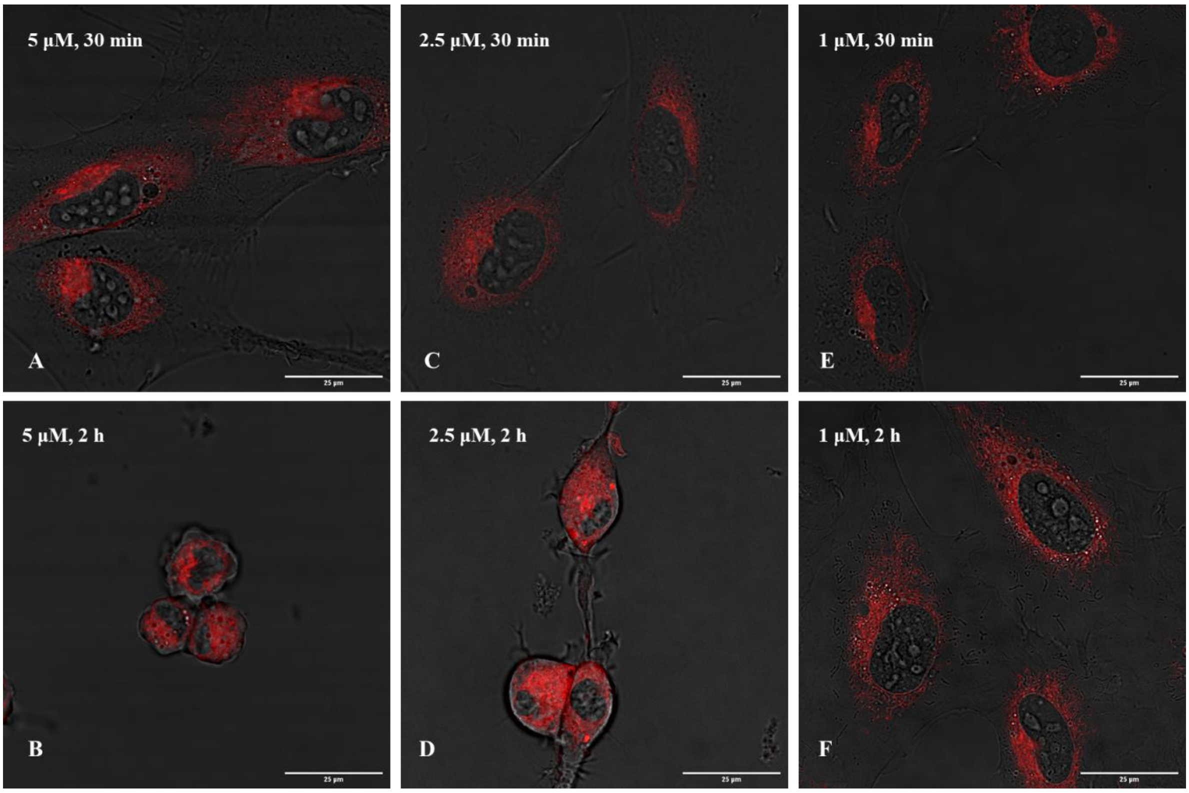

*Figure 4.18: Fluorescence microscopy transmission images (λ_{ex} = 543 nm, λ_{em} = 600-650 nm) of mouse skin fibroblast cells with varying concentrations of complex **4.8** for different incubation times*

Two photon excitation is an alternative technique allowing fluorescent compound to be excited by two photons (at half the energy of the usual one photo excitation). The benefit of this technique is that lower energy excitation reduces photobleaching and the longer wavelength excitation may also have better penetration through biological tissue for imaging in an organism. A two-photon excitation experiment was carried out with complex **4.8** (Figure 4.19). Using the concentration and incubation time determined above, the complex was illuminated inside the cells using two different types of excitations. In Figure 4.19, the red channel (A) shows an image of the complex **4.8** using single-photon excitation (λ_{ex} = 543 nm), with the complex localised inside the cell after crossing the cell membrane. The blue channel shows the same complex inside the cells using a two-photon excitation (λ_{ex} = 1080 nm) (Figure 4.19 B). In image Figure 4.19 C, the previous two fluorescence signals have been overlaid, which confirms the emission is coming from the same complex under each excitation mode. The ability to visualise the complex **4.8** under two photon excitation could have benefit if studies move towards animal models for these complexes, for the reasons explained above.

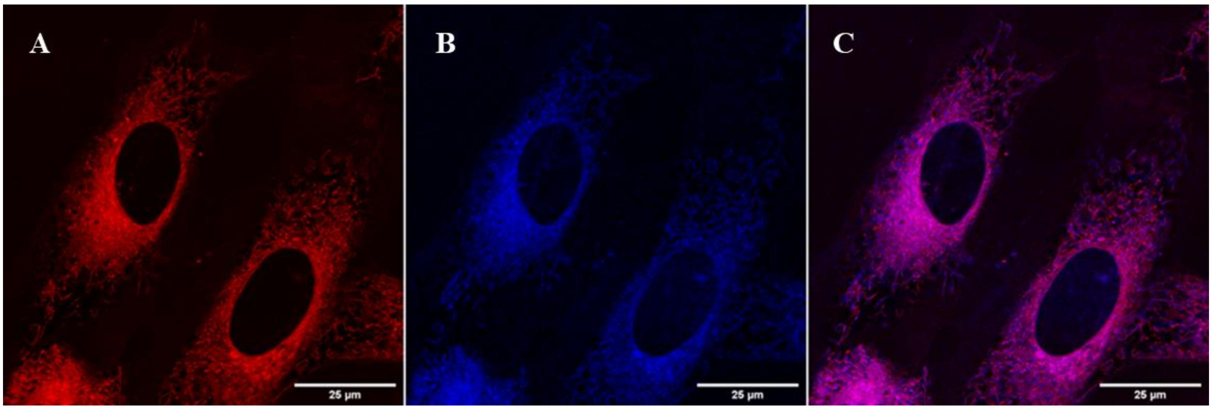

*Figure 4.19: Fluorescence microscopy images of complex **4.8** inside cell with (**A**) single photon excitation (λ_{ex} = 543 nm, λ_{em} = 600-650 nm), (**B**) two-photon excitation (λ_{ex} = 1080 nm, λ_{em} = 600-650 nm) and (**C**) overlap of both the signals*

Next, co-localisation studies were carried out to determine the specific location of this complex inside the cells. It was first anticipated that the compound could be going to the mitochondria. To confirm this localisation, the cells were excited with an additional laser line (λ_{ex} = 355 nm, λ_{em} = 380-550 nm), which excites mitochondria directly, leading to a green fluorescence signal. However, the fluorescent signals from complex **4.8** and mitochondria do not overlap with each other at either 30 minutes or 2 hours incubation times (Figure 4.20). This data rules out complex **4.8** localising in the mitochondria.

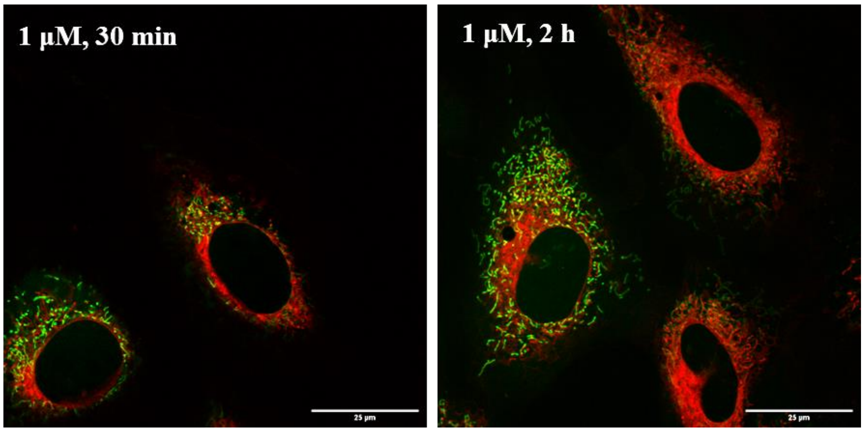

Figure 4.20: Overlaid images of fluorescent signals from 1 µM complex ***4.8*** *and cellular mitochondria for 30 minutes and 2 hours incubation times*

To provide further evidence that the complex doesn't localise at the mitochondria, a co-staining experiment was performed using Mitotracker Green™ (fluorescent stain specific for mitochondria). Fluorescence signal images of Mitotracker Green (λ_{ex} = 488 nm, λ_{em} = 500 -550 nm) were overlapped with the fluorescent signal of complex **4.8** after 30 minutes and 2 hours incubation times (Figure 4.21). The mismatch of signals in overlapped images confirms that this complex does not localise in the mitochondria (Figure 4.21).

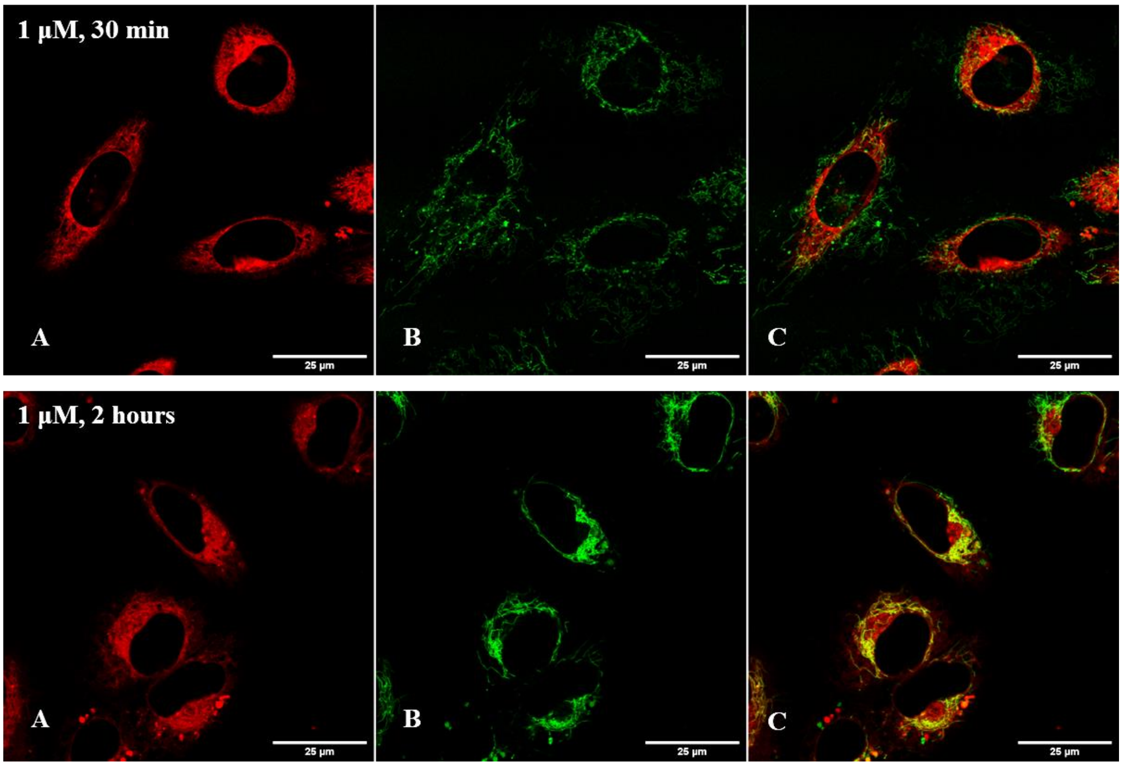

*Figure 4.21: (****A****) Fluorescent signals from 1 µM complex* ***4.8*** *for 30 minutes and 2 hours incubation, (****B****) fluorescent signals for cellular mitochondria using mitotracker green™ for 5 minutes and (****C****) overlapped images for both the signals*

Another co-staining was performed using a different fluorescent stain specific for the endoplasmic reticulum (ER), ER-tracker Green™. Emission from ER-tracker Green can be observed after 30 minutes using $\lambda_{ex} = 496$ nm, $\lambda_{em} = 510$ -550 nm (Figure 4.22B). The resulting signals were overlaid with the fluorescent signals obtained from 1 μM complex **4.8** after 2 hours incubation time (Figure 4.22C). The overlaid signals match almost perfectly, which leads to the conclusion that **4.8** is selectively localising at the ER in the cells (Figure 4.22).

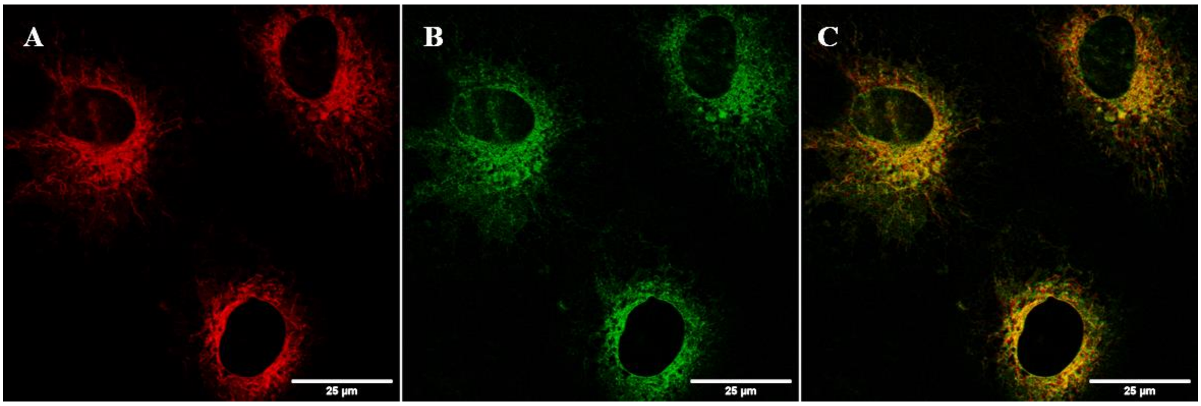

*Figure 4.22: (**A**) Fluorescent signals from 1 μM complex **4.8** after 2 hours incubation, (**B**) fluorescent signals for cellular ER using ER-tracker green™ for 30 minutes and (**C**) overlapped images for both the signals*

Finally, the fluorescence signals from 1 μM complex **4.8** after 2 hours incubation (A), ER tracker staining (B) and UV-activated mitochondrial auto-fluorescence (C) were overlaid to create the image in Figure 4.23 D. The image clearly shows that the fluorescence signals from complex **4.8** overlapped nicely with that for the ER tracker, but not with the mitochondrial signals. This gives further confirmation of this complex specifically localising at the ER and not to mitochondria inside the cells.

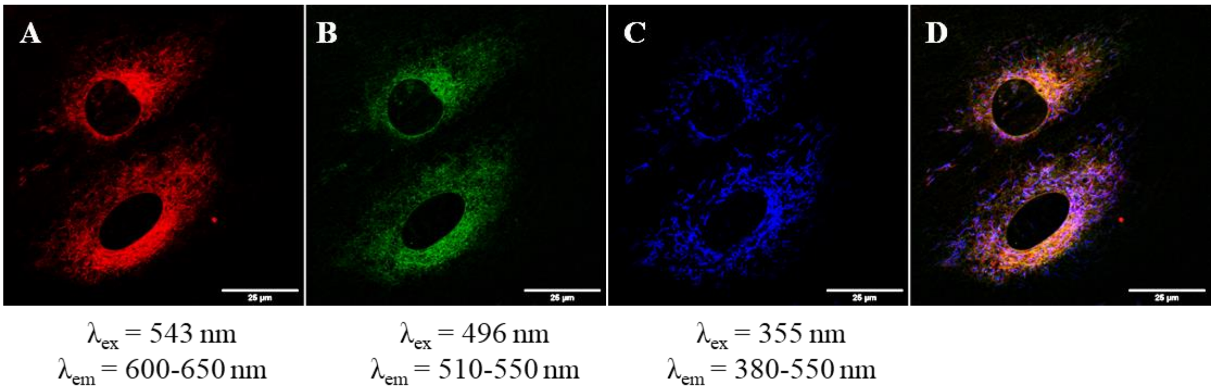

$\lambda_{ex} = 543$ nm
$\lambda_{em} = 600\text{-}650$ nm

$\lambda_{ex} = 496$ nm
$\lambda_{em} = 510\text{-}550$ nm

$\lambda_{ex} = 355$ nm
$\lambda_{em} = 380\text{-}550$ nm

*Figure 4.23: (**A**) Fluorescent signals from 1 μM complex **4.8** after 2 hours incubation, (**B**) fluorescent signals for ER using ER-tracker green™ for 30 minutes, (**C**) auto-fluorescence signals form UV-activation of mitochondria and (**D**) overlaid images for all the signals*

4.3 Conclusion and Future work

In summary, the synthesis and characterisation of a fluorescent copper pyrithione complex (**4.8**) have been presented in this chapter. To synthesise this copper pyrithione derivative, a copper-catalysed alkyne-azide ‘click reaction’ was utilised. The alkyne fragment was developed by introducing an O-alkyne substitution in the 5 position of pyrithione and using this ligand for further copper complexation. An azide derivative of well-known fluorophore, BODIPY, was used as the azide source and provides the fluorescent tag for microscopy studies.

The UV-absorbance and fluorescence spectroscopy data suggest that BDP-TR azide and the newly synthesised complex **4.8** have similar photoluminescence properties in terms of the Stokes’ shifts, absorption maxima and emission maxima wavelengths. They both also show similar solvatochromism (negative), where with increasing polarity of the solvents both the absorption and emission maxima show a hypsochromic shift. However, complex **4.8** shows a change in visible colour (from purple for BDP-TR azide to blue) and a significant reduction (~10 fold) of fluorescent intensity, which can be attributed to some quenching process of BDP-TR fluorophore by the presence of the copper pyrithione derivative.

In microscopy studies, the transmission images from live cell experiments show that complex **4.8** enters cells and can be visualised at 30 min and 2 h. At higher concentrations (5 µM) there is significant toxicity after 2 h, but lower concentration (1 µM) allow visualisation for 2 h with the cells staying viable. Furthermore, it was observed that this complex localises specifically to the endoplasmic reticulum and not the mitochondria inside the mouse skin cells, as confirmed by co-localisation studies.

In future, the other photoluminescent properties, such as the fluorescence lifetime of this complex should be determined, which could help to better understand the quenching mechanism. Moreover, further development of fluorescent active copper pyrithione derivatives can be carried out using different methods. In this process, a variety of fluorescent-active azide molecules (such as fluorescein azide) can be screened. Alternative methods to the ‘click reaction’ can also be developed as an alternative pathway towards introducing a fluorescent active substitution onto copper pyrithione. To allow longer incubation times without toxicity, it could be considered to use different metals (such as Zn instead of Cu) to reduce the cytotoxicity of these molecules but retain a similar structure and potentially the same localisation.

Finally, the ability to carry out alkyne-azide click reactions with the alkyne complex **4.4** means that we can conjugate alternative groups to the copper pyrithione complex. For example, groups that localised specifically to alternative organelles (e.g., mitochondria) could be added to see whether toxicity is related to localisation. In addition, groups that increase cell uptake or allow selective uptake to, for example, cancer cells could be conjugated to improve the future application of these complexes. With the alkyne handle in place, there are lots of future potential for this complex.

5. Pyridine based Copper Ionophores

5.1 Introduction

N-heterocycles and especially pyridine-derived compounds are at the forefront of research advances in the therapeutical field. The pyridine scaffold is present in the composition of many natural products and pyridine-based compounds have been studied extensively for their biocompatibility.[267] Moreover, the pyridine motif can improve pharmacological properties, such as permeability, metabolic stability and the protein binding ability of potential drug molecules. Around 14% of FDA approved drugs contain pyridine units. For example, enpiroline for malaria, piroxicam for arthritis, isoniazid for tuberculosis, omeprazole for ulcers and numerous other pyridine-based drugs are commercially available for treatment of various diseases (Figure 5.1).[268]

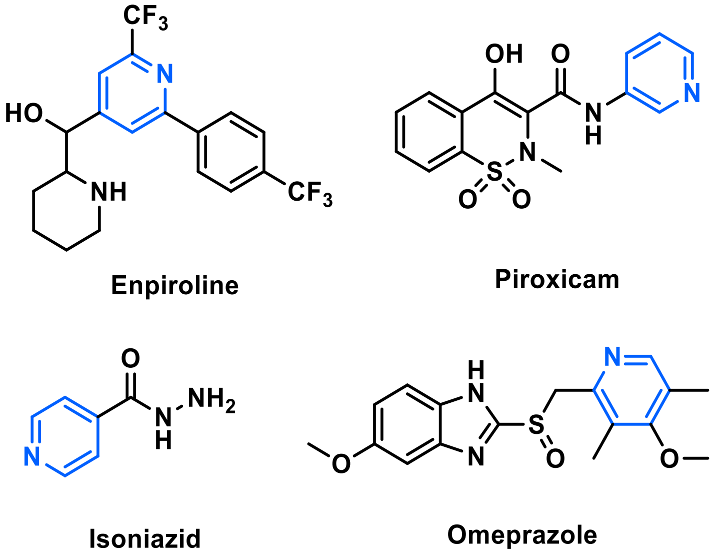
Enpiroline
Piroxicam
Isoniazid
Omeprazole

Figure 5.1: Some commercially available pyridine-based drugs

Furthermore, pyridine-derived ligands are good coordinating agents that readily form metal complexes with Pd, Pt, Ru, Ag, Au, Cu etc. through coordination of the N lone pair. These metal complexes have been studied as potential bioactive agents and some have also entered clinical trials. For example, a palladium pyridine complex (Figure 5.2 A) has great potential as an anticancer agent against colon carcinoma and melanoma cell lines.[269] Picoplatin is an excellent example of platinum pyridine drugs which is currently in use for treatment of solid tumours (Figure 5.2 B).[270] Another example is a cationic copper complex with pyridine derived ligands (Figure 5.2 C), which possesses very good potency as an antibacterial agent against various Gram negative and Gram positive bacterial strains (*E. coli*, *X. campestris* and *S. aureus*, *B. cereus*, *B. subtilis*).[271]

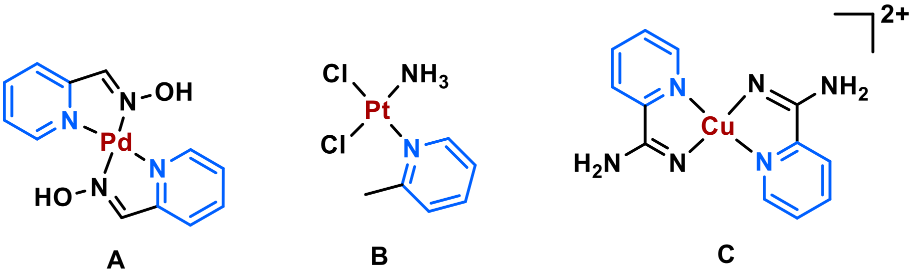

Figure 5.2: Metal complexes of pyridine derivatives as bioactive agents

Herein, we wanted to look beyond pyrithione as a ligand and selected some well-known (and some less well-known) pyridine derived ligands and aimed to synthesise their copper complexes in order to explore the potential of these complexes as bioactive agents.

5.2 Results and Discussions

5.2.1 Synthesis and Characterisation of Pyridine based Copper Complexes

Oxygen analogue of pyrithione

The oxygen analogue of pyrithione ligand has previously been documented to form metal complexes with ruthenium, exhibiting great potential as anticancer agents.[234] We considered that the copper complex of this oxygen analogue could potentially bring in variation in the physical properties of the complex compared to pyrithione, leading to improved biological activities.

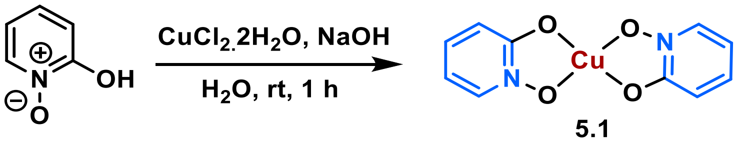

5.1

*Figure 5.3: Synthesis of [Copper(2-hydroxypyridine-N-oxide)$_2$] (**5.1**)*

To synthesise this complex, commercially available 2-hydroxypyridine-*N*-oxide was reacted with copper chloride dihydrate and sodium hydroxide to give the copper complex as a blue solid (Figure 5.3). Formation of this complex (**5.1**) was confirmed using mass spectrometry data (*m/z* $[M+H]^+$ = 283.986) and it was characterised from the crystallography data of single crystals grown from slow evaporation of a CH_2Cl_2: MeOH (1:2) solvent system. The structure confirms a 2:1 ratio of ligand:copper with the ligands arranged *trans* in a square planar geometry. The extended crystal packing structure reveals parallel arrangements of adjacent molecules where the copper atom of one molecule coordinates with oxygen atom from an adjacent molecule (intermolecular Cu-O bond distance = 2.594 Å) (Figure 5.4).

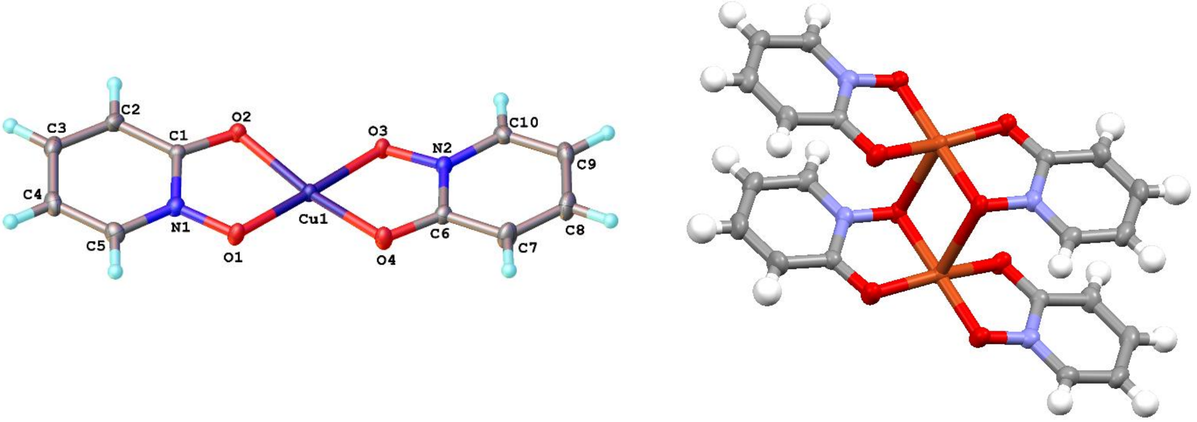

*Figure 5.4: Crystal packing structure of [Copper(2-hydroxypyridine-N-oxide)$_2$] (**5.1**)*

To understand any potential structure to activity relationship, attempts were made to synthesise a 6-methyl substituted 2-hydroxypyridine-*N*-oxide ligand. To synthesise the Me-substituted version, commercially available 2-hydroxy-6-methylpyridine was subjected to an oxidation reaction using *m*CPBA (Figure 5.5). Formation of the *N*-oxide product (**5.2**) was confirmed using ESI mass spectrometry. However, the ^{1}H NMR data suggested the presence of both unreacted starting material and *m*CPBA as impurities in the reaction mixture, along with the newly formed product. Purification through column chromatography was not successful due to the similar polarities of the product and impurities. The copper complexation step was performed using the crude mixture of **5.2** following the similar procedure as that for non-substituted one. However, the reaction failed to give the desired copper complex.

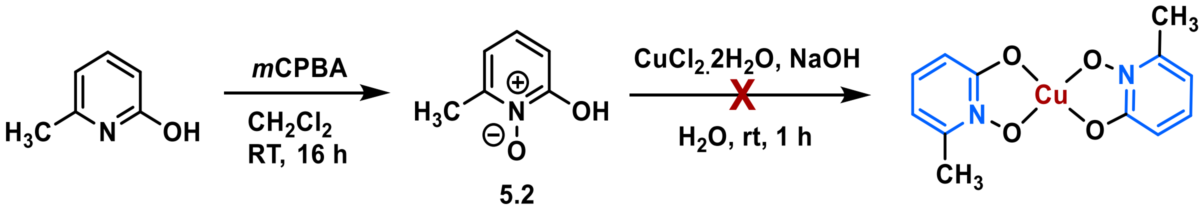

Figure 5.5: Synthetic route for methyl substituted [Copper(2-hydroxypyridine-N-oxide)$_2$]

Phenyl(2-pyridyl)phosphinate

Ruthenium and iridium complexes of pyridylphosphinate ligands have been observed to be potent against lung carcinoma cells[162] and pyridylphosphinate complexes of Eu and Tb have been shown to have interesting activity as luminescent cellular imaging agents.[272] Therefore, copper complexes of these ligands are considered worth assessing for any potential antibacterial bioactivity.

Synthesis of this pyridine substituted phenyl phosphinate ligand was carried out using an adapted literature procedure (Figure 5.6).[162] The first step involves a palladium-catalysed coupling reaction between commercially available 2-bromopyridine and ethyl phenylphosphinate. The product ethyl phenyl(2-pyridyl)phosphinate (**5.3**) was confirmed using mass spectrometry and NMR spectroscopy. Hydrolysis of this phosphinate compound using concentrated HCl at 100 °C, produced the corresponding aromatic phosphinate (**5.4**). Hydrolysis of the ethyl group from the starting material was confirmed by NMR spectroscopy and mass spectrometry data.

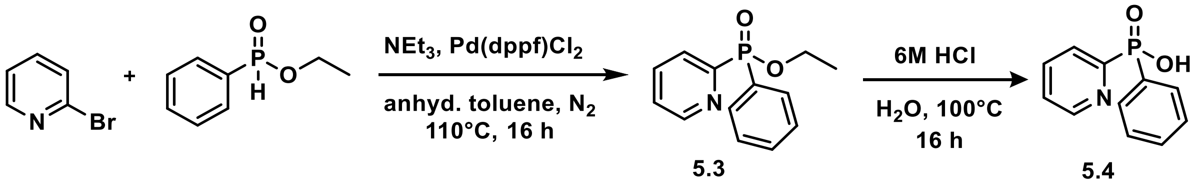

*Figure 5.6: Synthetic route for phenyl(2-pyridyl)phosphinate (**5.4**)*

The crude phosphinate ligand solution was neutralised using aqueous NaOH solution and $CuCl_2.2H_2O$ was added to attempt copper complexes. Complexation was attempted at pH = 2, 5 and 7 (Figure 5.7). In all cases, some pale blue solid precipitated. ESI mass spectrometry data of the blue solid and blue filtrate suggested formation of the expected 2:1 ligand:copper complex (**5.5**) (*m/z* $[M+H]^+$ = 500.254) (Figure 5.8). However, ASAP mass spectrometry data of the solid precipitates did not support formation of the desired metal-ligand complex. Elemental C, H, N analysis of the blue solid gave the expected ratio of C:H:N but the exact percentages were lower than expected for the desired complex. This inaccuracy is likely due to impurities in the solid, such as excess $CuCl_2$ or NaCl. No further purification was attempted on complex **5.5**.

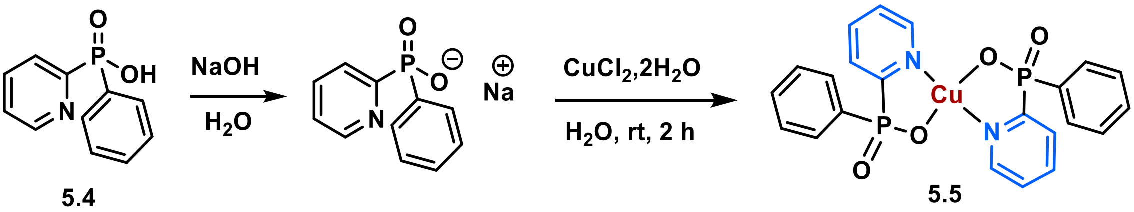

Figure 5.7: [Copper(phenyl(2-pyridyl)phosphate)₂] complex formation reaction

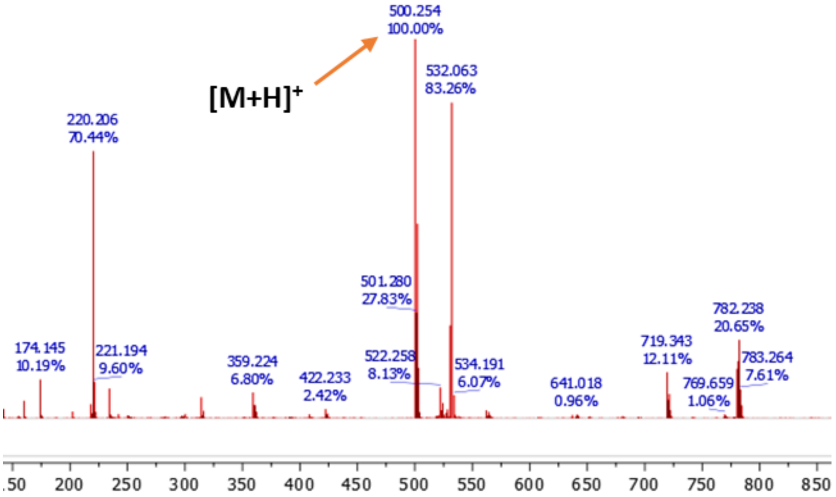

*Figure 5.8: ESI mass spectrum for Copper(phenyl(2-pyridyl)phosphate)$_2$ complex (**5.5**)*

Picolinic acid

Platinum and palladium complexes of picolinic acid have been studied for their activity against various cancer cell lines,[273] and, hence, it was anticipated that copper picolinate complexes could have some interesting bioactivity.

The synthesis of the copper picolinate complex involved reacting commercially available picolinic acid with $Cu(NO_3)_2.3H_2O$ in an alkaline solution (Figure 5.9). A violet solid formed and was collected through filtration. ASAP mass spectrometry data of the solid did not suggest formation of copper picolinate complex (**5.6**), but ESI mass spectrometry in MeOH solvent displayed the expected peak for the 2:1 ligand:metal complex (m/z $[M+H]^+$ = 308.042), along with a mass peak for the picolinate ligand (m/z $[M+H]^+$ = 124.051) (Figure 5.10). Elemental analysis data confirmed formation of the 2:1 ligand:metal complex.

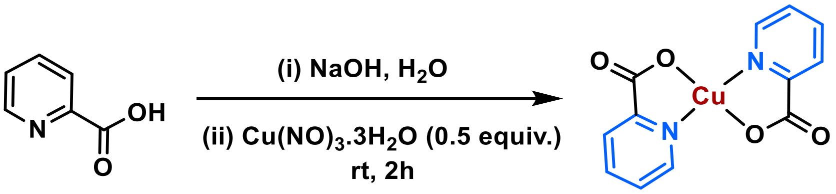

5.6 (56%)

*Figure 5.9: Synthesis of [copper(picolinate)$_2$] (**5.6**)*

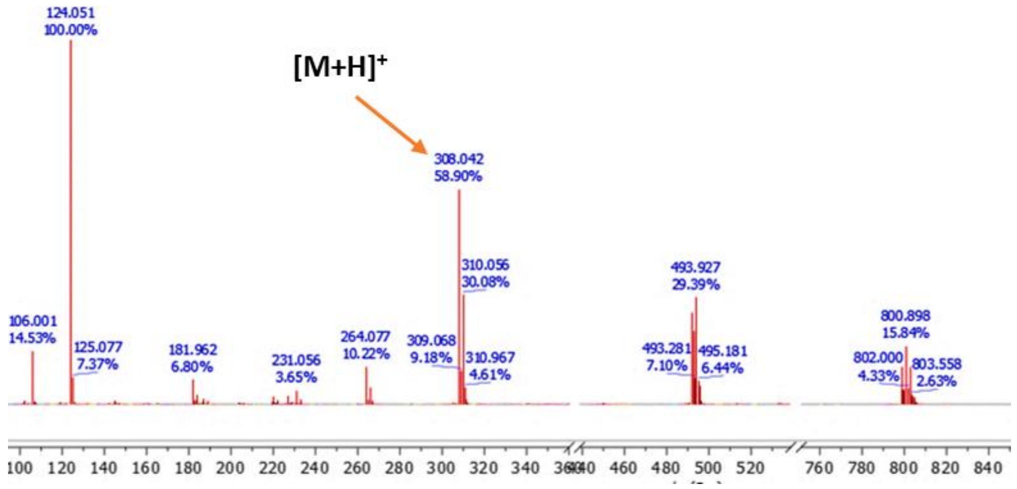

*Figure 5.10: ESI mass spectrum of [copper(picolinate)$_2$] (**5.6**)*

Bipyridine

Bipyridine ligands are used extensively throughout coordination chemistry and in bioinorganic chemistry, hence, we considered copper bipyridine as a sensible target compound. Commercially available 2,2'-bipyridine was reacted with copper chloride dihydrate in ethanol solvent to produce the corresponding 1:1 metal-ligand complex (**5.7**) as a green solid (Figure 5.11). Formation of the expected complex was supported by elemental (C, H, N) analysis data and X-ray crystallography data.

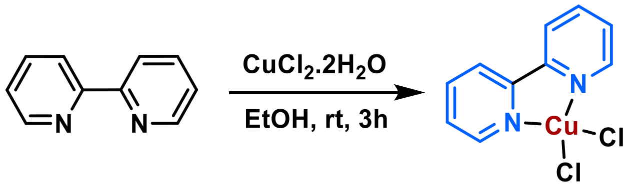

5.7 **(33%)**

*Figure 5.11: Synthetic pathway for formation of [copper(2,2'-bipyridine)]dichloride (**5.7**)*

Single crystals of this copper metal complex were grown *via* slow evaporation of an aqueous solution. The crystal structure reveals a square planar geometry around copper with intermolecular bonding between copper and the chloride ligand of parallel molecules (Figure 5.12). ASAP mass spectrometry data of the solid showed mass peaks for different fragments of the desired complex (*m/z* $[2M\text{-}Cl+2H]^+ = 544.957$ and $[M\text{-}2Cl+H]^+ = 220.037$) only, and not for the desired complex in whole (*m/z* $[M+H]^+ = 290.634$). ESI mass spectrometry showed an additional mass peak at 254.008 Da, which corresponds to the desired copper complex with loss of one chloride ligand $[M - Cl]^+$ (Figure 5.13).

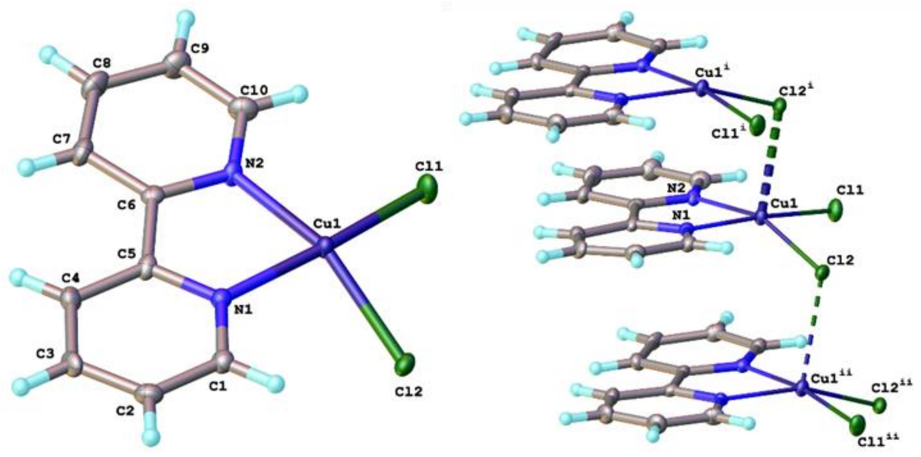

*Figure 5.12: Crystal structure of [copper(2,2′-bipyridine)dichloride] (**5.7**)*

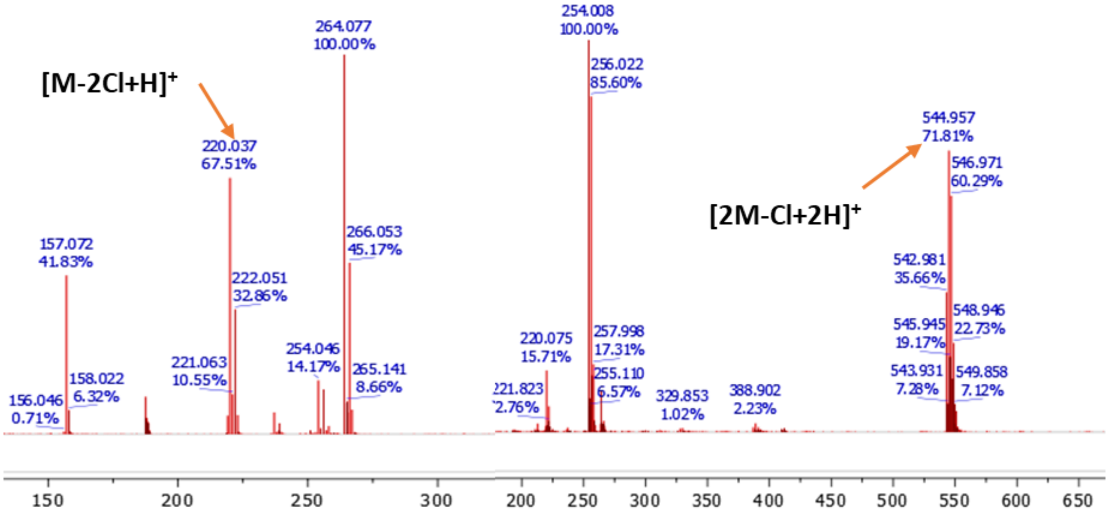

*Figure 5.13: ESI mass spectra of [copper(2,2′-bipyridine)]dichloride (**5.7**)*

N-Phenyl-1-(2-pyridinyl)methanimine and hydroxy-substituted analogue

The ligand *N*-phenyl-1-(2-pyridinyl)methanimine was used with several metal complexes to form active anticancer agents by McGowan, Lord *et al*.[274] Therefore, copper complexes of this ligand were considered for their potential bioactivity. An imine formation reaction from commercially available non-substituted and OH-substituted aniline and 2-formylpyridine produced the corresponding pyridinyl methanimine products (**5.8a-b**) (Figure 5.14). Formation of the desired ligands were confirmed using NMR spectroscopy and ESI mass spectrometry data. NMR spectroscopy of the crude reaction mixture for the non-substituted ligand suggested trace amount of starting material remaining, along with the desired product. Attempted purification through recrystallisation from hot EtOAc and hot MeOH was unsuccessful.

However, in the case of the OH-substituted ligand, the crude product was successfully recrystallised from hot MeOH to form the desired ligand as a yellow solid in high purity.

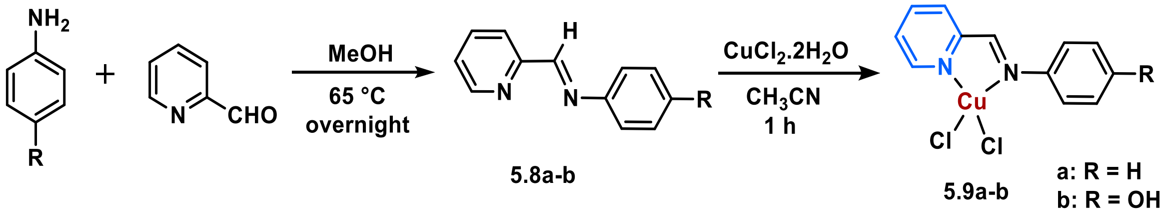

*Figure 5.14: Synthetic pathway for [Copper(II) (N-Phenyl-1-(2-pyridinyl)methanimine)dichloride] (**5.9a**) and its hydroxy-substituted form (**5.9b**)*

The non-substituted ligand (with small impurity) was reacted to $CuCl_2.2H_2O$ in acetonitrile at room temperature to produce the expected 1:1 ligand-metal dichloride complex (**5.9a**) as a green solid. The same procedure for the OH-substituted ligand required heating at 60 °C to produce the desired product as a red solid (**5.9b).** Both complexes were characterised using mass spectrometry and elemental analysis data. The elemental analysis data of both the complexes confirms the complex formation. However, ASAP mass spectrometry data did not support formation of copper complexes as no corresponding peaks (*m/z* $[M+H]^+$ = 314. 952 and *m/z* $[M+H]^+$ = 330.947 respectively) were observed. Instead, the presence of *m/z* peaks corresponding to ligands or singly chlorinated ligands (*m/z* $[M\text{-}CuCl]^+$ = 217.052 and 233.046 respectively) suggested either no occurrence of the metal complexation or fragmentation of the weak metal-ligand complex in the mass spectrometer (Figure 5.15).

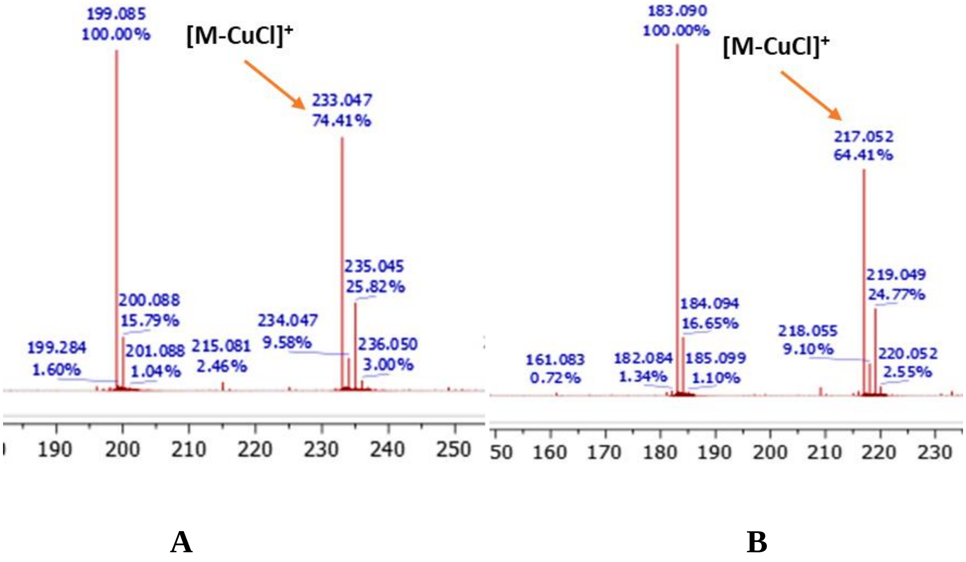

*Figure 5.15: ASAP mass spectrometry data for characterisation of (**A**) **5.9a** and (**B**) **5.9b***

Single crystals of the non-substituted complex (**5.9a**) were grown and analysed using X-ray diffraction. Two different single crystals were obtained following two different crystallisation techniques. In the first case, slow solvent evaporation from an equimolar solution of the bidentate ligand and $CuCl_2.2H_2O$ in H_2O produced green crystals. X-ray diffraction of these crystals suggested formation of the desired complex with one additional water molecule bound to the metal centre, giving a trigonal bipyramidal geometry about copper (Figure 5.16 A). The unit cell of this crystal also contained another water molecule in which the two hydrogen atoms serve as the hydrogen bond donors towards chloride ligands of the complex (Figure 5.16 B). A second technique for growing single crystals involved vapour diffusion of hexane in a solution of metal complex in CH_2Cl_2 solvent. Again, a 5-coordinate copper complexes was found, but in this case, chloride acts as a bridging ligand giving a dimeric copper complex, as shown in Figure 5.17 A. The unit cell crystal packing structure here also contains two solvent molecules, though neither was coordinated to the copper complex (Figure 5.17 B). the two different crystal structures show that solvent molecules play a major role in the crystallisation of these copper complexes.

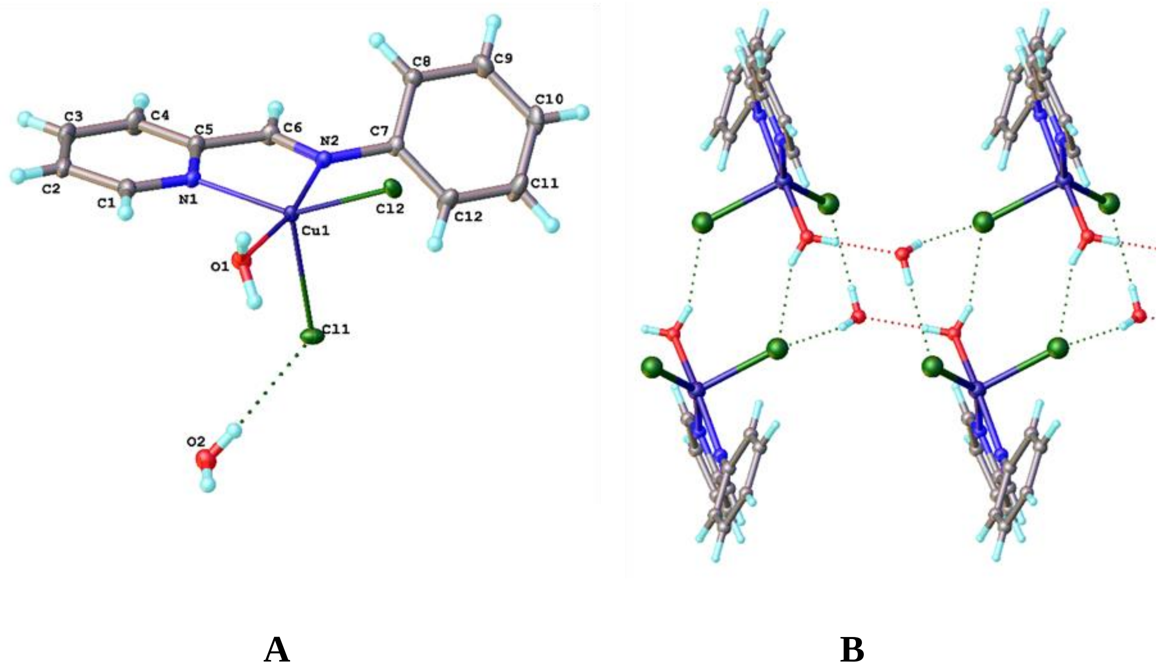

*Figure 5.16: **(A)** Crystal structure of [copper(II)(N-Phenyl-1-(2-pyridinyl)methanimine)dichloride] crystallised from water solvent and **(B)** hydrogen bonding in its crystal packing*

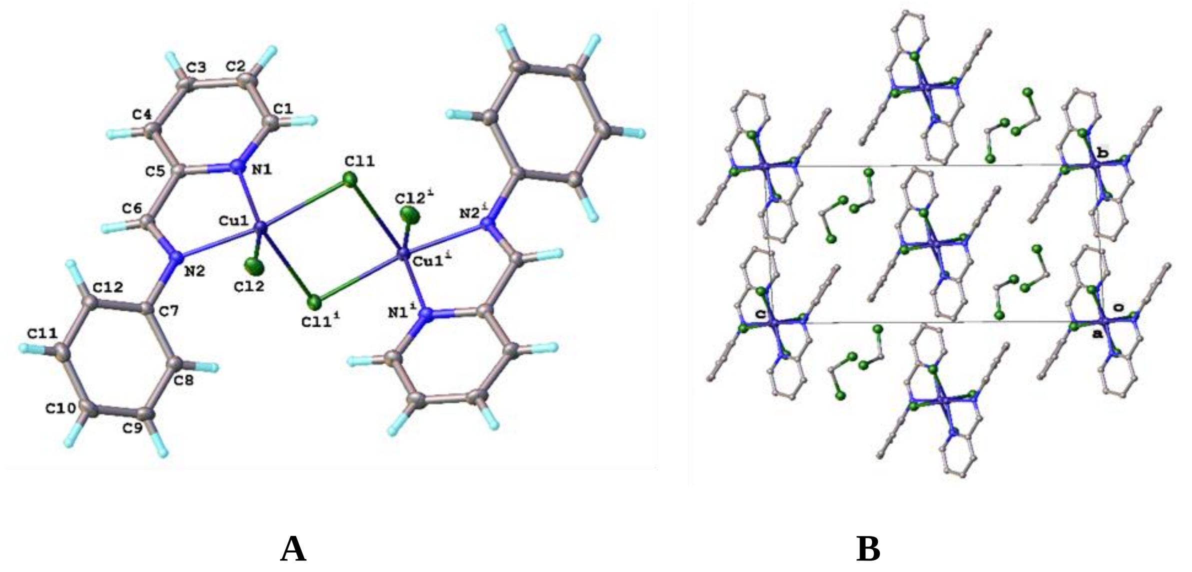

Figure 5.17: ***(A)*** *Crystal structure of [copper(II)(N-Phenyl-1-(2-pyridinyl)methanimine)dichloride] crystallised from* CH_2Cl_2 *solvent and* ***(B)*** *presence of solvent molecules in its unit cell crystal packing*

5.2.2 Biological Activity

5.2.2.1 In vitro Activity against ESKAPE Panel Organism

The above library of copper complexes, along with [Cu(PT)$_2$], CuCl$_2$, and levofloxacin were screened against the multidrug resistant ESKAPE panel organisms by our collaborator Dr. Sidharth Chopra, principal scientist, Central Drug Research Institute, Lucknow, India, following the same method mentioned in the previous chapters.

Table 5.1: Antibacterial data for copper complexes of pyridine derived ligands against ESKAPE panel pathogen

Complex	MIC(µg/ml)				
	E.coli **ATCC 25922**	***S.aureus*** **ATCC 29213**	***K.pneumoniae*** **BAA 1705**	***A.baumannii*** **BAA 1605**	***P.aeruginosa*** **ATCC 27853**
[Cu(PT)$_2$]	2	0.5	4	8	>64
5.1	64	64	64	64	64
5.5	>64	>64	>64	>64	>64
5.6	>64	>64	>64	>64	>64
5.7	>64	>64	>64	>64	>64
5.9a	>64	>64	>64	>64	>64
5.9b	>64	>64	>64	>64	>64
CuCl$_2$	>64	>64	>64	>64	>64
Levofloxacin	0.0156	0.25	64	8	1

The MIC value (µg/ml) data suggested that unlike [Cu(PT)$_2$], the copper complexes of other pyridine derived ligands from the above library are mostly inactive (no activity up to 64 µg/ml concentration) against the ESKAPE panel organism (Table 5.1). The only complex to show any activity was complex **5.1**, the oxygen analogue of pyrithione, which showed some activity at the highest tested concentration (64 µg/ml) against all the bacterial strains. Although the activity of this complex is broadly lower than that of levofloxacin and [Cu(PT)$_2$], there are some notable exceptions. For example, against *P. aeruginosa*, [Cu(PT)$_2$] does not show any activity, while this bacterial species is susceptible to growth inhibition by complex **5.1** at the 64 µg/ml concentration. Furthermore, **5.1** activity matches that of levofloxacin against *K. pneumoniae*. Overall, these results led us to pursue some additional bioactivity studies with complex **5.1**.

5.2.2.2 Antibiotic Synergy Study

Complex **5.1**, along with CuCl$_2$ and [Cu(PT)$_2$] were tested in synergy studies with known antibiotics against a β-lactam resistant strain of *E. coli* that produces the New Delhi metallo-β-lactamase 1 (NDM-1). The MIC values of the copper complex **5.1** alone is 100 µM. The MIC value of a known antibiotic, meropenem against this strain is 1 µM. This value does not change with addition of $CuCl_2$. However, when complex **5.1** is employed alongside meropenem there appeared some synergistic effect (Figure 5.18). The data shows **5.1** lowering the MIC value of meropenem to half the original MIC value at **5.1** concentrations 6.25 – 50 µM. At 100 µM **5.1**, the MIC value for meropenem drops significantly further. Though the synergistic activity is not as notable as that for $[Cu(PT)_2]$ (also shown in Figure 5.18), which lowers the MIC value >10 fold, **5.1** still exerts some good additive effects with FIC index = 0.56-1.03.

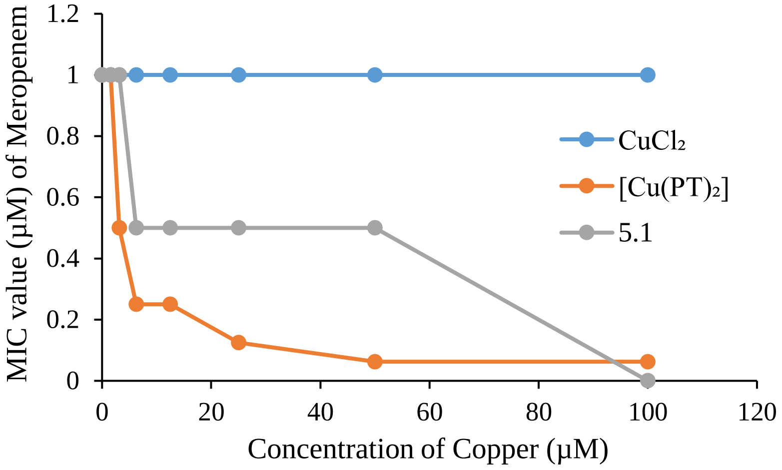

*Figure 5.18: Data of antibiotic synergy study for meropenem with $CuCl_2$, $[Cu(PT)_2]$ and complex **5.1***

Similar synergy studies were carried out with the antibiotic ertapenem. In contrast to the study with meropenem, **5.1** does not show any effect on the MIC value of the antibiotic up to 50 µM. Interestingly $[Cu(PT)_2]$ behave similarly in synergy studies with the two antibiotics ertapenem and meropenem (Figure 5.19). The fact that **5.1** shows a difference in activity between the two antibiotics could suggest a different mode of action compared to $[Cu(PT)_2]$.

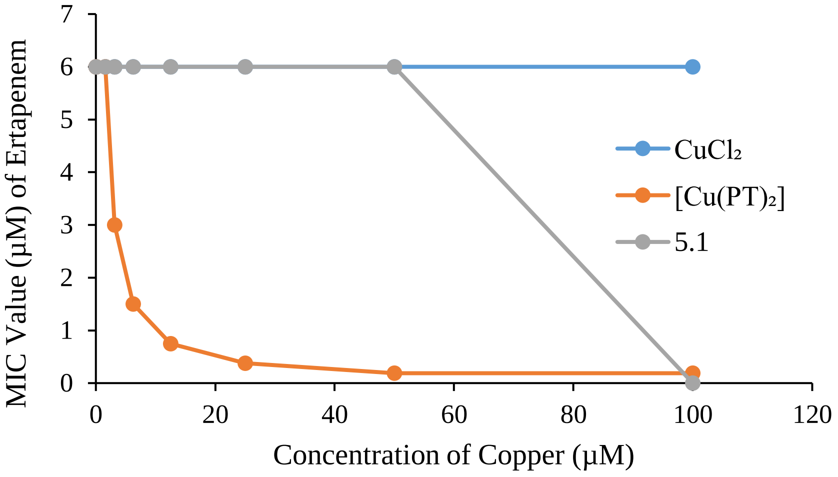

*Figure 5.19: Data of antibiotic synergy study for ertapenem with $CuCl_2$, $[Cu(PT)_2]$ and complex **5.1***

5.2.2.3 In vitro Cytotoxicity against Human Cell Lines

Antiproliferation studies were carried out by Dr. Rianne M. Lord in UEA, Norwich, UK using the MTT assay. In this study, complex **5.1** and [Cu(PT)$_2$] were screened along with CuCl$_2$, cisplatin and CARB as references against MIA PaCa-2 pancreatic carcinoma cells, 143B bone osteosarcoma cells and ARPE-19 healthy retinal epithelial cells. IC$_{50}$ values for complex **5.1** suggests that it is moderately active against both cancer cell lines, an improvement on CuCl$_2$, which shows no activity (Table 5.2). Complex **5.1** shows better activity (8.5 µM) against bone osteosarcoma cells than cisplatin (14 µM). In addition, complex **5.1** shows low activity against healthy ARPE-19 cell lines and therefore shows better selectivity (SI = 5.3) towards cancer cell lines compared to that of [Cu(PT)$_2$] and the other reference compounds. However, the activity of **5.1** does not reach the sub micromolar range of IC$_{50}$ value seen for [Cu(PT)$_2$].

*Table 5.2: IC$_{50}$ data for complex **5.1** and [Cu(PT)$_2$] along with CuCl$_2$, cisplatin and CARB as references against human cell lines and the selectivity indices (SI) data (normal vs cancer) in parenthesis*

Complex	**IC$_{50}$ values (µM ± SD)**		
	MIA PaCa-2	**143B**	**ARPE-19**
[Cu(PT)$_2$]	0.15 ± 0.04 (1.5)	0.20 ± 0.02 (1.1)	0.22 ± 0.02
5.1	19 ± 2 (2.4)	8.5 ± 0.3 (5.3)	45 ± 2
CuCl$_2$	>100 (<0.8)	75 ± 3 (1.1)	83 ± 2
CDDP	5.7 ± 0.1 (2.3)	14 ± 2 (1.0)	13.01 ± 0.1
CARB	>100 (n.d.)	70.8 ± 0.9 (>1.4)	>100

5.3 Conclusion and Future Work

In summary, we have successfully synthesised copper complexes of some well-known pyridine-based ligands and characterised them using various techniques. Furthermore, these complexes were screened for their antibacterial activity against ESKAPE organism panel where complex **5.1** was found to have some potential, unlike the other complexes, which showed no activity in our studies. Complex **5.1** was further assessed for its synergy effects with carbapenem antibiotics, where it showed some additive effects specifically for meropenem, but no strong effects with ertapenem. Data against cancer cell lines also suggested the potential of complex **5.1** as an anticancer agent, with some promising selectivity towards cancer cells over healthy cells. Hereby, it can be concluded that complex **5.1** has been the most promising complex in this part of the study. This uniqueness may be attributed to the fact that this complex structurally resembled [Cu(PT)$_2$], our parent complex, which possess very good bioactivity against both bacteria and cancer cells. One key conclusion of this study is that not all copper complexes show good activity in biological studies and the nature of the ligand is crucially important for the bioactivity. The results in this chapter help to highlight the impressive results obtained with copper pyrithione, as described in the previous chapters.

In future work, various substituted analogous of complex **5.1** should be synthesised to further improve its bioactivity. The selectivity of this complex towards cancer cells is a good starting point and future variants may allow increased activity against the cancer cells while maintaining the low activity against healthy cells. Furthermore, complex **5.1** should be fully analysed for its various physiochemical properties to get more insight into the structure-activity correlation. Moreover, different intracellular mechanistic studies can be carried out as future work. In the broader sense, other pyridine-derived motifs can be subjected to copper complex formation to assess their potential as bioactive agents.

6. Conclusion and Future Work

6.1 Project Conclusions

At the outset, this project was designed to develop pyrithione copper complexes with enhanced physiochemical properties compared to the parent complex [Cu(PT)$_2$], to be applied in antibacterial studies against the multidrug-resistant bacterial ESKAPE species. The non-substituted copper pyrithione complex was previously found to possess bioactivity against drug-resistant bacteria, but was facing issues with *in vitro* testing, due to very poor aqueous solubility. Moreover, no previous studies had been conducted to explore how modification of the pyrithione ligand would affect bioactivity and physical properties of the complex. Therefore, in last three years, this project has primarily evolved around developing various modified versions of the copper pyrithione complex, with an objective of improving its physical, chemical and biological properties.

At its inception, the overall aims of this project were as follows:

i. To design and synthesise a library of substituted copper pyrithione complexes with small functional groups as the substituents

ii. To measure the physiochemical properties of these complexes, such as solubility, lipophilicity and binding constant

iii. To discover an optimised complex with a good balance between solubility and lipophilicity

iv. To maximise the antibacterial activity of the complex

v. To determine any structure-activity correlation for these complexes

The project aims have further been developed and modified throughout the project. For example, anticancer activity of the complexes had not been anticipated, but became an important area of the work.

Initially, alkyl functional groups (Me, *i*-Pr and *t*-Bu) were the choice of substituents to introduce onto the copper pyrithione complex with the idea of destabilising the parallelly stacked crystal packings of this complex. The introduction of Me groups in various positions of the pyrithione ring was successful but attempts with the other two groups (*i*-Pr, *t*-Bu) did not result in formation of the desired complexes. Next, with the aim of varying the electronics of the pyrithione ring, different electron donating (-OH, -OMe, -OEt) and electron withdrawing (-CF_3, -Ph) groups were introduced in various positions of the copper pyrithione complex.

These complexes were characterised using mass spectrometry, elemental analysis and X-ray crystallography data. The crystal data of the substituted complexes suggested in some cases the formation of single crystals of both the *cis* and *trans* isomers (e.g., [Cu(6-Me-PT)$_2$]) and sometimes both isomers together as a co-crystal in the same unit cell (e.g., [Cu(3-OMe-PT)$_2$]). By contrast, the parent complex [Cu(PT)$_2$] forms only the *trans*-isomer. The crystal packings of the novel complexes also displayed different extended structures compared to the planes of stacked complexes for [Cu(PT)$_2$]. In part due to the disruption of these stacked extended structures, the solubility of the substituted complexes was generally higher than that of the parent complex.

Considering the physiochemical properties of these complexes, a general trend was observed that the binding constants (*K*, determined using the Benessi-Hildebrand method) of these complexes do not vary largely with variation in substituent-electronics. However, the lipophilicity (log *P* value) does show some variation with substituent. Electron donating group substituted complexes typically possess similar log *P* values to that of the parent complex [Cu(PT)$_2$], while the electron withdrawing group substituted complexes cause a decrease in the log P values. It is worth mentioning that in this project, log *P* values have been determined using an ICP-OES technique for quantification purpose, due to poor water solubility of these complexes.

In terms of bioactivity, antibacterial activity screening of these complexes against the multidrug-resistant ESKAPE panel of organisms showed a broad trend in which electron-donating group substituted complexes showed higher activity than the electron withdrawing group substituted complexes, which generally showed very low antimicrobial activity. The activity of the parent complex (MIC value in the micromolar range) was broadly maintained by the electron donating complexes, with highest activity seen against the Gram-positive species (*S. aureus*), and in some cases for the Gram-negative species (*E. coli*). The cytotoxicity data against healthy Vero cells of the copper pyrithione complexes suggested a high inhibition rate, leading to fairly low selectivity of these complexes towards bacterial cells over healthy cells (selectivity index <10). The only exception to this observation was the complex [Cu(5-Me-PT)$_2$], which possesses a selectivity index = 10 (Figure 6.1). Although it is not clear why this complex is more selective than the others, there is good potential for future studies with this lead compound.

The high cytotoxicity of these complexes led us to explore the bioactivity further towards screening against pancreatic carcinoma cells and bone osteosarcoma cells. This in vitro anticancer study also showed most copper complexes possessed sub-micromolar IC_{50} values against both cell lines, with the electron-donating substituted complexes showing the highest activity. The anticancer activities of these complexes were observed to be significantly higher (~10 fold) than the well-known anticancer agent, cisplatin, used as a reference compound. The highest activity of any complex was achieved by [Cu(3-OMe-PT)$_2$], which was observed to have nanomolar range activity, specifically against pancreatic carcinoma cells. It also showed a moderate selectivity (selectivity index = 9.1) for these cells over healthy retinal epithelial cells, in contrast with the other complexes studies (Figure 6.1). The high activity of this complex makes it an exciting prospect for future development as an anticancer agent.

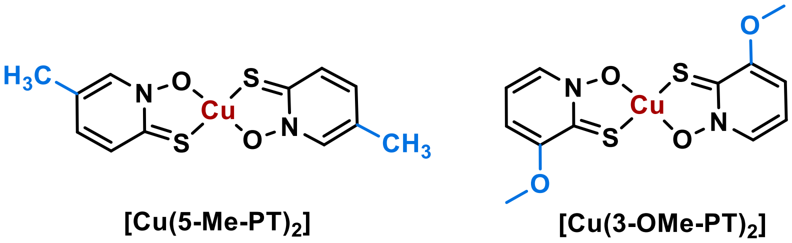

Figure 6.1: Structure of the copper pyrithione complexes with excellent activity outcomes. [Cu(5-Me-PT)$_2$] shows good selectivity towards ESKAPE pathogens over mammalian cells and [Cu(3-OMe-PT)$_2$] shows nanomolar activity against pancreatic cancer cells.

Although some of the compounds in the copper pyrithione library achieved excellent anticancer activity and good selectivity for antibacterial activity, the poor water-solubility still remained as a key issue in the bioassays of these complexes. Therefore, we moved onto introducing some amphiphilic substituents, such as small polyethylene glycol (PEG) chains, to improve the water solubility of the copper pyrithione complex. Three copper pyrithione derivatives with varying length of PEG chains (n = 1, 2 and 3) as substituents at the 5-position were synthesised and characterised. The water-solubility of these complexes was measured using UV/Vis spectroscopy. The data suggested a significant improvement in the solubility with the introduction of the PEG chains (up to 200 fold). As predicted, solubility increased with increasing PEG chain length. A lipophilicity study showed a trend of a slight decrease in log P values with increasing chain length. Overall, the complex [Cu(5-PEG1-PT)$_2$] with the shortest PEG chain showed the optimal balance of having a good lipophilicity and high water-solubility (Figure 6.2).

Moving onto the bioactivity assays of these complex, the antibacterial susceptibility screening with the panel of ESKAPE organisms shows a similar trend to previous copper pyrithione complexes, with better activity against Gram-positive species over Gram-negative ones. It was also observed that the activity increased with decreasing PEG chain length. The same trend is followed by the anticancer activity of these complexes. The anticancer activity of the PEG chain complexes remained similar to that of the parent complex [Cu(PT)$_2$], and was, in fact, slightly improved in case of [Cu(5-PEG1-PT)$_2$] against pancreatic carcinoma cells. Overall, it can be concluded that [Cu(5-PEG1-PT)$_2$] is the optimal complex so far with good water-solubility, balanced lipophilicity and excellent bioactivity.

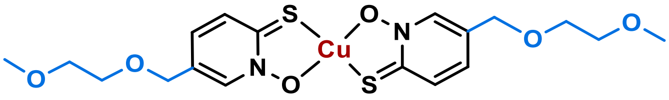

[Cu(5-PEG1-PT)$_2$]

Figure 6.2: Structure of the shortest PEG chain derived copper pyrithione complex with balanced solubility, lipophilicity and bioactivity

Antibiotic synergy studies were also performed for these complexes with well-known β-lactam antibiotics (meropenem and ertapenem) against NDM-resistant *E. coli* bacteria. Although these complexes alone were not very active against this particular species (MIC ~100 µM), they help in lowering down the MIC values of the specified antibiotic, and hereby clearly show some additive effect along with antibiotics. This effect might be justified by the improved inhibiting power of these complexes when employed with the antibiotics, possibly due to inhibition of the MBL-1 enzyme by the copper complex. Similar to the previous bioactivity assays, here also the antibiotic synergy effect increases with decreasing length of PEG chains. A further study also suggested these complexes being bactericidal and not bacteriostatic agents, as they kill the bacteria along with inhibiting the β-lactam enzymes.

Next, the focus of this project moved onto understanding the mechanistic details of copper pyrithione inside cellular system as there has little been known in this topic till date. To explore more in that front, live-cell fluorescence microscopy was chosen as the primary tool. Henceforth, the copper pyrithione complex was modified with a fluorescent BODIPY tag. A copper catalysed alkyne-azide ‘click’ reaction was used as the synthetic tool to attach the fluorescent source onto copper pyrithione. The photophysical properties of the final complex (**4.8**) were measured and compared with original fluorophore (Figure 6.3).

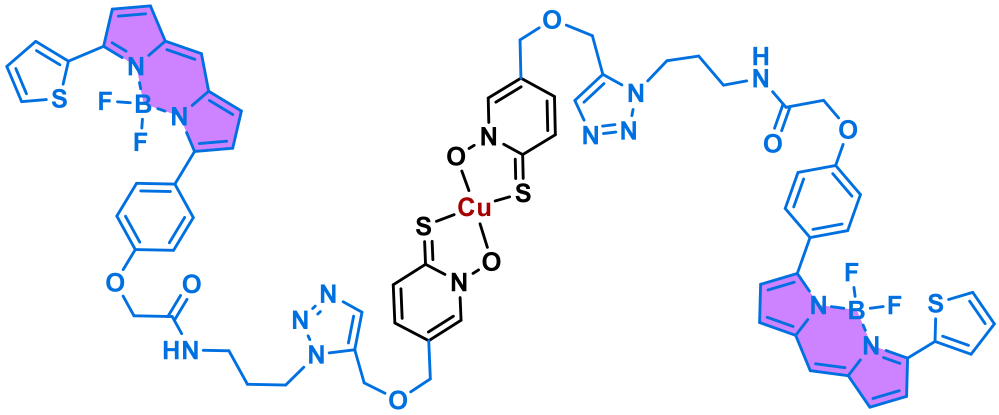

4.8

Figure 6.3: Structure of fluorescent copper pyrithione derivative

Live-cell microscopy images of mouse skin fibroblast cells with complex **4.8** (1 µM) showed the complex entering the cells within 30 min and co-localisation studies at 2 h revealed that **4.8** specifically localises at the endoplasmic reticulum (ER) and is not observed to localise at the mitochondria. ER localisation is quite unusual for such metal complexes and this localisation may help to explain the impressive activity of the complexes. At higher complex concentrations and longer incubation times, the cells were seen to undergo apoptosis, as is consistent with the cytotoxicity data previously determined for the copper pyrithione complexes.

Beyond the study of copper pyrithione complexes, a selection of other copper complexes, with pyridine-based ligands (bipyridine, picoline, pyridyl phosphine etc.) were synthesised and tested for their bioactivity. Most of these complexes showed little bioactivity, but the oxygen analogue of pyrithione (**5.1**) showed some antibacterial and anticancer activity. Notably, this complex showed better selectivity (selectivity index = 5.5) for bone osteosarcoma cells over retinal epithelial cells than that determined for $[Cu(PT)_2]$ (selectivity index = 1.5), which supports further study into this complex.

To conclude, a library of copper pyrithione complexes with different modifications of the pyrithione ligand have been synthesised, characterised and tested for their physiochemical properties and biological activities. Amongst the novel complexes, we observed one complex with excellent anticancer activity, one complex with good selectivity for antibacterial activity and several complexes with high water-solubility. Whilst the reason for the variation in bioactivity is not yet determined, these lead complexes show significant improvement over reference compounds and have great potential for future development. A comparative analysis of this library of substituted copper pyrithione complexes with the parent complex $[Cu(PT)_2]$, as shown in Table 6.1, gives a good overview of the whole work so far.

Table 6.1: Comparison of various physiochemical properties and biological activities for parent complex [Cu(PT)$_2$] and the collective library of modified copper pyrithione complexes

Properties	**[Cu(PT)$_2$]**	**Modified copper pyrithione complexes**	
			(Specific complex)
Stereochemistry	Trans	Both cis and trans, sometimes as co-crystals	**[Cu(6-Me-PT)$_2$]** **[Cu(3-OMe-PT)$_2$]** **[Cu(5-PEG1-PT)$_2$]**
Water solubility	Poor (0.001 ppm)	Very good (>25 g/l)	**[Cu(5-PEG3-PT)$_2$]**
Lipophilicity (log *P*)	Good (2.34)	1.2-1.8	**all**
Binding constant (*K*)	7.53	7.50-7.62	**all**
% Inhibition rate for mammalian Vero cells	91% (5 µg/ml concentration)	38% (5 µg/ml concentration)	**[Cu(5-Me-PT)$_2$]**
Selectivity for bacterial cells over healthy cells	Selectivity Index <10	Selectivity Index = 10	**[Cu(5-Me-PT)$_2$]**
Anticancer activity against pancreatic carcinoma cells (IC$_{50}$ ± SD)	0.15 ± 0.04 µM	0.018 ± 0.004 µM	**[Cu(3-OMe-PT)$_2$]**
		0.125 ± 0.008 µM	**[Cu(5-PEG1-PT)$_2$]**
Selectivity Index for carcinoma cells over healthy cells	1.5	9.1	**[Cu(3-OMe-PT)$_2$]**
Fluorescent activity	None	Good	**Complex 4.8**

6.2 Future Work

This project has explored various different aspects of modifications to the copper pyrithione complex and has a number of directions in which future studies may develop. Two broad areas of future work are synthetic modifications and biological property analysis.

There is still much work to do to understand more about the bioactivity of the complexes already tested. The mechanistic pathways and the mode of actions of these complexes are still unknown and therefore important future work must go into understanding how these complexes operate in cells and why we observe the variation in activity that we have seen. From prior knowledge, it can be predicted that the antibacterial growth inhibition of these complexes is happening through enzyme inhibition (e.g., the MBL-1 enzyme). However, further studies are needed to be carried out to confirm this assumption. Moreover, determination of the amount of copper inside the cells is needed to understand how much complex is actually permeating through the cell membrane. In terms of antibacterial activity, time-kill experiments and biofilm assays can be carried out to further explore this area. Inhibition of carcinoma cell growth by these compounds was high, but the mechanism of this cell death is not clear. We can hypothesise that the apoptosis is driven by generation of reactive oxygen species (ROS) inside the cells by copper, which has been observed by other copper complexes. However, such a hypothesis must be tested, for example by performing ROS assays. Further mechanism studies should be carried out to understand the relevance of the localisation of the complexes at the endoplasmic reticulum to determine whether localisation is key to the activity.

In terms of synthetic modifications, more idea can be put forward to design other types of substituted pyrithione (PT) ligands (Figure 6.4). Up to now, only one position of PT has been substituted at a time and multi-substituted PT is yet to be explored. Introduction of more than one substituent might help to distort the crystal packing of the respective copper complexes and improve the solubility of the complex, without the need for amphiphilic functional groups. Another approach to synthetic variation would be to synthesise copper complex of two non-identical pyrithione ligands, breaking the C_2 symmetry of the complex and potentially bringing in more function to the complex. Following on from the excellent selectivity of $[Cu(5\text{-Me-PT})_2]$ towards bacteria over healthy human cells, other substituents can be specifically introduced to this position to further explore the structure-activity relationship (e.g., Et, *i*-Pr or electron donating/withdrawing groups). Similarly, the high activity of $[Cu(3\text{-OMe-PT})_2]$ in anticancer assays can be better understood by moving the OMe group to other positions on the

PT ligand or by varying the 3-OMe group for alternative electron donating groups in this position.

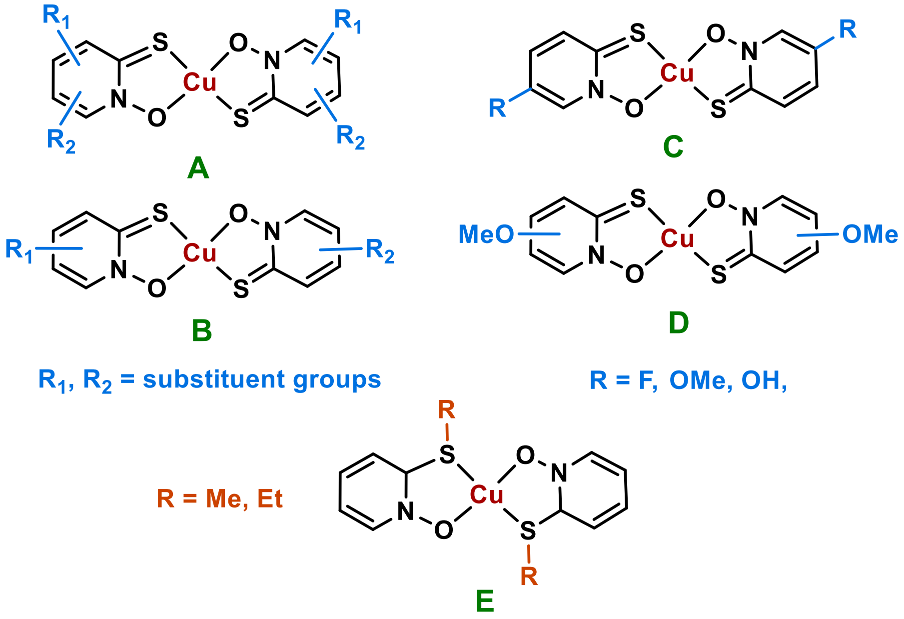

Figure 6.4: Structures for various modified copper pyrithione complexes as future scopes

Moving beyond functionalising the pyridine ring of pyrithione, alternative variations would include substitution at the sulfur of pyrithione (Figure 6.4 E) or exploring alternative metals in the pyrithione complex (Figure 6.5). As this project mainly focused on formation of copper complexes, the scope of other metals such as ruthenium, zinc, nickel, platinum was not explored at all. Zinc complex of PT as antifungal agent and ruthenium complex of PT as anticancer agents have been studied before. However, complexation of modified PT ligands with these metals has not been studied and can be explored further to develop improved antibacterial or anticancer agents.

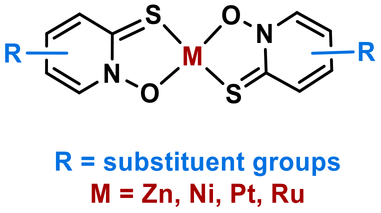

Figure 6.5: Insertion of different metals for complexation with modified PT ligands

In Chapter 4, a fluorescent copper pyrithione complex **4.8** was synthesised by reacting an alkyne pyrithione complex to a fluorescent tag containing an azide. The success of this conjugation opens up the prospect of attaching alternative groups to the pyrithione complex.

For example, groups could be added that increase cell uptake or selectively target specific cells (e.g., cancer cells). Alternatively, siderophores could be conjugated, which would potentially lead to higher uptake into bacteria cells, leading to improved bacteria selectivity. With the alkyne handle in place, there are many possibilities for future work in this area.

Overall, this class of complexes has an exciting future, but much more must be done to understand the activity of complexes and the variation between complexes for the full potential of these species to be realised.

7. Experimental Data

7.1 General Methods

Commercially available reagents were purchased from Merck Life-sciences, Fluorochem and Fischer Scientific and were used as received from suppliers. Solvents were laboratory reagent grade and dried using an appropriate drying agent when required. Reactions requiring anhydrous conditions were carried out under an atmosphere of dry nitrogen using Schlenk-line techniques.

Thin-layer chromatography was carried out on silica plates (Merck 5554) or neutral alumina plates (Merck Art 5550) and visualised under UV (254/365 nm) irradiation.

NMR spectra (^{1}H, ^{13}C {^{1}H}, ^{19}F) were recorded on Bruker Advance (III)-400 spectrometer (^{1}H at 400.130 MHz, ^{13}C {^{1}H} at 100.613 MHz, ^{19}F at 376 MHz), or a Varian VNMRS-600 spectrometer (^{1}H at 600.130 MHz, ^{13}C {^{1}H} at 150.903 MHz, ^{31}P at 161.91 MHz). Spectra were recorded at 295 K in commercially available deuterated solvents and referenced internally to the residual solvent proton resonances.

Electrospray, Atmospheric Pressure and high-resolution mass spectrometry were performed using SQD and QToF mass spectrometer with Acquity UPLC.

7.2 General Procedure for Optical Measurement

All samples for optical analyses were contained in quartz cuvettes with a path length of 1 cm and a polished base. Measurements were recorded at 298 K unless otherwise stated. UV/Vis absorbance spectra were measured on a Cary series 5000 UV/Vis/NIR spectrophotometer using Cary WinUV v4.20 software. Samples were measured relative to a reference of pure solvent contained in a matched cell.

Emission spectra were measured on a HORIBA Jobin-Yvon Fluoromax and Fluorolog using FluorEssence v3.8.0.60 software. Excitation wavelengths were selected according to the specific measurement and the excitation and emission slit width of 5 nm were used throughout. Photoluminescence quantum yield measurements were carried out using the same instrument. Measurements were performed at 298 K using solutions with absorbances of <0.1 at λ_{max}. Relative quantum yield was measured by comparison with a relevant, known standard, Rhodamine 101 (quantum yield = 1.0 in MeOH) in this case. The quantum yield was calculated by plotting the integrated emission as a function of the absorbance for both the known and unknown species according to the following equation:

$$\phi_{\mathrm{x}} = \phi_{\mathrm{s}} * \left(\frac{A_{\mathrm{s}}}{A_{\mathrm{x}}}\right) * \left(\frac{I_{\mathrm{x}}}{I_{\mathrm{s}}}\right) * \left(\frac{n_{\mathrm{x}}}{n_{\mathrm{s}}}\right)$$

Where:

- ϕ = Fluorescence quantum yield
- n = Refractive index of the solvent
- A = Absorbance of the solution
- I = Integrated fluorescence intensity of the emitted light
- Subscripts ‘s’ and ‘x’ refer to the standard and unknown fluorophore respectively

7.3 General Procedure for Binding Constant (log *K*) Measurement

A stock solution of $CuCl_2.2H_2O$ (0.1 mM) was prepared in a solvent system of $MeCN:H_2O$ = 1:1. Ligand solutions (5 mM) were prepared by combining solutions of the ligand (10 mM in $MeCN:H_2O$ = 1:1) and NaOH (10 mM in $MeCN:H_2O$ = 1:1) in a 1:1 ratio. The $CuCl_2.2H_2O$ solution (3.3 ml) was transferred to a cuvette and the absorption spectrum of the solution was measured using UV/Vis spectrometry. Next, the basic ligand solution was added gradually (10 µl aliquots) to the copper solution and UV/Vis spectra were recorded after each addition. The addition was stopped when the spectra started to show saturation and Benessi-Hildebrand graph was plotted using the following equation and considering the absorption maxima at wavelength ~320 nm.

$$\frac{[M]_0 b}{A} = \frac{1}{K\varepsilon[L]^2} + \frac{1}{\varepsilon}$$

Where [M] is concentration of copper, [L] is concentration of the activated ligand, b is the pathlength, the ε is molar extinction coefficient of the complex, A is absorbance and K = binding constant.

Binding constants were recording in the same way in HEPES buffer (1% DMSO) solution. Aqueous HEPES buffer solution was prepared by dissolving 119.15 mg of HEPES (free acid) in distilled H_2O (400 ml) and the pH of the solution was adjusted to 7.3 by adding a concentrated NaOH solution. $CuCl_2.2H_2O$ and ligand solutions were prepared in HEPES buffer (1% DMSO/99% HEPES buffer) at the same concentrations described above. UV/Vis spectra were recorded in the same way as described above for the acetonitrile:H_2O system.

7.4 General Procedure for log *P* Measurement

7.4.1 Spectrophotometric Determination of log *P*

Stock solutions (10 mM) of copper complexes were prepared in dimethyl sulfoxide (DMSO) solvent. Molar absorptivity or extinction coefficient (ε) of copper complexes in both water and *n*-octanol solvents were determined by preparing series of solutions with half dilutions. Water and octanol used in this experiment were saturated with each other to maintain the similar condition as that for later experiments. For both solvents, the starting solution with concentration of 0.1 mM was obtained by adding 100 µl of stock solution in 10 ml of respective solvents. Hereby, the maximum amount of DMSO in the experimental system was kept to 1%. UV/Vis absorbance spectra of prepared solutions were recorded in 200-600 nm range at 22 °C temperature and the absorbance maxima (A) around 320 nm have been utilised for calculating ε of the complexes. Absorbance maxima for different concentrations of solutions were plotted in *y* axis against the concentrations at *x* axis to obtain a straight-line plot. Following Beer-Lambert law ($A = \varepsilon cb$, where *c* = concentration and *b* = length of light path = 1 cm (constant)), ε were calculated from slope.

$$\mathbf{A = \varepsilon cb}$$

$$\mathbf{\varepsilon = A/cb}$$

Next, log *P* values for [Cu(5-PEG1-PT)$_2$], [Cu(5-PEG2-PT)$_2$] and [Cu(5-PEG3-PT)$_2$] were determined using shake-flask method. In this process, for each complex, 60 µl of the stock solution was added to a mixture of 3 ml water and 3 ml *n*-octanol. The solution was shaked using hand and vortex. After two layers got visibly separated, both layers were collected separately, and UV-absorbance spectra were recorded at 200-600nm. Previously determined extinction coefficients were utilised to determine the concentrations of copper complex in each layer following Beer-Lambert law ($c = A/\varepsilon l$) and considering absorbance maxima around 320 nm. Further calculations were done to determine partition coefficient (*P*) and respective logP value according to the following equation.

$$\log P = \log\left(\frac{[Cu(octanol)]}{[Cu(water)]}\right)$$

7.4.2 Determination of log *P* Value using ICP-OES Technique

As non-substituted copper pyrithione complex has very poor solubility in water, determining the extinction coefficient of this complex in water is highly inefficient. Therefore, another technique, ICP-MS analysis was utilised to measure concentrations of copper in each layer. In this process, sample preparation for each complex followed everything similar as that for shake-flask method until UV measurement. After separating two solvent layers, samples for measuring copper concentrations in octanol and water layer were prepared differently. For octanol layer, 100 µl was collected in a vial and the solvent was evaporated under high vacuum. Next, the residue complex in vial was dissolved in 100 µl methanol and further it was diluted with 10 ml of 5% aqueous nitric acid (HNO_3) solution for digestion. For water layer, 1 ml of solution was diluted with 9 ml of 5% aqueous HNO_3 solution. After analysis through ICP-MS technique, amount of copper in each sample could be determined in ppm. Thereafter, concentration of copper in starting solution of each layer was calculated considering dilution methods to determine the subsequent ***P*** and **log *P*** values.

7.5 General Procedure for Solubility Measurement

Solubility of PEG chain substituted copper pyrithione complexes in water was measured using UV/Vis spectroscopy. First, each copper complex was dissolved in 1 ml of 1% DMSO/water solvent system until the solution reaches saturation. Then, the saturated solutions were filtered using small pipette filtration and further diluted several times using 1% DMSO/water to measure UV absorbance data at different concentrations. Absorbance maxima at 319 nm were considered for further calculations using Beer-Lambert law to obtain concentration at different dilution. Consequently, this calculation led to concentration of the solution prepared initially in 1 ml solvent and could be concluded as the solubility (mg/ml or g/l) of respective copper complex.

7.6 General Method for HPLC Measurement

7.6.1 Analytical HPLC (Method A)

The samples were analysed using a Waters ARC Acquity HPLC system equipped with a diode array detector with chromtograms extracted at 230 nm, 260 nm and 300 nm. A Waters XBridge C18 (100 x 4.6 mm, 3.5 um) column was used with gradient elution at 1ml/min from 10% water with 0.1% formic acid, 90% Acetonitrile to 100% acetonitrile over 10 minutes then held at 100% acetonitrile for 5 minutes.

7.6.2 Preparative HPLC (Method B)

The samples were purified using an InterChim PuriFlash purification system equipped with a Waters XBridge C18 (19 x 100 mm, 5um). Separation was achieved using gradient elution at a flow rate of 17 ml/min starting with 10% water with 0.1% formic acid, 90% Acetonitrile to

100% acetonitrile over 10 minutes then held at 100% acetonitrile for 5 minutes. A diode array detector monitored the absorption of the eluent and fractions were collected when a threshold of 5 mAU was achieved at 260 nm

7.7 Material and methods for the Antibacterial study

7.7.1 Growth Media and Reagents

Mueller-Hinton cation supplemented broth II (MHBII) and Mueller-Hinton Agar (MHA) were purchased from Merck Life-Sciences. Meropenem and Ertapenem were obtained from Melford Laboratories.

7.7.2 Bacterial Strains

All copper pyrithione complexes along with copper chloride and levofloxacin were screened against ESKAPE pathogen panel, including *E. coli* ATCC 25922, *S. aureus* ATCC 29213, *K. pneumoniae* BAA-1705, *A. baumannii* BAA-1605, *P. aeruginosa* ATCC 27853 and *Enterococcus spp*. These strains were procured from Biodefense and Emerging Infections Research Resources Repository/American Type Culture Collection (BEI/ATCC, USA) and routinely cultivated on MHA and MHBII. Before starting the experiment, a single colony was picked from MHA plate, inoculated in MHBII and incubated overnight at 37 °C with shaking for 18–24 h to obtain the starter culture.

All copper pyrithione complexes were also screened against a β-lactam resistant strain of *E. coli* bacteria that carries the pSU2718::*bla*$_{\text{NDM-1}}$ plasmid expressing the New Delhi metallo-β-lactamase 1. This strain has been described previously (refer to the main article) and it is routinely cultivated in ampicillin containing MHBII and agar media at 37 °C. Before starting the experiments, single colonies were picked up from media plate and was inoculated in MHBII.

7.7.3 Antibiotic Susceptibility Testing

For screening of ESKAPE, antibiotic susceptibility tests were conducted according to the CLSI guidelines using the broth microdilution assay. Briefly, 10 mg/ml stock solutions of test compounds were prepared in DMSO. Bacterial cultures (~10^6 CFU/ml, 0.1 ml total) were prepared in MHBII in 96-well round bottom microtiter plates. The compounds were tested from 0.5 – 64 mg/L in two-fold serial diluted fashion. The plates were incubated at 37 °C for 18-24 h without shaking, following which the minimum inhibitory concentration (MIC) was determined. The MIC is defined as the lowest concentration of the compound at which there is absence of visible growth. For each test compound, MIC determinations were carried out independently three times using duplicate samples.

Antibiotic susceptibility testing against β-lactam resistant strain of *E. coli* was conducted as above but using 0.2 ml of bacterial cultures and 0 – 100 µM of copper(II) compounds.

7.7.4 Antibiotic Synergy Study

Antibiotic synergy study was again conducted following CLSI guidelines using the checkerboard assay method. Bacterial cultures were (~10^6 CFU/ml, 0.2 ml total) were prepared in MHBII in flat-bottomed, 96-well microtiter plates. Copper complexes (0 – 100 µM) and/or ertapenem (0 – 12 µM) or meropenem (0 – 4 µM) were tested in two-fold serial diluted fashion. Turbidity in each well was measured using a microtiter plate reader after incubation at 37 °C for 18-24 h. The MIC was defined as the lowest concentration of agent that completely inhibited bacterial growth.

The fractional inhibitory concentration (FIC) value for each agent was defined as its MIC in combination divided by its MIC alone. The FIC index was the sum of the FIC values for the two agents.

$$A/MICA + B/MICB = FICA + FICB = FIC\ Index$$

Where A and B are the MIC of antibiotic (meropenem or ertapenem) and MIC of copper pyrithione complex respectively in combination (in a single well), and MICA and MICB are the MIC of the respective agents individually.

FIC index is used to categorise the interaction of two agents in combination. FIC Index <0.5 indicates synergy effect whereas a range of 0.5-4.0 indicates the additive effect.

7.8 Material and methods for Anticancer Study

7.8.1 Growth Media and Reagents

Gicbo™ high glucose Dublecco’s Modified Eagle Medium (DMEM) and Gicbo™ Roswell Park Memorial Institute (RPMI-1640) medium supplemented with sodium pyruvate (1 mM) and L-glutamine (2 mM), Fetal bovine serum (FBS), phosphate buffer solution (PBS) and Trypsin-EDTA (0.25%) were all purchased from Fisher Scientific. The MIA PaCa-2, 143B and ARPE-19 cell lines were kindly gifted or purchased from the University of Bradford’s Institute of Cancer Therapeutics, Dr Darrell Green (UEA, School of Medicine) and Dr Simon Allison (University of Huddersfield, School of Applied Sciences) respectively.

7.8.2 Cell Viability Assay

All assays were conducted using human cell lines: pancreatic carcinoma (MIA PaCa-2), bone osteosarcoma (143B) and normal epithelial retinal (ARPE-19), and cell lines were routinely maintained as monolayer cultures in appropriate complete medium (MIA PaCa-2 and ARPE-19 in high glucose DMEM complete medium (+ 10% FBS); 143B in RPMI-1640 complete medium (+ 10% FBS)) and grown in either T-25 or T-75 flasks at 37 °C and 5% CO_2. Prior to chemosensitivity studies, cell monolayers were passaged using Trypsin-EDTA (0.25%) and diluted to a concentration of 1×10^4 cells/ml. All assays were conducted using 96-well plates, in which 100 μL of the cell suspension was added to columns 3-11 (column 2 = media blank), and columns 1 and 12, and rows A and H were filled with 200 μl PBS to prevent media evaporation. The plates were then incubated for 48 h at 37 °C and 5% CO_2. After 48 h, 100 μl of compound/media dilutions were added to the plates in columns 4-11 in a series of half dilutions (column 3 = 100% cells spiked with 0.1% DMSO). All compound stocks were made using DMSO at 100 mM prior to dilution. The plates were incubated for 24 h at 37 °C and 5% CO_2, then 20 μl MTT (3-(4,5-dimethylthiazol-2-yl)-2,5-diphenyltetrazolium bromide, 5 mg/ml) was added to each well and incubated for a further 3 h at 37°C and 5% CO_2. All solutions were then removed via pipette and 150 μl of DMSO added to each well, mixed using a pipette and the absorbance of each well measured at 540 nm using a ClarioStar spectrophotometer microplate reader. Results were plotted on a logarithmic scale, and the half maximal inhibitory concentration (IC_{50}) determined from triplicate of triplicate repeats and reported as an IC_{50} ± Standard Deviation (SD).

7.9 General Procedure for Fluorescence Microscopy Study

NIH-3T3 mouse skin fibroblasts were grown as a single monolayer in Dulbecco's Modified Eagle Medium (DMEM) 1:1 supplemented with 10% foetal bovine serum (FBS). Grown in 75 cm^2 plastic culture flasks, with no prior surface treatment. Incubation was carried out at 37 °C and 5% (v:v) CO_2, and in average humidity conditions. Cell harvesting was carried out *via* washing with 10% phosphate buffered saline (PBS) prior to the addition of trypsin solution (0.25%). 5-10 minutes of incubation at 37.5 ºC was carried out prior to resuspension in fresh media by repeated aspiration with a sterile plastic pipette.

Microscopy cells were seeded in untreated iBibi 100 μL live-cell channels and allowed to grow to roughly 50% confluence, at 37 °C in 5% CO_2. Following this, DMEM was replaced, and cells were treated with the studied complex (1 μM) and additional cellular stains (ER-Tracker, Mitrotracker green 100 nM), with <0.1% DMSO present in the final imaging medium. For live-cell imaging, DMEM/F12 media (10% FBS) lacking phenol red was used from this point onward to prevent unwanted fluorescence. Following incubation, the channels were washed with live-cell imaging media and imaged using a purposely built incubator housing the microscope maintaining 37 °C, 5% CO_2 and 10% humidity.

Live-cell experiments were performed on a custom built PhMoNa system based on a Leica SP5 II (DMI6000 inverted chassis) LSCM platform operating with a fibre-coupled 355 nm coherent laser (Nd:YAG third harmonic, 80 mW) for UV activation, as well as fibre-coupled HeNe and argon coherent lasers for visible wavelength selection. The modular PhMoNa technique is based on a laser scanning confocal microscope (LSCM) harnessing spatially modulated illumination intensities, using an in situ-generated raster-scanned standing wave excitation beam optical grid pattern.

Steady-state fluorescence images were recorded using the PhMoNa enhanced Leica SP5 II LSCM confocal microscope equipped with a HCX PL APO 63x/1.40 NA LambdaBlue Oil immersion objective. Data were collected using 2x digital magnification at 100 Hz/line scan speed (4-line average, bidirectional scanning) at 355 nm (third harmonic NdYAG laser, set at 20 mW, 400 nJ/voxel total dwell time). In order to achieve excitation with maximal probe emission, the microscope was equipped with a triple-channel imaging detector, comprising a conventional PMT system and two HyD hybrid avalanche photodiode detectors. The frame size was determined at 1024 x 1024 pixel, with 2x digital magnification to ensure illumination flatness of field and 0.6 airy disc unit determining the applied pinhole diameter rendering on voxel to correspond to 62 x 62 nm^2 (frame size 125 x 125 μm2) with a section thickness set at 188 nm (at 355 nm excitation). A HeNe or Ar ion laser was used to aid parallel transmission image capture of the PI signals, used to follow the onset of necrosis. All imaging parameters are kept constant across experiments. This includes voxel size, laser power, line speed, and averaging sequences, unless otherwise noted.

All post image processing was carried out on the open source, plugin prepacked, FIJI (ImageJ 1.52p Java 1.8.0_172 64 Bit). All adjustments to voxel brightness and contrast were kept at constant values within each image set.

7.10 Synthetic Procedures

2-Bromo-6-methylpyridine N-oxide

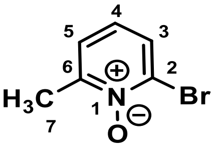

2.1a

2-Bromo-6-methylpyridine (0.33 ml, 2.91 mmol) was added to dichloromethane (10 ml) and the mixture was allowed to stir at room temperature. 3-Chloroperbenzoic acid (1.00 g, 5.81 mmol) was added slowly and the reaction mixture was stirred for a further 14 h. The reaction was quenched with the addition of saturated aqueous solution of sodium bicarbonate (approx. 10 ml) and the product was extracted with dichloromethane (3 x 25 ml). The organic layers were combined, dried over magnesium sulfate, filtered and the solvent removed under reduced pressure. The crude yellow solid was purified by column chromatography on silica (CH_2Cl_2: 3% MeOH) to produce the *title compound* (**2.1a**) as a light brown solid (300 mg, 55%).

^{1}H NMR (600 MHz, Chloroform-*d*) δ 7.54 (1H, d, $^3J_{H-H}$ 8.0 Hz, H^5), 7.22 (1H, d, $^3J_{H-H}$ 8.0 Hz, H^3), 6.99 (1H, t, $^3J_{H-H}$ 8.0 Hz, H^4), 2.57 (3H, s, H^7); ^{13}C NMR (151 MHz, Chloroform-*d*) δ 150.9 (1C, C^6), 133.3 (1C, C^2), 128.4 (1C, C^5), 124.9 (1C, C^3), 124.7 (1C, C^4), 19.0 (1C, C^7); *m/z* (ESI HRMS$^+$) 187.9715 $[M + H]^+$ ($C_6H_7{}^{79}BrNO$ requires 187.9711); R_f = 0.17 (silica, CH_2Cl_2 : 5% MeOH).

6-Methylpyridine-2-thiol-N-oxide

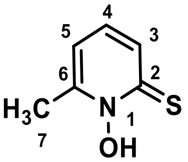

2.2a

2-Bromo-4-methylpyridine-*N*-oxide (**2.1a**) (200 mg, 1.06 mmol) was added to an aqueous saturated solution of $NaSH.H_2O$ (10 ml) and the mixture was allowed to stir at room temperature for 1 h. The solution was acidified with aqueous 4 M HCl (H_2S gas generated was quenched in aqueous solution of $ZnCl_2$) and extracted with ethyl acetate (3 x 50 ml). The organic layers were combined, dried over $MgSO_4$ and the solvent was evaporated under reduced pressure. Acetone (10 ml) was added to the purple residue and the undissolved yellow impurity was removed by filtration. Evaporation of the solvent under reduced pressure gave the *title compound* as a solid residue, from which a sample was taken for characterisation. To avoid decomposition, the remaining compound was dissolved in ethyl acetate and extracted with aqueous NaOH (1M, 10 ml). The aqueous layer was directly used for next step of copper complex formation, assuming the yield to be quantitative.

^{1}H NMR (600 MHz, D_2O) **δ** 7.34 (1H, d, $^3J_{H\text{-}H}$ 7.9 Hz, H^3), 6.91 (1H, t, $^3J_{H\text{-}H}$ 7.9 Hz, H^4), 6.76 (1H, d, $^3J_{H\text{-}H}$ 7.9 Hz, H^5), 2.29 (3H, s, H^7); ^{13}C NMR (151 MHz, D_2O) **δ** 163.4 (1C, C^2), 149.2 (1C, C^6), 129.7 (1C, C^3), 127.9 (1C, C^4), 118.4 (1C, C^5), 18.5 (1C, C^7); *m/z* (ESI HRMS$^+$) 142.0317 [M + H]$^+$ (C_6H_8NOS requires 142.0327).

[Copper(6-methylpyridine-2-thiolate-N-oxide)]$_2$

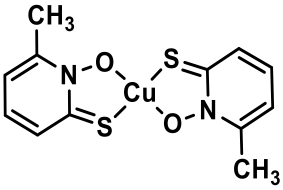

[Cu(6-Me-PT)$_2$]

To an aqueous solution (10 ml) of the sodium salt of 4-methylpyridine-2-thiol-*N*-oxide (**2.2b**) (200 mg, 1.42 mmol), a solution of copper sulfate dihydrate (121 mg, 0.71 mmol) in H_2O (5 ml) was added dropwise. The reaction mixture was stirred for 2 h. The grey precipitate that formed was collected by filtration and washed with water and ethanol. The crude grey solid obtained was purified by column chromatography on silica (CH_2Cl_2) to produce the *title compound* as a dark brown solid (120 mg, 25%*). Single molecule crystals of the product were produced *via* slow evaporation of dichloromethane.

*yield based on two steps from **2.1a**

m/z (ASAP HRMS$^+$) 342.9611 [M]$^{+\bullet}$ ($C_{12}H_{12}{}^{63}CuN_2O_2S_2$ requires 342.9636); Anal. Found (Expected) C 42.01 (41.91) H 3.51 (3.52) N 8.04 (8.15); Rf = 0.55 (silica, CH_2Cl_2); HPLC (method A): t_R = 9.0 min.

2-Bromo-3-methylpyridine-N-oxide

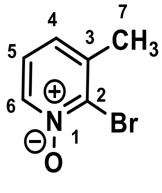

2.1b

2-Bromo-3-methylpyridine (0.13 ml, 1.16 mmol) was added to dichloromethane (8 ml) and the mixture was allowed to stir at room temperature. 3-Chloroperbenzoic acid (402 mg, 2.33 mmol) was added slowly and the reaction mixture was stirred for a further 16 h. The reaction was quenched with the addition of saturated aqueous solution of sodium bicarbonate (approx. 10 ml) and the product was extracted with dichloromethane (3 x 10 ml). The organic layers were combined, dried over magnesium sulfate, filtered and the solvent was removed under reduced pressure. The crude brown solid was dissolved in H_2O and the undissolved solid was removed from the filtrate through gravity filtration. The solvent was evaporated under vacuo to produce the *title compound* (**2.1b**) as a light brown solid (96 mg, 44%).

^{1}H NMR (600 MHz, D_2O) **δ** 8.21 (1H, dd, $^3J_{H-H}$ 6.5 Hz, $^4J_{H-H}$ 1.0 Hz, H^6), 7.44 (1H, dd, $^3J_{H-H}$ 7.9 Hz, $^4J_{H-H}$ 1.5 Hz, H^4), 7.30 (1H, dd, $^3J_{H-H}$ 7.9 Hz, $^3J_{H-H}$ 6.4 Hz, H^5), 2.35 (3H, s, H^7); ^{13}C NMR (151 MHz, D_2O) **δ** 140.5 (1C, C^3), 137.8 (1C, C^6), 135.5 (1C, C^2), 132.6 (1C, C^4), 124.3 (1C, C^5), 21.8 (1C, C^7); *m/z* (ESI HRMS$^+$) 187.9713 $[M + H]^+$ ($C_6H_7{}^{79}BrNO$ requires 187.9711); R_f = 0.45 (silica, CH_2Cl_2 : 5% MeOH).

3-Methylpyridine-2-thiol-N-oxide

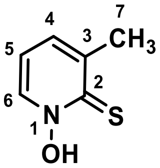

2.2b

2-Bromo-3-methylpyridine-*N*-oxide (**2.1b**) (60 mg, 0.32 mmol) was added to a saturated aqueous solution of NaSH.H_2O (5 ml) and the brown reaction mixture was allowed to stir overnight at room temperature. The reaction was quenched with aqueous 4 M HCl (15 ml) and hydrogen sulfide gas produced during quenching process was trapped into aqueous $ZnCl_2$ solution. The desired organic compound was extracted in ethyl acetate (3 x 10 ml), dried over $MgSO_4$ (anhydrous) and the solvent was evaporated under reduced pressure.

Acetone (5 ml) was added to yellow residue and the undissolved yellow impurity was removed by filtration. Evaporation of solvent under reduced pressure gave *title compound* (**2.2b**) as a yellow solid residue, from which a sample was taken for characterisation. To avoid decomposition, the remaining compound was dissolved in aqueous NaOH (1 M, 5 ml). The aqueous layer was directly used for next step of copper complex formation, assuming the yield to be quantitative.

^{1}H NMR (600 MHz, D_2O) **δ** 7.90 – 7.78 (1H, m, H^6), 7.13 (1H, d, $^3J_{H\text{-}H}$ 7.3 Hz, H^4), 6.68 (1H, t, $^3J_{H\text{-}H}$ 7.3 Hz, H^5), 2.23 (3H, s, H^7); ^{13}C NMR (151 MHz, D_2O) **δ** 163.8 (1C, C^2), 140.0 (1C, C^3), 136.2 (1C, C^6), 129.2 (1C, C^4), 115.6 (1C, C^5), 22.7 (1C, C^7); *m/z* (ESI HRMS$^+$) 142.0330 $[M + H]^+$ (C_6H_8NOS requires 142.0327).

[Copper(3-methylpyridine-2-thiolate-N-oxide)$_2$]

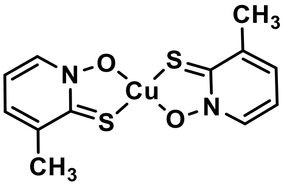

[Cu(3-Me-PT)$_2$]

To a solution (5 ml) of 3-methylpyridine-2-thiol-*N*-oxide (**2.2b**) (100 mg, 0.71 mmol) in aqueous NaOH (43 mg, 0.71 mmol), a solution of copper sulfate dihydrate (60 mg, 0.35 mmol) in H_2O (5 ml) was added dropwise. The reaction mixture was stirred for 2 h. The dark green precipitate that formed was collected by filtration and washed with water and ethanol. The crude dark green solid was dissolved in dichloromethane (3 ml). The solution was decanted from undissolved solid and evaporation of solvent produced the *title compound* as a dark green solid (82 mg, 34%*). Single crystals of the desired complex were achieved by layer diffusion method of dichloromethane solvent in methanol.

*yield based on two steps from **2.1b**

m/z (ASAP HRMS$^+$) 343.9712 $[M+H]^{+\bullet}$ ($C_{12}H_{13}{}^{63}CuN_2O_2S_2$ requires 343.9714) HPLC (method A): t_R = 9.1 min.

2-Chloro-4-methylpyridine N-oxide

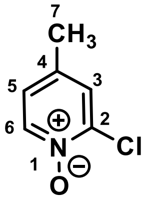

2.1c

2-Chloro-4-methylpyridine (0.18 ml, 1.57 mmol) was added to dichloromethane (10 ml) and the mixture was allowed to stir at room temperature. 3-Chloroperbenzoic acid (541 mg, 3.14 mmol) was added slowly and the reaction mixture was stirred for a further 14 h. The reaction was quenched with the addition of saturated aqueous solution of sodium bicarbonate (approx. 10 ml) and the product was extracted with dichloromethane (3 x 20 ml). The organic layers were combined, dried over magnesium sulfate, filtered and the solvent was removed under reduced pressure. The crude brown oily liquid was purified by column chromatography on silica (CH_2Cl_2: 3% MeOH) to produce the *title compound* (**2.1c)** as a light brown solid (126 mg, 56%).

^{1}H NMR (600 MHz, Chloroform-*d*) **δ** 8.17 (1H, d, $^3J_{H-H}$ 6.8 Hz, H^6), 7.25 (1H, d, $^4J_{H-H}$ 2.4 Hz, H^3), 6.97 (1H, dd, $^3J_{H-H}$ 6.8, $^4J_{H-H}$ 2.4 Hz, H^5), 2.28 (3H, s, H^7); ^{13}C NMR (151 MHz, Chloroform-*d*) **δ** 141.2 (1C, C^2), 139.8 (1C, C^6), 138.5 (1C, C^4), 127.5 (1C, C^3), 125.0 (1C, C^5), 20.1 (1C, C^7); *m/z* (ESI HRMS$^+$) 144.0213 $[M + H]^+$ ($C_6H_7{}^{35}ClNO$ requires 144.0216); Rf = 0.5 (silica, CH_2Cl_2 : 5% MeOH).

4-Methylpyridine-2-thiol-N-oxide

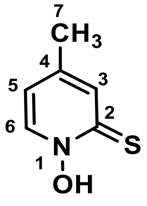

2.2c

2-Chloro-4-methylpyridine-*N*-oxide (**2.1c**) (100 mg, 0.7 mmol) was added to a saturated aqueous solution of $NaSH.H_2O$ (5 ml) and the orange reaction mixture was allowed to stir overnight at room temperature. The reaction was quenched with aqueous 4 M HCl (15 ml) and hydrogen sulfide gas produced during quenching was trapped into aqueous $ZnCl_2$ solution. The desired organic compound was extracted with ethyl acetate (3 x 10 ml), dried over $MgSO_4$ (anhydrous) and the solvent was evaporated under reduced pressure.

Acetone (10 ml) was added to yellow residue and the undissolved yellow impurity was removed by filtration. Evaporation of solvent under reduced pressure gave the *title compound* (**2.2c**) as yellow solid residue, from which a sample was taken for characterisation. To avoid decomposition, the remaining compound was dissolved in aqueous NaOH (1 M, 10 ml). The aqueous layer was directly used for next step of copper complex formation, assuming the yield to be quantitative.

^{1}H NMR (600 MHz, D_2O) **δ** 7.76 (1H, d, $^3J_{H\text{-}H}$ 6.7 Hz, H^6), 7.27 (1H, dq, $^4J_{H\text{-}H}$ 2.5 Hz, $^4J_{H\text{-}H}$ 0.7 Hz, H^3), 6.63 (1H, dd, $^3J_{H\text{-}H}$ 6.7 Hz, $^4J_{H\text{-}H}$ 2.5 Hz, H^5), 2.07 (3H, s, H^7); ^{13}C NMR (151 MHz, D_2O) 162.6 (1C, C^2), 141.0 (1C, C^4), 137.7 (1C, C^6), 132.4 (1C, C^5), 119.0 (1C, C^3), 19.2 (1C, C^7); *m/z* (ESI HRMS$^+$) 142.0329 $[M + H]^+$ (C_6H_8NOS requires 142.0327).

[Copper(4-methylpyridine-2-thiolate-N-oxide)$_2$]

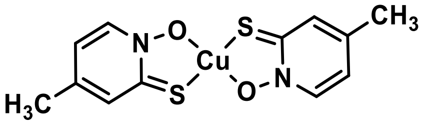

[Cu(4-Me-PT)$_2$]

To a solution (5 ml) of 4-methylpyridine-2-thiol-*N*-oxide (**2.2c**) (100 mg, 0.71 mmol) in aqueous NaOH (43 mg, 0.71 mmol), a solution of copper sulfate dihydrate (60 mg, 0.35 mmol) in H_2O (5 ml) was added dropwise. The reaction mixture was stirred for 2 h. The dark green precipitate that formed was collected by filtration and washed with water and ethanol. The crude dark green solid was dissolved in dichloromethane (3 ml). The solution was decanted from undissolved solid and evaporation of solvent produced the *title compound* as a dark green solid (78 mg, 32%*). Single crystals of the desired complex were achieved by layer diffusion of dichloromethane solvent in methanol.

*yield based on two steps from **2.1c**

m/z (ASAP HRMS$^+$) 343.9711 $[M+H]^{+\bullet}$ ($C_{12}H_{13}{}^{63}CuN_2O_2S_2$ requires 343.9714); Anal. Found (Expected) C 41.77 (41.91) H 3.50 (3.52) N 8.02 (8.15); HPLC (method A): t_R = 8.7 min.

2-Bromo-5-methylpyridine-N-oxide

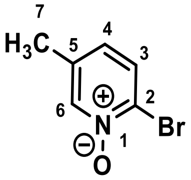

2.1d

2-Bromo-5-methylpyridine (1 g, 5.82 mmol) was added to dichloromethane (20 ml) and the mixture was allowed to stir at room temperature. 3-Chloroperbenzoic acid (2 g, 11.66 mmol) was added slowly and the reaction mixture was stirred for a further 14 h. The reaction was quenched with the addition of saturated aqueous solution of sodium bicarbonate (approx. 20 ml) and the product was extracted with dichloromethane (3 x 15 ml). The organic layers were combined, dried over magnesium sulfate, filtered and the solvent was removed under reduced pressure. The crude brown oily liquid was purified by column chromatography on silica (CH_2Cl_2: 3% MeOH) to produce the *title compound* (**2.1d**) as a light brown solid (500 mg, 46%).

^{1}H NMR (400 MHz, Chloroform-*d*) **δ** 8.27 (1H, d, $^4J_{H-H}$ 1.2 Hz, H^6), 7.53 (1H, dd, $^3J_{H-H}$ 8.3 Hz, H^3), 6.96 (1H, dd, $^3J_{H-H}$ 8.3 Hz, $^4J_{H-H}$ 1.2 Hz, H^4), 2.28 (3H, s, H^7); ^{13}C NMR (101 MHz, Chloroform-*d*) 140.5 (1C, C^6), 135.7 (1C, C^5), 130.1 (1C, C^3), 129.9 (1C, C^2), 128.0 (1C, C^4), 17.98 (1C, C^7); *m/z* (ESI HRMS$^+$) 187.9718 $[M + H]^+$ ($C_6H_7{}^{79}BrNO$ requires 187.9711); R_f = 0.45 (silica, CH_2Cl_2 : 5% MeOH).

5-Methylpyridine-2-thiol-N-oxide

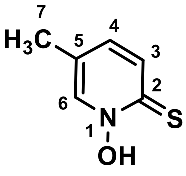

2.2d

2-Bromo-5-methylpyridine-*N*-oxide (**2.1d**) (200 mg, 1.06 mmol) was added to a saturated aqueous solution of $NaSH.H_2O$ (6 ml) and the yellow reaction mixture was allowed to stir overnight at room temperature. The reaction was quenched with aqueous 4 M HCl (15 ml) and hydrogen sulfide gas produced during quenching process was trapped into aqueous $ZnCl_2$ solution. The desired organic compound was extracted in ethyl acetate (3 x 15 ml), dried over $MgSO_4$ (anhydrous) and the solvent was evaporated under reduced pressure.

Acetone (10 ml) was added to yellow residue and the undissolved yellow impurity was removed by filtration. Evaporation of solvent under reduced pressure gave *title compound* (**2.2d**) as dark brown solid residue (85 mg, 56%), from which a sample was taken for characterisation. To avoid decomposition, the remaining compound was dissolved in aqueous NaOH (1 M, 5 ml). The basic aqueous solution was directly used for next step of copper complex formation.

^{1}H NMR (400 MHz, Chloroform-*d*) **δ** 7.94 (1H, d, $^4J_{\text{H-H}}$ 1.9 Hz, H^6), 7.61 (1H, d, $^3J_{\text{H-H}}$ 8.7 Hz, H^3), 7.15 (1H, dd, $^3J_{\text{H-H}}$ 8.7 Hz, $^4J_{\text{H-H}}$ 1.9 Hz, H^4), 2.29 (3H, s, H^7); ^{13}C NMR (101 MHz, Chloroform-*d*) **δ** 163.9 (1C, C^2), 134.7 (1C, C^6), 131.5 (1C, C^3), 130.2 (1C, C^4), 124.8 (1C, C^5), 17.6 (1C, C^7); *m/z* (ESI HRMS$^+$) 142.0330 [M + H]$^+$ (C_6H_8NOS requires 142.0327).

[Copper(5-methylpyridine-2-thiolate-N-oxide)₂]

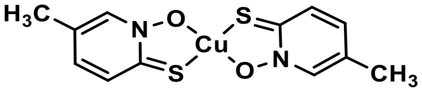

[Cu(5-Me-PT)$_2$]

To a solution (5 ml) of 3-methylpyridine-2-thiol-*N*-oxide (**2.2c**) (100 mg, 0.71 mmol) in aqueous NaOH (43 mg, 0.71 mmol), a solution of copper sulfate dihydrate (60 mg, 0.35 mmol) in H_2O (5 ml) was added dropwise. The reaction mixture was stirred for 1 h. The grey colour precipitate that formed was collected by filtration and washed with water and ethanol. The crude dark green solid was dissolved in dichloromethane (15 ml). The solution was decanted from undissolved solid, and evaporation of solvent produced the *title compound* as a dark green solid (45 mg, 25%).

m/z (ASAP HRMS$^+$) 343.9712 [M+H]$^{+\bullet}$ ($C_{12}H_{13}{}^{63}CuN_2O_2S_2$ requires 343.9714); Anal. Found (Expected) C 41.92 (41.91) H 3.48 (3.52) N 7.76 (8.15); HPLC (method A): t_R = 8.7 min.

2,6-dibromopyridine-N-oxide

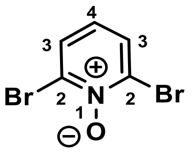

2.6

To a solution of 2,6-dibromopyridine (100 mg, 0.42 mmol) in CH_2Cl_2 (10 ml) at 0 °C, trifluoroacetic anhydride (0.6 ml, 0.42 mmol) was added dropwise. This was followed by the addition of urea hydrogen peroxide (376 mg, 4.0 mmol) at 0 °C with stirring. The reaction mixture was allowed to warm to the room temperature and left stirring overnight. The reaction was quenched with a saturated aqueous solution of $NaHCO_3$ (10 ml) and the mixture was extracted with CH_2Cl_2 (3 x 10 ml). The organic layers were combined, dried over $MgSO_4$, and the solvent was evaporated under reduced pressure. The crude yellow solid was purified by column chromatography on silica (CH_2Cl_2:5% MeOH) to produce the *title compound* as a white solid (47 mg, 43%).

^{1}H NMR (600 MHz, Chloroform-*d*) **δ** 7.63 (2H, d, $^{3}J_{H\text{-}H}$ 8.1, H^3), 6.92 (1H, t, $^{3}J_{H\text{-}H}$ 8.1 Hz, H^4); ^{13}C NMR (151 MHz, Chloroform-*d*) **δ** 133.8 (2C, C^2), 129.6 (2C, C^3), 124.8 (1C, C^4); *m/z* (ESI LRMS$^+$) 254.067 $[M+H]^+$ ($C_5H_4NO^{79}Br_2$ requires 253.867); R_f = 0.20 (silica, CH_2Cl_2: 10% MeOH).

tert-Butyl magnesium chloride

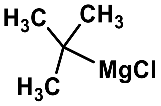

2.5

A mixture of Mg turnings (480 mg, 20 mmol) and iodine (266 mg, 1.05 mmol) were heated under inert atmosphere to remove any adventitious water. After cooling, a solution of 2-chloro-2-methyl-propane (2.0 g, 21 mmol) in anhydrous THF (12 ml) under an inert N_2 atmosphere was added dropwise and the resultant mixture was heated at reflux for 3 h. After cooling, the mixture was used directly for the next step, assuming the yield to be quantitative.

2-bromo-6-(tert-butyl)-pyridine

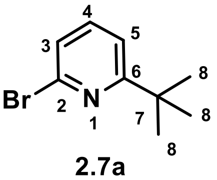

2.7a

Under a N_2 atmosphere, 2,6-dibromopyridine (500 mg, 2.11 mmol) and CuI (40.2 mg, 0.21 mmol, 10 mol%) were suspended in anhydrous THF (30 ml). At 0 °C and with stirring, *t*-BuMgCl (16.0 ml of a 2.0 M solution in THF, 30.0 mmol, 1.5 eq.) was added dropwise to the reaction mixture, which turned black upon addition. The mixture was allowed to warm to room temperature and was stirred for 14 h. The reaction was quenched with a saturated aqueous solution of NH_4Cl (20 ml) and the mixture was extracted with CH_2Cl_2 (3 x 100 ml). The combined organic layers were dried over $MgSO_4$, and the solvent was evaporated under reduced pressure. The crude brown liquid was purified by column chromatography on silica (hexane) to produce the *title compound* as a colourless liquid (250 mg, 55%).

^{1}H NMR (400 MHz, Acetone-d_6) **δ** 7.64 (1H, t, $^3J_{H\text{-}H}$ 7.8 Hz, H^4), 7.43 (1H, d, $^3J_{H\text{-}H}$ 7.8 Hz,H^5), 7.37 (1H, d, $^3J_{H\text{-}H}$ 7.8 Hz, H^3), 1.32 (9H, s, H^8); ^{13}C NMR (101 MHz, Acetone-d_6) **δ** 170.9 (1C, C^6), 140.7 (1C, C^2), 139.3 (1C, C^4), 125.0 (1C, C^3), 118.2 (1C, C^5), 37.2 (1C, C^7), 29.2 (1C, C^8); m/z (ESI HRMS$^+$) 214.0235 [M+H]$^+$ ($C_9H_{13}N^{79}Br$ requires 214.0231); R_f = 0.85 (silica, hexane).

2-Bromo-6-(tert-butyl)-pyridine-N-oxide

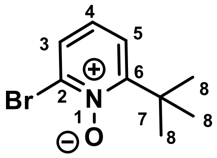

2.8a

To a solution of 2-bromo-6-(*tert*-butyl)-pyridine (200 mg, 2.34 mmol) in CH_2Cl_2 (10 ml) at 0 °C, trifluoroacetic anhydride (0.7 ml, 4.67 mmol) was added dropwise. This was followed by the addition of urea hydrogen peroxide (461 mg, 4.9 mmol) at 0 ˚C with stirring. The reaction mixture was allowed to warm to the room temperature and left stirring overnight. The reaction was quenched with a saturated aqueous solution of $Na_2S_2O_3$ (10 ml) and saturated aqueous solution of $NaHCO_3$ (20 ml) and the mixture was extracted with CH_2Cl_2 (3 x 30 ml). The organic layers were combined, dried over $MgSO_4$, and the solvent was evaporated under reduced pressure. The crude white solid was purified by column chromatography on silica (hexane: 30% EtOAc) to produce the *title compound* as a yellow oil (128 mg, 60%).

^{1}H NMR (600 MHz, Acetone-d_6) **δ** 7.74 (1H, dd, $^3J_{H\text{-}H}$ 8.0, $^4J_{H\text{-}H}$ 1.9 Hz, H^3), 7.47 (1H, dd, $^3J_{H\text{-}H}$ 8.0, $^4J_{H\text{-}H}$ 1.9 Hz, H^5), 7.15 (1H, t, $^3J_{H\text{-}H}$ 8.0 Hz, H^4), 1.47 (9H, s, H^8); ^{13}C NMR (151 MHz, Acetone-d_6) **δ** 159.1(1C, C^6), 134.8 (1C, C^2), 128.8 (1C, C^3), 124.0 (1C, C^4), 122.8 (1C, C^5), 36.6 (1C, C^7), 26.1 (3C, C^8); *m/z* (HRMS$^+$) 230.0189 [M+H]$^+$ ($C_9H_{13}NO^{79}Br$ requires 230.0181); R_f = 0.20 (silica, Hexane : 30% EtOAc).

6-(tert-Butyl)-2-thiol-pyridine-N-oxide

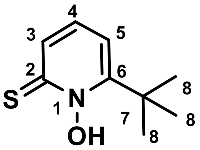

2.9

2-Bromo-6-(*tert*-butyl)-pyridine-*N*-oxide (200 mg, 0.87 mmol) was added to a saturated solution of NaSH.H_2O (10 ml) and stirred at 80 ˚C for 20 h. The reaction was quenched with aqueous 4M HCl (25 ml) and hydrogen sulfide gas produced during quenching process was trapped into aqueous $ZnCl_2$ solution. The desired organic compound was extracted in ethyl acetate (3 x 15 ml). The organic layers were combined, dried over $MgSO_4$ and the solvent was evaporated under reduced pressure.

Acetone (15 ml) was added to the purple residue and the undissolved yellow impurity was removed by filtration. Evaporation of the solvent under reduced pressure gave the *title compound* as a solid residue, from which a sample was taken for characterisation. To avoid decomposition, the remaining compound was dissolved in ethyl acetate and extracted with aqueous NaOH (1M, 10 ml). The aqueous layer was directly used for next step of copper complex formation, assuming the yield to be quantitative.

m/z (ASAP LRMS$^+$) 184.079 $[M+H]^+$ ($C_9H_{14}NOS$ requires 184.080).

2-bromo-6-isopropyl-pyridine

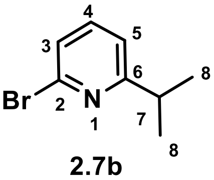

2.7b

Under a N_2 atmosphere, 2,6-dibromopyridine (300 mg, 1.26 mmol) and CuI (24 mg, 0.13 mmol, 10 mol%) were suspended in anhydrous THF (10 ml). At 0 °C and with stirring, *i*-PrMgCl (1.3 ml of a 2.0 M solution in THF, 30.0 mmol, 1.5 eq.) was added dropwise to the reaction mixture, which turned dark green upon addition. The mixture was allowed to warm to room temperature and was stirred for 14 h. The reaction was quenched with a saturated aqueous solution of NH_4Cl (20 ml) and the mixture was extracted with CH_2Cl_2 (3 x 20 ml). The combined organic layers were dried over $MgSO_4$, and the solvent was evaporated under reduced pressure. The crude brown liquid was purified by column chromatography on silica (hexane) to produce the *title compound* as a colourless liquid (58 mg, 23%).

^{1}H NMR (400 MHz, Acetone-*d$_6$*) **δ** 8.34 (1H, d, $^3J_{\text{H-H}}$ 7.7 Hz, H^6), 7.83 (1H, t, $^3J_{\text{H-H}}$ 7.7 Hz, H^5), 7.30 (1H, d, $^3J_{\text{H-H}}$ 7.7 Hz, H^4), 3.15 (1H, m, H^7)1.35 (6H, s, H^8); *m/z* (ESI LRMS$^+$) 200.145 [M+H]$^+$ ($C_8H_{11}N^{79}Br$ requires 200.007); R$_f$ = 0.85 (silica, hexane).

2-Bromo-3-methoxypyridine-N-oxide

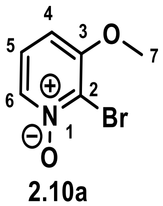

2.10a

To a solution of 2-bromo-3-methoxypyridine (200 mg, 1.06 mmol) in CH_2Cl_2 (15 ml) at 0 °C, trifluoroacetic anhydride (0.3 ml, 2.13 mmol) was added dropwise. This was followed by the addition of urea hydrogen peroxide (200 mg, 2.13 mmol) at 0 °C with stirring. The reaction mixture was allowed to warm to the room temperature and stirred for 14 h. The reaction was quenched with a saturated aqueous solution $NaHCO_3$ (20 ml) and the mixture was extracted with CH_2Cl_2 (3 x 15 ml). The organic layers were combined, dried over $MgSO_4$, and the solvent was evaporated under reduced pressure. The crude brown oil was purified by column chromatography on silica (CH_2Cl_2: 3% MeOH) to produce the *title compound* as a white solid (120 mg, 55%).

^{1}H NMR (599 MHz, Chloroform-*d*) **δ** 8.08 (1H, dd, $^3J_{\text{H-H}}$ 6.6 Hz, $^4J_{\text{H-H}}$ 1.2 Hz, H^6), 7.14 (1H, dd, $^3J_{\text{H-H}}$ 8.5 Hz, $^3J_{\text{H-H}}$ 6.6 Hz, H^5), 6.77 (1H, dd, $^3J_{\text{H-H}}$ 8.5 Hz, $^4J_{\text{H-H}}$ 1.2 Hz, H^4), 3.95 (3H, s, H^7); ^{13}C NMR (151 MHz, Chloroform-*d*) **δ** 156.36 (1C, C^3), 133.6 (1C, C^6), 126.03 (1C, C^2), 122.8 (1C, C^5), 107.8 (1C, C^4), 57.0 (1C, C^7); *m/z* (ESI HRMS$^+$) 203.9685 [M + H]$^+$ ($C_6H_7{}^{79}BrNO_2$ requires 203.9660); R$_f$ = 0.6 (silica, CH_2Cl_2 : 10% MeOH).

3-Methoxypyridine-2-thiol-N-oxide

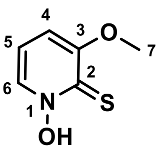

2.11a

2-Bromo-3-methoxypyridine-*N*-oxide (100 mg, 0.49 mmol) was added to a saturated aqueous solution of NaSH.H_2O (5 ml) and the orange reaction mixture was allowed to stir overnight at 80 °C. The reaction was then quenched with aqueous 4M HCl (25 ml) and hydrogen sulfide gas produced during quenching process was trapped into aqueous $ZnCl_2$ solution. The desired organic compound was extracted in ethyl acetate (3 x 10 ml). The organic layers were combined, dried over $MgSO_4$ (anhydrous) and the solvent was evaporated under reduced pressure.

Acetone (15 ml) was added to yellow residue and the undissolved yellow impurity was removed by filtration. Evaporation of solvent under reduced pressure gave *title compound* as solid residue, from which a sample was taken for characterisation. To avoid decomposition, the remaining compound was dissolved in aqueous NaOH (1M, 15 ml). The aqueous layer was directly used for next step of copper complex formation, assuming the yield to be quantitative.

^{1}H NMR (600 MHz, D_2O) **δ** 7.63 (1H, d, $^3J_{\text{H-H}}$ 5.6 Hz, H^6), 6.76 (1H, dd, $^3J_{\text{H-H}}$ 8.5 Hz, $^4J_{\text{H-H}}$ 3.8 Hz, H^4), 6.70 (1H, dt, $^3J_{\text{H-H}}$ 8.5 Hz, $^3J_{\text{H-H}}$ 5.6 Hz, H^5), 3.76 – 3.63 (3H, m, H^7); ^{13}C NMR (151 MHz, D_2O) **δ** 157.8 (1C, C^3), 155.8 (1C, C^2), 131.4 (1C, C^6), 114.7 (1C, C^5), 108.6 (1C, C^4), 56.2 (1C, C^7); *m/z* (ESI HRMS$^+$) 158.0302 $[M + H]^+$ ($C_6H_8NO_2S$ requires 158.0276).

[Copper(3-methoxy-2-thiolate-N-oxide)₂]

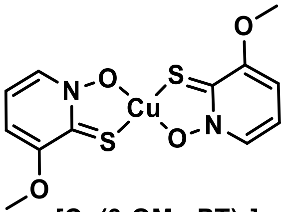

[Cu(3-OMe-PT)$_2$]

To a solution (10 ml) of the sodium salt of 3-methoxypyridine-2-thiol-*N*-oxide (100 mg, 0.63 mmol) in aqueous NaOH (25 mg, 0.63 mmol), a solution of copper chloride dihydrate (54 mg, 0.32 mmol) in H_2O (5 ml) was added dropwise. The reaction mixture was stirred for 1 h. The green precipitate that formed was collected by filtration and washed with water. The crude dark green solid obtained was dissolved in dichloromethane (5 ml). The solution was decanted from undissolved solid and evaporation of solvent produced the *title compound* as a dark green solid (25 mg, 11%*). Single crystals of the desired complex were achieved *via* slow evaporation of dichloromethane.

*yield based on two steps from **2.10a** *m/z* (ASAP HRMS$^+$) 375.9618 [M + H]$^+$ ($C_{12}H_{13}{}^{63}CuN_2O_4S_2$ requires 375.9613); Anal. Found (Expected) C 38.39 (38.34) H 3.29 (3.22) N 7.22 (7.45). HPLC (method A): t_R = 7.0 min.

2-Chloro-6-methoxypyridine-N-oxide

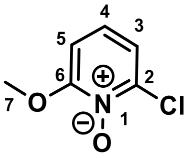

2.10b

To a solution of 2-chloro-6-methoxypyridine (500 mg, 3.48 mmol) in CH_2Cl_2 (15 ml) at 0 ˚C, trifluoroacetic anhydride (1.1 ml, 6.96 mmol) was added dropwise. This was followed by the addition of urea hydrogen peroxide (655 mg, 6.96 mmol) at 0 ˚C with stirring. The reaction mixture was allowed to warm to the room temperature and was stirred for 14 h. The reaction was quenched with saturated aqueous solutions of $NaHCO_3$ (30 mL) and extracted with CH_2Cl_2 (3 x 25 mL). The organic layer was dried over $MgSO_4$, and the solvent was evaporated under reduced pressure. This water-soluble product was also collected by evaporating H_2O layer under reduced pressure and further dissolving the organic compound in acetone. The undissolved solid salts were removed through filtration and the solvent was evaporated under vacuo to obtain *title compound* as a yellow solid (200 mg, 36%).

^{1}H NMR (600 MHz, Methanol-*d*$_4$) **δ** 7.54 (1H, t, $^3J_{H\text{-}H}$ 8.5, H^4), 7.40 (1H, d, $^3J_{H\text{-}H}$ 8.5, H^5), 7.25 (1H, d, $^3J_{H\text{-}H}$ 8.5, H^3), 4.13 (3H, s, H^3); ^{13}C NMR (151 MHz, Methanol-*d*$_4$) **δ** 159.88 (1C, C^6), 142.01 (1C, C^2), 130.02 (1C, C^4), 118.70 (1C, C^5), 106.61(1C, C^3), 57.44 (1C, C^7); *m/z* (ESI HRMS$^+$) 160.0179 [M+H]$^+$ ($C_6H_7NO_2{}^{35}Cl$ requires 160.0165); R_f = 0.40 (silica, CH_2Cl_2: 20% MeOH).

6-Methoxypyridine-2-thiol-N-oxide

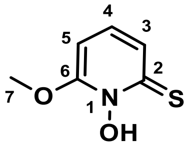

2.11b

2-Chloro-3-methoxypyridine-*N*-oxide (100 mg, 0.63 mmol) was added to a saturated aqueous solution of $NaSH.H_2O$ (5 ml) and the orange reaction mixture was allowed to stir overnight at 60 °C. The reaction was then quenched with aqueous 4M HCl (10 ml) and hydrogen sulfide gas produced during quenching process was trapped into aqueous $ZnCl_2$ solution. The desired organic compound was extracted in ethyl acetate (3 x 10 ml). The organic layers were combined, dried over $MgSO_4$ (anhydrous) and the solvent was evaporated under reduced pressure.

Acetone (5 ml) was added to purple residue and the undissolved yellow impurity was removed by filtration. Evaporation of solvent under reduced pressure gave *title compound* as solid residue, from which a sample was taken for characterisation. To avoid decomposition, the remaining compound was dissolved in aqueous NaOH (1M, 5 ml). The aqueous layer was directly used for next step of copper complex formation, assuming the yield to be quantitative.

m/z (ESI HRMS$^+$) 158.0270 $[M+H]^+$ ($C_6H_8NO_2S$ requires 158.0276).

2-Bromo-6-methoxypyridine-N-oxide

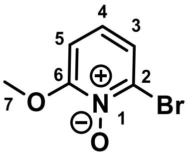

2.10c

To a solution of 2-bromo-6-methoxypyridine (0.33 ml, 2.66 mmol) in CH_2Cl_2 (15 ml) at 0 ˚C, trifluoroacetic anhydride (1.1 mL, 6.96 mmol) was added dropwise. This was followed by the addition of urea hydrogen peroxide (500 mg, 5.3 mmol) at 0 ˚C with stirring. The reaction mixture was allowed to warm to the room temperature and was stirred for 14 h. The reaction was quenched with saturated aqueous solution of $NaHCO_3$ (30 mL) and extracted with CH_2Cl_2 (3 x 20 mL). The organic layers were combined, dried over $MgSO_4$, filtered and the solvent was removed under vacuum. The crude dark brown solid was dissolved in H_2O and the undissolved solid was removed to collect the purified product in in filtrate through gravity filtration. The purple-red filtrate was evaporated to produce the *title compound* as a brown solid (220 mg, 40%).

^{1}H NMR (400 MHz, Chloroform-*d*) **δ** 7.37 (1H, d, $^3J_{H\text{-}H}$ 8.3 Hz, $^4J_{H\text{-}H}$ 1.8 Hz, H^5), 7.16 (1H, t, $^3J_{H\text{-}H}$ 8.3 Hz, H^4), 6.90 (1H, d, $^3J_{H\text{-}H}$ 8.3 Hz, $^4J_{H\text{-}H}$ 1.8 Hz, H^3), 4.11 (3H, s, H^7); ^{13}C NMR (101 MHz, Chloroform-*d*) **δ** 160.1 (1C, C^6), 134.1 (1C, C^2), 126.6 (1C, C^5), 122.5 (1C, C^4), 106.4 (1C, C^3), 57.8 (1C, C^7); *m/z* (ESI LRMS$^+$) 204.091 $[M+H]^+$ ($C_6H_7NO_2{}^{79}Br$ requires 203.966).

2-Bromo-3-ethoxypyridine

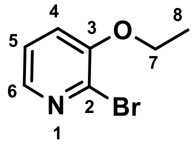

2.12

To a solution of 2-bromo-3-hydroxypyridine (200 mg, 1.15 mmol) in DMF (6 ml), ethyl iodide (0.2 ml, 1.9 mmol) and potassium carbonate (250 mg, 1.8 mmol) were added. The reaction mixture was warmed to 80 °C and stirred for 2 h. Completion of the reaction was confirmed using thin layer chromatography (silica, Hexane:30% EtOAc) and DMF was evaporated in vacuo to obtain the crude product. Excess ethyl iodide was removed by washing the crude product with H_2O (2 x 10 ml) and the desired product was extracted in EtOAc (3 x 10 ml). Then solvent was evaporated to obtain the *title compound* as a yellow oil (110 mg, 48%).

^{1}H NMR (600 MHz, Methanol-d_4) **δ** 7.88 (1H, dd, $^3J_{\text{H-H}}$ 4.7 Hz, $^4J_{\text{H-H}}$ 1.6 Hz, H^6), 7.40 (1H, dd, $^3J_{\text{H-H}}$ 8.2 Hz, $^4J_{\text{H-H}}$ 1.6 Hz, H^4), 7.33 (1H, dd, $^3J_{\text{H-H}}$ 8.2 Hz, $^3J_{\text{H-H}}$ 4.7 Hz, H^5), 4.14 (2H, q, $^3J_{\text{H-H}}$ 7.0 Hz, H^7), 1.44 (3H, t, $^3J_{\text{H-H}}$ 7.0 Hz, H^8); ^{13}C NMR (151 MHz, Methanol-d_4) **δ** 152.7 (1C, C^3), 140.3 (1C, C^6), 132.0 (1C, C^2), 123.8 (1C, C^4), 120.3 (1C, C^5), 64.8 (1C, C^7) 13.4 (1C, C^8); *m/z* (ESI HRMS$^+$) 201.9863 [M+H]$^+$ ($C_7H_9NO^{79}Br$ requires 201.9868); R_f = 0.80 (silica, Hexane: 10% EtOAc).

2-Bromo-3-ethoxypyridine-N-oxide

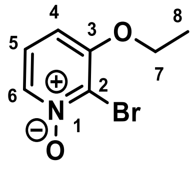

2.13

To a solution of 2-bromo-3-ethoxypyridine (500 mg, 2.45 mmol) in CH_2Cl_2 (20 ml) at 0 °C, trifluoroacetic anhydride (2 ml, 14.7 mmol) was added dropwise. This was followed by the addition of urea hydrogen peroxide (922, 9.8 mmol) at 0 °C with stirring. The reaction mixture was allowed to warm to 37 °C and stirred for 2 days. The reaction was quenched with a saturated aqueous solution of $NaHCO_3$ (20 ml) and the mixture was extracted with CH_2Cl_2 (3 x 15 ml). The organic layers were combined, dried over $MgSO_4$, and the solvent was evaporated under reduced pressure to produce the *title compound* as a yellow solid (400 mg, 74%).

^{1}H NMR (600 MHz, Chloroform-*d*) **δ** 8.07 (1H, dd, $^3J_{H\text{-}H}$ 6.6 Hz, $^4J_{H\text{-}H}$ 1.2 Hz, H^6), 7.11 (1H, dd, $^3J_{H\text{-}H}$ 8.3 Hz, $^3J_{H\text{-}H}$ 6.6 Hz, H^5), 6.75 (1H, dd, $^3J_{H\text{-}H}$ 8.3 Hz, $^4J_{H\text{-}H}$ 1.2 Hz, H^4), 4.14 (2H, q, $^3J_{H\text{-}H}$ 7.0 Hz, H^7), 1.49 (3H, t, $^3J_{H\text{-}H}$ 7.0 Hz, H^8); ^{13}C NMR (151 MHz, Chloroform-*d*) **δ** 155.8 (1C, C^3), 133.4 (1C, C^6), 126.4 (1C, C^2), 122.7 (1C, C^5), 108.7 (1C, C^4), 66.0 (1C, C^7) 14.5 (1C, C^8); *m/z* (ESI HRMS$^+$) 217.9818 [M+H]$^+$ ($C_7H_9NO_2{}^{79}Br$ requires 217.9817).

3-Ethoxypyridine-2-thiol-N-oxide

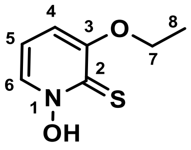

2.14

2-Bromo-3-ethoxypyridine-*N*-oxide (350 mg, 1.61 mmol) was added to a saturated aqueous solution of $NaSH.H_2O$ (6 ml) and the orange reaction mixture was allowed to stir overnight at 80 °C. The reaction was then quenched with aqueous 4M HCl (15 ml) and hydrogen sulfide gas produced during quenching process was trapped into aqueous $ZnCl_2$ solution. The desired organic compound was extracted in ethyl acetate (3 x 15 ml). The organic layers were combined, dried over $MgSO_4$ (anhydrous) and the solvent was evaporated under reduced pressure.

Acetone (10 ml) was added to purple residue and the undissolved yellow impurity was removed by filtration. Evaporation of solvent under reduced pressure gave *title compound* as solid residue (160 mg, 58%), from which a sample was taken for characterisation. To avoid decomposition, the remaining compound was dissolved in aqueous NaOH (1M, 10 ml). The aqueous layer was directly used for next step of copper complex formation.

^{1}H NMR (600 MHz, D_2O) **δ** 7.64 (1H, d, $^3J_{H\text{-}H}$ 6.6 Hz, H^6), 6.76 (1H, d, $^3J_{H\text{-}H}$ 8.3 Hz, H^4), 6.75 (1H, dd, $^3J_{H\text{-}H}$ 7.4 Hz, H^5), 3.99 (2H, q, $^3J_{H\text{-}H}$ 7.0 Hz, H^7), 1.28 (3H, t, $^3J_{H\text{-}H}$ 7.0 Hz, H^8); ^{13}C NMR (151 MHz, D_2O) **δ** 157.0 (1C, C^3), 156.2 (1C, C^2), 131.3 (1C, C^6), 114.6 (1C, C^5), 109.7 (1C, C^4), 65.3 (1C, C^7) 13.7 (1C, C^8); *m/z* (ESI HRMS$^+$) 172.0425 [M+H]$^+$ ($C_7H_{10}NO_2S$ requires 174.0432).

[Copper(3-ethoxy-2-thiolate-N-oxide)$_2$]

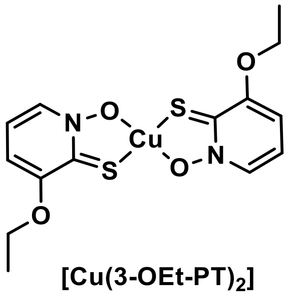

[Cu(3-OEt-PT)$_2$]

To a solution (6 ml) of the sodium salt of 3-methoxypyridine-2-thiol-*N*-oxide (100 mg, 0.58 mmol) in aqueous NaOH (23 mg, 0.58 mmol), a solution of copper chloride dihydrate (50 mg, 0.29 mmol) in H_2O (4 ml) was added dropwise. The reaction mixture was stirred for 1 h. The brown precipitate that formed was collected by filtration and washed with water. The crude dark brown solid obtained was dissolved in dichloromethane (15 ml). The solution was decanted from undissolved solid and evaporation of solvent produced the *title compound* as a dark orange solid (77 mg, 33%).

m/z (ASAP HRMS$^+$) 403.9931 [M+H]$^+$ ($C_{14}H_{17}{}^{63}CuN_2O_4S_2$ requires 403.9926) HPLC (method A): t_R = 8.3 min.

2-Bromo-3-hydroxypyridine-N-oxide

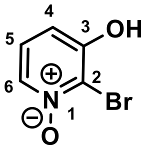

2.15

To a solution of 2-bromo-3-hydroxypyridine (500 mg, 2.87 mmol) in acetic acid (3 ml) and trifluoroacetic acid (0.4 ml) at 0 °C, hydrogen peroxide (30%, 0.6 ml, 5.74 mmol) was added at 0 °C while stirring. The reaction mixture was allowed to warm to the room temperature and left stirring for two days. The reaction mixture was then concentrated to one-third of its original volume under reduced pressure and kept refrigerated overnight leading to the formation of a white precipitation. The crude white solid was collected by filtration and was purified by recrystallisation from chloroform to produce the *title compound* as a white solid (230 mg, 42%).

^{1}H NMR (400 MHz, Methanol-d_4) **δ** 8.08 (1H, dd, $^3J_{H\text{-}H}$ 6.4 Hz, $^4J_{H\text{-}H}$ 1.3 Hz, H^6), 7.30 (1H, dd, $^3J_{H\text{-}H}$ 8.6 Hz, $^3J_{H\text{-}H}$ 6.4 Hz, H^5), 7.06 (1H, dd, $^3J_{H\text{-}H}$ 8.6 Hz, $^4J_{H\text{-}H}$ 1.3 Hz, H^4); ^{13}C NMR (101

MHz, Methanol-d_4) **δ** 155.8 (1C, C^3), 131.7 (1C, C^6), 124.5 (1C, C^2), 123.8 (1C, C^5), 115.2 (1C, C^4); *m/z* (ESI HRMS$^+$) 189.9482 [M + H]$^+$ ($C_5H_4{}^{79}BrNO_2$ requires 189.9504).

3-Hydroxypyridine-2-thiol-N-oxide

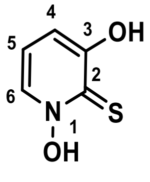

2.16

2-Bromo-3-hydroxypyridine-*N*-oxide (100 mg, 0.52 mmol) was added to a saturated aqueous solution of NaSH.H_2O (10 ml) and the orange reaction mixture was allowed to stir overnight at 80 °C. The reaction was then quenched with aqueous 4M HCl (15 ml) and hydrogen sulfide gas produced during quenching process was trapped into aqueous $ZnCl_2$ solution. The desired organic compound was extracted in ethyl acetate (3 x 15 ml). The organic layer was dried over $MgSO_4$ (anhydrous) and the solvent was evaporated under reduced pressure.

Acetone (5 ml) was added to yellow residue and the undissolved yellow impurity was removed by filtration. Evaporation of solvent under reduced pressure gave *title compound* as a yellow solid residue (55 mg, 58%), from which a sample was taken for characterisation. To avoid decomposition, the remaining compound was dissolved in aqueous NaOH (1M, 5 ml). The aqueous layer was directly used for next step of copper complex formation.

^{1}H NMR (600 MHz, D_2O) **δ** 7.26 (1H, dd, $^3J_{H-H}$ 6.5 Hz, $^4J_{H-H}$ 1.5 Hz, H^6), 6.48 (1H, dd, $^3J_{H-H}$ 8.1 Hz, $^3J_{H-H}$ 6.5 Hz, H^5), 6.32 (1H, dd, $^3J_{H-H}$ 8.1 Hz, $^4J_{H-H}$ 1.5 Hz, H^4); ^{13}C NMR (151 MHz, D_2O) **δ** 165.7 (1C, C^3), 155.6 (1C, C^2), 125.2 (1C, C^6), 115.7 (1C, C^5), 113.2 (1C, C^4); *m/z* (ESI LRMS$^+$) 144.194 [M + H]$^+$ ($C_5H_6NO_2S$ requires 144.012).

[Copper(3-hydroxy-2-thiolate-N-oxide)₂]

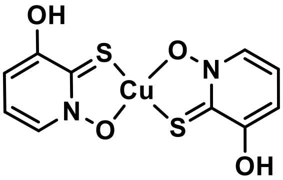

[Cu(3-OH-PT)$_2$]

To an aqueous solution (5 ml) of 3-hydroxypyridine-2-thiol-*N*-oxide (100 mg, 0.69 mmol) and sodium hydroxide (28 mg, 0.69 mmol), a solution of copper chloride dihydrate (60 mg, 0.35 mmol) in H_2O (5 ml) was added dropwise. The reaction mixture was stirred for 1 h. The grey precipitate that formed was collected by filtration and washed with water. The crude dark brown solid obtained was dissolved in H_2O and methanol solvent mixture (5 ml). The solution was decanted from undissolved solid, and evaporation of solvent produced the *title compound* as a brown solid (86 mg, 36%).

m/z (ESI HRMS$^+$) 347.9300 $[M + H]^+$ ($C_{10}H_9{}^{63}CuN_2O_4S_2$ requires 347.9300); HPLC (method A): $t_R = 8.1$ min.

2-Chloro-4-trifluoromethylpyridine-N-oxide

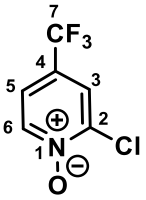

2.17a

2-Chloro-4-trifluoromethylpyridine (0.36 ml, 2.75 mmol) was dissolved in a mixture of trifluoroacetic acid (5 ml) and trifluoroacetic anhydride (4.5 ml, 12 equiv.). The solution was cooled on ice, followed by the dropwise addition of 30% H_2O_2 (30% aq., 3 ml, 12 equiv.). The solution was then allowed to warm to room temperature before being heated to reflux at 80 °C temperature overnight. The solvent was removed *in vacuo* and the crude yellow liquid product (321 mg, 59%) was used without further purification.

^{1}H NMR (600 MHz, D_2O) **δ** 8.46 – 8.33 (1H, m, H^6), 8.01 (1H, dd, $^4J_{H\text{-}H}$ 2.7 Hz, $^5J_{H\text{-}H}$ 1.1 Hz, H^3), 7.69 – 7.55 (1H, m, H^5); ^{13}C NMR (151 MHz, D_2O) **δ** 142.8 (1C, C^2), 141.3 (1C, C^6), 131.1 (1C, q, $^2J_{C\text{-}F}$ 36.0 Hz, C^4), 125.2 (1C, q, $^3J_{C\text{-}F}$ 3.9 Hz, C^3), 121.7 (1C, q, $^3J_{C\text{-}F}$ 3.6 Hz, C^5), 121.5 (1C, q, $^1J_{C\text{-}F}$ 272.5 Hz, C^7); ^{19}F NMR (375 MHz, Chloroform-*d*) **δ** -63.7; *m/z* (ESI HRMS$^+$) 197.9938 $[M+H]^{+\bullet}$ ($C_6H_4F_3{}^{35}ClNO$ requires 197.9934).

4-Trifluoromethyl-2-thiol-N-oxide

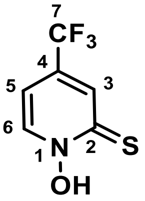

2.18a

2-Chloro-4-trifluoromethylpyridine-*N*-oxide (100 mg, 1.01 mmol) was added to a saturated aqueous solution of NaSH.H_2O (5 ml) and the orange reaction mixture was allowed to stir at

80 °C overnight, until the starting material was consumed. The reaction was quenched with aqueous 4 M HCl (10 ml) and extracted with ethyl acetate (3 x 5 ml). The organic layers were combined, dried over $MgSO_4$ (anhydrous) and the solvent was evaporated under reduced pressure.

Acetone (5 ml) was added to the purple residue and the undissolved yellow impurity was removed by filtration. Evaporation of the solvent under reduced pressure gave the *title compound* as a solid residue, from which a sample was taken for characterisation. To avoid decomposition, the remaining compound was dissolved in ethyl acetate and extracted with aqueous NaOH (1 M, 15 ml). The aqueous layer was directly used for next step of copper complex formation, assuming the yield to be quantitative.

^{1}H NMR (600 MHz, D_2O) **δ** 8.09 (1H, d, $^3J_{H\text{-}H}$ 6.9 Hz, H^6), 7.75 (1H, d, $^4J_{H\text{-}H}$ 2.6 Hz, H^3), 7.05 (1H, dd, $^3J_{H\text{-}H}$ 6.9 Hz, $^4J_{H\text{-}H}$ 2.6 Hz, H^5); ^{13}C NMR (151 MHz, D_2O) **δ** 143.1 (1C, C^2), 139.6 (1C, C^6), 137.5 (1C, q, $^2J_{C\text{-}F}$ 30.2 Hz, C^4), 128.9 (1C, q, $^3J_{C\text{-}F}$ 3.0 Hz, C^3), 112.9 (1C, $^3J_{C\text{-}F}$ 3.0 Hz C^5), 107.7 (1C, q, $^1J_{C\text{-}F}$ 271.8 Hz, C^7); ^{19}F NMR (375 MHz, Chloroform-*d*) **δ** -64.3; *m/z* (ESI LRMS$^+$) 196.0054 [M+H]$^+$ ($C_6H_5F_3NOS$ requires 196.0044).

[Copper(4-trifluoromethyl-2-thiolate-N-oxide)$_2$]

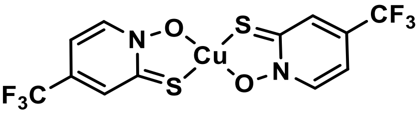

[Cu(4-CF$_3$-PT)$_2$]

To a solution (5 ml) of 4-trifluoromethylpyridine-2-thiol-*N*-oxide (200 mg, 1.02 mmol) in aqueous NaOH, a solution of copper sulfate dihydrate (87 mg, 0.51 mmol) in H_2O (10 ml) was added dropwise. The reaction mixture was stirred for 2 h. The dark green precipitate that formed was collected by filtration and washed with water and ethanol. The crude dark green solid obtained was dissolved in dichloromethane (3 ml). The solution was removed from undissolved solid, and evaporation of solvent produced the *title compound* as a dark green solid (80 mg, 17%*).

*yield based on two steps from **2.17a**

m/z (ASAP HRMS$^+$) 450.9132 [M+H]$^{+\bullet}$ ($C_{12}H_7{}^{63}CuF_6N_2O_2S_2$ requires 451.9149); Anal. Found (Expected) C 32.00 (31.9) H 1.34 (1.34) N 6.18 (6.20); HPLC (method A): t_R = 10.7 min.

2-Chloro-6-trifluoromethylpyridine-N-oxide

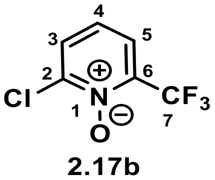

2.17b

2-Chloro-6-trifluoromethylpyridine (500 mg, 2.21 mmol) was dissolved in a mixture of trifluororacetice acid (5 ml) and trifluoroacetic anhydride (5 ml, 16 equiv.). The solution was cooled on ice, followed by the dropwise addition of 30% H_2O_2 (30% aq., 3 ml, 12 equiv.). The solution was then allowed to warm to room temperature before being heated to reflux for 45 minutes. The solvent was removed *in vacuo* and the crude yellow oil product was used without further purification.

^{1}H NMR (600 MHz, Chloroform-*d*) **δ** 7.69 (1H, dd, $^3J_{\text{H-H}}$ 8.2 Hz, $^4J_{\text{H-H}}$ 2.0 Hz, H^3), 7.65 (1H, dd, $^3J_{\text{H-H}}$ 8.2 Hz, $^4J_{\text{H-H}}$ 2.0 Hz, H^5), 7.29 (1H, t, $^3J_{\text{H-H}}$ 8.2 Hz, H^4); ^{13}C NMR (151 MHz, Chloroform-*d*) **δ** 144.6 (1C, C^2), 140.9 (1C, q, $^2J_{\text{C-F}}$ 33.8 Hz, C^6), 129.7 (1C, C^3) 124.1 (1C, C^4), 123.1 (1C, q, $^1J_{\text{C-F}}$ 4.2 Hz, C^5), 119.5 (1C, q, $^3J_{\text{C-F}}$ 272.9 Hz, C^7); ^{19}F NMR (375 MHz, Chloroform-*d*) -69.2; *m/z* (ESI LRMS$^+$) 197.997 [M + H]$^+$ ($C_6H_4F_3{}^{35}ClNO$ requires 197.993).

6-Trifluoromethyl-2-thiol-N-oxide

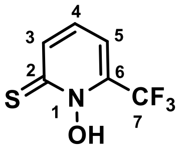

2.18b

2-Chloro-6-trifluoromethylpyridine-*N*-oxide (440 mg, 2.22 mmol) was added to a saturated aqueous solution of $NaSH.H_2O$ (20 ml) and the orange reaction mixture was allowed to stir at room temperature for 3 h, until the starting material was consumed. The reaction was quenched with aqueous 4 M HCl (25 ml) and extracted with ethyl acetate (3 x 15 ml). The organic layers were combined, dried over $MgSO_4$ (anhydrous) and the solvent was evaporated under reduced pressure.

Acetone (15 ml) was added to the purple residue and the undissolved yellow impurity was removed by filtration. Evaporation of the solvent under reduced pressure gave the *title compound* as a solid residue, from which a sample was taken for characterisation. To avoid decomposition, the remaining compound was dissolved in ethyl acetate and extracted with aqueous NaOH (1 M, 15 ml). The aqueous layer was directly used for next step of copper complex formation, assuming the yield to be quantitative.

^{1}H NMR (700 MHz, D_2O) **δ** 7.69 (1H, d, $^3J_{H-H}$ 8.0 Hz, H^3), 7.27 (1H, d, $^3J_{H-H}$ 8.0 Hz, H^5), 7.11 (1H, t, $^3J_{H-H}$ 8.0 Hz, H^4); ^{13}C NMR (175 MHz, D_2O) **δ** 151.4 (1C, C^6), 128.0 (1C, C^2), 135.6 (1C, C^3), 126.7 (1C, C^5), 117.1 (1C, C^4), 106.3 (1C, C^7); *m/z* (ESI HRMS$^+$) 196.034 [M+H]$^+$ ($C_6H_5F_3NOS$ requires 196.004).

[Copper(6-trifluoromethyl-2-thiolate-N-oxide)₂]

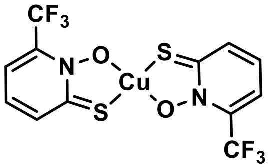

[Cu(6-CF$_3$-PT)$_2$]

To a solution of the sodium salt of 6-trifluoromethylpyridine-2-thiolate-*N*-oxide (200 mg, 1.02 mmol), a solution of copper sulfate dihydrate (87 mg, 0.51 mmol) in H_2O (5 ml) was added dropwise. The reaction mixture was stirred for 2 h. The green precipitate that formed was collected by filtration and washed with water. The crude dark green solid obtained was dissolved in dichloromethane (5 ml). Insoluble material was removed by syringe filtration before the solution was purified by column chromatography on silica (100% CH_2Cl_2) to produce the *title compound* as a dark brown solid (93 mg, 20%*). Single molecule crystals of the product were produced *via* a slow evaporation of CH_2Cl_2.

*yield based on two steps from **2.17b**

m/z (ASAP HRMS$^+$) 450.9066 [M]$^{+\bullet}$ ($C_{12}H_6{}^{63}CuF_6N_2O_2S_2$ requires 450.9071); Anal. Found (Expected) C 32.12 (31.9) H 1.45 (1.34) N 6.08 (6.20); R_f = 0.8 (silica, CH_2Cl_2); HPLC (method A): t_R = 9.9 min.

2-Bromo-5-phenylpyridine-N-oxide

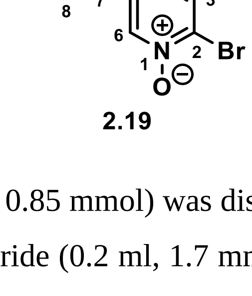

2.19

2-Bromo-5-phenylpyridine (200 mg, 0.85 mmol) was dissolved in a mixture of trifluoroacetic acid (2 ml) and trifluoroacetic anhydride (0.2 ml, 1.7 mmol). The solution was cooled on ice, followed by the dropwise addition of H_2O_2 solution (30% aq., 3 ml, 2.5 mmol). The reaction mixture was then allowed to warm to room temperature before being heated to reflux at 80 °C temperature for 14 h. The solvent was removed *in vacuo* to give the crude product as an orange gel. The crude product was purified by dissolving in chloroform and undissolved yellow solid impurities were removed by filtration. The solvent was evaporated under reduced pressure to obtain the *title compound* as a yellow solid (190 mg, 89%).

^{1}H NMR (600 MHz, Methanol-d_4) **δ** 8.76 (1H, s, H^6), 7.95 (1H, d, $^3J_{H\text{-}H}$ 8.5 Hz, H^3), 7.69 (1H, d, $^3J_{H\text{-}H}$ 8.5 Hz, H^4), 7.68-7.65 (2H, m, H^{8,12}), 7.52-7.47 (3H, m, H^{9,10,11}); ^{13}C NMR (151 MHz, Methanol-d_4) **δ** 139.6 (1C, C^5), 138.2 (1C, C^6), 134.0 (1C, C^7), 131.1 (1C, C^3), 129.1 (2C, C^{9,11}), 128.9 (1C, C^{10}), 127.4 (1C, C^4), 126.6 (2C, C^{8,12}); *m/z* (ESI HRMS$^+$) 249.9873 [M+H]$^+$ ($C_{11}H_9{}^{79}BrNO$ requires 249.9868).

5-Phenylpyridine-2-thiol-N-oxide

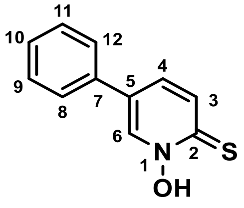

2.20

2-Bromo-5-phenylpyridine-*N*-oxide (100 mg, 0.40 mmol) was added to a saturated aqueous solution of $NaSH.H_2O$ (5 ml) and the orange reaction mixture was allowed to stir overnight at 80 °C. The reaction was then quenched with aqueous 4M HCl (25 ml) and extracted with ethyl acetate (3 x 10 ml). The organic layers were combined, dried over $MgSO_4$ (anhydrous) and the solvent was evaporated under reduced pressure.

Acetone (15 ml) was added to yellow residue and the undissolved yellow impurity was removed by filtration. Evaporation of solvent under reduced pressure gave the *title compound* as a dark green solid (60 mg, 73%).

^{1}H NMR (700 MHz, Methanol-d_4) **δ** 8.72 (1H, d, $^4J_{H\text{-}H}$ 2.0 Hz, H^6), 7.75 (1H, d, $^3J_{H\text{-}H}$ 8.9 Hz, $^4J_{H\text{-}H}$ 2.0 Hz, H^4), 7.71 (1H, d, $^3J_{H\text{-}H}$ 8.9 Hz, H^3), 7.68-7.64 (2H, m, H^{8,12}), 7.53-7.47 (2H, m, H^{9,11}), 7.46-7.40 (1H, m, H^{10}); ^{13}C NMR (175 MHz, Methanol-d_4) **δ** 165.8 (1C, C^2), 134.6 (1C, C^5), 131.8 (1C, C^7), 131.6 (1C, C^6), 130.0 (1C, C^4), 129.0 (2C, C^{9,11}), 128.3 (1C, C^3), 126.0 (2C, C^{8,12}); *m/z* (ESI HRMS$^+$) 204.0476 [M + H]$^+$ ($C_{11}H_{10}NOS$ requires 204.0483).

[Copper(5-phenylpyridine-2-thiolate-N-oxide)$_2$]

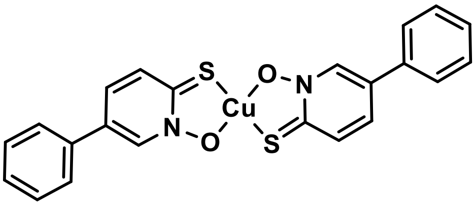

[Cu(5-Ph-PT)$_2$]

To an aqueous solution of sodium hydroxide (39 mg, 0.98 mmol) and 5-phenylpyridine-2-thiol-*N*-oxide (200 mg, 0.98 mmol) in H_2O (5 ml), a solution of copper chloride dihydrate (84 mg, 0.49 mmol) in H_2O (5 ml) was added dropwise. The reaction mixture was stirred for 1 h at room temperature. The green precipitate that formed was collected by filtration and washed with water. The crude light green solid was purified by trituration with CH_2Cl_2. Undissolved green solid was removed by filtration and the solvent removed to produce the *title compound* as a dark green solid (150 mg, 32%).

m/z (ASAP HRMS$^+$) 468.0031 [M + H]$^+$ ($C_{22}H_{17}{}^{63}CuN_2O_2S_2$ requires 468.0027) HPLC (method A): t_R = 11.5 min.

2-Chloro-quinoline-N-oxide

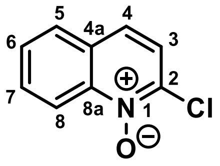

2.21

To a solution of 2-chloro-quinoline (200 mg, 1.22 mmol) in CH_2Cl_2 (10 ml) at 0 °C, trifluoroacetic anhydride (0.33 ml, 2.44 mmol) was added dropwise. This was followed by the addition of urea hydrogen peroxide (230 mg, 2.44 mmol) at 0 °C with stirring. The reaction mixture was allowed to warm to the room temperature and stirred for 14 h. The reaction was quenched with a saturated aqueous solution of $NaHCO_3$ (20 ml) and the mixture was extracted with CH_2Cl_2 (3 x 30 ml). The organic layers were combined, dried over $MgSO_4$, and the solvent was evaporated under reduced pressure. The crude brown oil was purified by dissolving in H_2O. Undissolved material was removed by filtration and the filtrate was collected and solvent was evaporated under reduced pressure to give the *title compound* as a brown solid (156 mg, 70%).

^{1}H NMR (600 MHz, Chloroform-*d*) **δ** 8.75 (1H, d, $^{3}J_{\text{H-H}}$ 8.8 Hz, H^{8}), 7.88 – 7.82 (1H, m, H^{3}), 7.78 (1H, ddd, $^{3}J_{\text{H-H}}$ 8.8, $^{4}J_{\text{H-H}}$ 4.2, $^{5}J_{\text{H-H}}$ 1.6 Hz, H^{7}), 7.68 – 7.58 (2H, m, H$^{4,\,6}$), 7.47 (1H, dd, $^{3}J_{\text{H-H}}$ 8.8, $^{4}J_{\text{H-H}}$ 4.2 Hz, H^{5}); ^{13}C NMR (151 MHz, Chloroform-*d*) **δ** 142.6 (1C, C^{2}), 138.7 (1C, C^{8a}), 131.1 (1C, C^{7}), 128.7 (1C, C^{6}), 128.7 (1C, C^{4a}), 128.2 (1C, C^{3}), 125.7 (1C, C^{4}), 122.7 (1C, C^{5}), 119.9 (1C, C^{8}); *m/z* (ESI HRMS^{+}) 180.0214 [M+H]$^{+}$ ($C_9H_7{}^{35}ClNO$ requires 180.0216).

Quinoline-2-thio-N-oxide

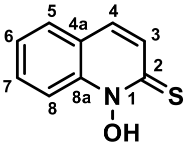

2.22

2-Chloro-quinoline-*N*-oxide (200 mg, 1.13 mmol) was added to a saturated solution of NaSH.H_2O (10 ml) and stirred at 80 ˚C for 20 h. The reaction was quenched with aqueous 4M HCl (15 ml) and extracted with ethyl acetate (3 x 10 ml). The organic layers were combined, dried over $MgSO_4$ and the solvent was evaporated under reduced pressure.

Acetone (10 ml) was added to the purple residue and the undissolved yellow impurity was removed by filtration. Evaporation of the solvent under reduced pressure gave the *title compound* as a brown oil, from which a sample was taken for characterisation. To avoid decomposition, the remaining compound was dissolved in ethyl acetate and extracted with aqueous NaOH (1M, 10 ml). The yellow aqueous layer was directly used for next step of copper complex formation, assuming the yield to be quantitative.

^{1}H NMR (400 MHz, D_2O) **δ** 8.20 (1H, d, $^{3}J_{\text{H-H}}$ 8.8 Hz, H^{4}), 7.80 (1H, m, H^{8}), 7.71 (1H, m, H^{5}), 7.61– 7.50 (2H, m, H^{6,7}), 7.44 (1H, d, $^{3}J_{\text{H-H}}$ 8.8 Hz, H^{3}); *m/z* (ESI HRMS^{+}) 178.0319 [M+H]$^{+\bullet}$ (C_9H_8NOS requires 178.0327).

[Copper(quinoline-2-thiolate-N-oxide)$_2$]

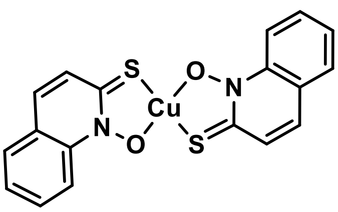

[Cu(Q-PT)$_2$]

To an aqueous solution of the sodium salt of quinoline-2-thiol-N-oxide (10 ml), a solution of copper sulfate dihydrate (114 mg, 0.71 mmol) in H_2O (5 ml) was added dropwise. The reaction mixture was stirred for 2 h at room temperature. The green precipitate that formed was collected by filtration and washed with water and ethanol. The crude light green solid obtained was purified by trituration with CH_2Cl_2. Undissolved blue solid was removed by filtration and the solvent removed to produce the *title compound* as a dark green solid (120 mg, 26%*).

*yield based on two steps from **2.17a**

m/z (ASAP HRMS$^+$) 415.9714 $[M+H]^+$ ($C_{18}H_{13}{}^{63}CuN_2O_2S_2$ requires 415.9714); Anal. Found (Expected) **C** 51.25 (51.97) **H** 2.90 (2.91) **N** 6.41 (6.73); HPLC (method A): t_R = 11.3 min.

2-Bromo-5-bromomethylpyridine

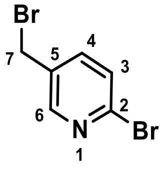

3.1

2-Bromo-5-methylpyridine (0.33 ml, 2.91 mmol) was dissolved in dry chloroform (20 ml) under N_2 atmosphere. To the solution was then added *N*-bromosuccinimide (570 mg, 3.2 mmol) and benzoyl peroxide (35 mg, 0.15 mmol) and the reaction mixture was heated at reflux for 14 h. After cooling the mixture to room temperature, the solvent was evaporated to obtain the crude product as a yellow oil. The crude product was purified by silica gel column chromatography on silica (90% hexane:10% EtOAc) to produce the *title compound* as white solid (316 mg, 44%).

^{1}H NMR (600 MHz, Chloroform-*d*) **δ** 8.37 (1H, d, $^4J_{H-H}$ 2.5 Hz, H^6), 7.58 (1H, dd, $^3J_{H-H}$ 8.2 Hz, $^4J_{H-H}$ 2.5 Hz, H^4), 7.47 (1H, dd, $^3J_{H-H}$ 8.2 Hz, $^5J_{H-H}$ 0.7 Hz, H^3), 4.40 (2H, s, H^7); ^{13}C NMR (151 MHz, Chloroform-*d*) **δ** 150.0 (1C, C^6), 141.9 (1C, C^2), 139.1 (1C, C^4), 133.0 (1C, C^5), 128.3 (1C, C^3), 28.3 (1C, C^7); *m/z* (ESI HRMS$^+$) 249.8872 $[M + H]^+$ ($C_6H_6{}^{79}Br_2N$ requires 249.8867); R_f = 0.5 (silica, Hexane : 20% EtOAc).

2-Bromo-5-(2-methoxyethoxy)methyl)pyridine

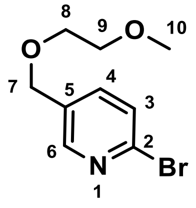

3.2a

2-Bromo-5-(bromomethyl)pyridine (500 mg, 1.99 mmol) was added to a solution of 2-methoxyethanol (0.19 ml, 2.39 mmol) and sodium hydride (96 mg, 2.39 mmol) in dry THF (15 ml) under N_2 atmosphere at 0 °C. The reaction mixture was then stirred at room temperature overnight under N_2 atmosphere. After completion, the reaction mixture was quenched with H_2O and product was extracted in EtOAc. The organic layer was washed with H_2O (3 x 20 ml), dried over $MgSO_4$ and the solvent was evaporated under reduced pressure to produce *compound* ***3.2a*** as a yellow oil (350 mg, 71%).

^{1}H NMR (599 MHz, Chloroform-*d*) **δ** 8.32 (1H, d, $^4J_{\text{H-H}}$ 2.4 Hz, H^6), 7.56 (1H, dd, $^3J_{\text{H-H}}$ 8.1 Hz, $^4J_{\text{H-H}}$ 2.4 Hz, H^3), 7.45 (1H, d, $^3J_{\text{H-H}}$ 8.1 Hz, H^4), 4.53 (2H, s, H^7), 3.67 – 3.61 (2H, m, H^8), 3.60-3.53 (2H, m, H^9), 3.38 (3H, s, H^{10}); ^{13}C NMR (151 MHz, Chloroform-*d*) **δ** 149.3 (1C, C^6), 141.3 (1C, C^5), 138.0 (1C, C^4), 133.1 (1C, C^2), 127.9 (1C, C^3), 71.9 (1C, C^9), 69.9 (1C, C^8), 69.9 (1C, C^7), 59.1 (1C, C^{10}); *m/z* (ESI HRMS$^+$) 246.0130 [M + H]$^+$ ($C_9H_{13}{}^{79}BrNO_2$ requires 246.0130).

2-Bromo-5-((2-methoxyethoxy)methyl)pyridine-N-oxide

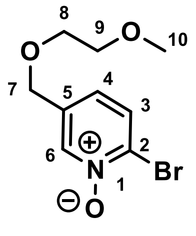

3.3a

2-Bromo-5-((2-methoxyethoxy)methyl)pyridine (300 mg, 0.85 mmol) was added to chloroform (20 ml) and the mixture was allowed to stir at room temperature. Then 3-chloroperbenzoic acid (444 mg, 2.57 mmol) was added slowly and the reaction mixture was stirred for a further 14 h. The reaction was quenched with the addition of saturated aqueous solution of sodium bicarbonate (approx. 10 ml) and the product was extracted with chloroform (3 x 20 ml). The organic layers were combined, dried over $MgSO_4$, filtered and the solvent was removed under reduced pressure. The crude yellow solid was purified by column chromatography on silica (95% CH_2Cl_2:5% MeOH) to produce *compound **3.3a*** as a brown liquid (200 mg, 63%).

^{1}H NMR (600 MHz, Chloroform-*d*) **δ** 8.39 (1H, s, H^6), 7.59 (1H, d, $^3J_{\text{H-H}}$ 8.3 Hz, H^4), 7.07 (1H, d, $^3J_{\text{H-H}}$ 8.3 Hz, H^3), 4.50 (2H, s, H^7), 3.71 – 3.60 (2H, m, H^9), 3.60-3.53 (2H, m, H^8), 3.38 (3H, s, H^{10}); ^{13}C NMR (151 MHz, Chloroform-*d*) **δ** 139.1 (1C, C^6), 136.8 (1C, C^5), 131.5 (1C, C^2), 130.3 (1C, C^4), 124.7 (1C, C^3), 71.8 (1C, C^9), 70.3 (1C, C^8), 69.1 (1C, C^7), 59.1 (1C, C^{10}); *m/z* (ESI HRMS$^+$) 262.0057 [M + H]$^+$ ($C_9H_{13}{}^{79}BrNO_3$ requires 262.0079).

5((2-methoxyethoxy)methyl)pyridine-2-thiol-N-oxide

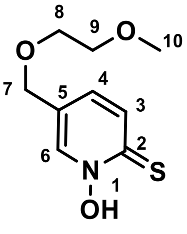

3.4a

2-Bromo-5-((2-methoxyethoxy)methyl)pyridine-*N*-oxide (300 mg, 1.14 mmol) was dissolved in H_2O (5 ml). A solution of sodium sulfide (446 mg, 5.7 mmol) and sodium hydroxide (137 mg, 3.43 mmol) in H_2O (10 ml) was then added to above solution and the reaction mixture was stirred at 93 °C overnight. After cooling reaction to room temperature, the yellow solution was acidified to pH 1-2 with 1 M HCl and product was extracted with EtOAc (3 x 20 ml). The organic layer was collected, dried over $MgSO_4$, filtered and the solvent was removed under reduced pressure. The crude product was then purified by dissolving in acetone where yellow solid impurity precipitated out. Residue yellow solution was collected through gravity filtration and solvent was evaporated under vacuum to obtain *compound **3.4a*** as a brown solid (125 mg, 51%).

^{1}H NMR (600 MHz, Chloroform-*d*) **δ** 8.12 (1H, s, H^6), 7.63 (1H, d, $^3J_{\text{H-H}}$ 8.7 Hz, H^3), 7.22 (1H, d, $^3J_{\text{H-H}}$ 8.7 Hz, H^4), 4.45 (2H, s, H^7), 3.67 – 3.64 (2H, m, H^8), 3.58-3.54 (2H, m, H^9), 3.38 (3H, s, H^{10}); ^{13}C NMR (151 MHz, Chloroform-*d*) **δ** 165.9 (1C, C^2), 132.1 (1C, C^4), 131.7 (1C, C^3), 129.9 (1C, C^6), 125.7 (1C, C^5), 71.7 (1C, C^9), 70.1 (1C, C^8), 69.1 (1C, C^7), 59.1 (1C, C^{10}); *m/z* (ESI HRMS$^+$) 216.0696 [M + H]$^+$ ($C_9H_{14}NO_3S$ requires 216.0694).

[Copper(5-(2-methoxyethoxy)methyl)pyridine-2-thiolate-N-oxide)$_2$]

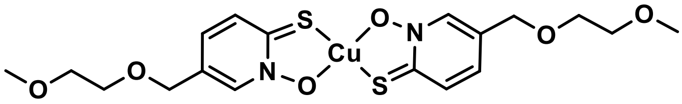

[Cu(5-PEG1-PT)$_2$]

5((2-methoxyethoxy)methyl)pyridine-2-thiol-*N*-oxide (100 mg, 0.46 mmol) was dissolved in a solution of sodium hydroxide (18 mg, 0.46 mmol) in H_2O (5 ml). A solution of copper chloride dihydrate (39 mg, 0.23 mmol) in H_2O (2 ml) was added dropwise to the reaction mixture and grey solid was observed. After 1 h of stirring the reaction mixture at room temperature, the grey solid was collected through filtration in a sintered funnel. This crude product was further purified through trituration process using dichloromethane as the solvent. The solvent was evaporated under reduced pressure to obtain *[Cu(5-PEG1-PT)$_2$]* as a dark green solid (110 mg, 43%).

m/z (ESI HRMS$^+$) 492.0434 [M + H]$^+$ ($C_{18}H_{25}{}^{63}CuN_2O_6S_2$ requires 492.0450); Anal. Found (Expected) **C** 43.79 (43.94) **H** 4.92 (4.92) **N** 5.64 (5.69); HPLC (method A): t_R = 4.9 min.

2-Bromo-5((2-(2-methoxyethoxy)ethoxy)methyl)pyridine

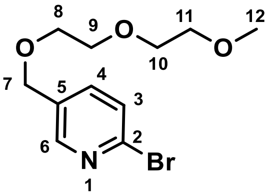

3.2b

2-Bromo-5-(bromomethyl)pyridine (100 mg, 0.4 mmol) was added to a solution of 2-(2-methoxyethoxy)ethanol (0.06 ml, 0.48 mmol) and sodium hydride (19 mg, 0.48 mmol) in dry THF (10 ml) under N_2 atmosphere at 0 °C. The reaction mixture was then stirred at room temperature overnight under N_2 atmosphere. After completion, the reaction mixture was quenched with H_2O and extracted in EtOAc, dried over $MgSO_4$, and the solvent was evaporated under reduced pressure. The crude orange solid was further purified using silica gel column chromatography (80% hexane:20% EtOAc) to produce *compound* ***3.2b*** as a brown oil (127 mg, 90%).

^{1}H NMR (600 MHz, Chloroform-*d*) **δ** 8.26 (1H, d, $^4J_{H\text{-}H}$ 2.4 Hz, H^6), 7.59 – 7.45 (1H, dd, $^3J_{H\text{-}H}$ 8.1 Hz, $^4J_{H\text{-}H}$ 2.4 Hz, H^4), 7.39 (1H, d, $^3J_{H\text{-}H}$ 8.1 Hz, H^3), 4.48 (2H, s, H^7), 3.65 – 3.60 (4H, m, H^{8,9}), 3.59 – 3.56 (2H, m, H^{10}), 3.50 – 3.47 (2H, m, H^{11}), 3.31 (3H, s, H^{12}); ^{13}C NMR (151

MHz, Chloroform-*d*) **δ** 149.3 (1C, C^5), 141.1 (1C, C^2), 138.0 (1C, C^4), 133.2 (1C, C^6), 127.9 (1C, C^3), 71.9 (1C, C^{11}), 70.6 (1C, C^{10}), 70.5 (1C, C^9), 70.0 (1C, C^8), 69.8 (1C, C^7), 59.0 (1C, C^{12}); *m/z* (ESI HRMS$^+$) 290.0413 $[M + H]^+$ ($C_{11}H_{17}{}^{79}BrNO_3$ requires 290.0392); R_f = 0.2 (silica, 80% Hexane:20% EtOAc).

2-Bromo-5((2-(2-methoxyethoxy)ethoxy)methyl)pyridine-N-oxide

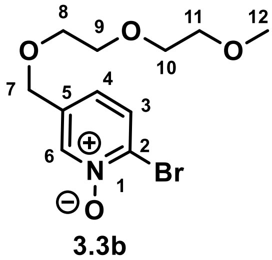

3.3b

2-Bromo-5((2-(2-(2-methoxyethoxy)ethoxy)ethoxy)methyl)pyridine (450 mg, 1.35 mmol) was added to chloroform (20 ml) and the mixture was allowed to stir at room temperature. Then 3-Chloroperbenzoic acid (700 mg, 4.05 mmol) was added slowly, and the reaction mixture was stirred for a further 16 h. The reaction was quenched with the addition of saturated aqueous solution of sodium bicarbonate (approx. 20 ml) and the product was extracted with chloroform (3 x 15 ml). The organic layers were combined, dried over $MgSO_4$, filtered and the solvent was removed under reduced pressure. The crude yellow solid was purified by column chromatography on silica (95% CH_2Cl_2:5% MeOH) to produce *compound **3.3b*** as a brown oil (200 mg, 48%).

^{1}H NMR (600 MHz, Chloroform-*d*) **δ** 8.40 (1H, s, H^6), 7.59 (1H, d, $^3J_{H-H}$ 8.3 Hz, H^3), 7.09 (1H, dt, $^3J_{H-H}$ 8.3 Hz, $^4J_{H-H}$ 1.1 Hz, H^4), 4.50 (2H, s, H^7), 3.69 – 3.61 (10H, m, $H^{8,9,10,11,12}$), 3.55 – 3.52 (2H, m, H^{13}), 3.36 (3H, s, H^{14}); ^{13}C NMR (151 MHz, Chloroform-*d*) **δ** 139.1 (1C, C^6), 136.9 (1C, C^2), 131.5 (1C, C^5), 130.3 (1C, C^3), 124.8 (1C, C^4), 71.9 (1C, C^{13}), 70.7-70.3 (5C, $C^{8,9,10,11,12}$), 69.0 (1C, C^7), 59.0 (1C, C^{14}); *m/z* (ESI HRMS$^+$) 350.0619 $[M + H]^+$ ($C_{13}H_{21}{}^{79}BrNO_5$ requires 350.0603); R_f = 0.4 (silica, 95% CH_2Cl_2:5% MeOH).

5((2-(2-methoxyethoxy)ethoxy)methyl)pyridine-2-thiol-N-oxide

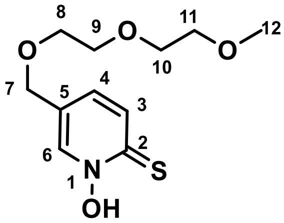

3.4b

2-Bromo-5((2-(2-(2-methoxyethoxy)ethoxy)ethoxy)methyl)pyridine-*N*-oxide (150 mg, 0.43 mmol) was dissolved in H_2O (5 ml). A solution of sodium sulfide (168 mg, 2.15 mmol) and sodium hydroxide (52 mg, 1.29 mmol) in H_2O (5 ml) was then added to above solution and the reaction mixture was stirred at 93 °C overnight. After cooling the reaction to room temperature, the yellow solution was acidified to pH 1-2 with 1 M HCl and product was extracted with EtOAc (3 x 10 ml). The organic layer was collected, dried over $MgSO_4$, filtered and the solvent was removed under reduced pressure. The crude product was then purified by dissolving in acetone where a yellow solid impurity precipitated out. The residue yellow solution was collected through gravity filtration and the solvent was evaporated under vacuum to obtain *compound* ***3.4b*** as a brown oil. A small amount of dried product was kept for characterisation purpose and rest of the product was dissolved in aqueous NaOH solution to stabilise the compound and this ligand solution then directly used for the next step of copper complex formation.

^{1}H NMR (600 MHz, Chloroform-*d*) **δ** 8.19 (1H, s, H^6), 7.67 (1H, d, $^3J_{\text{H-H}}$ 8.7 Hz, H^3), 7.26 (1H, d, $^3J_{\text{H-H}}$ 8.7 Hz, H^4), 4.50 (2H, s, H^7), 3.78 – 3.61 (10H, m, $H^{8, 9, 10, 11, 12}$), 3.61 – 3.56 (2H, m, H^{13}), 3.40 (3H, s, H^{14}); ^{13}C NMR (151 MHz, Chloroform-*d*) **δ** 149.4 (1C, C^6), 141.3 (1C, C^2), 138.1 (1C, C^4), 133.2 (1C, C^5), 127.9 (1C, C^3), 71.9 (1C, C^7), 70.6 (1C, $C^{8, 9, 10, 11}$), 70.0 (1C, C^{12}), 69.9 (1C, C^{13}), 59.1 (1C, C^{14}); *m/z* (ESI HRMS$^+$) 304.1230 $[M + H]^+$ ($C_{13}H_{21}NO_5S$ requires 304.1219).

[Copper(5((2-(2-methoxyethoxy)ethoxy)methyl)pyridine-2-thiolate-N-oxide)₂]

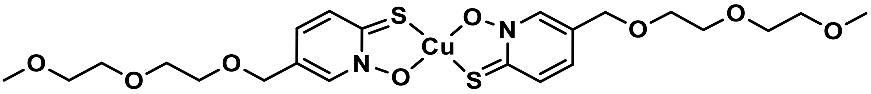

[Cu(5-PEG2-PT)₂]

5((2-(2-methoxyethoxy)ethoxy)methyl)pyridine-2-thiolate-*N*-oxide (80 mg, 0.31 mmol) was dissolved in a solution of sodium hydroxide (12 mg, 0.31 mg) in H_2O (5 ml). A solution of copper chloride dihydrate (27 mg, 0.16 mmol) in H_2O (2 ml) was added dropwise to the reaction mixture and the resulted dark green solution was then allowed to be stirred for 1 h. Mass spectrometry data of reaction mixture suggested formation of desired complex and after evaporation of water, complex [Cu(5-PEG2-PT)$_2$] was obtained as a dark green sticky oil (30 mg, 33%).

m/z (ESI HRMS$^+$) 668.1506 $[M + H]^+$ ($C_{26}H_{41}{}^{63}CuN_2O_{10}S_2$ requires 668.1499); Anal. Found (Expected) **C** 46.63 (46.73) **H** 6.20 (6.03) **N** 4.10 (4.19); HPLC (method A): t_R = 4.7 min.

2-Bromo-5((2-(2-(2-methoxyethoxy)ethoxy)ethoxy)methyl)pyridine

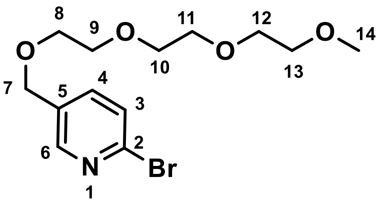

3.2c

2-Bromo-5-(bromomethyl)pyridine (500 mg, 1.99 mmol) was added to a solution of 2-(2-(2-methoxyethoxy)ethoxy)ethanol (0.4 ml, 2.39 mmol) and sodium hydride (96 mg, 2.39 mmol) in dry THF (15 ml) under N_2 atmosphere at 0 °C. The reaction mixture was then stirred at room temperature overnight under N_2 atmosphere. After completion, the reaction mixture was quenched with H_2O and product was extracted in EtOAc. The organic layer was washed with H_2O (3 x 20 ml), dried over $MgSO_4$ and solvent was evaporated under reduced pressure to produce the *compound* ***3.2c*** as yellow oil (460 mg, 69%).

^{1}H NMR (600 MHz, Chloroform-*d*) **δ** 8.31 (1H, d, $^4J_{\text{H-H}}$ 2.4 Hz, H^6), 7.56 (1H, dd, $^3J_{\text{H-H}}$ 8.2 Hz, $^4J_{\text{H-H}}$ 2.4 Hz, H^3), 7.45 (1H, d, $^3J_{\text{H-H}}$ 8.2 Hz, H^4), 4.53 (2H, s, H^7), 3.68 – 3.62 (10H, m, $H^{8, 9, 10, 11, 12}$), 3.53 (2H, m, H^{13}), 3.36 (3H, s, H^{14}); ^{13}C NMR (151 MHz, Chloroform-*d*) **δ** 149.3 (1C, C^6), 141.2 (1C, C^2), 138.0 (1C, C^3), 133.2 (1C, C^5), 127.9 (1C, C^4), 71.9 (1C, C^{13}), 70.7 (1C, C^{11}), 70.6 (2C, $C^{9, 10}$), 70.5 (1C, C^{12}), 70.0 (1C, C^8), 69.8 (1C, C^7), 59.0 (1C, C^{14}); *m/z* (ESI HRMS$^+$) 334.0667 $[M + H]^+$ ($C_{13}H_{21}{}^{79}BrNO_4$ requires 334.0654).

2-Bromo-5((2-(2-(2-methoxyethoxy)ethoxy)ethoxy)methyl)pyridine-N-oxide

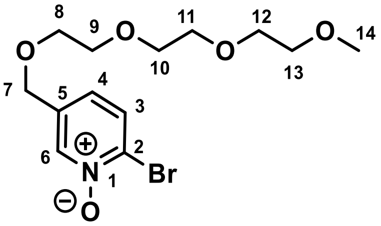

3.3c

2-Bromo-5((2-(2-(2-methoxyethoxy)ethoxy)ethoxy)methyl)pyridine (450 mg, 1.35 mmol) was added to chloroform (20 ml) and the mixture was allowed to stir at room temperature. Then 3-Chloroperbenzoic acid (700 mg, 4.05 mmol) was added slowly, and the reaction mixture was stirred for a further 16 h. The reaction was quenched with the addition of saturated aqueous solution of sodium bicarbonate (approx. 20 ml) and the product was extracted with chloroform (3 x 15 ml). The organic layers were combined, dried over $MgSO_4$, filtered and the solvent was removed under reduced pressure. The crude yellow solid was purified by column chromatography on silica (95% CH_2Cl_2:5% MeOH) to produce *compound* ***3.3c*** as a brown oil (200 mg, 48%).

^{1}H NMR (600 MHz, Chloroform-*d*) **δ** 8.40 (1H, s, H^6), 7.59 (1H, d, $^3J_{\text{H-H}}$ 8.3 Hz, H^3), 7.09 (1H, dt, $^3J_{\text{H-H}}$ 8.3 Hz, $^4J_{\text{H-H}}$ 1.1 Hz, H^4), 4.50 (2H, s, H^7), 3.69 – 3.61 (10H, m, H$^{8, 9, 10, 11, 12}$), 3.55 – 3.52 (2H, m, H^{13}), 3.36 (3H, s, H^{14}); ^{13}C NMR (151 MHz, Chloroform-*d*) **δ** 139.1 (1C, C^6), 136.9 (1C, C^2), 131.5 (1C, C^5), 130.3 (1C, C^3), 124.8 (1C, C^4), 71.9 (1C, C^{13}), 70.7-70.3 (5C, C$^{8, 9, 10, 11, 12}$), 69.0 (1C, C^7), 59.0 (1C, C^{14}); *m/z* (ESI HRMS$^+$) 350.0619 [M + H]$^+$ ($C_{13}H_{21}{}^{79}BrNO_5$ requires 350.0603); R_f = 0.4 (silica, CH_2Cl_2 : 5% MeOH).

5((2-(2-(2-methoxyethoxy)ethoxy)ethoxy)methyl)pyridine-2-thiol-N-oxide

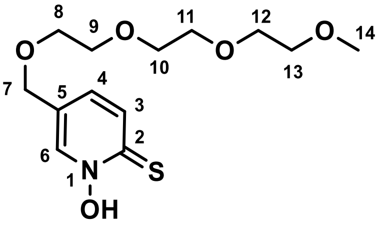

3.4c

2-Bromo-5((2-(2-(2-methoxyethoxy)ethoxy)ethoxy)methyl)pyridine-*N*-oxide (150 mg, 0.43 mmol) was dissolved in H_2O (5 ml). A solution of sodium sulfide (168 mg, 2.15 mmol) and sodium hydroxide (52 mg, 1.29 mmol) in H_2O (5 ml) was then added to above solution and the reaction mixture was stirred at 93 °C overnight. After cooling the reaction to room temperature, the yellow solution was acidified to pH 1-2 with 1 M HCl and product was extracted with EtOAc (3 x 10 ml). The organic layer was collected, dried over $MgSO_4$, filtered and the solvent was removed under reduced pressure. The crude product was then purified by dissolving in acetone where a yellow solid impurity precipitated out. The residue yellow solution was collected through gravity filtration and the solvent was evaporated under vacuum to obtain *compound* ***3.4c*** as a brown oil. A small amount of dried product was kept for characterisation purpose and rest of the product was dissolved in aqueous NaOH solution to stabilise the compound and this ligand solution then directly used for the next step of copper complex formation.

δ_H (599 MHz, D_2O) 7.91 (1H, s, H^6), 7.42 (1H, d, $^3J_{\text{H-H}}$ 8.7 Hz, H^3), 7.06 (1H, d, $^3J_{\text{H-H}}$ 8.7 Hz, H^4), 4.70 (2H, s, H^7), 3.52 – 3.48 (10H, m, H $^{8, 9, 10, 11, 12}$), 3.46 – 3.44 (2H, m, H^{13}), 3.19 (3H, s, H^{14}); **δ_C** (151 MHz, D_2O) 170.7 (1C, C^2), 145.8 (1C, C^6), 148.1 (1C, C^4), 137.2 (1C, C^3), 122.9 (1C, C^5), 70.9 (1C, C^7), 70.9 – 69.3 (5C, C$^{8, 9, 10, 11, 12}$), 68.8 (1C, C^{13}), 58.0 (1C, C^{14}); *m/z* (ESI HRMS$^+$) 304.1230 [M + H]$^+$ ($C_{13}H_{21}NO_5S$ requires 304.1219).

[Copper(5((2-(2-(2-methoxyethoxy)ethoxy)ethoxy)methyl)pyridine-2-thiolate-N-oxide)₂]

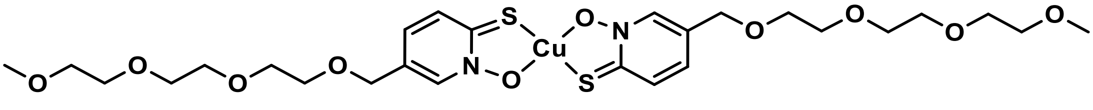

[Cu(5-PEG3-PT)₂]

5((2-(2-(2-methoxyethoxy)ethoxy)ethoxy)methyl)pyridine-2-thiol-*N*-oxide (300 mg, 0.99 mmol) was dissolved in a solution of sodium hydroxide (40 mg, 0.99 mmol) in H_2O (10 ml). A solution of copper chloride dihydrate (84 mg, 0.49 mmol) in H_2O (5 ml) was added dropwise to the reaction mixture and the resulted dark green solution was then allowed to be stirred for 1 h. Mass spectrometry data of reaction mixture suggested formation of desired complex and after evaporation of water, dark brown oily liquid was obtained. The crude product was further purified by column chromatography on silica (CH_2Cl_2) to produce the complex [Cu(5-PEG2-PT)₂] as dark green oil (135 mg, 20%).

m/z (ESI HRMS$^+$) 668.1506 $[M + H]^+$ ($C_{26}H_{41}{}^{63}CuN_2O_{10}S_2$ requires 668.1499); Anal. Found (Expected) **C** 46.63 (46.73) **H** 6.20 (6.03) **N** 4.10 (4.19); HPLC (method A): t_R = 4.6 min.

2-Bromo-5-(methoxy)methylpyridine

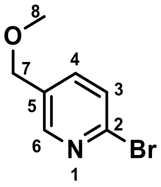

3.5

2-Bromo-5-(bromomethyl)pyridine (500 mg, 1.99 mmol) was added to a solution of methanol (0.08 ml, 2.19 mmol) and sodium hydride (60% dispersion in mineral oil) (146 mg, 2.19 mmol) in dry THF (15 ml) under N_2 atmosphere at 0 °C. The reaction mixture was stirred at room temperature overnight under N_2 atmosphere. After completion, the reaction mixture was quenched with H_2O and the product was extracted with EtOAc (20 ml). The organic layer was washed with H_2O (3 x 20 ml), dried over $MgSO_4$ and solvent was evaporated under reduced pressure to produce the *title compound* as pale yellow oil (385 mg, 95%).

^{1}H NMR (400 MHz, Chloroform-*d*) **δ** 8.35 (1H, dd, $^4J_{H\text{-}H}$ 2.5 Hz, $^5J_{H\text{-}H}$ 0.7 Hz, H^6), 7.57 (1H, dd, $^3J_{H\text{-}H}$ 8.1 Hz, $^4J_{H\text{-}H}$ 2.5 Hz, H^4), 7.09 (1H, dd, $^3J_{H\text{-}H}$ 8.1 Hz, $^5J_{H\text{-}H}$ 0.7 Hz, H^3), 4.45 (2H, s, H^7), 3.43 (3H, s, H^8); *m/z* (ESI HRMS$^+$) 201.9871 $[M + H]^+$ ($C_7H_9{}^{79}BrNO$ requires 201.9868).

2-Bromo-5-(methoxy)methylpyridine-N-oxide

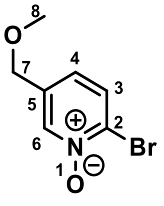

3.6

2-Bromo-5-(methoxy)methylpyridine (300 mg, 1.49 mmol) was added to chloroform (20 ml) and the mixture was allowed to stir at room temperature. 3-Chloroperbenzoic acid (512 mg, 2.98 mmol) was added slowly and the reaction mixture was stirred for a further 14 h. The reaction was quenched with the addition of saturated aqueous solution of sodium bicarbonate (approx. 10 ml) and the product was extracted with dichloromethane (3 x 20 ml). The organic layers were combined, dried over magnesium sulfate, filtered and the solvent was removed under reduced pressure. The crude orange solid was purified by dissolving in H_2O and removing solid impurities by filtration. The yellow filtrate was concentrated under reduced pressure to produce the *title compound* as yellow oil (254 mg, 78%).

^{1}H NMR (600 MHz, Chloroform-*d*) **δ** 8.41 (1H, s, H^6), 7.62 (1H, d, $^3J_{\text{H-H}}$ 8.3 Hz, H^3), 7.09 (1H, d, $^3J_{\text{H-H}}$ 8.3 Hz, H^4), 4.38 (2H, s, H^7), 3.40 (3H, s, H^8); ^{13}C NMR (151 MHz, Chloroform-*d*) **δ** 139.2 (1C, C^6), 136.7 (1C, C^5), 130.4 (1C, C^3), 130.0 (1C, C^2), 125.1 (1C, C^4), 70.2 (1C, C^7), 58.6 (1C, C^8); *m/z* (ESI HRMS$^+$) 217.9823 [M + H]$^+$ ($C_7H_9{}^{79}BrNO_2$ requires 217.9817).

5-(methoxy)methylpyridine-2-thiol-N-oxide

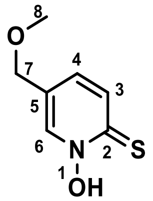

3.7

2-Bromo-5-(methoxy)methylpyridine-N-oxide (300 mg, 1.14 mmol) was dissolved in H_2O (5 ml). A solution of sodium sulfide (446 mg, 5.7 mmol) and sodium hydroxide (137 mg, 3.43 mmol) in H_2O (10 ml) was then added and the reaction mixture was stirred at 90 °C for 16 hours. After cooling the reaction to room temperature, the yellow solution was acidified to pH 1-2 with 1 M HCl and the product was extracted with EtOAc (3 x 20 ml). The organic layers were combined, dried over magnesium sulfate, filtered and the solvent was removed under reduced pressure. The crude product was purified by dissolving in acetone, leading to formation of a yellow solid impurity, which was removed by filtration. The filtrate was concentrated under reduced pressure to give the *title compound* as a brown solid (125 mg, 51%).

^{1}H NMR (400 MHz, D_2O) 7.95 (1H, $^4J_{\text{H-H}}$ 2.0 Hz, H^6), 7.45 (1H, d, $^3J_{\text{H-H}}$ 8.5 Hz, H^3), 7.04 (1H, dd, $^3J_{\text{H-H}}$ 8.5 Hz, $^4J_{\text{H-H}}$ 2.0 Hz, H^4), 4.26 (2H, s, H^7), 3.26 (3H, s, H^8); *m/z* (ESI HRMS$^+$) 172.0435 [M + H]$^+$ ($C_7H_9NO_2S$ requires 172.0432).

[Copper(5-(methoxy)methyl)pyridine-2-thiolate-N-oxide)$_2$]

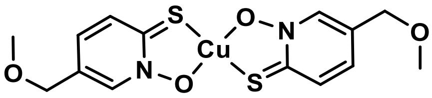

3.8

5-(methoxy)methylpyridine-2-thiol-*N*-oxide (100 mg, 0.58 mmol) and aqueous NaOH (23 mg, 0.58 mmol) were dissolved in water (5 ml) and a solution of copper chloride dihydrate (50 mg, 0.29 mmol) in H_2O (2 ml) was added dropwise. The reaction mixture was stirred for 1 h. The grey precipitate that formed was collected by filtration and washed with water. The crude grey solid obtained was dissolved in dichloromethane (5 ml). The solution was decanted from undissolved solid and evaporation of the solvent produced the *title compound* as a dark green solid (68 mg, 29%).

m/z (ASAP HRMS$^+$) 403.9926 [M+H]$^+$ ($C_{14}H_{17}{}^{63}CuN_2O_4S_2$ requires 403.9926); Anal. Found (Expected) **C** 40.78 (41.63) **H** 3.90 (3.99) **N** 6.64 (6.93).

2-Bromo-5-(prop-2-ynoxy)pyridine

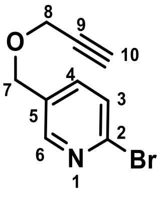

4.1

2-Bromo-5-(bromomethyl)pyridine (500 mg, 1.99 mmol) was added to a solution of 2-methoxyethanol (0.12 ml, 1.99 mmol) and sodium hydride (60% dispersion in mineral oil) (120 mg, 2.98 mmol) in dry THF (22 ml) under N_2 atmosphere at 0 °C. The reaction mixture was stirred at room temperature 16 hours under N_2 atmosphere. The reaction mixture was quenched with H_2O and the product was extracted with EtOAc (2 x 20 ml). The organic layer was washed with H_2O (3 x 20 ml), dried over $MgSO_4$ and the solvent was evaporated under reduced pressure to produce the *title compound* as yellow oil (370 mg, 83%).

^{1}H NMR (600 MHz, Chloroform-*d*) **δ** 8.33 (1H, dd, $^{4}J_{\text{H-H}}$ 2.5 Hz, $^{5}J_{\text{H-H}}$ 0.8 Hz, H^{6}), 7.55 (1H, dd, $^{3}J_{\text{H-H}}$ 8.1 Hz, $^{4}J_{\text{H-H}}$ 2.5 Hz, H^{4}), 7.46 (1H, dd, $^{3}J_{\text{H-H}}$ 8.1 Hz, $^{5}J_{\text{H-H}}$ 0.8 Hz, H^{3}), 4.57 (2H, s, H^{7}), 4.19 (2H, d, $^{4}J_{\text{H-H}}$ 2.4 Hz, H^{8}), 2.48 (1H, t, $^{4}J_{\text{H-H}}$ 2.4 Hz, H^{8}); ^{13}C NMR (151 MHz, Chloroform-*d*) **δ** 149.6 (1C, C^{6}), 141.6 (1C, C^{2}), 138.1 (1C, C^{4}), 132.3 (1C, C^{5}), 127.8 (1C, C^{3}), 78.6 (1C, C^{9}), 75.2 (1C, C^{10}), 68.1 (1C, C^{7}), 57.4 (1C, C^{8}); *m/z* (ESI HRMS^{+}) 225.9871 [M + H]$^{+}$ ($C_9H_9{}^{79}BrNO$ requires 225.9868).

2-Bromo-5-(prop-2-ynoxy)pyridine-N-oxide

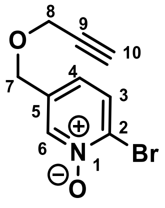

4.2

2-Bromo-5-(prop-2-ynoxy)pyridine (300 mg, 1.33 mmol) was added to chloroform (20 ml) and the mixture was allowed to stir at room temperature. 3-Chloroperbenzoic acid (687 mg, 3.99 mmol) was added slowly and the reaction mixture was stirred for a further 16 h. The reaction was quenched with the addition of saturated aqueous solution of sodium bicarbonate (approx. 20 ml) and the product was extracted with chloroform (3 x 15 ml). The organic layers were combined, dried over magnesium sulfate, filtered and the solvent was removed under reduced pressure. The crude brown solid was dissolved in H_2O and undissolved solid impurities were removed by filtration. The solvent was then evaporated under reduced pressure to produce the *title compound* as pale red solid (175 mg, 54%).

^{1}H NMR (600 MHz, Chloroform-*d*) **δ** 8.39 (1H, s, H^{6}), 7.61 (1H, d, $^{3}J_{\text{H-H}}$ 8.4 Hz, H^{4}), 7.09 (1H, d, $^{3}J_{\text{H-H}}$ 8.4 Hz, H^{3}), 4.53 (2H, s, H^{7}), 4.21 (2H, d, $^{4}J_{\text{H-H}}$ 2.4 Hz, H^{8}), 2.49 (1H, t, $^{4}J_{\text{H-H}}$ 2.4 Hz, H^{10}); ^{13}C NMR (151 MHz, Chloroform-*d*) **δ** 139.3 (1C, C^{6}), 136.0 (1C, C^{5}), 130.4 (2C, C^{2,4}), 125.0 (1C, C^{3}), 78.5 (1C, C^{9}), 75.8 (1C, C^{10}), 67.2 (1C, C^{7}), 57.9 (1C, C^{8}); *m/z* (ESI HRMS^{+}) 241.9816 [M + H]$^{+}$ ($C_9H_9{}^{79}BrNO_2$ requires 241.9817).

5-(prop-2-ynoxy)pyridine-2-thiol-N-oxide

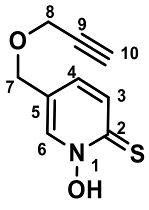

4.3

2-Bromo-5-(prop-2-ynoxy)pyridine-*N*-oxide (200 mg, 0.83 mmol) was dissolved in H_2O (5 ml). A solution of sodium sulfide (323 mg, 4.15 mmol) and sodium hydroxide (100 mg, 2.5 mmol) in H_2O (5 ml) was then added to above solution and the reaction mixture was stirred at 95 °C overnight. After cooling the reaction to room temperature, the yellow solution was acidified to pH 1-2 with 1 M HCl and product was extracted with EtOAc (3 x 20 ml). The organic layer was collected, dried over magnesium sulfate, filtered and the solvent was removed under reduced pressure to obtain *title compound* as brown oil. The crude product was then directly used as ligand for the next step of copper complex formation without further purification, assuming the yield to be quantitative.

^{1}H NMR (400 MHz, Chloroform-*d*) **δ** 12.13 (1H, s, O-H), 8.14 (1H, dd, $^4J_{\text{H-H}}$ 1.9 Hz, H^6), 7.68 (1H, d, $^3J_{\text{H-H}}$ 8.7 Hz, H^3), 7.27 (1H, dd, $^3J_{\text{H-H}}$ 8.7 Hz, $^4J_{\text{H-H}}$ 1.9 Hz, H^4), 4.53 (2H, s, H^7), 4.25 (2H, d, $^4J_{\text{H-H}}$ 2.4 Hz, H^8), 2.54 (1H, t, $^4J_{\text{H-H}}$ 2.4 Hz, H^8); *m/z* (ESI HRMS$^+$) 196.0425 [M + H]$^+$ ($C_9H_{10}NO_2S$ requires 196.0432).

[Copper(5(prop-2-ynoxy)pyridine-2-thiol-N-oxide)₂]

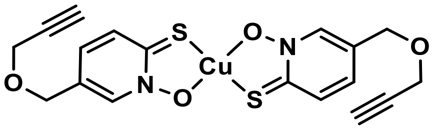

4.4

5-(Prop-2-ynoxy)pyridine-2-thiol-N-oxide (600 mg, 3.07 mmol) was dissolved in a solution of sodium hydroxide (122 mg, 3.07 mmol) in H_2O (10 ml). A solution of copper chloride dihydrate (262 mg, 1.54 mmol) in H_2O (5 ml) was added dropwise to the reaction mixture and a green solid formed, which was separated by filtration. This crude product was further purified through trituration with dichloromethane as solvent. The solvent was evaporated under reduced pressure to obtain dark green solid as the *title compound* (102 mg, 27%*).

*yield based on two steps from **4.2**

m/z (ASAP HRMS$^+$) 451.9914 [M + H]$^+$ ($C_{18}H_{17}{}^{63}CuN_2O_4S_2$ requires 451.9926); Anal. Found (Expected) **C** 48.11 (47.83) **H** 3.48 (3.57) **N** 5.82 (6.20); HPLC (method A): t_R = 9.1 min.

2-Bromo-5-azidemethylpyridine

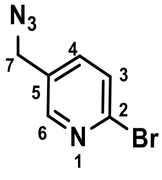

4.5

2-Bromo-5-(bromomethyl)pyridine (100 mg, 0.40 mmol) and sodium azide (28 mg, 0.44 mmol) were dissolved in anhydrous *N,N'*-dimethylformamide (2 ml) under N_2 atmosphere. The reaction mixture was left stirring overnight under N_2 atmosphere at room temperature. Completion of reaction was confirmed using mass spectrometry and the solvent was evaporated to obtain the crude product as an oil. The crude product was dissolved in chloroform and solid impurities were removed by filtration. Removal of the solvent under reduced pressure gave the *title product*, as a yellow oil (75 mg, 88%).

^{1}H NMR (600 MHz, Acetone-*d6)* **δ** 8.41 (1H, d, $^4J_{\text{H-H}}$ 2.5 Hz, H^6), 7.77 (1H, dd, $^3J_{\text{H-H}}$ 8.2 Hz, $^4J_{\text{H-H}}$ 2.5 Hz, H^4), 7.64 (1H, d, $^3J_{\text{H-H}}$ 8.2 Hz, H^3), 4.56 (2H, s, H^7); ^{13}C NMR (151 MHz, Acetone-*d6)* **δ** 149.9 (1C, C^6), 141.3 (1C, C^2), 139.2 (1C, C^4), 131.7 (1C, C^5), 127.9 (1C, C^3), 50.7 (1C, C^7); *m/z* (ESI HRMS$^+$) 212.9792 [M+H]$^+$ ($C_6H_6{}^{79}BrN_4$ requires 212.9776)

2-Bromo-5-azidemethylpyridine-N-oxide

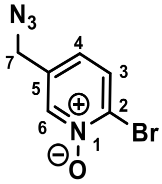

4.6

2-Bromo-5-azidemethylpyridine (550 mg, 2.58 mmol) was added to chloroform (20 ml) and the mixture was allowed to stir at room temperature. 3-Chloroperbenzoic acid (890 mg, 4.05 mmol) was added slowly, and the reaction mixture was stirred for a further 16 h. The reaction was quenched with the addition of saturated aqueous solution of sodium bicarbonate (approx. 20 ml) and the product was extracted with chloroform (3 x 15 ml). The organic layers were combined, dried over magnesium sulfate, filtered and the solvent was removed under reduced pressure. The crude yellow solid was purified by column chromatography on silica (CH_2Cl_2:2% MeOH) to produce the *title compound* as yellow liquid (200 mg, 48%).

^{1}H NMR (400 MHz, Chloroform-*d*) **δ** 8.48 (1H, d, $^4J_{\text{H-H}}$ 1.9 Hz, H^6), 7.70 (1H, d, $^3J_{\text{H-H}}$ 8.4 Hz, H^3), 7.14 (1H, dd, $^3J_{\text{H-H}}$ 8.2 Hz, $^4J_{\text{H-H}}$ 1.9 Hz, H^4), 4.40 (2H, s, H^7); *m/z* (ESI HRMS$^+$) 228.9733 [M + H]$^+$ ($C_6H_6{}^{79}BrN_4O$ requires 228.9725).

[Copper(5-(1-benzyl-1,2,3-triazole)-methoxymethyl)-pyridine-2-thiol-N-oxide)$_2$]

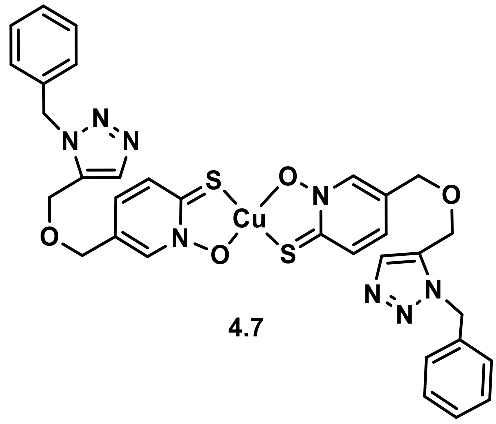

4.7

To a mixture of THF:H$_2$O (1:1) (8 ml), copper[5(prop-2-ynoxy)pyridine-2-thiol-*N*-oxide]$_2$ (20 mg, 0.04 mmol) was dissolved. Benzyl azide (0.5 M in CH$_2$Cl$_2$, 0.12 ml, 0.08 mmol) was added dropwise to the reaction mixture with stirring. Copper sulfate (10 mg, 0.08 mmol) and (+)sodium ascorbate (13 mg, 0.08 mmol) were added and the reaction mixture was stirred at 55 °C. After 2 h, completion of reaction was confirmed using mass spectrometry. The reaction mixture was quenched with saturated aqueous solution of ammonium chloride (3 ml) and washed with brine (2 ml) and H$_2$O (3 ml). The organic layer was dried over anhydrous magnesium sulfate and the solvent was evaporated under reduced pressure to obtain *title compound* as dark green solid (15 mg, 24%)

m/z (ESI HRMS$^+$) 718.1194 [M + H]$^+$ ($C_{32}H_{31}{}^{63}CuN_8O_4S_2$ requires 718.1206); HPLC (method A): t_R = 8.9 min.

[Copper(5-(1-(BDP-TR)-1,2,3-triazole)-methoxymethyl)-pyridine-2-thiol-N-oxide)$_2$]

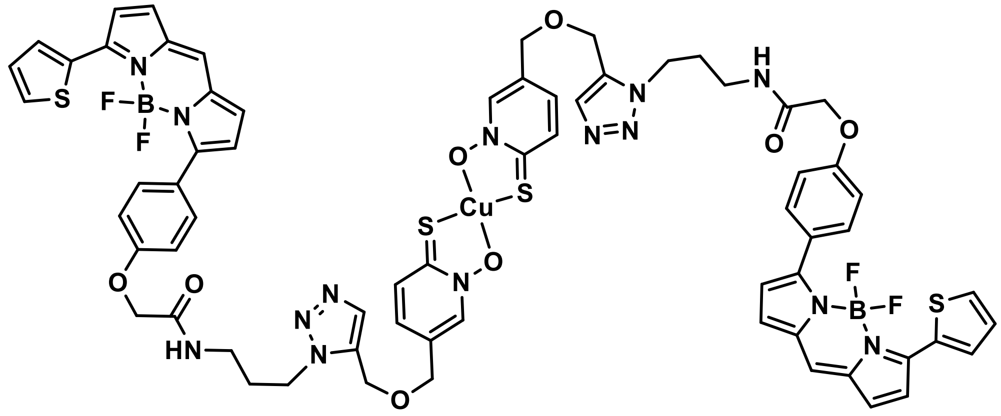

4.8

Copper[5(prop-2-ynoxy)pyridine-2-thiol-*N*-oxide]$_2$ (2 mg, 0.004 mmol) was dissolved in THF (1 ml). A solution of BDP-TR azide (4.5 mg, 0.01 mmol) in CH_2Cl_2 (0.2 ml) was added dropwise to the reaction mixture with stirring. Copper sulfate (1.6 mg, 0.009 mmol) and (+)sodium ascorbate (1.7 mg, 0.009 mmol) were added and the reaction mixture was stirred at 55 °C. After 3 h, completion of reaction was confirmed using ESI mass spectrometry. The reaction mixture was quenched with saturated aqueous solution of ammonium chloride (2 ml) and washed with brine (2 ml) and H_2O (3 ml). The organic layer was dried over anhydrous magnesium sulfate and the solvent was evaporated under reduced pressure to obtain the crude product. Preparative HPLC (method B) was used to purify the crude compound using the acetonitrile:H_2O solvent system as the eluent to give the *title compound* as dark purple solid residue (3 mg, 46%).

m/z (ESI HRMS$^+$) 1464.2795 [M + H]$^+$ ($C_{66}H_{59}B_2{}^{63}CuF_4N_{14}O_8S_4$ requires 1464.2963), 1486.2576 [M + Na]$^+$ ($C_{66}H_{58}B_2{}^{63}CuF_4N_{14}NaO_8S_4$ requires 1464.2756); HPLC (method A): t_R = 10.2 min; ϕ_{em} (MeCN) = 0.44.

[Copper(2-hydroxypyridine-N-oxide)$_2$]

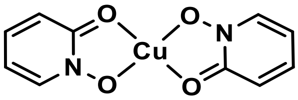

5.1

2-Hydroxypyridine-*N*-oxide (80 mg, 0.9 mmol) was dissolved in a solution of sodium hydroxide (36 mg, 0.9 mmol) in H_2O (10 ml). A solution of copper chloride dihydrate (77 mg, 0.45 mmol) in H_2O (2 ml) was added dropwise to the reaction mixture and the reaction was stirred for 1 h. The blue precipitate that formed was collected by filtration and washed with water. The crude blue solid was dissolved in dichloromethane (3 ml). The solution was decanted from undissolved solid and evaporation of the solvent produced the *title compound* as a green-blue solid (77 mg, 38%). Blue single crystals of this copper complex were grown from slow evaporation of a CH_2Cl_2: MeOH (1:2) solvent system.

m/z (ASAP HRMS$^+$) 283.9857 $[M+H]^+$ ($C_{10}H_9{}^{63}CuN_2O_4$ requires 283.9858); Anal. Found (Expected) **C** 42.03 (42.33) **H** 2.81 (2.84) **N** 9.68 (9.87).

2-Hydroxy-6-methylpyridine-N-oxide

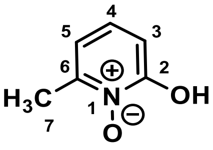

5.2

To a solution of 2-hydroxy-3-methylpyridine (200 mg, 1.8 mmol) in CH_2Cl_2 (10 ml) at 0 °C, trifluoroacetic anhydride (0.6 ml, 3.7 mmol) was added dropwise. This was followed by the addition of urea hydrogen peroxide (344 mg, 3.7 mmol) at 0 °C with stirring. The reaction mixture was allowed to warm to the room temperature and stirred for 14 h. The reaction was quenched with a saturated aqueous solution of $NaHCO_3$ (20 ml) and the mixture was extracted with CH_2Cl_2 (3 x 10 ml). The organic layers were combined, dried over $MgSO_4$, and the solvent was evaporated under reduced pressure to produce the *title compound* as a yellow solid (120 mg, 52%).

^{1}H NMR (400 MHz, Chloroform-*d*) 7.90 (1H, dd, $^3J_{\text{H-H}}$ 8.6 Hz, $^3J_{\text{H-H}}$ 7.3 Hz, H^4), 6.89 (1H, d, $^3J_{\text{H-H}}$ 8.6 Hz, H^3), 6.82 (1H, dd, $^3J_{\text{H-H}}$ 7.3 Hz, H^6), 2.58 (3H, s, H^7); *m/z* (ESI HRMS$^+$) 126.0560 $[M + H]^+$ ($C_6H_8NO_2$ requires 126.0555).

Ethyl phenyl(2-pyridyl)phosphinate

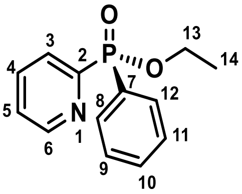

5.3

A Shlenck flask filled with anhydrous degassed toluene (5 ml) was charged with 2-bromopyridine (0.3 ml, 3.16 mmol), ethyl phenylphosphinate (0.8 ml, 3.5 mmol) and triethylamine (1.8 ml, 12.9 mmol) under nitrogen. [1,1'-Bis(diphenylphosphino)-ferrocene] dichloropalladium (II) (0.04 g, 0.055 mmol) was added and the mixture was degassed, heated to reflux and stirred under nitrogen for 16 h. The dark brown reaction mixture was diluted with CH_2Cl_2 (10 ml) and washed with HCl (1 M, 2 x 15 ml) and water (3 x 20 ml). The organic layer was dried over K_2CO_3, filtered and the solvent was removed under reduced pressure to give a clear yellow oil. Purification by column chromatography on silica (CH_2Cl_2 : 0-3% MeOH) gave the *title compound* as a yellow oil (0.82 g, 53%).

^{1}H NMR (600 MHz, Methanol-d_4) **δ** 8.72 (1H, d, $^3J_{H\text{-}H}$ 4.8 Hz, H^6), 8.06 (1H, t, $^3J_{H\text{-}H}$ 7.3 Hz, H^4), 7.95 (1H, td, $^3J_{H\text{-}H}$ 7.3 Hz $^4J_{H\text{-}H}$ 5.5 Hz, H^3), 7.92 – 7.84 (2H, m, H$^{8,\ 12}$), 7.62 – 7.56 (1H, m, H^5), 7.56 – 7.44 (3H, m, H$^{9,\ 10,\ 11}$), 4.21 – 3.87 (2H, m, H^{13}), 1.40 (3H, td, $^3J_{H\text{-}H}$ 7.1 Hz $^4J_{H\text{-}H}$ 1.7 Hz, H^{14}); ^{13}C NMR (151 MHz, Methanol-d_4) **δ** 153.5 (d, $^2J_{C\text{-}P}$ 169.5 Hz, C^2), 150.4 (d, $^3J_{C\text{-}P}$ 20.5 Hz, C^6), 136.7 (d, $^3J_{C\text{-}P}$ 10.2 Hz, C^3), 132.7 (d, $^4J_{C\text{-}P}$ 2.8 Hz, C^5), 131.8 (d, $^3J_{C\text{-}P}$ 10.1 Hz, C$^{8,\ 12}$), 129.19 (d, $^3J_{C\text{-}P}$ 140.4 Hz, C^7) 128.3 (d, $^3J_{C\text{-}P}$ 13.3 Hz, C$^{9,\ 11}$), 127.9 (d, $^4J_{C\text{-}P}$ 22.4 Hz, C^4), 126.3 (d, $^4J_{C\text{-}P}$ 3.4 Hz, C^{10}), 62.0 (d, $^3J_{C\text{-}P}$ 6.4 Hz, C^{13}), 15.3 (d, $^3J_{C\text{-}P}$ 6.3 Hz, C^{14}); ^{31}P NMR (162 MHz, Methanol-d_4) **δ** 27.0; *m/z* (ESI HRMS$^+$) 248.0846 [M + H]$^+$ ($C_{13}H_{15}NO_2P$ requires 248.0840); R_f = 0.5 (silica, CH_2Cl_2 : 5% MeOH).

Phenyl(2-pyridyl)phosphate

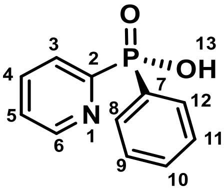

5.4

Ethyl phenyl(2-pyridyl)phosphinate (100 mg, 3.32 mmol) was dissolved in aqueous HCl (6 M, 2 ml) solution and stirred at 100 °C for 16 h. A small amount of sample from the brown reaction mixture was taken and the solvent was evaporated for characterisation. The remaining solution was adjusted to pH 5 using aqueous NaOH and the mixture was directly used for the next step of copper complex formation, assuming a quantitative yield.

m/z (ESI HRMS$^+$) 220.0532 [M + H]$^+$ ($C_{11}H_{11}NO_2P$ requires 220.0527).

[Copper(phenyl(2-pyridyl)phosphate)₂]

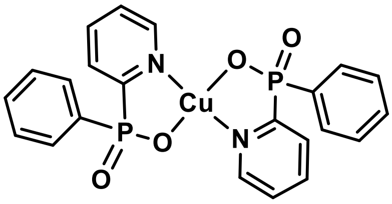

5.5

A solution of copper chloride dihydrate (114 mg, 0.71 mmol) in water (2 ml) was added dropwise to a solution of phenyl(2-pyridyl)phosphate in H_2O from the previous step. The blue reaction mixture was left stirring for 3 h at room temperature. The resulting precipitate was filtered and washed with water and dried under high vacuum to give the *title compound* as pale blue solid (67 mg*, 33%).

m/z (ESI HRMS$^+$) 500.0107 $[M+H]^+$ ($C_{22}H_{18}{}^{63}CuN_2O_4P_2$ requires 500.0116)

*yield calculated over two steps from **5.3**

[Copper(picolinate)₂]

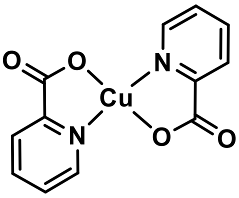

5.6

To an aqueous solution (15 ml) of picolinic acid (500 mg, 4.06 mmol) and sodium hydroxide (325 mg, 8.16 mmol), a solution of copper nitrate trihydrate (490.5 mg, 2.03 mmol) in H_2O (5 ml) was added dropwise. The reaction mixture was stirred for 2 h at room temperature. The precipitate that formed was collected by filtration, washed with water and dried under high vacuum to give the *title compound* as a violet solid (550 mg, 56%).

m/z (ESI HRMS$^+$) 307.9850 $[M-Cl]^+$ ($C_{12}H_9{}^{63}CuN_2O_4$ requires 307.9858); Anal. Found (Expected) **C** 46.45 (46.83) **H** 2.63 (2.62) **N** 9.06 (9.10).

[Cu(II)(2,2′-bipyridine)]dichloride

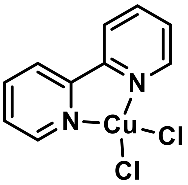

5.7

To a solution of 2,2′-bipyridine (500 mg, 3.20 mmol) in ethanol (15 ml), a solution of copper chloride dihydrate (541 mg, 3.20 mmol) in EtOH (5 ml) was added dropwise. The reaction mixture was stirred for 3 h at room temperature. The precipitate that formed was collected by filtration and washed with ethanol to produce the *title compound* as a green solid (310 mg, 33%).

m/z (ESI LRMS$^+$) 544.957 [2M-Cl+2H]$^+$ ($C_{20}H_{18}{}^{35}Cl_3{}^{63}Cu_2N_4$ requires 544.919), 220.037 [M-2Cl+H]$^+$ ($C_{10}H_9{}^{63}CuN_2$ requires 220.006); Anal. Found (Expected) **C** 41.09 (41.33) **H** 2.78 (2.77) **N** 9.62 (9.64).

N-Phenyl-1-(2-pyridinyl)methanimine

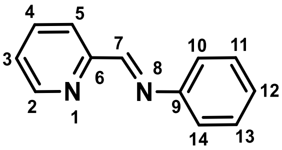

5.8a

A mixture of aniline (500 mg, 5.37 mmol) and 2-pyridinecarboxaldehyde (575 mg, 5.37 mmol) in MeOH (10 ml) was heated at 65 °C for 16 h. The yellow reaction mixture turned into a dark green solution and the completion of reaction was confirmed using thin layer chromatography (silica, CH_2Cl_2: MeOH 5%). Evaporation of solvent under reduced pressure resulted in the *title compound* as a brown oil (418 mg, 42%).

^{1}H NMR (400 MHz, Chloroform-*d*) **δ** 8.73 (1H, ddd, $^3J_{H\text{-}H}$ 6.3, $^4J_{H\text{-}H}$ 1.8, $^5J_{H\text{-}H}$ 1.1 Hz, H^2), 8.63 (1H, s, H^7), 8.22 (1H, td, $^3J_{H\text{-}H}$ 6.3, $^4J_{H\text{-}H}$ 2.9 Hz, H^3), 7.85–7.77 (1H, m, H^4), 7.47 – 7.39 (2H, m, H$^{10,\ 14}$), 7.37 (1H, ddd, $^3J_{H\text{-}H}$ 7.5, $^4J_{H\text{-}H}$ 2.9, $^5J_{H\text{-}H}$ 1.1 Hz, H^5), 7.34–7.25 (3H, m, H$^{11,\ 12,\ 13}$); ^{13}C NMR (101 MHz, Chloroform-*d*) **δ** 160.7 (1C, C^7), 154.6 (1C, C^9), 151.0 (1C, C^6), 149.7 (1C, C^2), 136.7 (1C, C^4), 129.3 (1C, C^{11,13}), 126.8 (1C, C^5), 125.2 (1C, C^{12}), 121.9 (1C, C^3), 121.1 (2C, C^{10,14}); *m/z* (ESI HRMS$^+$) 183.0917 [M+H]$^+$ ($C_{12}H_{10}N_2$ requires 183.0922).

[Copper(II) (N-Phenyl-1-(2-pyridinyl)methanimine)]dichloride

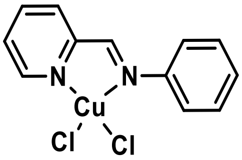

5.9a

To a solution of *N*-phenyl-1-(2-pyridinyl)methanimine (200 mg, 1.09 mmol) in acetonitrile (10 ml), a solution of $CuCl_2$. $2H_2O$ (187 mg, 1.09 mmol) in acetonitrile (5 ml) was added and the mixture was stirred at 25 °C for 1 h. The green precipitate that formed was collected through filtration and washed with acetonitrile and MeOH. Drying under high vacuum gave the *title compound* as a green solid (74 mg, 65%). Single crystals of the product were grown by vapour diffusion of hexane in CH_2Cl_2 solvent.

m/z (ASAP LRMS$^+$) 217.052 [M-CuCl]$^+$ ($C_{10}H_8{}^{35}ClN_2$ requires 217.053); Anal. Found (Expected) **C** 45.61 (45.51) **H** 3.23 (3.18) **N** 9.11 (8.85).

4-(2-Pyridinylmethylene)aminophenol

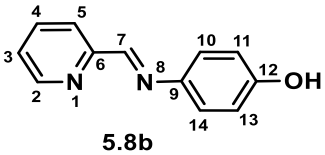

5.8b

A mixture of 4-aminophenol (200 mg, 1.83 mmol) and 2-pyridinecarboxaldehyde (196 mg, 1.83 mmol) in MeOH (10 ml) was heated at 65 °C for 16 h. The yellow reaction mixture turned into a dark green solution. After removing the solvent under reduced pressure, the crude green residue was recrystallised from hot methanol to produce the *title compound* as yellow solid (215 mg, 59%).

^{1}H NMR (600 MHz, Methanol-d_4) **δ** 8.64 (1H, dd, $^3J_{H\text{-}H}$ 6.3, $^4J_{H\text{-}H}$ 1.2 Hz, H^2), 8.60 (1H, s, H^7), 8.16 (1H, d, $^3J_{H\text{-}H}$ 7.7 Hz, H^5), 7.93 (1H, td, $^3J_{H\text{-}H}$ 7.7, $^4J_{H\text{-}H}$ 1.2 Hz, H^4), 7.47 (1H, ddd, $^3J_{H\text{-}H}$ 6.3, $^4J_{H\text{-}H}$ 1.2 Hz, H^3), 7.30 – 7.23 (2H, m, H$^{11,\ 13}$), 6.87 – 6.80 (2H, m, H$^{10,\ 14}$); ^{13}C NMR (151 MHz, Methanol-d_4) **δ** 157.2 (1C, C^{12}), 156.3 (1C, C^7), 154.4 (1C, C^6), 149.0 (1C, C^2) , 142.1 (1C, C^9), 137.3 (1C, C^4), 125.1 (1C, C^3), 122.4 (2C, C$^{11,\ 13}$), 121.6 (1C, C^5), 115.5 (2C, C$^{10,\ 14}$); *m/z* (ESI HRMS$^+$) 199.0859 [M+H]$^+$ ($C_{12}H_{11}N_2O$ requires 199.0871).

[Copper(II)(4-(2-pyridinylmethylene) aminophenol)]dichloride

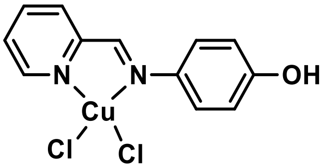

5.9b

4-(2-Pyridinylmethylene)aminophenol (100 mg, 0.50 mmol) was dissolved in acetonitrile (8 ml) at 60 °C. A solution of $CuCl_2,2H_2O$ (86 mg, 0.50 mmol) in acetonitrile (2 ml) was added dropwise and the mixture was stired at 60 °C for 1h. The red coloured precipitate that formed was collected through filtration and washed with acetonitrile and MeOH. Drying under high vacuum gave the *title compound* as a red solid (75 mg, 45%).

m/z (ASAP LRMS$^+$) 233.046 [M-CuCl]$^+$ ($C_{10}H_8{}^{35}ClN_2$ requires 233.048); Anal. Found (Expected) **C** 42.86 (43.33) **H** 2.94 (3.03) **N** 8.36 (8.42).

Appendix

Crystallography Data:

The X-ray single crystal data have been collected for substituted copper pyrithione complexes by Dr. Dmitry S. Yufit using λMoKα radiation (λ = 0.71073Å) on a Bruker D8 Venture (Photon III MM C7 CPAD detector, IμS micro-source, focusing mirrors) 3-circle diffractometer equipped with a Cryostream-700 (Oxford Cryosystems) open-flow nitrogen cryostat at the temperature 130.0 (2)K. The structure was solved by direct method and refined by full-matrix least squares on F2 for all data using Olex2[275] and SHELXTL[276] software. All non-hydrogen atoms were refined in anisotropic approximation, hydrogen atoms were placed in the calculated positions and refined in riding mode. Crystal data and parameters of refinement are listed in Tables S1-S12. Data Centre as supplementary publication CCDC-2184348 ([Cu(5-PEG1-PT)$_2$]).

1. *trans*-[Cu(6-Me-PT)$_2$]

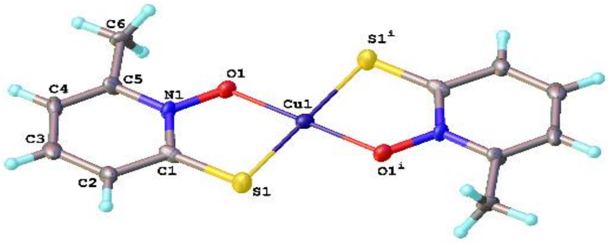

Table S1: Crystal data and structure refinement for ***trans*-[Cu(6-Me-PT)$_2$]**

Empirical formula	$C_{12}H_{12}CuN_2O_2S_2$
Formula weight	343.90
Temperature/K	120.0
Crystal system	monoclinic
Space group	$P2_1/c$
a/Å	7.478(3)
b/Å	13.630(5)
c/Å	6.982(2)
α/°	90
β/°	106.895(9)
γ/°	90
Volume/Å^3	680.9(4)
Z	2
ρ_{calc}g/cm^3	1.677
μ/mm^{-1}	1.907
F(000)	350.0
Crystal size/mm^3	0.14 × 0.08 × 0.005
Radiation	MoKα (λ = 0.71073)
2Θ range for data collection/°	5.694 to 52.976
Index ranges	$-9 \leq h \leq 9$, $-17 \leq k \leq 17$, $-8 \leq l \leq 8$
Reflections collected	10114
Independent reflections	1416 [R_{int} = 0.1711, R_{sigma} = 0.1211]
Data/restraints/parameters	1416/0/89
Goodness-of-fit on F^2	1.095
Final R indexes [I>=2σ (I)]	R_1 = 0.0976, wR_2 = 0.2402
Final R indexes [all data]	R_1 = 0.1806, wR_2 = 0.2772
Largest diff. peak/hole / e Å^{-3}	2.70/-0.85

2. [Cu(3-Me-PT)$_2$]

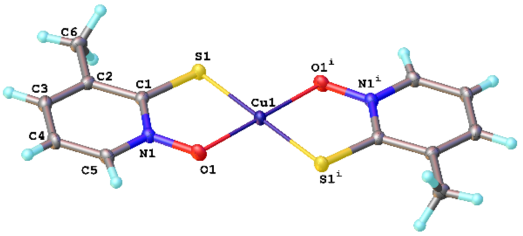

Table S2: Crystal data and structure refinement for **[Cu(3-Me-PT)$_2$]**

Empirical formula	$C_{12}H_{12}N_2O_2S_2Cu$
Formula weight	343.90
Temperature/K	120.0
Crystal system	triclinic
Space group	P-1
a/Å	3.9634(2)
b/Å	7.5851(4)
c/Å	10.8927(6)
α/°	82.893(2)
β/°	86.756(2)
γ/°	80.578(2)
Volume/Å^3	320.34(3)
Z	1
ρ_{calc}g/cm^3	1.783
μ/mm^{-1}	2.027
F(000)	175.0
Crystal size/mm^3	0.14 × 0.13 × 0.02
Radiation	Mo Kα (λ = 0.71073)
2Θ range for data collection/°	7.006 to 59.988
Index ranges	$-5 \leq h \leq 5$, $-10 \leq k \leq 10$, $-15 \leq l \leq 15$
Reflections collected	5538
Independent reflections	1859 [R_{int} = 0.0255, R_{sigma} = 0.0288]
Data/restraints/parameters	1859/0/112
Goodness-of-fit on F^2	1.078
Final R indexes [I>=2σ (I)]	R_1 = 0.0295, wR_2 = 0.0697
Final R indexes [all data]	R_1 = 0.0332, wR_2 = 0.0711
Largest diff. peak/hole / e Å^{-3}	0.94/-0.44

3. [Cu(4-Me-PT)$_2$]

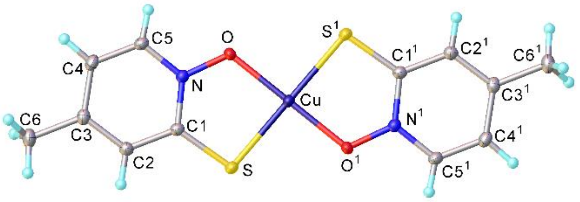

Table S3: Crystal data and structure refinement for **[Cu(4-Me-PT)$_2$]**

Empirical formula	$C_{12}H_{12}N_2O_2S_2Cu$
Formula weight	343.90
Temperature/K	120.0
Crystal system	triclinic
Space group	P-1
a/Å	4.1289(3)
b/Å	7.5872(5)
c/Å	10.9528(7)
α/°	10.9528(7)
β/°	89.980(3)
γ/°	83.141(3)
Volume/Å^3	323.88(4)
Z	1
ρ_{calc}g/cm^3	1.763
μ/mm^{-1}	2.005
F(000)	175.0
Crystal size/mm^3	0.265 × 0.082 × 0.081
Radiation	Mo Kα (λ = 0.71073)
2Θ range for data collection/°	5.82 to 69.914
Index ranges	$-6 \le h \le 6$, $-12 \le k \le 12$, $-17 \le l \le 17$
Reflections collected	7639
Independent reflections	2818 [R_{int} = 0.0320, R_{sigma} = 0.0424]
Data/restraints/parameters	2818/0/112
Goodness-of-fit on F^2	1.061
Final R indexes [I>=2σ (I)]	R_1 = 0.0334, wR_2 = 0.0701
Final R indexes [all data]	R_1 = 0.0471, wR_2 = 0.0747
Largest diff. peak/hole / e Å^{-3}	0.54/-0.53

4. *cis*-[Cu(3-OMe-PT)$_2$]

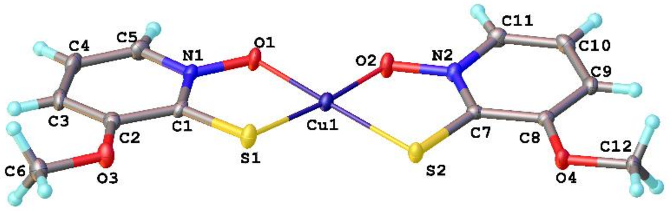

Table S4: Crystal data and structure refinement for ***cis*-[Cu(3-OMe-PT)$_2$]**

Empirical formula	$C_{12}H_{12}CuN_2O_4S_2$
Formula weight	375.90
Temperature/K	120.0
Crystal system	triclinic
Space group	P-1
a/Å	7.0485(2)
b/Å	7.2975(2)
c/Å	14.1070(5)
α/°	78.535(2)
β/°	78.6840(10)
γ/°	79.0980(10)
Volume/Å^3	688.75(4)
Z	2
ρ_{calc}g/cm^3	1.813
μ/mm^{-1}	1.905
F(000)	382.0
Crystal size/mm^3	0.21 × 0.06 × 0.03
Radiation	MoKα (λ = 0.71073)
2Θ range for data collection/°	5.768 to 59.99
Index ranges	$-9 \leq h \leq 9$, $-10 \leq k \leq 10$, $-19 \leq l \leq 19$
Reflections collected	10359
Independent reflections	3987 [R_{int} = 0.0370, R_{sigma} = 0.0509]
Data/restraints/parameters	3987/0/238
Goodness-of-fit on F^2	1.050
Final R indexes [I>=2σ (I)]	R_1 = 0.0410, wR_2 = 0.0754
Final R indexes [all data]	R_1 = 0.0549, wR_2 = 0.0797
Largest diff. peak/hole / e Å^{-3}	0.45/-0.41

5. ***trans* and *cis*-[Cu(3-OMe-PT)$_2$]**

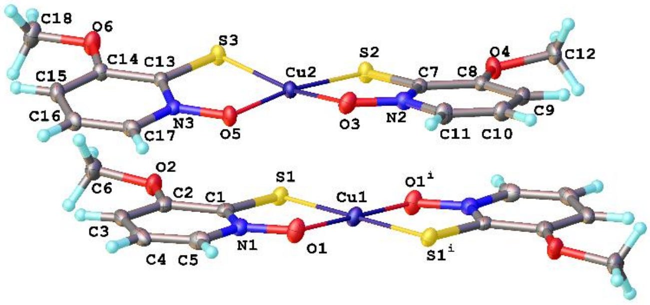

Table S5: Crystal data and structure refinement for ***cis and trans*-[Cu(3-OMe-PT)$_2$]**

Empirical formula	$C_{12}H_{12}CuN_2O_4S_2$
Formula weight	375.90
Temperature/K	120.0
Crystal system	orthorhombic
Space group	Pbca
a/Å	16.8078(5)
b/Å	13.2442(4)
c/Å	18.6661(5)
α/°	90
β/°	90
γ/°	90
Volume/Å^3	4155.2(2)
Z	12
ρ_{calc}g/cm^3	1.803
μ/mm^{-1}	1.894
F(000)	2292.0
Crystal size/mm^3	0.09 × 0.08 × 0.001
Radiation	MoKα (λ = 0.71073)
2Θ range for data collection/°	4.364 to 59.998
Index ranges	$-23 \leq h \leq 23$, $-18 \leq k \leq 18$, $-26 \leq l \leq 26$
Reflections collected	96553
Independent reflections	6056 [R_{int} = 0.0716, R_{sigma} = 0.0284]
Data/restraints/parameters	6056/0/289
Goodness-of-fit on F^2	1.123
Final R indexes [I>=2σ (I)]	R_1 = 0.0438, wR_2 = 0.0854
Final R indexes [all data]	R_1 = 0.0538, wR_2 = 0.0887
Largest diff. peak/hole / e Å^{-3}	0.86/-0.41

6. Compound 2.18b

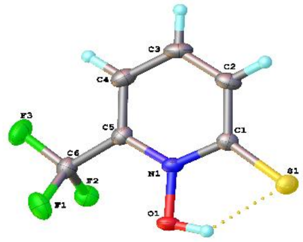

Table S6: Crystal data and structure refinement for 6-CF$_3$-PT (**2.18b**)

Empirical formula	$C_6H_4F_3NOS$
Formula weight	195.16
Temperature/K	120.0
Crystal system	monoclinic
Space group	C2/c
a/Å	56.645(2)
b/Å	4.4698(2)
c/Å	24.7781(10)
α/°	90
β/°	108.3630(10)
γ/°	90
Volume/Å^3	5954.1(4)
Z	32
ρ_{calc}g/cm^3	1.742
μ/mm^{-1}	0.435
F(000)	3136.0
Crystal size/mm^3	0.36 × 0.07 × 0.04
Radiation	MoKα (λ = 0.71073)
2Θ range for data collection/°	3.816 to 60
Index ranges	$-78 \leq h \leq 78, -6 \leq k \leq 6, -34 \leq l \leq 34$
Reflections collected	58256
Independent reflections	8684 [R_{int} = 0.0637, R_{sigma} = 0.0398]
Data/restraints/parameters	8684/0/449
Goodness-of-fit on F^2	1.071
Final R indexes [I>=2σ (I)]	R_1 = 0.0398, wR_2 = 0.0875
Final R indexes [all data]	R_1 = 0.0561, wR_2 = 0.0945
Largest diff. peak/hole / e Å^{-3}	0.52/-0.27

7. [Cu(6-CF$_3$-PT)$_2$]

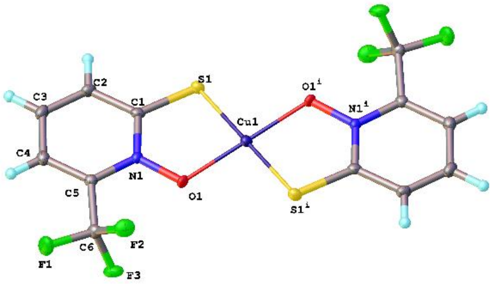

Table S7: Crystal data and structure refinement for **[Cu(6-CF$_3$-PT)$_2$]**

Empirical formula	$C_{12}H_6CuF_6N_2O_2S_2$
Formula weight	451.85
Temperature/K	120.0
Crystal system	triclinic
Space group	P-1
a/Å	4.4334(2)
b/Å	12.6398(6)
c/Å	13.3645(7)
α/°	98.982(2)
β/°	94.392(2)
γ/°	90.911(2)
Volume/Å^3	737.26(6)
Z	2
ρ_{calc}g/cm^3	2.035
μ/mm^{-1}	1.844
F(000)	446.0
Crystal size/mm^3	0.32 × 0.05 × 0.03
Radiation	Mo Kα (λ = 0.71073)
2Θ range for data collection/°	4.128 to 58.998
Index ranges	$-6 \leq h \leq 6$, $-17 \leq k \leq 17$, $-18 \leq l \leq 18$
Reflections collected	15705
Independent reflections	4100 [$R_{int} = 0.0550$, $R_{sigma} = 0.0520$]
Data/restraints/parameters	4100/0/229
Goodness-of-fit on F^2	1.048
Final R indexes [I>=2σ (I)]	$R_1 = 0.0297$, $wR_2 = 0.0709$
Final R indexes [all data]	$R_1 = 0.0426$, $wR_2 = 0.0754$
Largest diff. peak/hole / e Å^{-3}	0.48/-0.47

8. [Cu(5-PEG1-PT)$_2$]

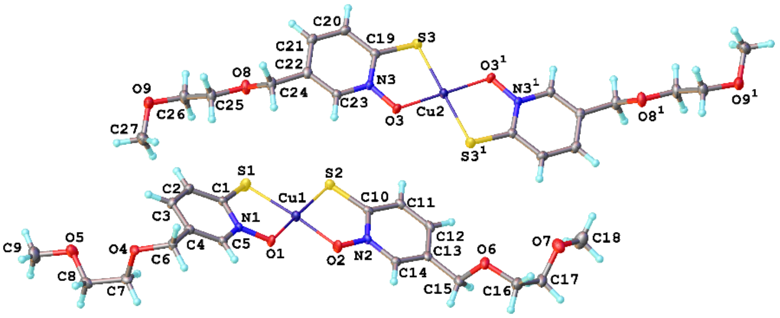

Table S8: Crystal data and structure refinement for **[Cu(5-PEG1-PT)$_2$]**

Empirical formula	$C_{18}H_{24}CuN_2O_6S_2$
Formula weight	492.05
Temperature/K	130.0
Crystal system	triclinic
Space group	P-1
a/Å	4.2745(2)
b/Å	16.1974(7)
c/Å	23.4885(11)
α/°	106.784(2)
β/°	92.454(2)
γ/°	95.446(2)
Volume/Å^3	1545.73(12)
Z	3
ρ_{calc}g/cm^3	1.586
μ/mm^{-1}	1.300
F(000)	765.0
Crystal size/mm^3	0.17 × 0.1 × 0.02
Radiation	MoKα (λ = 0.71073)
2Θ range for data collection/°	3.62 to 59.996
Index ranges	$-6 \leq h \leq 6$, $-22 \leq k \leq 22$, $-33 \leq l \leq 33$
Reflections collected	26528
Independent reflections	8894 [R_{int} = 0.0375, R_{sigma} = 0.0478]
Data/restraints/parameters	8894/0/397
Goodness-of-fit on F^2	1.040
Final R indexes [I>=2σ (I)]	R_1 = 0.0399, wR_2 = 0.0694
Final R indexes [all data]	R_1 = 0.0557, wR_2 = 0.0740
Largest diff. peak/hole / e Å^{-3}	0.40/-0.58

9. Compound 5.1

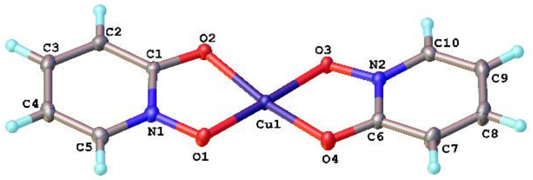

Table S9: Crystal data and structure refinement for **Compound 5.1**

Empirical formula	$C_{10}H_8CuN_2O_4$
Formula weight	283.72
Temperature/K	120.0
Crystal system	monoclinic
Space group	$P2_1/c$
a/Å	6.8669(3)
b/Å	9.6846(4)
c/Å	15.3668(6)
α/°	90
β/°	96.881(2)
γ/°	90
Volume/$Å^3$	1014.58(7)
Z	4
ρ_{calc}g/cm^3	1.857
μ/mm^{-1}	2.156
F(000)	572.0
Crystal size/mm^3	0.14 × 0.13 × 0.09
Radiation	Mo Kα (λ = 0.71073)
2Θ range for data collection/°	6.8 to 59.99
Index ranges	$-9 \leq h \leq 9$, $-13 \leq k \leq 13$, $-21 \leq l \leq 21$
Reflections collected	23681
Independent reflections	2943 [$R_{int} = 0.0284$, $R_{sigma} = 0.0160$]
Data/restraints/parameters	2943/0/154
Goodness-of-fit on F^2	1.079
Final R indexes [I>=2σ (I)]	$R_1 = 0.0210$, $wR_2 = 0.0591$
Final R indexes [all data]	$R_1 = 0.0229$, $wR_2 = 0.0600$
Largest diff. peak/hole / e Å^{-3}	0.53/-0.34

10. Compound 5.7

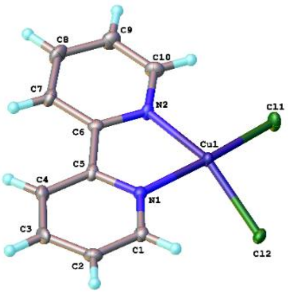

Table S10: Crystal data and structure refinement for **Compound 5.7**

Empirical formula	$C_{10}H_8N_2Cl_2Cu$
Formula weight	290.62
Temperature/K	120.0
Crystal system	monoclinic
Space group	Ia
a/Å	7.1062(3)
b/Å	17.7273(6)
c/Å	8.4498(3)
α/°	90
β/°	110.179(5)
γ/°	90
Volume/$Å^3$	999.13(7)
Z	4
ρ_{calc}g/cm^3	1.932
μ/mm^{-1}	2.680
F(000)	580.0
Crystal size/mm^3	0.17 × 0.11 × 0.08
Radiation	Mo Kα (λ = 0.71073)
2Θ range for data collection/°	5.628 to 58.996
Index ranges	$-9 \leq h \leq 9$, $-24 \leq k \leq 24$, $-11 \leq l \leq 11$
Reflections collected	4831
Independent reflections	2206 [R_{int} = 0.0504, R_{sigma} = 0.0769]
Data/restraints/parameters	2206/2/136
Goodness-of-fit on F^2	1.013
Final R indexes [I>=2σ (I)]	R_1 = 0.0445, wR_2 = 0.0760
Final R indexes [all data]	R_1 = 0.0543, wR_2 = 0.0812
Largest diff. peak/hole / e $Å^{-3}$	0.62/-0.49
Flack parameter	-0.01(2)

11. Compound 5.9a

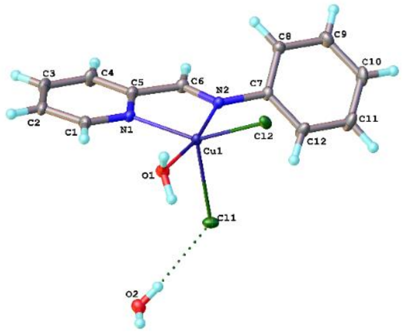

Table S11: Crystal data and structure refinement for **Compound 5.9a**

Empirical formula	$C_{12}H_{14}Cl_2CuN_2O_2$
Formula weight	352.69
Temperature/K	120.0
Crystal system	monoclinic
Space group	$P2_1/n$
a/Å	9.2973(15)
b/Å	7.6410(12)
c/Å	20.015(3)
α/°	90
β/°	90.154(6)
γ/°	90
Volume/Å^3	1421.9(4)
Z	4
ρ_{calc}g/cm^3	1.648
μ/mm^{-1}	1.909
F(000)	716.0
Crystal size/mm^3	0.23 × 0.22 × 0.13
Radiation	Mo Kα (λ = 0.71073)
2Θ range for data collection/°	4.07 to 58.998
Index ranges	$-12 \le h \le 12$, $-10 \le k \le 10$, $-27 \le l \le 27$
Reflections collected	21669
Independent reflections	3945 [R_{int} = 0.0302, R_{sigma} = 0.0204]
Data/restraints/parameters	3945/0/228
Goodness-of-fit on F^2	1.062
Final R indexes [I>=2σ (I)]	R_1 = 0.0204, wR_2 = 0.0538
Final R indexes [all data]	R_1 = 0.0236, wR_2 = 0.0551
Largest diff. peak/hole / e Å^{-3}	0.42/-0.50

12. Dimer of Compound 5.9a

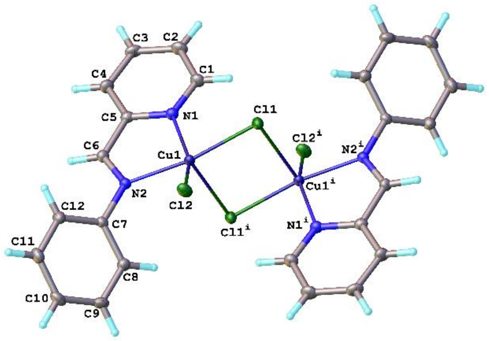

Table S12: Crystal data and structure refinement for **Dimer of Compound 5.9a**

Empirical formula	$C_{26}H_{24}Cl_8Cu_2N_4$
Formula weight	803.17
Temperature/K	120.0
Crystal system	triclinic
Space group	P-1
a/Å	8.7690(8)
b/Å	9.7734(9)
c/Å	18.6137(17)
α/°	87.101(3)
β/°	84.835(3)
γ/°	87.051(3)
Volume/Å^3	1585.0(3)
Z	2
ρ_{calc}g/cm^3	1.683
μ/mm^{-1}	2.041
F(000)	804.0
Crystal size/mm^3	0.27 × 0.13 × 0.04
Radiation	Mo Kα (λ = 0.71073)
2Θ range for data collection/°	4.178 to 58.998
Index ranges	$-12 \leq h \leq 12$, $-13 \leq k \leq 13$, $-25 \leq l \leq 25$
Reflections collected	34151
Independent reflections	8828 [R_{int} = 0.0320, R_{sigma} = 0.0309]
Data/restraints/parameters	8828/0/361
Goodness-of-fit on F^2	1.036
Final R indexes [I>=2σ (I)]	R_1 = 0.0342, wR_2 = 0.0737
Final R indexes [all data]	R_1 = 0.0581, wR_2 = 0.0815
Largest diff. peak/hole / e Å^{-3}	1.51/-1.36

References

1 J. M. Willey, L. M. Sherwood and C. J. Woolverton, *Prescott's Microbiology*, 2013.

2 G. J. Tortora, B. R. Funke and C. L. Case, *Microbiology: An Introduction*, 2018.

3 C. Gram, *Fortschritte der Med.*, 1884, **2**, 185–189.

4 S. Doron and S. L. Gorbach, *Int. Encycl. Public Heal.*, 2008, 273–282.

5 WHO, *Glob. Heal. Estim. Tech. Pap.*, 2020, 1–59.

6 WHO, *Global Tuberculosis Report 2021*, 2021.

7 K. E. Rudd, S. C. Johnson, K. M. Agesa, K. A. Shackelford, D. Tsoi, D. R. Kievlan, D. V. Colombara, K. S. Ikuta, N. Kissoon, S. Finfer, C. Fleischmann-Struzek, F. R. Machado, K. K. Reinhart, K. Rowan, C. W. Seymour, R. S. Watson, T. E. West, F. Marinho, S. I. Hay, R. Lozano, A. D. Lopez, D. C. Angus, C. J. L. Murray and M. Naghavi, *Lancet*, 2020, **395**, 200–211.

8 L. Zaffiri, J. Gardner and L. H. Toledo-Pereyra, *J. Investig. Surg.*, 2012, **25**, 67–77.

9 H. W. Jones, *Bost. Med Surg J*, 1911, 381–383.

10 G. Kalkut, *Cancer Invest.*, 1998, **16**, 12–18.

11 A. Fleming, *Lab. Inoculation Dep. St. Mary's Hosp.*, 1922, 306–317.

12 G. N. Karachalios, J. G. Parigorakis, S. J. Bountas and A. N. Georgiopoulos, *IRCS Med. Sci.*, 1984, **12**, 154–155.

13 K. H. Pfuetze, M. M. Pyle, H. C. HInshaw and W. H. Feldman, *Am. Rev. Tuberc. Pulm. Dis.*, 1955, **71**, 752–754.

14 G. L. Patrick, *An Introduction to Medicinal Chemistry*, Oxford Univ. Press, 1995.

15 R. J. Henry, *Am. Soc. Microbiol.*, 1944, **7**, 175–262.

16 J. T. Park and J. L. Strominger, *Science*, 1957, **125**, 99–101.

17 M. Devansh and S. Kumar, *Inven. Rapid Mol. Pharmacol.*, 2016, **2016**, 1–6.

18 M. Vaara and T. Vaara, *Antimicrob. Agents Chemother.*, 1981, **19**, 578–583.

19 C. Lang and C. Staiger, *Pharmazie*, 2016, **71**, 299–305.

20 W. Wehrli, F. Knüsel, K. Schmid and M. Staehelin, *Proc. Natl. Acad. Sci. U. S. A.*, 1968, **61**, 667–673.

21 S. Neidle, L. H. Pearl, P. Herzyk and H. M. Berman, *Nucleic Acids Res.*, 1988, **16**, 8999–9015.

22 K. Bush and P. A. Bradford, *Cold Spring Harb Perspect Med*, 2016, **6**, 1–22.

23 S. M. Drawz and R. A. Bonomo, *Clin. Microbiol. Rev.*, 2010, **23**, 160–201.

24 B. G. Spratt, *Eur. J. Biochem.*, 1977, **72**, 341–352.

25 C. J. Murray, K. S. Ikuta, F. Sharara, L. Swetschinski, G. Robles Aguilar, A. Gray and C. Han, *Lancet*, 2022, **399**, 629–655.

26 A. Telenti, P. Imboden, F. Marchesi, L. Matter, K. Schopfer, T. Bodmer, D. Lowrie, M. J.

Colston and S. Cole, *Lancet*, 1993, **341**, 647–651.

27 S. K. Morgan-Linnell, L. B. Boyd, D. Steffen and L. Zechiedrich, *Antimicrob. Agents Chemother.*, 2009, **53**, 235–241.

28 G. L. Daikos, P. Petrikkos, M. Psichogiou, C. Kosmidis, E. Vryonis, A. Skoutelis, K. Georgousi, L. S. Tzouvelekis, P. T. Tassios, C. Bamia and G. Petrikkos, *Antimicrob. Agents Chemother.*, 2009, **53**, 1868–1873.

29 L. T. Dong, H. V. Espinoza and J. L. Espinoza, *AIMS Microbiol.*, 2020, **6**, 176–182.

30 A. J. Kallen, Y. Mu, S. Bulens, A. Reingold, S. Petit, K. Gershman, S. M. Ray, L. H. Harrison, R. Lynfield, G. Dumyati, J. M. Townes, W. Schaffner, P. R. Patel and S. K. Fridkin, *Am. Med. Asssociation*, 2010, **304**, 641–648.

31 S. N. Khan and A. U. Khan, *Front. Microbiol.*, 2016, **7**, 1–11.

32 WHO Report, https://www.who.int/news-room/fact-sheets/detail/antimicrobial-resistance, (accessed January, 2022).

33 G. Kapoor, S. Saigal and A. Elongavan, *J. Anaesthesiol. Clin. Pharmacol.*, 2017, **33**, 300–305.

34 M. Babic, A. M. Hujer and R. A. Bonomo, *Drug Resist. Updat.*, 2006, **9**, 142–156.

35 E. Azucena and S. Mobashery, *Drug Resist. Updat.*, 2001, **4**, 106–117.

36 J. L. Burns, P. M. Mendelman, J. Levy, T. L. Stull and A. L. Smith, *Antimicrob. Agents Chemother.*, 1985, **27**, 46–54.

37 A. Zapun, C. Contreras-Martel and T. Vernet, *FEMS Microbiol. Rev.*, 2008, **32**, 361–385.

38 D. N. Wilson, *Nat. Rev. Microbiol.*, 2014, **12**, 35–48.

39 C. Bornet, A. Davin-Regli, C. Bosi, J. M. Pages and C. Bollet, *J. Clin. Microbiol.*, 2000, **38**, 1048–1052.

40 D. Szabó, F. Silveira, A. M. Hujer, R. A. Bonomo, K. M. Hujer, J. W. Marsh, C. R. Bethel, Y. Doi, K. Deeley and D. L. Paterson, *Antimicrob. Agents Chemother.*, 2006, **50**, 2833–2835.

41 K. Poole, *Clin. Microbiol. Infect.*, 2004, **10**, 12–26.

42 B. G. Hall and M. Barlow, *J. Antimicrob. Chemother.*, 2005, **55**, 1050–1051.

43 K. Bush, *Antimicrob. Agents Chemother.*, 1989, **33**, 259–263.

44 M. W. Crowder, J. Spencer and A. J. Vila, *Acc. Chem. Res.*, 2006, **39**, 721–728.

45 C. Bebrone, *Biochem. Pharmacol.*, 2007, **74**, 1686–1701.

46 K. K. Kumarasamy, M. A. Toleman, T. R. Walsh, J. Bagaria, F. Butt, R. Balakrishnan, U. Chaudhary, M. Doumith, C. G. Giske, S. Irfan, P. Krishnan, A. V. Kumar, S. Maharjan, S. Mushtaq, T. Noorie, D. L. Paterson, A. Pearson, C. Perry, R. Pike, B. Rao, U. Ray, J. B. Sarma, M. Sharma, E. Sheridan, M. A. Thirunarayan, J. Turton, S. Upadhyay, M. Warner, W. Welfare, D. M. Livermore and N. Woodford, *Lancet Infect. Dis.*, 2010, **10**, 597–602.

47 R. C. Moellering, *New Engl. J. Med. Perspect.*, 2010, **363**, 2377–2379.

48 D. Yong, M. A. Toleman, C. G. Giske, H. S. Cho, K. Sundman, K. Lee and T. R. Walsh, *J. Gastroenterol.*, 2003, 38, 104–105.

49 P. Nordmann, L. Poirel, T. Mark A. and W. Timothy R., *J. Antimicrob. Chemother.*, 2011, **66**, 689–692.

50 P. Nordmann, T. Naas and L. Poirel, *Emerg. Infect. Dis.*, 2011, **17**, 1791–1798.

51 J. R. Knowles, *Acc. Chem. Res.*, 1985, **18**, 97–104.

52 H. Ogawara and H. Umezawa, *J. Antibiot. (Tokyo).*, 1974, **27**, 567–569.

53 C. M. Rotondo and G. D. Wright, *Curr. Opin. Microbiol.*, 2017, **39**, 96–105.

54 Faridoon and N. U. Islam, *Sci. Pharm.*, 2013, **81**, 309–327.

55 F. M. Klingler, T. A. Wichelhaus, D. Frank, J. Cuesta-Bernal, J. El-Delik, H. F. Müller, H. Sjuts, S. Göttig, A. Koenigs, K. M. Pos, D. Pogoryelov and E. Proschak, *J. Med. Chem.*, 2015, **58**, 3626–3630.

56 T. Christopeit, T. J. O. Carlsen, R. Helland and H.-K. S. Leiros, *J. Med. Chem.*, 2015, **58**, 8671−8682.

57 J. Brem, R. Cain, S. Cahill, M. A. McDonough, I. J. Clifton, J. C. Jiménez-Castellanos, M. B. Avison, J. Spencer, C. W. G. Fishwick and C. J. Schofield, *Nat. Commun.*, 2016, **7**, 1–8.

58 S. B. Falconer, S. A. Reid-Yu, A. M. King, S. S. Gehrke, W. Wang, J. F. Britten, B. K. Coombes, G. D. Wright and E. D. Brown, *ACS Infect. Dis.*, 2016, **1**, 533–543.

59 A. M. King, S. A. Reid-Yu, W. Wang, D. T. King, G. De Pascale, N. C. Strynadka, T. R. Walsh, B. K. Coombes and G. D. Wright, *Nature*, 2014, **510**, 503–519.

60 H. Sung, J. Ferlay, R. L. Siegel, M. Laversanne, I. Soerjomataram, A. Jemal and F. Bray, *CA. Cancer J. Clin.*, 2021, **71**, 209–249.

61 G. M. Cooper, *The Cell: A molecular Approach*, Oxford Univ. Press, 2019.

62 B. A. Chabner and T. G. Roberts, *Nat. Rev. Cancer*, 2005, **5**, 65–72.

63 A. Gilman, *Am. J. Surg.*, 1963, **105**, 574–578.

64 J. A. Farber, S , Diamond, L. K., Mercer, R. D., Sylvester, R. F., & Wolff, *New Engl. J. Med.*, 1948, **238**, 787–793.

65 M. C. Li, R. Hertz and D. M. Bergenstal, *N Engl. J. Med.*, 1958, **259**, 66–74.

66 H. E. Skipper, J. R. Thomson, G. B. Elion and G. H. Hitchings, *Cancer Res.*, 1954, **14**, 294–298.

67 D. Hanahan and R. A. Weinberg, *Cell*, 2000, **100**, 57–70.

68 J. C. Dabrowiak, *Metals in Medicine*, John Wiley & Sons Ltd, 2017.

69 G. B. Bauer and L. F. Povirk, *Nucleic Acids Res.*, 1997, **25**, 1211–1218.

70 S. Ahmad, *Chem. Biodivers.*, 2010, **7**, 543–566.

71 S. A. Kazakov and S. M. Hecht, *Nucleic Acid – Metal Ion Interactions*, John Wiley & Sons Ltd, 2011.

72 S. Dasari and P. Bernard, *Eur. J. Pharmacol.*, 2014, 1–15.

73 H. Liu and P. J. Sadler, *Acc. Chem. Res.*, 2011, **44**, 349–359.

74 M. F. Brana, M. Cacho, A. Gradillas, B. de Pascual-Teresa and A. Ramos, *Curr. Pharm. Des.*, 2005, **7**, 1745–1780.

75 T. Aoyagi, M. Ishizuka, T. Takeuchi and H. Umezawa, *Jpn. J. Antibiot.*, 1977, **30**, 121—132.

76 Z. Wang, C. Zang, K. Cui, D. E. Schones, A. Barski, W. Peng and K. Zhao, *Cell*, 2009, **138**,

1019–1031.

77 J. E. Bolden, M. J. Peart and R. W. Johnstone, *Nat. Rev. Drug Discov.*, 2006, **5**, 769–784.

78 J. W. Walton, J. M. Cross, T. Riedel and P. J. Dyson, *Org. Biomol. Chem.*, 2017, **15**, 9186–9190.

79 P. A. Marks, *Oncogene*, 2007, **26**, 1351–1356.

80 J. L. Delgado, C. M. Hsieh, N. L. Chan and H. Hiasa, *Biochem. J.*, 2018, **475**, 373–398.

81 N. Staropoli, D. Ciliberto, C. Botta, L. Fiorillo, A. Grimaldi, S. Lama, M. Caraglia, A. Salvino, P. Tassone and P. Tagliaferri, *Cancer Biol. Ther.*, 2014, **15**, 707–720.

82 B. Nicholson, J. G. Marblestone, T. R. Butt and M. R. Mattern, *Futur. Oncol.*, 2007, **3**, 191–199.

83 Z. Wang, W. Kang, Y. You, J. Pang, H. Ren, Z. Suo, H. Liu and Y. Zheng, *Front. Pharmacol.*, 2019, **10**, 1–15.

84 M. K. Paul and A. K. Mukhopadhyay, *Int. J. Med. Sci.*, 2012, **1**, 101–115.

85 B. J. Druker, *Trends Mol. Med.*, 2002, **8**, 14–18.

86 M. L. Circu and T. Y. Aw, *Free Radic Biol Med.*, 2010, **48**, 749–762.

87 S. Mitra, L. N. Nguyen, M. Akter, G. Park, E. H. Choi and N. K. Kaushik, *Cancers (Basel).*, 2019, **11**, 1–31.

88 P. L. De Sá Junior, D. A. D. Câmara, A. S. Porcacchia, P. M. M. Fonseca, S. D. Jorge, R. P. Araldi and A. K. Ferreira, *Oxid. Med. Cell. Longev.*, 2017, 1-13.

89 J. M. Matés and F. M. Sánchez-Jiménez, *Int. J. Biochem. Cell Biol.*, 2000, **32**, 157–170.

90 M. Landriscina, F. Maddalena, G. Laudiero and F. Esposito, *Antioxidants Redox Signal.*, 2009, **11**, 2701–2716.

91 R. L. Levine and E. R. Stadtman, *Facts, Res. Interv. Geriatr.*, 2001, **36**, 1495–1502.

92 J. M. Zdolsek and I. Svensson, *Virchows Arch. B Cell Pathol. Incl. Mol. Pathol.*, 1993, **64**, 401–406.

93 G. Kroemer, B. Dallaporta and M. Resche-Rigon, *Annu. Rev. Physiol.*, 1998, **60**, 619–642.

94 S. Tan, Y. Sagara, Y. Liu, P. Maher and D. Schubert, *J. Cell Biol.*, 1998, **141**, 1423–1432.

95 L. Yuan, R. Mishra, H. Patel, S. Abdulsalam, K. D. Greis, A. L. Kadekaro, E. J. Merino and J. T. Garrett, *J. Cancer*, 2018, **9**, 4665–4676.

96 N. Samadi, P. Ghanbari, M. Mohseni, M. Tabasinezhad, S. Sharifi, H. Nazemieh and M. R. Rashidi, *J. Cancer Res. Ther.*, 2014, **10**, 715–721.

97 A. Meshkini and R. Yazdanparast, *Exp. Toxicol. Pathol.*, 2012, **64**, 357–365.

98 H. Miki, N. Uehara, A. Kimura, T. Sasaki, T. Yuri, K. Yoshizawa and A. Tsubura, *Int. J. Oncol.*, 2012, **40**, 1020–1028.

99 Z. Huang, Y. Xu and W. Peng, *Mol. Med. Rep.*, 2015, 12, 5939–5944.

100 A. E. Martell, R. D. Hancock and R. J. Motekaitis, *Coord. Chem. Rev.*, 1994, **133**, 39–65.

101 K. L. Haas and K. J. Franz, *Chem Rev.*, 2009, **109**, 4921–4960.

102 A. De Almeida, B. L. Oliveira, J. D. G. Correia, G. Soveral and A. Casini, *Coord. Chem. Rev.*,

2013, **257**, 2689–2704.

103 J. H. Laity, B. M. Lee and P. E. Wright, *Curr. Opin. Struct. Biol.*, 2001, **11**, 39–46.

104 A. D. Richards and A. Rodger, *Chem. Soc. Rev.*, 2007, **36**, 471–483.

105 M. Patra, G. Gasser and N. Metzler-Nolte, *Dalton Trans.*, 2012, **41**, 6350–6358.

106 J. R. Lambert and P. Midolo, *Aliment Pharmacol Ther*, 1997, **11**, 27–33.

107 D. J. Barillo, A. R. Barillo, S. Korn, K. Lam and P. S. Attar, *Burns*, 2017, **43**, 1189–1194.

108 A. F. Granger, MD thesis, University of Glasgow, 1946.

109 S. N. Sovari and F. Zobi, *Chemistry*, 2020, **2**, 418–452.

110 Y. Zhu and W. H. Li, *Transit. Met. Chem.*, 2010, **35**, 745–749.

111 S. Shaygan, H. Pasdar, N. Foroughifar, M. Davallo and F. Motiee, *Appl. Sci.*, 2018, **8**, 1–12.

112 E. Kouris, S. Kalogiannis, F. Perdih, I. Turel and G. Psomas, *J. Inorg. Biochem.*, 2016, **163**, 18–27.

113 P. Nagababu, J. Naveena Lavanya Latha, P. Pallavi, S. Harish and S. Satyanarayana, *Can. J. Microbiol.*, 2006, **52**, 1247–1254.

114 O. V. Salishcheva and A. Y. Prosekov, *Foods Raw Mater.*, 2020, **8**, 298–311.

115 W. Guerra, P. P. Silva-caldeira, H. Terenzi and E. C. Pereira-maia, *Coord. Chem. Rev.*, 2016, 1–12.

116 R. Arancibia, C. Quintana, C. Biot, M. E. Medina, S. Carrère-Kremer, L. Kremer and A. H. Klahn, *Inorg. Chem. Commun.*, 2015, **55**, 139–142.

117 F. F. Bobinihi, D. C. Onwudiwe, A. C. Ekennia, O. C. Okpareke, C. Arderne and J. R. Lane, *Polyhedron*, 2019, **158**, 296–310.

118 M. V. Lunagariya, K. P. Thakor, B. N. Waghela, C. Pathak and M. N. Patel, *Appl. Organomet. Chem.*, 2018, **32**, 1–25.

119 A. Terbouche, C. Ait-Ramdane-Terbouche, Z. Bendjilali, H. Berriah, H. Lakhdari, D. Lerari, K. Bachari, D. Mezaoui, N. E. H. Bensiradj, J. P. Guegan and D. Hauchard, *Spectrochim. Acta - Part A Mol. Biomol. Spectrosc.*, 2018, **205**, 146–159.

120 F. P. Dwyer, I. K. Reid, A. Shulman, G. M. Laycock and S. Dixson, *Aust. J. Exp. Biol. Med. Sci.*, 1969, **47**, 203–218.

121 A. Bolhuis, L. Hand, J. E. Marshall, A. D. Richards, A. Rodger and J. Aldrich-Wright, *Eur. J. Pharm. Sci.*, 2011, **42**, 313–317.

122 G. Devagi, F. Dallemer, P. Kalaivani and R. Prabhakaran, *J. Organomet. Chem.*, 2018, **854**, 1–14.

123 A. Frei, *Antibiotics*, 2020, **9**, 1–24.

124 Y. Feng, W.-Z. Sun, X.-S. Wang and Q.-X. Zhou, *Chem. Eur.J.*, 2019, **25**, 13879 –13884.

125 E. M. Lewandowski, J. Skiba, N. J. Torelli, A. Rajnisz, J. Solecka, K. Kowalski and Y. Chen, *Chem. Commun.*, 2015, **51**, 6186–6189.

126 M. Pandrala, F. Li, M. Feterl, Y. Mulyana, J. M. Warner, L. Wallace, F. R. Keene and J. G. Collins, *Dalton Trans.*, 2013, **42**, 4686–4694.

127 P. Appelt, J. P. da Silva, O. Fuganti, L. E. N. Aquino, B. Sandrino, K. Wohnrath, V. A. Q.

Santos, M. A. A. Cunha, A. Veiga, F. S. Murakami, D. F. Back and M. P. de Araujo, *J. Organomet. Chem.*, 2017, **846**, 326–334.

128 L. Lu, L. J. Liu, W. C. Chao, H. J. Zhong, M. Wang, X. P. Chen, J. J. Lu, R. N. Li, D. L. Ma and C. H. Leung, *Sci. Rep.*, 2015, **5**, 1–9.

129 E. Sauvageot, M. Elie, S. Gaillard, R. Daniellou, P. Fechter, I. J. Schalk, V. Gasser, J. L. Renaud and G. L. A. Mislin, *Metallomics*, 2017, **9**, 1820–1827.

130 V. Fiorini, I. Zanoni, S. Zacchini, A. L. Costa, A. Hochkoeppler, V. Zanotti, A. M. Ranieri, M. Massi, A. Stefan and S. Stagni, *Dalton Trans.*, 2017, **46**, 12328–12338.

131 F. Chen, J. Moat, D. McFeely, G. Clarkson, I. J. Hands-Portman, J. P. Furner-Pardoe, F. Harrison, C. G. Dowson and P. J. Sadler, *J. Med. Chem.*, 2018, **61**, 7330–7344.

132 C. M. Duchane, G. W. Karpin, M. Ehrich, J. O. Falkinham and J. S. Merola, *Medchemcomm*, 2019, **10**, 1391–1398.

133 K. Y. Djoko, M. D. Phan, K. M. Peters, M. J. Walker, M. A. Schembri and A. G. McEwan, *Proc. Natl. Acad. Sci. U. S. A.*, 2017, **114**, 6818–6823.

134 M. F. Zaltariov, M. Cazacu, M. Avadanei, S. Shova, M. Balan, N. Vornicu, A. Vlad, A. Dobrov and C. D. Varganici, *Polyhedron*, 2015, **100**, 121–131.

135 A. Boughougal, F. Z. Cherchali, A. Messai, N. Attik, D. Decoret, M. Hologne, C. Sanglar, G. Pilet, J. B. Tommasino and D. Luneau, *New J. Chem.*, 2018, **42**, 15346–15352.

136 R. Koch, *Dtsch. Med. Wochenschr*, 1890, **16**, 650–660.

137 M. B. Harbut, C. Vilchèze, X. Luo, M. E. Hensler, H. Guo, B. Yang, A. K. Chatterjee, V. Nizet, W. R. Jacobs, P. G. Schultz and F. Wang, *Proc. Natl. Acad. Sci. U. S. A.*, 2015, **112**, 4453–4458.

138 P. Hikisz, Ł. Szczupak, A. Koceva-Chyła, A. Gušpiel, L. Oehninger, I. Ott, B. Therrien, J. Solecka and K. Kowalski, *Molecules*, 2015, **20**, 19699–19718.

139 B. Glišić and M. I. Djuran, *J. Chem. Soc. Dalton Trans.*, 2014, **43**, 5950–5969.

140 G. Zhao and S. E. Stevens, *Biometals*, 1998, **11**, 27–32.

141 C. L. Fox and S. M. Modak, *Antimicrob. Agents Chemother.*, 1974, **5**, 582–588.

142 I. Mgt and H. Senior, *J. Wound Care*, 2013, **11**, 125–130.

143 K. Nomiya, A. Yoshizawa, K. Tsukagoshi, N. C. Kasuga, S. Hirakawa and J. Watanabe, *J. Inorg. Biochem.*, 2004, **98**, 46–60.

144 T. Aiyelabola, E. Akinkunmi, E. Obuotor, I. Olawuni, D. Isabirye and J. Jordaan, *Bioinorg. Chem. Appl.*, 2017, 1–9.

145 O. Z. Yeşilel, G. Kaştaş, C. Darcan, I. Ilker, H. Paşaoğlu and O. Büyükgüngör, *Inorganica Chim. Acta*, 2010, **363**, 1849–1858.

146 V. Bobbarala, *A Search for Antibacterial Agents*, 2012.

147 K. Nomiya, S. Takahashi and R. Noguchi, *J. Chem. Soc. Dalton Trans.*, 2000, 2091–2097.

148 K. Nomiya, Y. Kondoh, K. Onoue, N. C. Kasuga, H. Nagano, M. Oda, T. Sudoh and S. Sakuma, *J. Inorg. Biochem.*, 1995, **58**, 255-267.

149 C. Lok, C. Ho, R. Chen, Q. H. Yu, W. Yu, H. Sun, P. K. Tam, J. Chiu and C. Che, *J. Biol. Inorg. Chem.*, 2007, **12**, 527–534.

150 S. Eckhardt, P. S. Brunetto, J. Gagnon, M. Priebe, B. Giese and K. M. Fromm, *Chem. Rev.*, 2013, **113**, 4708–4754.

151 E. M. V. Marambio-Jones, C.; Hoek, *J. Nanoparticle Res.*, 2010, **12**, 1531–1551.

152 C. C. Hopkins, R. C. Moellering and M. N. Swartz, *Lancet*, 1975, **305**, 235–240.

153 I. Kostova, *Recent Pat. Anticancer. Drug Discov.*, 2006, **1**, 1–22.

154 N. Farrell, *J. Nerv. Ment. Dis.*, 1976, **162**, 313–322.

155 M. J. Cleare and J. D. Hoeschele, *Bioinorg. Chem.*, 1973, **2**, 187–210.

156 U. Jungwirth, C. R. Kowol, B. K. Keppler, C. G. Hartinger, W. Berger and P. Heffeter, *Antioxidants Redox Signal.*, 2011, **15**, 1085–1127.

157 U. Ndagi, N. Mhlongo and M. E. Soliman, *Drug Des. Devel. Ther.*, 2017, **11**, 599–616.

158 S. Yano, H. Ohi, M. Ashizaki, M. Obata, Y. Mikata, R. Tanaka, T. Nishioka, I. Kinoshita, Y. Sugai, I. Okura, S. I. Ogura, J. A. Czaplewska, M. Gottschaldt, U. S. Schubert, T. Funabiki, K. Morimoto and M. Nakai, *Chem. Biodivers.*, 2012, **9**, 1903–1915.

159 T. C. Johnstone, J. J. Wilson and S. J. Lippard, *Inorg. Chem.*, 2013, **52**, 12234–12249.

160 M. Arsenijević, M. Milovanović, V. Volarević, D. Cˇanović, N. Arsenijević, T. Soldatović, S. Jovanović and Z. D. Bugarĉić, *Transit. Met Chem*, 2012, **37**, 481–488.

161 J. Reedijk, *Proc. Natl. Acad. Sci. U. S. A.*, 2003, **100**, 3611–3616.

162 J. M. Cross, N. Gallagher, J. H. Gill, M. Jain, A. W. McNeillis, K. L. Rockley, F. H. Tscherny, N. J. Wirszycz, D. S. Yufit and J. W. Walton, *Dalton Trans.*, 2016, **45**, 12807–12813.

163 G. Sava, S. Pacor, A. Bergamo, M. Cocchietto, G. Mestroni and E. Alessio, *Chem. Biol. Interact.*, 1995, **95**, 109–126.

164 I. Kostova, *Curr. Med. Chem.*, 2006, **13**, 1085–1107.

165 C. S. Allardyce and P. J. Dyson, *Dalt. Trans.*, 2016, **45**, 3201–3209.

166 M. A. Jakupec, E. Reisner, A. Eichinger, M. Pongratz, V. B. Arion, M. Galanski, C. G. Hartinger and B. K. Keppler, *J. Med. Chem.*, 2005, **48**, 2831–2837.

167 J. M. Cross, T. R. Blower, N. Gallagher, J. H. Gill, K. L. Rockley and J. W. Walton, *Chempluschem*, 2016, **81**, 1276–1280.

168 B. Wu, M. S. Ong, M. Groessl, Z. Adhireksan, C. G. Hartinger, P. J. Dyson and C. A. Davey, *Chem. - A Eur. J.*, 2011, **17**, 3562–3566.

169 J. M. Cross, T. R. Blower, A. D. H. Kingdon, R. Pal, D. M. Picton and J. W. Walton, *Molecules*, 2020, **25**, 1–8.

170 B. Peña, A. David, C. Pavani, M. S. Baptista, J. P. Pellois, C. Turro and K. R. Dunbar, *Organometallics*, 2014, **33**, 1100–1103.

171 Z. J. Li, Y. Hou, D. A. Qin, Z. M. Jin and M. L. Hu, *PLoS One*, 2015, **10**, 1–13.

172 M. R. Gill and J. A. Thomas, *Chem. Soc. Rev.*, 2012, **41**, 3179–3192.

173 M. R. Gill, J. Garcia-Lara, S. J. Foster, C. Smythe, G. Battaglia and J. A. Thomas, *Nat. Chem.*, 2009, **1**, 662–667.

174 M. R. Gill, D. Cecchin, M. G. Walker, R. S. Mulla, G. Battaglia, C. Smythe and J. A. Thomas, *Chem. Sci.*, 2013, **4**, 4512–4519.

175 D. Gaynor and D. M. Griffith, *Dalton Trans.*, 2012, **41**, 13239–13257.

176 C. Collins, J. F. Eaiy, G. Donaldson, C. Vernon, N. E. Bush, S. Petersdorf, R. B. Livingston, E. E. Gordon, C. R. Chapman and F. R. Appelbaum, *J. Nucl. Med.*, 1993, **34**, 1839–1844.

177 F. Tisato, C. Marzano, M. Porchia, M. Pellei and C. Santini, *Med. Res. Rev.*, 2010, **30**, 708–749.

178 D. Reinen, *Comments Inorg. Chem.*, 1983, **2**, 227–246.

179 M. Wehbe, A. W. Y. Leung, M. J. Abrams, C. Orvig and M. B. Bally, *Dalton Trans.*, 2017, **46**, 10758–10773.

180 M. E. Helsel and K. J. Franz, *Dalt. Trans.*, 2015, **44**, 8760–8770.

181 G. Grass, C. Rensing and M. Solioz, *Appl. Environ. Microbiol.*, 2011, **77**, 1541–1547.

182 Y. Yoshida, S. Furuta and E. Niki, *Biochim. Biophys. Acta*, 1993, **1210**, 81–88.

183 I. Iakovidis, I. Delimaris and S. M. Piperakis, *Mol. Biol. Int.*, 2011, **2011**, 1–13.

184 K. D. Karlin, *Science*, 1993, **261**, 701–708.

185 L. Macomber and J. A. Imlay, *PNAS*, 2009, **106**, 8344–8349.

186 C. M. Galhardi, Y. S. Diniz, L. A. Faine, H. G. Rodrigues, R. C. M. Burneiko, B. O. Ribas and E. L. B. Novelli, *Food Chem. Toxicol.*, 2004, **42**, 2053–2060.

187 C. Duncan and A. R. White, *Metallomics*, 2012, **4**, 127–138.

188 C. E. Santo, E. W. Lam, C. G. Elowsky, D. Quaranta, D. W. Domaille, C. J. Chang and G. Grass, *Appl. Environ. Microbiol.*, 2011, **77**, 794–802.

189 K. Y. Djoko, M. M. Goytia, P. S. Donnelly, M. A. Schembri, W. M. Shafer and A. G. McEwan, *Antimicrob. Agents Chemother.*, 2015, **59**, 6444–6453.

190 E. K. Efthimiadou, M. E. Katsarou, A. Karaliota and G. Psomas, *J. Inorg. Biochem.*, 2008, **102**, 910–920.

191 G. Psomas, A. Tarushi, E. K. Efthimiadou, Y. Sanakis, C. P. Raptopoulou and N. Katsaros, 2006, **100**, 1764–1773.

192 N. Raman, A. Kulandaisamy and C. Thangaraja, *Transit. Met. Chem.*, 2004, **29**, 129–135.

193 D. Johnston, H. Freiser, W. D. Johnston and H. Freiser, *J. Am. Chem. Soc.*, 1952, **74**, 8–11.

194 B. I. Anderson and R. J. Swaby, *Aust. J. Biol. Sci.*, 1951, **4**, 275–282.

195 K. Y. Djoko, B. M. Paterson, P. S. Donnelly and A. G. Mcewan, *Metallomics*, 2014, 854–863.

196 C. Rodrı, P. Pelagatti and F. Zani, *J. Inorg. Biochem.*, 2005, **99**, 2231–2239.

197 D. M. Perrin, V. M. Hoang, Y. Xu, A. Mazumder and D. S. Sigman, *Biochemistry*, 1996, **35**, 5318–5326.

198 H. Smit, H. van Der Goot, W. T. Nauta, H. Timmerman, M. W. de Bolster, A. G. Jochemsen, A. H. Stouthamer and R. D. Vis, *Antimicrob. Agents Chemother.*, 1981, **20**, 455–462.

199 Z. H. Chohan, *Appl. Organomet. Chem.*, 2002, **16**, 17–20.

200 C. F. Sousa, M. Ferreira, B. Abreu, C. J. Medforth and P. Gameiro, *Int. J. Pharm.*, 2015, **495**, 761–770.

201 A. G. Dalecki, A. P. Malalasekera, K. Schaaf, O. Kutsch, S. H. Bossmann and F.

Wolschendorf, *Metallomics*, 2016, **8**, 412–421.

202 A. G. Dalecki, C. L. Crawford and F. Wolschendorf, *Copper and Antibiotics: Discovery, Modes of Action, and Opportunities for Medicinal Applications*, Elsevier Ltd., 1st edn., 2017, vol. 70.

203 M. Hans, S. Mathews, F. Mücklich and M. Solioz, *Biointerphases*, 2016, **11**, 018902.

204 L. J. Wheeldon, T. Worthington, P. A. Lambert, A. C. Hilton, C. J. Lowden and T. S. J. Elliott, *J. Antimicrob. Chemother.*, 2008, **62**, 522–525.

205 J. Easmon, G. Pürstinger, G. Heinisch, T. Roth, H. H. Fiebig, W. Holzer, W. Jäger, M. Jenny and J. Hofmann, *J. Med. Chem.*, 2001, **44**, 2164–2171.

206 V. Barve, F. Ahmed, S. Adsule, S. Banerjee, S. Kulkarni, P. Katiyar, C. E. Anson, A. K. Powell, S. Padhye and F. H. Sarkar, *J. Med. Chem.*, 2006, **49**, 3800–3808.

207 S. Adsule, V. Barve, D. Chen, F. Ahmed, Q. P. Dou, S. Padhye and F. H. Sarkar, *J. Med. Chem.*, 2006, **49**, 7242–7246.

208 H. Zhang and Q. Hao, *FASEB J.*, 2011, **25**, 2574–2582.

209 S. Dutta, S. Padhye, F. Ahmed and F. Sarkar, *Inorganica Chim. Acta*, 2005, **358**, 3617–3624.

210 S. Tardito, O. Bussolati, F. Gaccioli, R. Gatti, S. Guizzardi, J. Uggeri, L. Marchiò, M. Lanfranchi and R. Franchi-Gazzola, *Histochem. Cell Biol.*, 2006, **126**, 473–482.

211 C. Deegan, M. McCann, M. Devereux, B. Coyle and D. A. Egan, *Cancer Lett.*, 2007, **247**, 224–233.

212 M. Barceló-Oliver, Á. García-Raso, Á. Terrón, E. Molins, M. J. Prieto, V. Moreno, J. Martínez, V. Lladó, I. López, A. Gutiérrez and P. V. Escribá, *J. Inorg. Biochem.*, 2007, **101**, 649–659.

213 V. Rajendiran, R. Karthik, M. Palaniandavar, H. Stoeckli-Evans, V. S. Periasamy, M. A. Akbarsha, B. S. Srinag and H. Krishnamurthy, *Inorg. Chem.*, 2007, **46**, 8208–8221.

214 K. Laws, G. Bineva-Todd, A. Eskandari, C. Lu, N. O'Reilly and K. Suntharalingam, *Angew. Chem*, 2018, **130**, 293–297.

215 J. N. Boodram, I. J. Mcgregor, P. M. Bruno, P. B. Cressey, M. T. Hemann and K. Suntharalingam, *Angew. Chem. Int. Ed.*, 2016, **128**, 2895–2900.

216 C. Mejia and L. Ruiz-Azuara, *Pathol. Oncol. Res.*, 2008, **14**, 467–472.

217 A. Marín-Hernández, I. Gracia-Mora, L. Ruiz-Ramírez and R. Moreno-Sánchez, *Biochem. Pharmacol.*, 2003, **65**, 1979–1989.

218 N. J. Sanghamitra, P. Phatak, S. Das, A. G. Samuelson and K. Somasundaram, *J. Med. Chem.*, 2005, **48**, 977–985.

219 C. Marzano, M. Pellei, D. Colavito, S. Alidori, G. G. Lobbia, V. Gandin, F. Tisato and C. Santini, *J. Med. Chem.*, 2006, **49**, 7317–7324.

220 C. Shobha Devi, B. Thulasiram, R. R. Aerva and P. Nagababu, *J. Fluoresc.*, 2018, **28**, 1195–1205.

221 D. D. Li, J. L. Tian, W. Gu, X. Liu, H. H. Zeng and S. P. Yan, *J. Inorg. Biochem.*, 2011, **105**, 894–901.

222 B. M. Aveline, I. E. Kochevar and R. W. Redmond, *J. Am. Chem. Soc.*, 1996, **118**, 10113–10123.

223 B. L. Barnett, H. C. Kretschamar and F. A. Hartman, *Inorg. Chem.*, 1977, **16**, 1834–1838.

224 D. Z. Niu, L. Yao, X. Min and H. Zou, *Acta Crystallogr. Sect. C Struct. Chem.*, 2011, **226**, 527–528.

225 X. Chen, Y. Hu, D. Wu, L. Weng and B. Kang, *Polyhedron*, 1991, **10**, 2651–2657.

226 R. Muthyala, W. S. Shin, J. Xie and Y. Y. Sham, *Bioorganic Med. Chem. Lett.*, 2015, **25**, 4320–4324.

227 E. G. Salina, O. Ryabova, A. Vocat, B. Nikonenko, S. T. Cole and V. Makarov, *J. Infect. Chemother.*, 2017, **23**, 794–797.

228 M. Park, Y. J. Cho, Y. W. Lee and W. H. Jung, *Sci. Rep.*, 2018, **8**, 1–11.

229 C. Blanchard, L. Brooks, K. Ebsworth-Mojica, L. Didione, B. Wucher, S. Dewhurst, D. Krysan, P. M. Dunman and R. A. F. Wozniak, *mSphere*, 2008, **1**, 1-14.

230 N. Kumari, S. N. Bhattacharya, S. Das, S. Datt, T. Singh, M. Jassal and A. K. Agrawal, *ACS Appl. Mater. Interfaces*, 2021, **13**, 47382–47393.

231 G. Srivastava, A. Matta, G. Fu, R. T. Somasundaram, A. Datti, P. G. Walfish and R. Ralhan, *Mol. Oncol.*, 2015, **9**, 1720–1735.

232 C. Zhao, X. Chen, C. Yang, D. Zang, X. Lan, S. Liao, P. Zhang, J. Wu, X. Li, N. Liu, Y. Liao, H. Huang, X. Shi, L. Jiang, X. Liu, Q. Ping Dou, X. Wang and J. Liu, *Oncotarget*, 2017, **8**, 13942–13956.

233 M. Chen, Y. Ding, Y. Ke, Y. Zeng, N. Liu, Y. Zhong, X. Hua, Z. Li, Y. Xiong, C. Wu and H. Yu, *Artif. Cells, Nanomedicine Biotechnol.*, 2020, **48**, 824–833.

234 J. Kljun, M. Anko, K. Traven, M. Sinreih, R. Pavlič, Š. Peršič, Ž. Ude, E. E. Codina, J. Stojan, T. Lanišnik Rižner and I. Turel, *Dalton Trans.*, 2016, **45**, 11791–11800.

235 J. Kladnik, S. Ristovski, J. Kljun, A. Defant, I. Mancini, K. Sepčić and I. Turel, *Int. J. Mol. Sci.*, 2020, **21**, 1–17.

236 J. Kladnik, J. Kljun, H. Burmeister, I. Ott, I. Romero-Canelón and I. Turel, *Chem. - A Eur. J.*, 2019, **25**, 14169–14182.

237 J. Kladnik, J. P. C. Coverdale, J. Kljun, H. Burmeister, P. Lippman, F. G. Ellis, A. M. Jones, I. Ott, I. Romero-Canelón and I. Turel, *Cancers (Basel).*, 2021, **13**, 1–21.

238 X. Lan, C. Zhao, X. Chen, P. Zhang, D. Zang, J. Wu, J. Chen, H. Long, L. Yang, H. Huang, B. Z. Carter, X. Wang, X. Shi and J. Liu, *J. Hematol. Oncol.*, 2016, **9**, 1–16.

239 H. Huang, N. Liu, Y. Liao, N. Liu, J. Cai, X. Xia, Z. Guo, Y. Li, Q. Wen, Q. Yin, Y. Liu, Q. Wu, D. Rajakumar, X. Sheng and J. Liu, *J. Exp. Clin. Cancer Res.*, 2017, **36**, 79.

240 X. Chen, J. Wu, Q. Yang, X. Zhang, P. Zhang, S. Liao, Z. He, X. Wang, C. Zhao and J. Liu, *BioMetals*, 2018, **31**, 29–43.

241 I. MacHado, L. B. Marino, B. Demoro, G. A. Echeverría, O. E. Piro, C. Q. F. Leite, F. R. Pavan and D. Gambino, *Eur. J. Med. Chem.*, 2014, **87**, 267–273.

242 X. Chen, Q. Yang, L. Xiao, D. Tang, Q. P. Dou and J. Liu, *Cancer Metastasis Rev.*, 2017, **36**, 655–668.

243 X. Chen, Q. P. Dou, J. Liu and D. Tang, *Front. Mol. Biosci.*, 2021, **8**, 1–9.

244 M. Wehbe, C. Lo, A. W. Y. Leung, W. H. Dragowska, G. M. Ryan and M. B. Bally, *Invest. New Drugs*, 2017, **35**, 682–690.

245 K. Chiem, B. A. Fuentes, D. L. Lin, T. Tran, A. Jackson, M. S. Ramirez and M. E. Tolmasky, *Antimicrob. Agents Chemother.*, 2015, **59**, 5851–5853.

246 E. G. Salina, S. Huszar, J. Zemanova, J. Keruchenko, O. Riabova, E. Kazakova, A. Grigorov, T. Azhikina, A. Kaprelyants, K. Mikušova and V. Makarov, *Metallomics*, 2018, **10**, 992–1002.

247 M. E. Helsel, E. J. White, S. Z. A. Razvi, B. Alies and K. J. Franz, *Metallomics*, 2017, **9**, 69–81.

248 J. M. Zaengle-Barone, A. C. Jackson, D. M. Besse, B. Becken, M. Arshad, P. C. Seed and K. J. Franz, *ACS Infect Dis.*, 2018, **4**, 1019–1029.

249 K. Y. Djoko, M. E. S. Achard, M.-D. Phan, A. W. Lo, M. Miraula, S. Prombhul, S. J. Hancock, K. M. Peters, H. E. Sidjabat, P. N. Harris, N. Mitic´, T. R. Walsh, G. J. Anderson, W. M. Shafer, D. L. Paterson, G. Schenk, A. G. Mcewan and A. Schembri, *Antimicrob. Agents Chemother.*, 2018, **62**, 1–10.

250 A. D. Bond, N. Feeder, S. J. Teat and W. Jonesa, *Acta Crystallogr.*, 2001, **C57**, 1157–1158.

251 F. J. Higes-Rolando, A. Perez-Florindo and C. Valenzuela-Calahorro, *Thermochim. Acta*, 1991, **186**, 43–52.

252 D. P. Martin, P. G. Blachly, J. A. Mccammon and S. M. Cohen, *J. Med. Chem.*, 2014, **57**, 7126–7135.

253 D. X. West, C. A. Brown, J. P. Jasinski, J. M. Jasinski, R. M. Heathwaite, D. G. Fortier, R. J. Staples and R. J. Butcher, *J. Chem. Crystallogr.*, 1998, **28**, 853–860.

254 G. Henrion, T. E. J. Chavas, X. Le Goff and F. Gagosz, *Angew. Chem. Int. Ed.*, 2013, 6277–6282.

255 M. J. Genin, T. J. Poel, Y. Yagi, C. Biles, I. Althaus, B. J. Keiser, L. A. Kopta, J. M. Friis, F. Reusser, W. J. Adams, R. A. Olmsted, R. L. Voorman, R. C. Thomas and D. L. Romero, *J. Med. Chem.*, 1996, **39**, 5267–5275.

256 H. A. Benesi and J. H. Hildebrand, *J. Am. Chem. Soc.*, 1949, **71**, 2703–2707.

257 R. Chotima, 2008.

258 N. Hata and I. Tanaka, *J. Chem. Phys.*, 1962, 36, 2072–2077.

259 R. Wang and Z. Yu, *Acta Phys. - Chim. Sin.*, 2007, **23**, 1353–1359.

260 S. Santajit and N. Indrawattana, *Biomed Res. Int.*, 2016, **2016**, 1–8.

261 J. A. Arnott and S. L. Planey, *Expert Opin. Drug Discov.*, 2012, **7**, 863–875.

262 J. A. Arnott, R. Kumar and S. L. Planey, *J. Appl. Biopharm. Pharmacokinet.*, 2013, **1**, 31–36.

263 L. Di, P. V. Fish and T. Mano, *Drug Discov. Today*, 2012, **17**, 486–495.

264 S. Zalipsky, *Bioconjugate Chem.*, 1995, **6**, 150–165.

265 J. R. Lakowicz, *Principles of Fluorescence Spectroscopy*, Springer Science, 2006.

266 Lumiprobe Data Sheet, https://www.lumiprobe.com/p/bodipy-tr-azide?gclid=CjwKCAjwmJeYBhAwEiwAXlg0AdwtcSnmoxMNfnrwG_MNNKUZTqbokxQalHaXNH1VuLEE6DoFVK6EMhoC6UEQAvD_BwE, (accessed July, 2022).

267 E. Khan, *ChemistrySelect*, 2021, **6**, 3041–3064.

268 Y. Ling, Z. Y. Hao, D. Liang, C. L. Zhang, Y. F. Liu and Y. Wang, *Drug Des. Devel. Ther.*, 2021, **15**, 4289–4338.

269 M. Alinaghi, K. Karami, A. Shahpiri, A. K. nasab, A. A. Momtazi-Borojeni, E. Abdollahi and J. Lipkowski, *J. Mol. Struct.*, 2020, **1219**, 128479.

270 N. J. Wheate, S. Walker, G. E. Craig and R. Oun, *Dalton Trans.*, 2010, **39**, 8113–8127.

271 S. Perontsis, G. D. Geromichalos, A. Pekou, A. G. Hatzidimitriou, A. Pantazaki, K. C. Fylaktakidou and G. Psomas, *J. Inorg. Biochem.*, 2020, **208**, 111085.

272 J. W. Walton, R. Carr, N. H. Evans, A. M. Funk, A. M. Kenwright, D. Parker, D. S. Yufit, M. Botta, S. De Pinto and K. L. Wong, *Inorg. Chem.*, 2012, **51**, 8042–8056.

273 L. E. Mihajlović-Lalić, J. Poljarević and S. Grgurić-Šipka, *Inorganica Chim. Acta*, 2021, **527**, 1–18.

274 S. J. Lucas, R. M. Lord, R. L. Wilson, R. M. Phillips, V. Sridharan and P. C. McGowan, *Dalton Trans.*, 2012, **41**, 13800–13802.

275 O. V. Dolomanov, L. J. Bourhis, R. J. Gildea, J. A. K. Howard and H. Puschmann, *J. Appl. Crystallogr.*, 2009, **42**, 339–341.

276 G. M. Sheldrick, *Acta Crystallogr. Sect. C Struct. Chem.*, 2015, **71**, 3–8.